Functional brain connectivity analysis based on the solution of the inverse problem and on covariance analysis.

José Alfonso Sánchez De Lucio

Ph.D.

University of York
Electronics

January 2015

Abstract

The Linearly Constrained Minimum Variance (LCMV) beamformer is one of the most accepted techniques used to estimate the solution of the inverse problem in functional brain dynamics studies, using magnetoencephalograms (MEG). However, since it is based on the assumption of uncorrelated brain sources, its performance decreases in the presence of correlated brain activity, compromising the accuracy of estimates of brain interactions. This problem has not stopped the use of the beamformer in techniques such as Dynamic Imaging of Coherent Sources (DICS), which estimates the functional brain dynamics in a more direct way than the LCMV, and with less computational cost. In this work it is proposed to use a modified version of the well known Minimum Norm Estimates (MNE) spatial filter to estimate the functional brain dynamics of highly correlated activity. This is achieved by using the filter to estimate the cross-spectral density matrices for the brain activity in the same way that DICS does with the LCMV beamformer. The MNE spatial filter is used as a basis because it is not affected by the presence of correlated brain activity. The results obtained from simulations shown that it is possible to estimate highly correlated brain interactions using the proposed method. However, additional methods and constraints need to be applied because of the distorted and weighted output characteristic of the MNE spatial filter. Methods such as the FOcal Undetermined System Solution (FOCUSS) and Singular Value Decomposition Truncation (SVDT) are used to reduce the distorted output, while the estimation of brain dynamics is limited to cortical surface interactions to avoid weighted solutions.

Knowing others is intelligent
Knowing yourself is enlightened
Conquering others takes force
Conquering yourself is true strength
Knowing what is enough is wealth
Forging ahead shows inner resolve

Tao Te Ching

Lao-Tzu

Contents

List of Figures

List of Tables

Acknowledgments

I would like to thank my supervisor *Dr David Halliday* for all the support and encouragement he gave me during my PhD studies and thesis.

I would like to express my gratitude to my family and friends for helping me to never forget that knowledge, effort and determination are necessary in order to achieve any goal.

I would like also to thank Antonio, Luis P., Luis F., Omer, Mike, Marco, Joao, Angela, Federico, Tiago, Karina, Vitor, Bruno, Walid, Yujung, Edgar and to all those people who made my time in the UK more pleasant.

Last but not least, I would like to thank the Mexican National Council of Science and Technology and the University of York, for give me the opportunity to pursue part of my dream.

Declaration of Authorship

I, José Alfonso Sánchez De Lucio, declare that this thesis titled, 'Functional brain connectivity analysis based on the solution of the inverse problem and on covariance analysis', and the work presented in it are my own. I hereby certify that:

- This thesis has been composed by me and is based on my own work, unless stated otherwise.
- No other persons work has been used without due acknowledgement in this thesis.
- All references and verbatim extracts have been quoted, and all sources of information, including graphs and data sets, have been specifically acknowledged.

List of publications:

- J. A. Sanchez and D. M. Halliday. Reducing the effect of correlated brain sources in MEG using a linearly constrained spatial filter based on minimum norm. In Signals, Systems and Computers, 2013 Asilomar Conference on, pages 1828 – 1832. IEEE, 2013.

Chapter 1

Introduction

1.1 Motivation

The study of the brain has been an important field of research motivated by the relevance that this organ has in many aspects of our lives, from the performing of our daily tasks, to the correct functionality of our bodies (Bear et al., 2007). However, its study has not been an easy task, as the brain is the most complex organ that can be found in our bodies (Zigmond et al., 1999). Nevertheless, advances in brain studies have helped to understand the effects that brain diseases and conditions have on our lives. For example, damage and functional degeneration of the brain, which are related with important problems such as change of behaviour and physical motor limitations (Stam et al., 2006; Stam, 2010). Brain studies have also led to developments of brain control interfaces (BCI), where the brain is used to control robotic devices with practical applications that help people with physical limitations to improve their quality of life (Schalk et al., 2004).

Part of the advances in brain studies have been possible because of several invasive and non-invasive methods developed to measure the activity generated by brain processes in the form of electric and magnetic fields (Nunez and Srinivasan, 2006; Niedermeyer and Silva, 2005; Sekihara and Nagarajan, 2008; Buxton, 2009). The methods developed for brain studies have different characteristics that enhance their applications for different types of studies. For example, non-invasive methods are easier to implement, but their measurements are not as accurate as measurements obtained using invasive methods. This decrease in the accuracy is related with external factors that reduce and distort the measurement of brain activity outside the head, and because of assumptions used in the design of the methods (Nunez and

Srinivasan, 2006; Niedermeyer and Silva, 2005; Sekihara and Nagarajan, 2008; Buxton, 2009). This brings different areas of improvements for increasing the accuracy of measurements of brain activity using non-invasive methods.

There have been several discussions about which of the signals obtained from non-invasive techniques is better to use for brain studies, between measured magnetic fields known as Magnetoencephalograms (MEG), and measured electric fields also called Electroencephalograms (EEG). These two techniques measure the brain activity generated from the same underlying brain electrical currents (Lu and Kaufman, 2003; Papanicolaou, 2009; Preissl, 2005). Both types of signals share similar characteristics, good time resolution and poor spatial resolution, especially when compared against another common non-invasive technique known as functional Magnetic Resonance Imaging (fMRI), used to measure the brain activity in the form of changes of oxygen levels in the brain's blood vessels (Buxton, 2009).

One of the main reasons for the use of EEG instead of MEG has been the expensive and complex acquisition system used in the measurements of MEG signals, which needs a special isolated room to avoid external artefacts that affects their quality. In contrast, the EEG acquisition systems are much simpler and less expensive (Malmivuo et al., 1997). Nonetheless, there has been a lot of research using MEG data to understand the brain, where techniques called spatial filters are used, these are also applied in fields such as communications and the oil industry (Van Veen and Buckley, 1988; Liu and Sacchi., 2004). Spatial filters have been used to find the active brain regions and to estimate, or reconstruct, the brain activity generated in those regions from the measured magnetic fields (Sekihara and Nagarajan, 2008; Clarke and Braginski, 2006). The implementation of these techniques has increased the use of MEG data for brain studies, by increasing the accuracy of brain activity measurements, and therefore, by improving the results obtained in different types of brain studies.

Two of the most used spatial filters for estimating brain activity from MEG data are the Linearly Constrained Minimum Variance beamformer (LCMV) (Van Veen et al., 1997), an adaptive spatial filter, and the Minimum Norm Estimate (MNE) (Hämäläinen et al., 1993), a non-adaptive spatial filter. These techniques have become the basis for MEG studies, even with the limitations that both of them have (Sekihara and Nagarajan, 2008). The LCMV beamformer has proved to be one of the most useful techniques for MEG studies as a result of the simplicity of its implementation and its robustness. Unfortunately, the LCMV performance is limited by the amount of correlation present between the brain activity found in different brain regions. The MNE is a spatial filter based on the least-squares method.

It is a useful technique and easy to implement, like the LCMV, but it has a distorted and weighed output as the magnetic fields measurements are more sensitive to cortical activity (Uutela et al., 1999).

Thus, one of the main research areas for MEG studies is the improvement of the spatial filters. This research area can be divided in two main branches, each of them related with improvements to the LCMV and the MNE spatial filters. For the LCMV case, research has focused on the filter performance reduction due to the effects of correlated activity, by reducing the spatial filter dependence to brain activity located in multiple regions (Brookes et al., 2007; Dalal et al., 2006; Huang et al., 2004). On the other hand, MNE research has focused on the reduction of the distorted and weighted output of the filter, by using complementary regularization techniques to focus the brain activity on their correct locations (Gorodnitsky and Rao, 1997; Pascual-Marqui, 2002; Mosher and Leahy, 1998). The results obtained with these improvements have shown that it is possible to increase the performance of spatial filters, and therefore, the accuracy of brain studies.

A different approach known as Dynamic Imaging of Coherent Sources (DICS) (Gross et al., 2001) has been implemented based on the LCMV spatial filter. This filter is used to estimate the covariance matrix, or the cross-spectral density matrix in the frequency domain, between different brain regions. Thus, DICS allows a more direct estimation of the functional brain dynamics. Nevertheless, the DICS approach also has areas of improvements, especially since it is based on the LCMV spatial filter, which decreases its performance depending on the amount of correlation present among the activity present in different brain regions (Sekihara and Nagarajan, 2008). However, the LCMV has proved to have good performance, especially when prior information is available, and in the presence of not highly correlated brain activity between distant brain regions (Sekihara and Nagarajan, 2008).

The motivation for this work is the improvement of the covariance matrix estimation, or the cross-spectral density matrix in the frequency domain, among different active brain regions from MEG data. This relies on the previously mentioned spatial filters as a starting point, by using them in the same way that DICS does. Improvements in the estimation of those matrices could help functional brain dynamics studies, not only because the approach is more direct than the normal one followed, but also because it can increase the accuracy of estimates. This work has also been motivated for the use of spatial filters in different fields, which give different perspectives and tools that can be used for their improvements. A study based on this problem can also help to increase understanding by trying different approaches

based on spatial filters modifications, and, as a consequence, it could also help to increase the understanding of the limitations of spatial filters.

1.2 Literature review

1.2.1 Beginnings of neuroscience

Neuroscience is a very old discipline, however it started as a well organised research field in the late 1960*s*. Nowadays, it is a discipline that unites different fields related with the study of the brain. This synergy among different brain research areas was born in order to share a common language, common concepts and a common goal among people studying the brain (Zigmond et al., 1999). However, the understanding of the brain as a vital organ started in prehistoric times, as the evidence suggests with the findings of hominid skulls from more than a million years old that show cranial-damage, presumable inflicted by other hominids (Bear et al., 2007). Trephination provides more evidence from 7000 years ago, when people drilled holes in other people skulls in order to cure brain conditions (Bear et al., 2007). Nonetheless, even when the importance of the brain was known, the brain was not considered the most important organ until the end of the eighteenth century.

Since the beginning of our understanding as a specie, and until the appearance of Hippocrates, the heart was considered the place where consciousness and intelligence were generated, while the brain was treated with complete indifference (Finger, 2001). In the fifth century B.C. the perception of the brain started to change, when several Greek scholars consider the brain as the responsible organ for sensations, to be more specific, when Hippocrates stated his belief about the brain as the responsible organ for intelligence (Bear et al., 2007). However, this new perception of the brain was not universally accepted, because other important philosophers such as Aristotle, could not believe that the heart was not the main reason for intelligence. Then, Aristotle proposed that the function of the brain was to cool down the blood that was overheated in the heart, instead of being the main reason for intelligence(Bear et al., 2007).

In the second century A.D., the Roman physician Claudius Galenus, under the influence of Hippocrates and Aristotle, helped with the understanding of the brain by providing directives for brain dissection (Finger, 2001). He also changed the brain perception to an organ related with the physical sensations and with generation of movements (Finger, 2001). Galen embraced Hippocrates vision of the brain, however, Galen did not believe that the brain was the organ responsible for intelligence, but an organ composed of ventricles, as the heart,

where sensations and muscle actions were stored until they were needed (Bear et al., 2007). He stated that sensations and muscle actions were sent to the brain ventricles from the left ventricle of the heart, and then, were sent to the muscles, through the nerves, in order to generate movements or sensations when required (Finger, 2001).

Galen's vision of the brain remained unchanged for almost 1500 years, until philosophers, such as Rene Descartes, started questioning that statement (Bear et al., 2007). Descartes denied that the ventricles were responsible for the generation of complex sensations and movements, he also stated that non-human animals do not have any sensations in the same way that the human mind does (Bennett et al., 2003). The sensations and movements generated in the ventricles, and transmitted through the nerves, were called animal spirits, a term popularized by Galen to refer to invisible entities that flowed through the nerves to control the body functions (Finger, 2001). Descartes proposed that the brain was in charge of human behaviour only when this resembles the behaviour of beasts. He also believed that the mind was a spiritual entity in charge of receiving sensations and generating movements by using the pineal gland as a control mechanism (Bear et al., 2007), Figure 1.1. The mind was not considered as part of the brain (Bear et al., 2007).

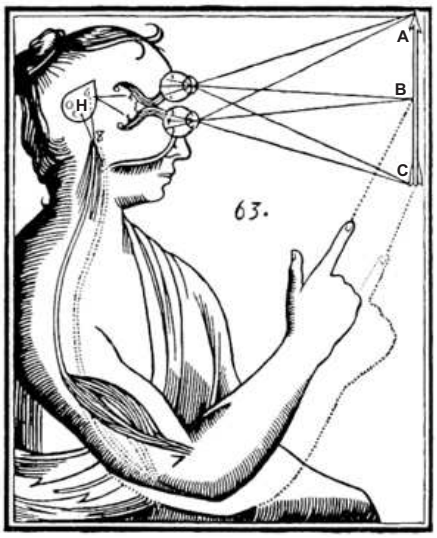

Figure 1.1: Illustration that describes the brain according to Descartes[1]. The figure shows the hollow nerves and the brain ventricles, also the pineal gland (H), used by the mind to control the animal spirits (Bear et al., 2007).

[1]Image from *http://en.wikipedia.org/wiki/Dualism_(philosophy_of_mind)*

1.2.2 Functional localization of the brain

During the seventeenth and eighteenth centuries studies of the brain took a different path from the one established by Galen and Descartes. This change started when Thomas Willis reached the conclusion that the physiological characteristics of humans are functionally dependent on the brain cortex, instead of the ventricles (Bennett et al., 2003). He found the relation between the brain function and the gyrus, or hills on the brain surface. He also compared the number of gyri present in the human brain with the brain of animals, and stated that the number of gyri is much more in the human brain than in animals brains because of the superior intellectual power of human beings (Bennett et al., 2003). Another important contribution for the brain understanding was made by Domenico Mistichelli and Francois Pourfour du Petit, they described the crossing over nerves in the spinomedullary junction known as the pyramid (Bennett et al., 2003).

More important discoveries were made during the 1700s and 1800s, when Antoine Charles de Lorry and Jean-Cesar Legallois discovered the respiratory centre, and when Charles Bell and Francois Magandie defined important functions for the nervous system. Charles de Lorry challenged the predominant idea in the 1700s about the medulla and the cerebellum, when they were considered an extension of the spinal cord and the seat for the animal spirits, respectively. He found that the medulla is the site of vital functions, and later, Legallois complemented Lorry's work with the finding of the respiratory centre, the part of the medulla that is in charge of respiration (Finger, 2001). On the other hand, Bell and Magandie helped with the change of the predominant perception, at that time, about the spinal nerves, when they were considered as mixed sensory and motor structures where messages could travel in both directions at the same time. Both of them helped brain studies by discovering that the dorsal roots of the spinal cord are sensory, whereas the ventral roots are related with motor actions (Finger, 2001).

By the end of the eighteenth century the nervous system was completely dissected, and its raw anatomy was described in detail. Furthermore, scientists recognized the different parts of the nervous system, consisting of the central nervous system (CNS), or the brain and the spinal cord, and the peripheral nervous system (PNS), composed of the network of nerves found in the rest of the body (Bear et al., 2007). Another important discovery was the general pattern of gyrus, or hills, and sulcus, or valleys, on the brain surface, which could be generally identified in the brain surface of every individual (Bear et al., 2007). The patterns allowed scientists to identify the cerebrum divisions as lobes. It was the basis for the conjecture that

different brain functions are related with the gyrus of the brain (Bear et al., 2007).

Franz Joseph Gall is one of the main persons responsible for the era of cortical functional localization. Gall stated that human skull features were an indication of underlying brain processes generated in specific cortical regions that were correlated with specific talents or behaviours (Bear et al., 2007), Figure 1.2. However, even when this theory, known as Phrenology, was visionary, it was not well accepted among the contemporary scientist of its era. Marie-Jean-Pierre Flourens, known for his influence in the development of the ablation method to study the brain, was one of the main persons that opposed Galls phrenology theory (Finger, 2001). Flourens argued that the cerebral cortex could not be divided into functional units. Instead, he believed that the brain cortex functioned as a whole (Finger, 2001). As was proved later, the Gall's idea about the different functions in the brain cortex was correct, but he did not use the correct method to prove this theory. Nonetheless, validation of the functional brain cortex was possible because of brain damage, and brain stimulation techniques, techniques promoted by Flourens (Finger, 2001).

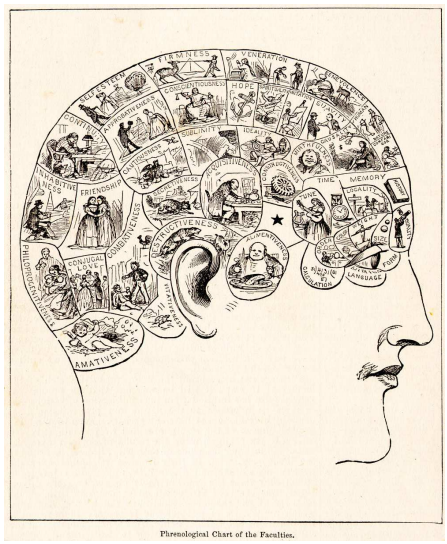

Figure 1.2: An 1883 phrenology chart[2].

Studies of localized functions in the brain cortex continued, and important contributions were made by Paul Broca, Eduart Hitzig, Gustav Fritsch, and Sir David Ferrier (Finger, 2001). They helped in defining the brain cortex locations related with specific brain functions. Broca's brain study helped with the acceptance of the idea of cortical localization. This was possible with his study of a brain in poor condition due to infractions in the left frontal lobe, a brain that belonged to a patient that could understand language, but could not speak because of the brain damage (Finger, 2001; Bear et al., 2007). Then, Broca concluded that

[2] Image from *http://en.wikipedia.org/wiki/Phrenology*

the frontal lobe is the region of the human cerebrum that is responsible for the production of speech (Bear et al., 2007). Eduart Hitzing and Gustav Fritsh helped with the understanding of the different functions of the cortex. They proved that cortical localization was not limited to a single function. They discovered that part of the cortical surface was responsible for generation of movements, by applying an electrical stimulation to a specific part of a dog brain (Finger, 2001). Then, Sir David Ferrier complemented Hitzing and Fritsh's discovery by reproducing their work with monkeys in order to produce detailed maps of localized cortical functions (Finger, 2001).

The acceptance of functional localization of the brain cortex was supported by the development of cytoarchitectonic studies of the cortex, electrophysiological recordings from the brain, and the belief that the neurons are independent entities (Finger, 2001). The functional localization of the brain cortex was supported in the early twentieth century in a different way from that of Ferrier. Instead, it was supported by the physiological characterization of the brain cortex, when the fine anatomy of the brain was revealed following the efforts of anatomists Oscar Vogt, Cecile Vogt, Alfred Walter Campbell, and Korbinian Brodmann (Finger, 2001). They discovered that there exist areas in the cortex that share similar structures and cellular compositions, and are clearly different from the characteristics found in other areas of the brain (Finger, 2001; Penfield and Jasper, 1954), Figure 1.3.

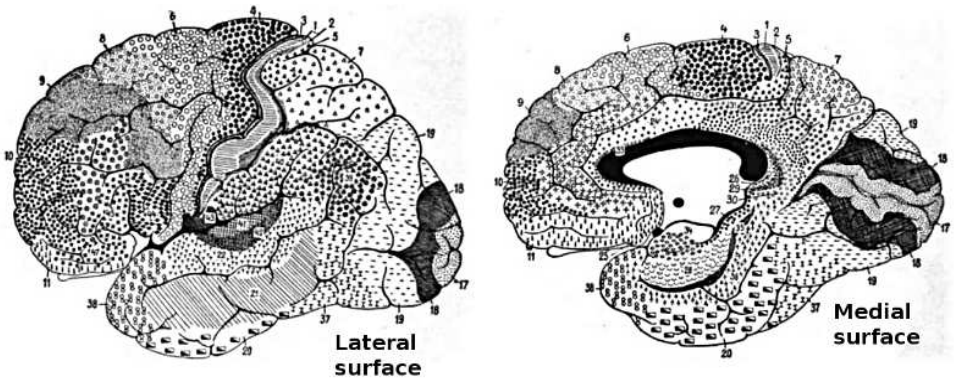

Figure 1.3: Brain areas with different cytoarchitectural organization defined by Brodmann[3].

A different approach was used by Richard Caton to support functional brain localization. His research was based on Ferrier's description of stimulation of the brain cortex (Finger, 2001). Caton used a mirror galvanometer to amplify very small voltage signals that were measured on a large scale placed on a wall, in order to measure the brain activity in the form of weak electrical currents (Niedermeyer and Silva, 2005; Greenfield et al., 2012). Caton found that

[3] Figure adapted from *http://en.wikipedia.org/wiki/Korbinian_Brodmann*

interrupting a light stimulus to a dog eye altered the electrical currents detected on the other side of the dog's head, where the measurements were made with electrodes placed at two points of the dog head, or one electrode in the brain cortex, and the other on the surface of the skull (Greenfield et al., 2012). Caton reported, from the results of his experiments, that the electrical changes in the brain varied in location and with the peripheral stimulus, supporting cortical function localization (Finger, 2001). In 1942, Hans Berger achieved the first recording of electrical potential from a human brain. Nowadays, this field of study is known as electroencephalography (Niedermeyer and Silva, 2005).

1.2.3 The neuron doctrine

The neuron doctrine was the last proof for cortical function localization, which presents the neuron as the independent elementary unit for brain function. This was the last proof because cortical localization demanded some degree of independence (Jirsa and McIntosh, 2007). The neuron doctrine was possible because of improvements in the microscope design, which allowed scientists to obtain high magnification low distortion images, and therefore, generated better images of the brain. It was also possible because of Camillo Golgi, who improved histological techniques by developing a new silver nitrate staining method which allowed the analysis of the elements in the nervous system with more precision than with the available staining methods at that time (Finger, 2001).

However, Golgi stated, based on the results that he obtained with his method, that the brain elements were not independent, but they were fused forming a complex network, opposing the cortical functional localization theory. Santiago Ramon y Cajal obtained different results based also on the Golgi method, but with the difference that he tried to get better results by making thicker slides of the brain which were stained more intensively, Figure1.4. Thus, Ramon y Cajal found the basis for the neuron doctrine, which states that neurons are independent elements that do not form physical connections with other neurons (Finger, 2001). Then, Sir Charles Scott Sherrington found the gap between neurons, and between neurons and muscles. He called those junctions synapses, where the communication between neurons, and neurons and muscles, takes place in the form of a chemical process to transmit information (Finger, 2001).

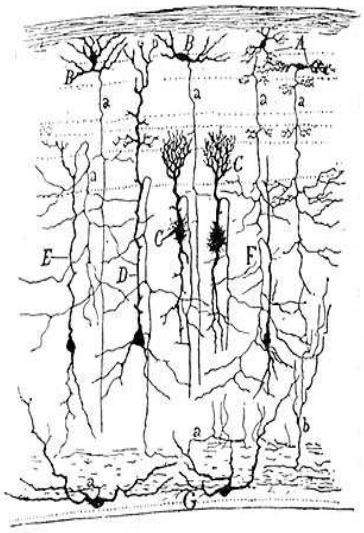

Figure 1.4: Ramon y Cajal original draw. A section of the optic tectum of a sparrow, Madrid 1905.

1.2.4 Modern neuroscience

The increment in neuroscience developments reached its higher point around 1960, after 30 years of maintained progress. Since then, the amount of progress started to decrease, mainly because of computers, which allowed automatic analysis of brain data, making brains studies easy to implement reducing the necessity of developing new methods. However, this was not the first time computers were used to analyse the brain. In 1932, Berger's co-worker Dietsch, along with other important researchers, used analogue computers for this purpose (Niedermeyer and Silva, 2005). However, the increase of computational processing started a second tendency for their use, reaching a point to be considered as a new field for brain study known as computational neuroscience. Computational neuroscience is formally defined as the theoretical study of the brain used to uncover the principles and mechanisms that define the different nervous system processes (Trappenberg, 2002).

Nowadays, neuroscience is considered the field for the brain study, from its molecular biology, to the biological basis for normal behaviours, cognition, diseases and brain conditions (Zigmond et al., 1999). Neuroscience is rapidly growing and has more tools available for the study of the brain than ever. The measurements of brain activity achieved by Richard Caton and the increase of the computational processing available have led to the development and implementation of different ideas and techniques that have increased understanding of the brain. Improvements in the methods used to obtain the brain activity have allowed analysis of the brain in more scenarios and provided data with better quality than before. On the other hand, the amount of data that can be analysed has dramatically increased because of

the computational processing increment.

The discovery reported by Richard Caton in 1875, and the reproduction of its work in human beings by Hans Berger in 1929, were the beginning for the development of different non-invasive techniques. These techniques made possible the measurements, outside the head, of the three main processes that occurs inside the brain, neural signalling, the metabolism of neurons, and brain blood flow (Preissl, 2005). The measurements of these processes with non-invasive techniques allows a different understanding of the brain compared with the invasive techniques, and hence, a more wide understanding of the brain functional organization, which has been one of the most important problems over the last 100 years (Buxton, 2009).

On the other hand, the increment of the computational precessing has allowed the analysis of data that represents brain activity using different signal processing techniques such as the Fourier transform and spatial filters. The use of computers has also allowed the modelling of brain processes, like the neuronal signalling and brain interactions (Trappenberg, 2002). Therefore, computational neuroscience has allowed different ideas to be tested with simulations analysis that later on are implemented in real experiments. This is in order to have certainty that the models and methods developed work, and to know their limitations.

1.2.5 Non-invasive techniques for brain studies

Three of the most important non-invasive developed techniques to study the brain are the Electroencephalography (EEG), the Magnetoencephalography (MEG) and the functional Magnetic Resonance Imaging (fMRI). EEG is a technique developed from the results of Berger's and Caton's work. It is a technique used to record human brain electric fields on the surface of the head, generated from the brain electrochemical process known as neural signalling (Clarke and Braginski, 2006; Papanicolaou, 2009). MEG is a technique based on the discovery made by David Cohen in 1968, who showed that it was possible to measure, or record, magnetic fields outside the head generated from the same processes that generate the EEG voltages (Preissl, 2005; Baillet et al., 2001). The fMRI technique was developed by William James in 1890, who based his work on Angelo Mosso's work. It is a technique that measures, or images, functional brain activity by measuring changes in the brain blood flow (Buxton, 2009).

The previously mentioned techniques share similar characteristics, but also have differences that determine their applications for diverse types of studies. For example, EEG and MEG techniques have very good time resolution, but poor spatial resolution, especially when com-

pared against fMRI, which has good spatial resolution but poor time resolution (Hansen et al., 2010). Thus, EEG and MEG give a different perspective of brain behaviour with respect to fMRI. However, even when EEG and MEG have similar characteristics, differences can be found between the performance of both of them that can enhance the use of one over the other for specific studies. MEG records are not affected by the different layers that compose the head, in contrast to EEG, but EEG can measure brain activity in the whole cortex, while MEG records are more sensitive to neuronal currents tangential to the surface of the brain (Niedermeyer and Silva, 2005).

1.2.6 Magnetoencephalography

The first measurement of magnetic fields outside the head generated by electric brain currents was made by Cohen, and was achieved using a conventional induction coil of two million turns of wire in a room temperature environment (Senior et al., 2006; Niedermeyer and Silva, 2005). Since that event, the way that magnetic fields are measured has changed over the last three decades because of the development of the Superconducting QUantum Interference Device (SQUID) sensor, that was used for the first time to measure magnetic fields generated by brain currents in 1972 (Vrba, 2002; Lu and Kaufman, 2003). Nevertheless, the use of SQUIDS requires expensive instrumentation and, most of the time, isolated shielded rooms in order to reduce the effects of external noise, which can make the cost of MEG acquisition systems at least 25 times the cost of the EEG acquisition system (Malmivuo et al., 1997). This difference in price is one of the reasons that has limited the use of the MEG technique.

Nowadays, and since the early 1990s, different high-density MEG acquisition systems are able to measure, or record, magnetic fields in the whole head using a high-density grid composed of more than 200 SQUID sensors (Hansen et al., 2010; Clarke and Braginski, 2006). SQUID sensors are used because of their high sensitivity to magnetic fields, even when these have very small amplitudes, as is the case for the MEG signals, which have a strength in the order of pico to femto Teslas (Clarke and Braginski, 2006; Pizzela et al., 2001). The instrumentation required for the use of the SQUIDs sensors is expensive because it is composed of parts such as a cooling block containing cryogenic liquid and a shielded room (Clarke and Braginski, 2004; Pizzela et al., 2001; Vrba and Robinson, 2001), Figure 1.5. The cooling block is required to maintain the temperature for the super conductive sensors, in order to work properly, while the shielded room is necessary to reduce the effects of the external sources, which are stronger than the brain magnetic fields, as can be observed in Figure 1.6.

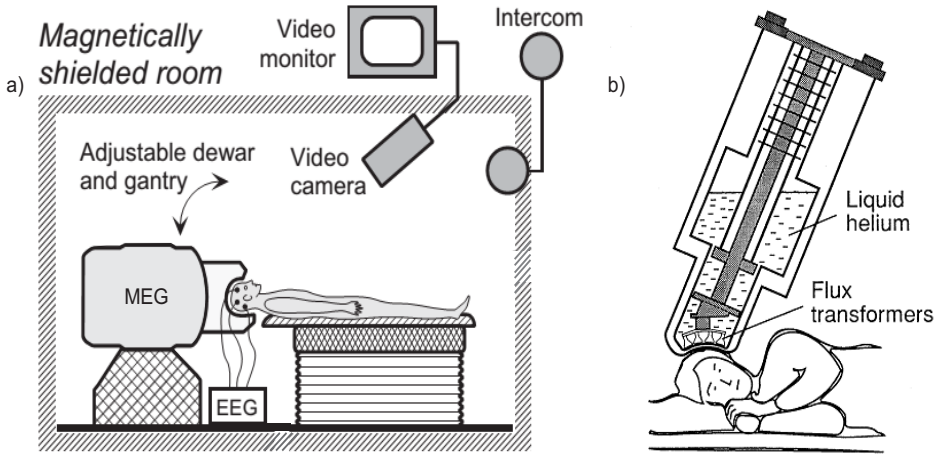

Figure 1.5: MEG acquisition system. a) Shielded room used to reduce interferences from the outside[5]. b) Instrumentation required for the use of the SQUIDs sensors[6].

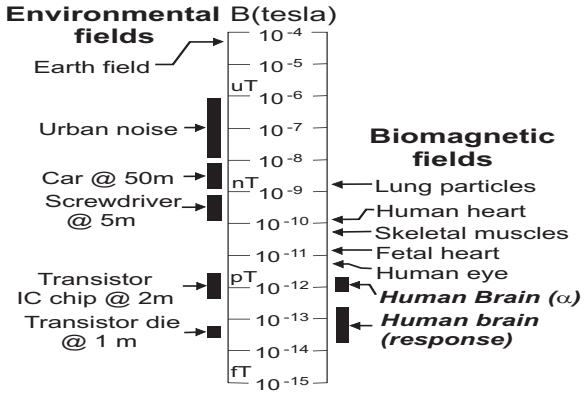

Figure 1.6: Range of strength of various magnetic fields sources[5].

The SQUIDs are superconducting rings, or washers, that consist of two superconductors separated by insulated layers that form Josephson junctions (Vrba and Robinson, 2001; Clarke and Braginski, 2004). The sensors combine the flux quantization and Josephson tunnelling effects to measure magnetic fields generated by the brain activity (Clarke and Braginski, 2004). The magnetic flux is coupled to the SQUIDs using superconductive flux transformers (Vrba and Robinson, 2001). Then, the Josephson junctions are used to quantify the flux in order to measure the effect of the magnetic fields on the sensors, in the form of electric voltages that are known as MEG signals (Clarke and Braginski, 2004). Therefore, a MEG record represents the brain activity generated by electrochemical processes known as neuronal signalling (Papanicolaou, 2009; Hansen et al., 2010). These measurements are used to study

[5] Figure adapted from (Clarke and Braginski, 2006)
[6] Image from (Hämäläinen et al., 1993)

the brain based on the Neuromagnetism principles, which is defined as the study of the magnetic fields generated from electrical currents inside the brain (Clarke and Braginski, 2006; Hansen et al., 2010; Lu and Kaufman, 2003).

1.2.7 MEG forward and inverse problems

It is necessary to solve the forward and inverse neuromagnetism problems in order to study the brain using MEG data (Sarvas, 1987; Hämäläinen et al., 1993; Mosher et al., 1999). The forward problem consists of the measurements of magnetic fields outside the head generated by the brain electrical activity, while the inverse problem consists in the finding of the distribution of current inside the brain that are responsible for the generation of the measured magnetic fields. These problems are the core of MEG studies, and many assumptions and constraints are used for their solutions.

The forward problem is solved with the use of the Biot-Savart law, which describes magnetic fields generated by electric currents (Cheng, 1989; Griffiths and College, 1999), that in the brain are represented by neuronal currents generated by the neurosignalling process (Hämäläinen et al., 1993; Sarvas, 1987). The Biot-Savart law estimates the three components of the magnetic fields, but the magnetic fields measured by the SQUIDs are only those components that are normal to the surface of the sensors. Then, a dot product is required between the estimated magnetic fields and the orientation of the SQUIDs (Hämäläinen et al., 1993; Sarvas, 1987). It is possible to use the Biot-Savart law because of the characteristics of the neuronal currents responsible for the generation of the magnetic fields, which have a range of frequencies below 1 kHz (Baillet et al., 2001; Vrba and Robinson, 2001). Then, the forward problem can be seen as a magnetostatic problem, where the magnetic fields are generated by steady currents (Cheng, 1989; Griffiths and College, 1999).

One of the main issues with the solution of the inverse problem is its non-unique solution, as the problem can be seen as an undetermined system where there exist more uncertainties than the amount of information obtained from the sensors (Clarke and Braginski, 2006; Hämäläinen and Ilmoniemi, 1994). Therefore, there are always ambiguities with the estimated solutions since these can correspond to different electrical brain current distributions that generate the same magnetic fields as the ones that are found solving the forward problem (van Drongelen et al., 1996; Lütkenhöner, 2003). The inverse problem solution requires the discretization of the space that contains the brain electrical currents in order to look for the brain activity, where the defined locations are known as voxels (Clarke and Braginski, 2006). Once the

voxels are defined, it is possible to estimate the solution of the inverse problem based on regression analysis (Hämäläinen et al., 1993; Sekihara and Nagarajan, 2008).

1.2.8 The Biot-Savart law

The Biot-Savart law allows the estimation of magnetic fields generated by electrical currents, as is presented in Equation 1.1, where $\mathbf{r}$ and $\mathbf{r}_i$ represent the locations where the magnetic fields are measured and the locations for the electrical currents, respectively. Moreover, μ_0 and $\mathbf{J}$ represent the permeability of the free space and the continuous electrical current distribution responsible for the generation of the magnetic fields, respectively.

$$\mathbf{B}(\mathbf{r}) = \frac{\mu_0}{4\pi} \int \mathbf{J}(\mathbf{r}_i) \times \frac{\mathbf{r} - \mathbf{r}_i}{|\mathbf{r} - \mathbf{r}_i|^3} dv' \tag{1.1}$$

As was mentioned before, the solution of the forward problem is related with the Biot-Savart law. Thus, in the neurogmanetism context the continuous electrical currents distributions are represented by the electrical brain currents responsible for the generation of the brain activity, while the measured magnetic fields are the obtained MEG data. Therefore, the locations where the magnetic fields are measured are determined by the SQUIDs locations, while the locations where the brain activity is generated are represneted by the voxels obtained from the discretization of volume used to represent the brain.

The complexity of the Biot-Savart implementation in MEG studies is related with the way the brain currents and the brain volume are modelled, as their characteristics affects the measurements of the magnetic fields (Hämäläinen et al., 1993; Sarvas, 1987; Williamson and Kaufman, 1981). The brain currents can be modelled considering all their components, as is explained in Chapter 3. However, this increase the complexity of the Biot-Savart law implementation because in most cases not all the components affects the measurements. On the other hand, the brain volume can also be simplified in order to reduce the complexity of the problem, for example using a spherical volume to represent the brain.

It can be said that the neuromagnetism expression for the Biot-Savart law consists of two main parts, the sensitivity of the sensors to electrical sources located in the brain, and the electrical brain sources responsible for the generation of the magnetic fields. The sensitivity profile of the sensors to a source located at a specific location is obtained using unit strength dipoles oriented on each of the three main axes, in order to represent the effects of the brain source components. Thus, the sensitivity of the sensors for that brain source is obtained by

estimating the magnetic fields produced for each of the three dipoles, where the effects can be combined using the magnetic fields superposition property (Malmivuo, 2000; Sekihara and Nagarajan, 2008; Lu and Kaufman, 2003). These sensitivity components are known as the leadfields, and are composed of the sensitivity of M sensors to the three components of a brain source located at a specific location.

1.2.9 Spatial filters

Most approaches used to estimate the inverse problem solution are normally regression based on the least-squares method and on Lagrange multipliers. The non-adaptive spatial filter Minimum Norm Estimate (Hämäläinen et al., 1993) and the Linearly Constrained Minimum Variance beamformer, an adaptive spatial filter (Van Veen et al., 1997), are the most common approaches that represent these two methods. The estimation, or reconstruction of brain activity, is possible using a set of weights that define the filters, designed to allow the estimation on specific locations while the activity located on different locations is reduced. The characteristics and mathematical expressions of the spatial filters can be observed better in Sections 3.3.1 and 3.3.2, for the MNE and the LCMV, respectively.

The MNE and the LCMV spatial filters have advantages and disadvantages with respect to each other. The MNE spatial filter is not affected by the presence of correlated brain activity as it is not adaptive (Kumihashi and Sekihara, 2010; Sekihara et al., 2005). However, since it is based on the least-squares method, it presents a biased solution in favour of solutions near the sensors, and a distorted output because of the the external noise effects (Gorodnitsky et al., 1995; Clarke and Braginski, 2006; Kumihashi and Sekihara, 2010). On the other hand, the LCMV has a solution that does not have a considerable bias, but its performance decreases in terms of the amount of correlation that exists between the neuronal currents (Sekihara et al., 2002). This decrease in performance happens because the spatial filter was built under the assumption that brain sources responsible for the generation of magnetic fields are uncorrelated (Van Veen et al., 1997; Sekihara and Nagarajan, 2008).

Therefore, the performance of MNE and the LCMV spatial filters depends on the characteristics of the brain studies, even when it is impossible to have complete certainty of how much correlated is the activity or where this is located the brain activity (Sekihara et al., 2002; Schoffelen and Gross, 2009). However, in auditory brain studies highly correlated brain activity is expected, and then, it is expected that the LCMV beamformer will have a low performance. On the other hand, the MNE should have a good performance in brain studies

related with expected cortical brain activity, as for example studies related with the brain motor cortex region.

The uncorrelated brain sources assumption and the weighted solution characteristic of the MNE spatial filter have been important issues in the research fields of brain sources reconstruction and imaging, and as a result important techniques have been developed for their improvement. This has resulted in techniques such as the FOcal Undetermined System Solution (FOCUSS) (Gorodnitsky and Rao, 1997), the standardized Low Resolution Electromagnetic Tomography (sLORETA) (Pascual-Marqui, 2002), the Multiple-Signal Classification algorithm (MUSIC) (Mosher and Leahy, 1998), the dual-core beamformer (Brookes et al., 2007; Diwakar et al., 2011), the null-beamformer (Dalal et al., 2006), and a beamformer based on the use of a high order covariance matrix (Huang et al., 2004).

Nonetheless, the previously mentioned techniques do not modify the design of the spatial filters used as a basis. The techniques unclude improvements that are related with the way the spatial filters are implemented, or use small additions to their design. For example, the FOCUSS algorithm uses the MNE estimated activity as a filter in order to reduce the finding of false brain estimations, while the null beamformer and the dual-core beamformer add one more location to the LCMV filter design in order to consider, or to remove, the effects present on the extra location. More complex solutions can be found on the sLORETA and the MUSIC algorithms, implementing a non-linear search and a search based on the standard deviation and on the estimated activity to find the locations with the real brain activity, respectively.

The estimation for the inverse problem solution, in the neuroscience context, is a research area where a lot of contributions can still be made, especially with current techniques that have been positioned as standard tools to study the brain using MEG signals (Sekihara and Nagarajan, 2008). These techniques are very similar, even when the methods used to estimate the weights that define the filters look different (Mosher et al., 2003). Research has been implemented in order to reduce the effects of correlated brain activity and the biased solutions on the spatial filters. However, research has also been developed to reduce the artefacts generated by the external noise and the linearity between the leadfields, as these also affect the performance of spatial filters (Sekihara and Nagarajan, 2008).

The techniques presented to solve the inverse problem rely on the inversion of the product between the leadfield vectors, or on the expression for the covariance matrix of the measured magnetic fields, which in some sense also depends on the leadfield vectors, which are used to map the brain activity sources from the source domain to the sensor domain (Van Veen

et al., 1997). A problem is present for the MNE when the leadfields for different locations are linearly dependent, which causes numerical instability in the inversion of the product between the leadfields vectors, and hence, it requires the use of regularization techniques for the inversion of the matrix (Hämäläinen et al., 1993; Sarvas, 1987). The LCMV beamformer does not present that problem but its performance is sensitive to errors in the calculations of the leadfields (Sekihara et al., 2001).

The external noise is an important factor as it is not considered in the design of the spatial filters causing the estimation of false brain current distributions (Sarvas, 1987; Van Veen et al., 1997). Most studies based on the spatial filters consider the noise as Gaussian uncorrelated noise, which nowadays is a reasonable assumption using state-of-the-art noise reduction methods (Imada, 2010). The MNE deals with noise by reducing the number of eigenvalues in the inversion of the leadfields product matrix, unfortunately this also reduces the accuracy of the estimated brain sources time series (Sarvas, 1987). The LCMV reduces the effect of noise using the matrix inversion lemma in order to find the form of additive noise in the output of the filter, and therefore, the output of the filter is regularized to reduce the noise (Van Veen et al., 1997; Huang et al., 2004).

The estimation of underlying brain sources from MEG data is a problem that has been improved over the last four decades. However, there still exists many problems that make the current techniques to fail, depending on the characteristics of brain studies and on environmental factors. A priori knowledge of possible active brain regions can reduce the finding of spurious activity (Jirsa and McIntosh, 2007), also the combination of MEG, EEG and fMRI techniques (Preissl, 2005; Handy, 2009). The inverse problem solution is used in different types of studies to have a better understanding of the brain. In brain dynamics studies the estimated solution of the inverse problem is used in metrics such as correlation and spectral coherence in order to find any relationships that exist between the different brain regions.

1.2.10 Magnetoencephalography and brain dynamics

The study of brain interactions is an important field in neuroscience that helps to understand the effects that different brain regions have on other regions. The interactions are possible because the brain is able to perform, at the same time, many cognitive processes generated in different brain regions that interact between them in order to achieve more complex processes (Schoffelen and Gross, 2011; Fingelkurts et al., 2005). Thus, interactions between brain regions are known as brain dynamics, and can be classified into three dif-

ferent categories known as the structural connectivity, the functional connectivity and the effective connectivity (Sporns, 2011; Sporns and Tononi, 2007), Figure 1.7. The structural connectivity, or anatomical connectivity, are the physical connections between neurons and the networks of the brain, while the functional and the effective interactions are those generated by coordinated activity of different brain regions, with the difference that the effective connectivity also shows the direction of those interactions, often interpreted as causality.

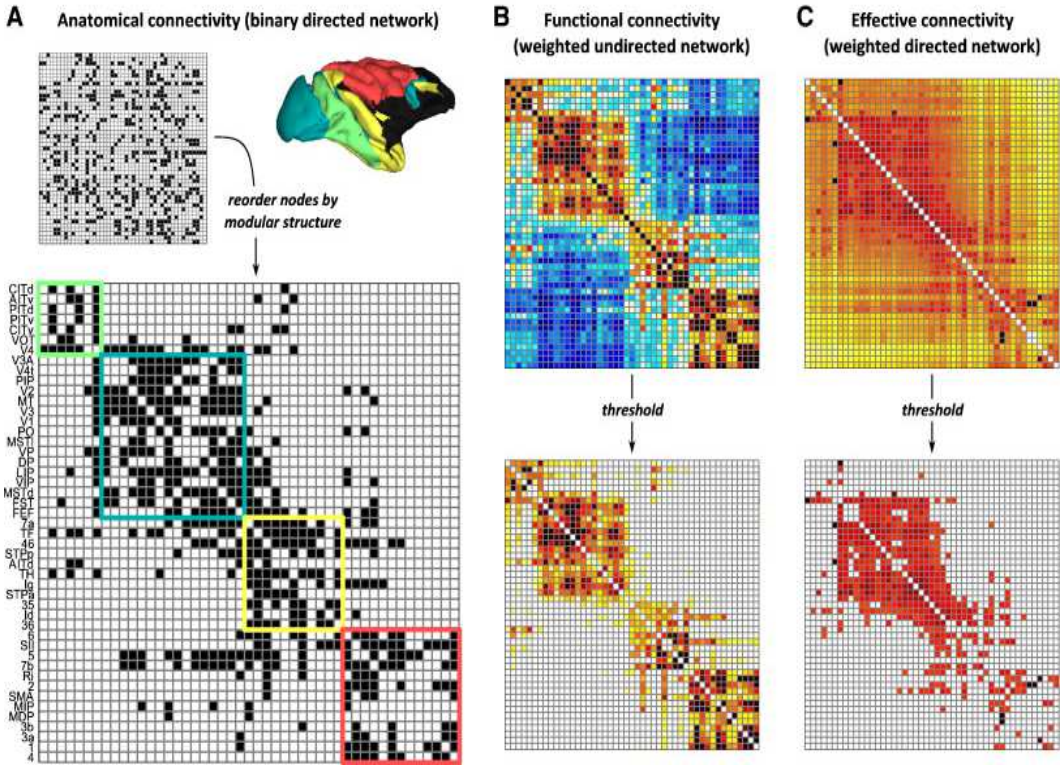

Figure 1.7: Representation of anatomical, functional, and effective connectivity networks[7]. A) Represents an anatomical network of a macaque cortex, in the form a cortical map and with a cross-correlation matrix. B) Top, Functional connectivity network represented by a cross-correlation matrix, in the bottom is presented the matrix thresholded to remove negative and self-self correlations. C) Top, effective connectivity network, obtained with inter regional transfer entropy, in the bottom is presented the same matrix thresholded to maintain the strongest connections.

Brain functional dynamics obtained from MEG data are normally calculated in the source space rather than in the sensor space, because of the magnetic fields spread effect (Dalal et al., 2008). It is necessary to use the inverse problem solution in order to estimate the functional interactions by calculating the correlation coefficient between the estimated brain currents in the time domain (Schoffelen and Gross, 2009), or by calculating the spectral coherences in the frequency domain (Jerbi et al., 2007). The accuracy of the brain interactions calculations depends on the performance of the spatial filters to solve the inverse problem for the time domain case, while for the frequency domain case also depends on techniques such as the

[7] Image from (Sporns, 2011)

Welch periodograms (Welch, 1967) and the multitaper approach (Percival and Walden, 1998). Moreover, there exist other approaches to estimate the brain dynamics using MEG data, as the Dynamic Imaging of Coherent Sources (DICS) (Gross et al., 2001) and the use of a neural mass model (David et al., 2004).

DICS is a technique based on the estimation of the covariance matrices of the brain sources in the time domain, or on the estimation of the cross-spectral density matrices in the frequency domain. It uses the estimated cross-spectral matrix to obtain metrics for brain sources relationships using singular value decomposition, where the metrics, in combination with the calculation of the spectral coherences, gives an estimation of the functional brain dynamics (Gross et al., 2003). The main advantage that DICS has against the normal approach is its computational efficiency, if we are interested in looking for all possible interactions among the different brain regions. However, more information regarding the brain currents can be obtained in the normal approach, as these are needed for the estimation of the brain sources time series in order to estimate their spectrum. On the other hand, DICS only gives metrics based on the covariance matrices between the brain sources, or on the cross-spectral density matrix in the frequency domain case. It does not give more information about the distribution of currents that generate the magnetic fields (Gross et al., 2001).

The DICS approach has the same limitations as the LCMV, which is expected as it is based on the LCMV beamformer, which decreases its performance in the presence of correlated brain activity (Sekihara and Nagarajan, 2008). Nevertheless, it is not common in brain studies to deal with highly correlated activity among distant brain regions (Liljeström et al., 2005). This gives the use of DICS a justification to be implemented, even when the assumption used as a base for the LCMV, and then for DICS, contradict its use for brain dynamics studies (David et al., 2003). The use of the LCMV as an independent tool from DICS to estimate the functional brain dynamics gives the same results as DICS, if the singular value decomposition used in DICS is implemented with the LCMV, which is expected as DICS is a modified version of the LCMV (David et al., 2003). On the other hand, the use of the MNE spatial filter has proved to be able to estimate the brain sources oscillatory activity, and therefore, brain dynamics (Jensen and Vanni, 2002; Liljeström et al., 2005). The use of the MNE to estimate the brain dynamics is obtained by spatial filtering the spectrum of the measured magnetic fields, and then, by calculating the spectral coherences between them, where the use of the Welch periodograms has shown to be a good tool to estimate the spectrum of brain sources (Jensen and Vanni, 2002; Liljeström et al., 2005).

The use of the previously mentioned approaches based on the MNE and the LCMV spatial filters have proved to be useful for the estimation of functional brain dynamics (Schoffelen and Gross, 2011, 2009; David et al., 2003; Liljeström et al., 2005). However, the same studies have also remarked that there exist many problems related with the way in which the brain dynamics are estimated, especially because of the presence of highly spurious interactions between different brain regions (Schoffelen and Gross, 2011). Those false interactions could originate from conditions specific to oscillations in the SNR of the system, due to the amplitude changes in the brain activity, which can cause similar fluctuation in the sensor noise (Schoffelen and Gross, 2009). Another reason is the symmetrical conductor geometry used to model the brain that can result in artefact effects, which in connectivity studies are translated into spurious interactions (Kujala et al., 2007). These problems are more evident in all-to-all pairwise connectivity analysis, where the brain connectivity is estimated between voxels, or between group of voxels, in order to generate maps of brain interactions (Kujala et al., 2008).

The problem related with finding spurious interactions has limited the use of MEG signals to implement brain dynamics studies between all-to-all pairwise brain locations (Schoffelen and Gross, 2009). Different techniques and methods have been presented to reduce the finding of false interactions, these are presented in Chapter 4. However, even when these techniques and methods have proved in simulations that reduce the amount of detected spurious interactions, there exist external factors that will always generate changes that cause spurious measurements, making it difficult to eliminate all possible false brain interactions (Schoffelen and Gross, 2009; Kujala et al., 2007).

Functional brain interactions are normally estimated in the form of the spectral coherence matrix, or correlation matrix in the time domain. These matrices are used to estimate the brain networks depending on the amount of interaction between different regions, which are normally represented by the matrices off diagonal elements. The matrices are normally used together with the estimated brain activity in the form of power maps to represent the synchronized activities and their locations (Lin et al., 2004; Schoffelen and Gross, 2009; Liljeström et al., 2005). The representation of the power maps is possible using co-registration techniques, where the space used to solve the inverse problem is mapped onto a brain surface obtained with the use of the fMRI technique (Hansen et al., 2010; Fuchs, 2007). This allows a more realistic representation of the brain dynamics, and therefore, a better understanding of the brain regions that are interacting.

Thus, MEG brain dynamics studies are affected by different problems related with the dif-

ferent stages needed for their estimations. One of the main issues is found with the use of the spatial filters, where the LCMV shows a good performance estimating the brain sources activity, but not when those are correlated. The MNE does not have that problem, but it is biased to solutions near the sensors. A different problem is the finding of spurious interactions, generated by the SNR of the system oscillations, and by the symmetry of the geometry used for the volume that define the brain, which can make the leadfields more dependent. Nevertheless, functional brain dynamics studies are an important field, and their estimation needs to be improved in order to increase the confidence of the results obtained. The improvement of the performance of this analysis will help gain a better understanding of the brain. Moreover, the use of MEG data for the estimation of brain dynamics can increase to the same level of the EEG and fMRI data. This can also help brain studies by having more standardized tools to analyse it, and then, by having metrics to compare when each of these technique can gives better results than the others.

1.3 Hypothesis

In this thesis, accordingly with what has been presented in this chapter so far, is proposed the following hypothesis: *"Improvements in MEG functional brain connectivity studies are possible following the DICS approach using a spatial filter that it is not affected by the presence of correlated brain activity".*

To be more specific, in this work are proposed two different approaches to improve the estimation of functional brain interactions from MEG data using the MNE and the LCMV spatial filters. The first approach changes the design of the LCMV spatial filter in order to consider the effect of correlated brain sources on its solution, while the second approach explores the idea of using the MNE spatial filter to estimate the cross-spectral density matrices from the measured magnetic fields in the same way that DICS does with the LCMV.

1.4 Thesis outline

This thesis is organised in seven chapters. In the first chapter are presented the motivation, the literature review and the hypothesis related to this work. The second, third and fourth chapters are used to introduce the theoretical background for the problem, and the basis for the simulated system used to test the hypothesis. The second chapter presents the basis

for the generation of the magnetic fields, and how the neuronal currents that generate the magnetic fields originate. The third and fourth chapters are used to explain the basis for the magnetoencephalography and for the techniques used for the measuring of functional brain interactions, respectively. The fifth chapter presents the analysis of the results obtained using the first approach presented in the hypothesis, based on the LCMV beamformer. The sixth chapter presents the results obtained following the second approach presented in the hypothesis, based on the use of the MNE spatial filter. The last chapter is used to discuss and to present the conclusions related to the results obtained in this work, also to present future work that can be implemented based on the results obtained.

Chapter 2

Electromagnetic fields of the brain

The brain has been the object of many studies from a long time by now, as presented in Chapter 1. During this time, many theories have been created, changed and discarded in order to understand its behaviour. As a consequence, the view of the brain has changed over time, at the same time that new techniques and methods have been developed and adapted from other fields for its study. The first methods developed to analyse the brain anatomy and its functionality were based on dissection and external electrical stimulus to the brain (Bear et al., 2007). However, it was in 1875 when the first attempt to measure the brain electrical activity generated was made by Richard Caton, providing the evidence for the existence of electrical brain currents, and the bases for studies such as the Electroencephalograms (EEG) and the Magnetoencephalograms (MEG) (Niedermeyer and Silva, 2005).

In this chapter are presented the bases for the generation and transmission of the brain electrical currents related to the generation of the brain activity. The chapter is divided in three main sections. The first section introduces some of the most important characteristics of the brain related to the generation of neuronal currents, and a brief description of some of the elements of the brain cortex. The second section introduces the brain processes that generate the action potentials and the transmission of information between neurons, and between neurons and the different part of the human body. The last section is used to explain how the neuronal currents and the magnetic fields are generated by the brain activity.

2.1 The human brain

The human brain has been defined as the most complex organ that can be found in nature. The brain is composed of cells like the rest of the organs that can be found in the human body, where the cells are the ones that determine the functionality of each of these organs. Most of the brain cells are in the range of $.01 - .05$ mm in diameter. This was one of the main problems for neuroscientists in the beginning of the brain study, when they were trying to understand the brain function by analysing the structures of the cells (Bear et al., 2007). Nowadays we know that the neuron and glia are the main structures for the brain cells, also that there are approximately 100 billion neurons in the brain, while the glia cells outnumber the number of neurons by tenfold (Bear et al., 2007).

Brain cells can be found in the two main components of the central nervous system, the brain and the spinal cord, which are composed by white and grey matters. The grey matter consists mainly of neurons, while the white matter is mostly composed of the glial cells and myelinated axons (Chudler, 2009). The grey matter is distributed along the brain surface or cortex, whereas the white matter provides the support for the neurons located in the grey matter (Bear et al., 2007). Thus, the brain functionality relies on how the different cell structures interact with each other, as explained in the following subsections.

2.1.1 Neurons

Neurons are considered as the unit of brain function, as is stated in the neuron doctrine established by Ramon y Cajal (Jirsa and McIntosh, 2007). The neurons are specialized brain cells designed to transmit information to other neurons or to different parts of the human body (Carey and Kibiuk, 1990). This transmission of information is possible because of the characteristics of the different parts that compose the neurons, which consists of the soma, the axon and the dendrites. In the Figure 2.1 is presented a general structure for the neuron, composed by parts that are important to understand the generation of the action potentials and the neuronal currents, as is explained in the next section.

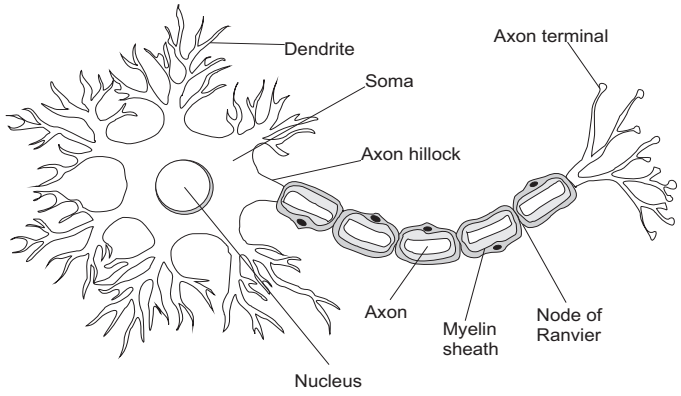

Figure 2.1: General structure and components of a neuron[1].

The soma is the main body of a neuron, it is the spherical central part which is rich in potassium solution known as cytosol. The solution that is separated from the outside of the cell by the neuron membrane (Bear et al., 2007). The soma also contains specialized components called organelles, which are small structures that maintain the cell and help with its functionality (Chudler, 2009). The nucleus, the rough endoplasmic reticulum, the smooth endoplasmic reticulum, the Golgi apparatus and the mitochondria, are some of the most important organelles that are found inside the soma, where each of these performs different processes in order to help with the correct behaviour of the cell (Carey and Kibiuk, 1990).

The axons and dendrites make possible the communication between neurons and between neurons and different parts of the human body, where a neuron can have many dendrites but only one axon (Chudler, 2009). The information generated in a neuron is sent away from the cell body, or is transmitted, by the axon, while the dendrites bring information from other sources to the neuron. This flow of information is possible because of the mechanisms provided by the different parts of the neuron, where the information is generated, amplified and transmitted in the form of electrical and chemical signals (Trappenberg, 2002), as is explained in the next section.

The axon begins with the axon hillock, and then continues through the main axon branch until the axon terminals, the sites where the axon interacts with other neurons or cells in order transmit information, as is presented in Figure 2.1. The junction between the axon terminal and other neurons or cells is known as a synapse, and the sides for the interactions with the transmitting and receiving neurons and cells can be classified as presynaptic and postsynaptic terminals, respectively. The presynaptic terminal side consists of the axon terminal, while the postsynaptic terminal side refers to the soma or dendrites of another cell or neuron, as

[1] Figure adapted from (Chudler, 2009)

can be seen in the Figure 2.2. The space between the presynaptic and the postsynaptic terminals is known as synaptic cleft, and the transmission of information between them is called synaptic transmission (Bear et al., 2007). This transmission is possible because of the synaptic terminal vesicles, which use a special type of chemistry involving neurotransmitters that allows the flux of information between the synapse terminals.

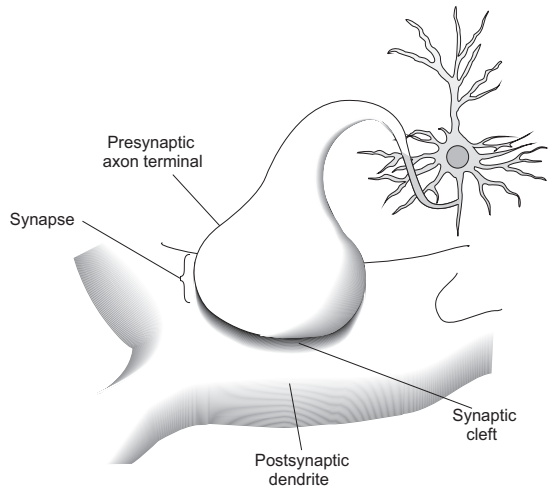

Figure 2.2: The axon and the synapse terminals[2].

2.1.2 Glial cells

Another important component in the brain are the glial cells, which have different functions and physical properties than the neurons. The glial cells are the main support for the neurons, and without them the neurons would not work properly. The glial cells destroy pathogens and remove dead cells from the brain, while providing the neurons insulation and their physical and nutritional support (Chudler, 2009). This support to the neurons is possible because of the two different structures of glial cells that can be found in the brain, the astrocytes and the myelinating glial (Bear et al., 2007).

The astrocytes are the most common glial cells found in the brain, which are used to fill the spaces between neurons. The main functions for the astrocytes are the provision of nutrient to the nervous tissue and the regulation of the chemical content of the extracellular space (Bear et al., 2007). On the other hand, the myelinating glial, or myelin sheath, is a special tissue produced by some glial cells that insulate sections of the axon by covering some of its parts. The brakes in the myelin sheath insulation are called nodes of Ranvier, as can be seen in Figure 2.1. This combination of the myelin sheath with the nodes of Ranvier increases the

[2] Figure adapted from (Bear et al., 2007)

speed for the transmission of information down the axon (Chudler, 2009).

2.1.3 The cortex

As was mentioned before, the grey matter is distributed along the brain surface or cortex, where are found most of the neurons responsible for the brain functionality. Moreover, the white matter consists of the glial cells and the myelinated axons, which are surrounded by the grey matter, providing the support required for the neurons located in the cortex (Bear et al., 2007). The cortex is divided in two hemispheres connected by a bundle of 200 to 300 million of axons called the corpus callosum (Chudler, 2009). Each hemisphere consist of four lobes composed of various sulcus and gyrus, or the hills and valleys of the brain surface (Chudler, 2009). The particular pattern of sulcus and gyrus folds of the cortex hide the true size of the brain surface, as can be seen in the Figure 2.3, where are also presented the brain grey matter and the white matter.

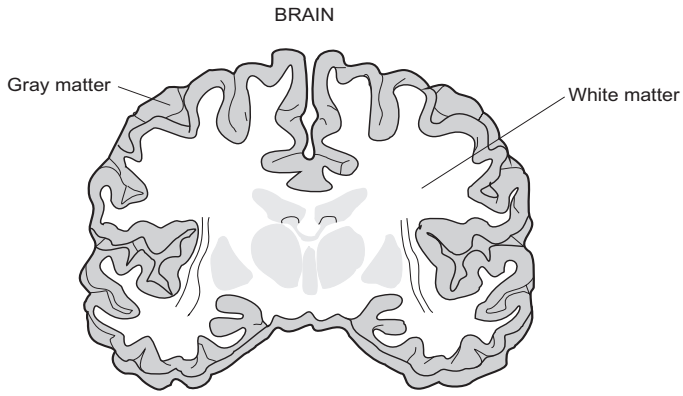

Figure 2.3: The brain cortex and the gray and white matters. The figure presents a slice of the brain, where the grey and white matters can be observed[3].

The four lobes located on the brain surface are the frontal lobe, the parietal lobe, the temporal lobe, and the occipital lobe, each of these performs functions related to different actions and stimulus such as speech, movement, pain and vision (Chudler, 2009). Thus, the functionality of the four lobes, or brain cortex, rely on the neurons located in the grey matter, which are orientated according to the brain surface characteristics. To be more specific, the orientations of the neurons follows the gyrus and sulcus brain cortex pattern, as is presented in Figure 2.4. Thereby, the generation of the brain activity follows the same orientation as the neurons, as will be explained in the next section.

[3] Figure adapted from (Chudler, 2009)

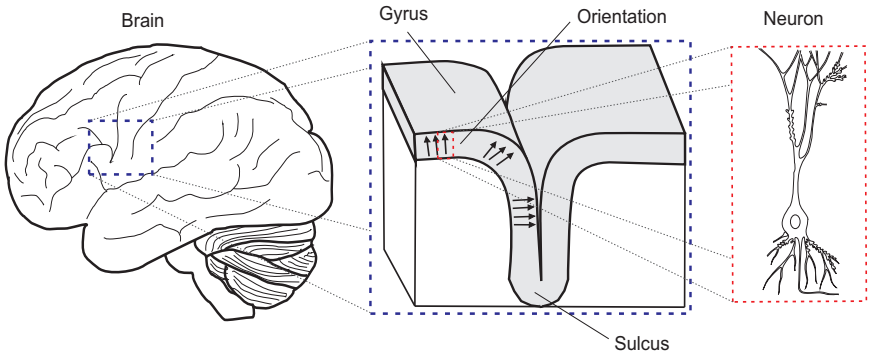

Figure 2.4: The orientation of neurons in the brain surface (cortex)[4].

2.2 Generation of brain activity

The human body responses to external stimulus are possible because of the brain structure and functionality, where sensations are interpreted and processed in order to control our actions. The external sensations are translated into our bodies as electrical signals that travel at great speed through the different parts of the peripheral nervous system. This flow of electrical signals continues until the interneurons, where the signals are send to the brain in order to be processed (Chudler, 2009). The electrical signals are known as neuronal signals once they are in the brain, where they are directed to different regions depending on the type of the external stimulus (Bear et al., 2007; Carey and Kibiuk, 1990). This transmission of information is known as neuronal signalling, and it is the basis for the generation of brain activity, or neuronal currents.

2.2.1 Action potentials

The transmission of electrical signals in the brain is achieved in a different way than in the well known case of an insulated copper wire (Bear et al., 2007). In a wire, the transmission of information is possible because of its conductivity property, allowing a flow of electrons through the wire. Moreover, the wire is well insulated, increasing the flow of electrons instead of their radiation away (Bear et al., 2007). Brain cells have less conductivity and insulation, limiting the transmission of electrons. However, the transmission of signals is possible by transmitting electrically charged atoms through the axons, also known as nerve impulses or action potentials (Bear et al., 2007). The action potentials start on the neurons and muscle cells with excitable membranes (Bear et al., 2007), and are characterized to have fixed duration and to travel through the axons at speeds up to 268 miles/hr (Chudler, 2009).

[4] The neuron figure used was adapted from (Hämäläinen et al., 1993)

The normal state of the neuron membrane is present when the cytosol has a negative electrical charge compared with the outside of the neuron body, this difference in electrical charges across the membrane is known as the resting state potential. The action potential occurs when the neuron is activated, and temporally reverses the electrical charge of the interior of the membrane, from a negative value to a more positive one (Carey and Kibiuk, 1990). This electrical charge can travel down the axon until it reaches the axon terminal, where the charge is transmitted to other neurons or cells generating the brain signals.

The generation of action potentials starts with a process known as depolarization, which changes the neuron resting state potential to a more positive value. Then, the value of the action potential reaches a peak. After this peak, the value of the membrane potential changes from a positive value to a more negative one, a process known as repolarization. The next process is the hyperpolarization, where the potential of the membrane passes from a negative value to a more negative one, until reaching the resting state potential again, where there is a last change in the direction of the action potential value known as after polarization. The generation of action potentials can be separated into fours main parts, the rising phase (depolarization), the overshoot (repolarization), the falling phase (hyperpolarization) and the undershoot (after polarization) (Bear et al., 2007), as can be seen in Figure 2.5.

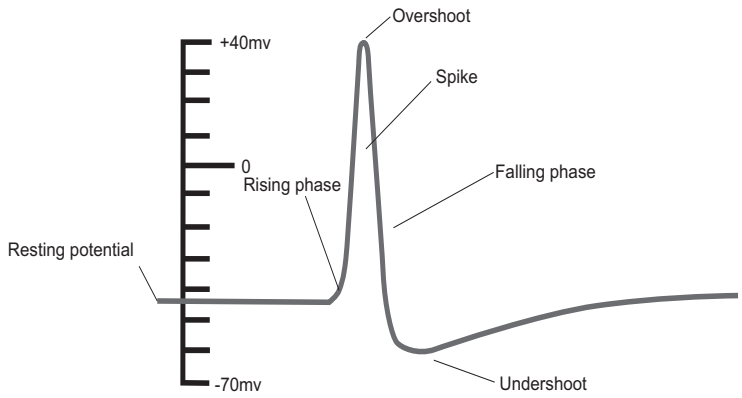

Figure 2.5: Generation of action potentials[5].

2.2.2 Neural signalling

Signal transmission between neurons or cells in the nervous system is essential for the correct functionality of the brain. This process is achieve by transmitting action potentials to the different parts of the nervous system. This is possible since an action potential generates a depolarization in the potential of the neuron, generating a depolarization in the axon, where

[5]Figure adapted from (Trappenberg, 2002)

the influx of positive charges depolarizes the next segment of the axon membrane until a next action potential is generate in the axon. This process allows the transmission of the action potential through the main axon branch until it reaches the axon terminals (Bear et al., 2007). The propagation of the action potential through the axon is presented in Figure 2.6.

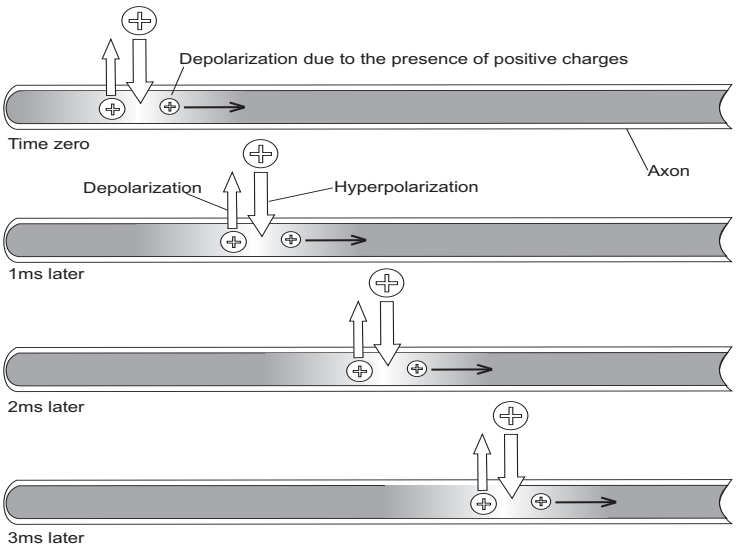

Figure 2.6: Transmission of action potentials[6].

Connections between neurons are made on specific locations of the neurons called synapses, which are composed by presynaptic and postsynaptic terminals in order to interact with the transmitter and receiver neurons, respectively (Trappenberg, 2002), Figure 2.7. The effect of action potentials on the synapse can be classified as two different types, depending on how the postsynaptic potential affects the potential of the receiving neuron membrane. It is called excitatory postsynaptic potential when it increases the potential in the receiving neuron , while the potential is called inhibitory postsynaptic potential in the opposite case (Trappenberg, 2002). This transmission of action potentials though the axons and between beurois can also be seen as the generation of ionic currents, explained in more detail in the following subsection.

[6] Figure adapted from (Bear et al., 2007)

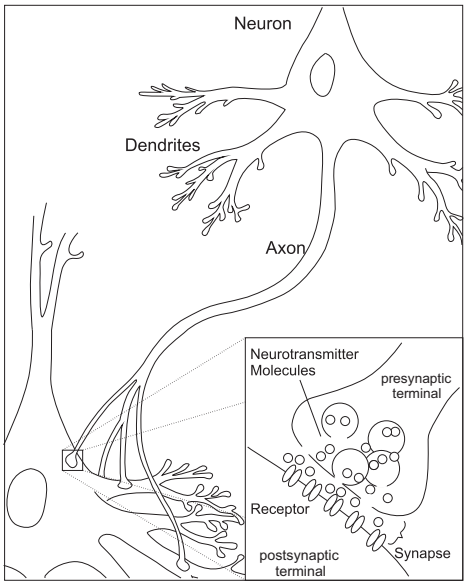

Figure 2.7: Transmission of information between neurons[7].

2.3 Magnetic fields of the brain

The neural signalling underlying brain processes are responsible for the generation of electric currents that generate magnetic and electric fields measurable outside the head and on the scalp, respectively. The generation of magnetic fields follows the neuromagnetism principle, defined as the study of magnetic fields generated from the brain activity (Lu and Kaufman, 2003). Neuromagnetism is based on the electromagnetism laws, to be more specific, in the magnetic flux generated from electric currents flowing through a conductor (Cheng, 1989). The produced magnetic fields depend on many of the brain characteristics, from the transmission of action potentials, to the simultaneous activation of groups of neurons that generate currents with enough strength to generate measurable magnetic fields. The magnetic fields produced by brain currents are the base for the Magnetoencephalography technique, explained in more detail in the next chapter.

2.3.1 Neural currents

Changes in the postsynaptic potential polarizes the neuron, generating a flux of ions that flows through and along the neuron membrane. These ionic currents are better known as neuronal currents, which direction of flow depends on the effects of the postsynaptic potential, Figure 2.8. The transmembrane currents are known as primary currents $\mathbf{J}^p$, and are respon-

[7] Figure adapted from *http://en.wikipedia.org/wiki/Neuron*

sible for the generation of passive currents $\mathbf{J}^v$, or volume currents, which are induced as a consequence of the conductive medium that surrounds the neuron (Niedermeyer and Silva, 2005). The volume currents are responsible for most of the generated electric potentials that can be measured on the scalp (Nunez and Srinivasan, 2006), while the primary currents are responsible for the generation of most of the measurable magnetic fields outside the head (Hämäläinen et al., 1993).

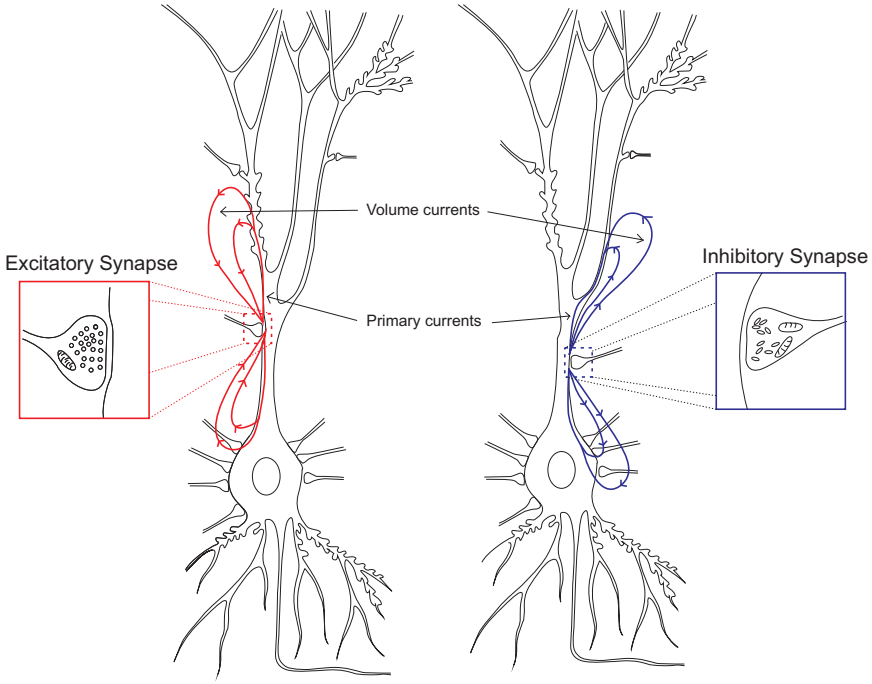

Figure 2.8: Neuronal currents, their directions depends on the postsynaptic potential [8].

However, even when the volume and primary currents are mostly responsible for the generation of the scalp potentials and the magnetic fields, respectively, they also generate part of both measurable fields (Baillet et al., 2001). Although, the measurable magnetic fields are produced from combined neuronal currents generated in spatially structured arrangements of cells, because the strength of magnetic fields generated by a single neuron is too weak. This is possible because of the magnetic fields superposition property (Baillet et al., 2001). Typically, the measurable magnetic fields are produced by the simultaneous brain activity generated by 10^4 to 10^5 neurons (Vrba and Robinson, 2001). Therefore, brain studies based on the magnetic fields are limited to the macroscopic space (Sarvas, 1987), where primary currents are seen as currents generated inside and in the vicinity of a neuron, while the volume currents as currents flowing everywhere else in the medium (Hämäläinen et al., 1993).

[8] Figure adapted from (Hämäläinen et al., 1993)

There are different assumptions for the brain conductivities in order to consider the volume currents. The two most common are the brain as a homogeneous volume conductor, and the brain composed of regions with different homogeneous conductivities. This is an important factor to considerer, as the magnetic fields generated by the brain activity respond to these changes in conductivities (Hämäläinen et al., 1993). In the second assumption, the volume currents that affect the generation of magnetic fields are only those located on the boundaries between regions with different conductivities (Hämäläinen et al., 1993). However, at the macroscopic level, the complexities added from consideration of different conductivities are ignored, as a results it is assumed that the whole brain is a homogeneous conductor where the volume currents do not generated measurable magnetic fields (Hämäläinen et al., 1993).

2.3.2 Magnetic fields

Electric currents are always associated with magnetic fields perpendicular to its direction (Papanicolaou, 2009), this same principle also applies to neuronal currents. The magnetic fields generated from brain activity are possible in the same way that magnetic fields are produced from a current flowing through a wire, but in the brain the wire is replaced by a single neuron, or by a bundle of neurons with simultaneous activity. The direction of the generated magnetic fields follows the right hand rule with respect to the direction of the neuronal currents, as is presented in Figure 2.9. The magnetic fields generated are additive and do not affect each other. Their strengths are proportional to the strength of the neuronal currents that generate them, and their intensity decreases as a function of the square of the distance from the neuronal currents (Lu and Kaufman, 2003), as is show in Figure 2.9.

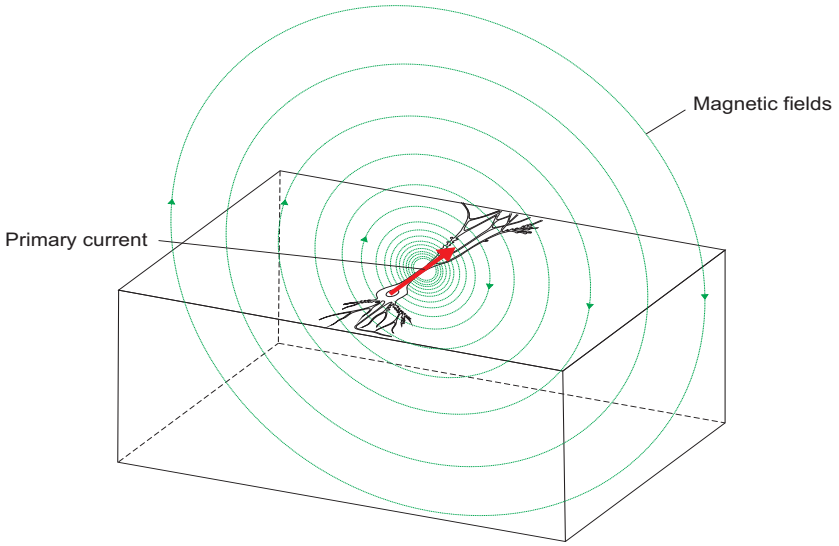

Figure 2.9: Direction and strength of neuronal generated magnetic fields. The direction follows the right hand rule with respect to the brain currents, while its amplitude is reduced as a function of the square of the distance from the brain activity [9].

The very small dissipation of the magnetic fields because of the different layers that compose the head is an important characteristics that has increased their use for the study of the brain, as is explained in the next chapter. This lack of distortion from the effects of the different layers that compose the head is possible because the biological tissues offer almost zero resistance to the flux of magnetic fields (Lu and Kaufman, 2003). This means that the magnetic permeability of the head tissues are practically the same as the empty space (Lu and Kaufman, 2003). Magnetic permeability is used as a metric to indicate the effects of magnetic fields in the magnetization of a specific material (Hansen et al., 2010). However, a different scenario is presented for potentials generated in the scalp by the volume currents, which are distorted and attenuated while they emerge to the surface of the head (Papanicolaou, 2009).

One assumption used in neuroscience for the study of the magnetic fields generated from the brain is the model of the head as a sphere. This modelling simplifies their study, as the contribution to the generated magnetic fields from the volume currents depends on the geometry of the head (Hämäläinen et al., 1993). In the spherical shape case, all the generated magnetic fields will be induced only by the effects of primary currents. The contribution of volume currents to the generation of magnetic fields tends to increase as the model used for the head deviates from the spherical shape (Papanicolaou, 2009). This is one example of an assumption used for a study of the magnetic fields generated by the brain activity, also known as magnetoencephalograms, which are explained in more detail in the next chapter.

[9] Figure adapted from (Hämäläinen et al., 1993; Clarke and Braginski, 2006)

2.4 Summary

The generation of magnetic fields involves many brain processes, from the receiving of the external stimulus in the form of potentials, to their transmission to the brain in order to generate electrical neuronal currents. However, the study of the brain magnetic fields is not straight forward, as are required many assumptions to have a better understanding. This because of the brain complexity, which makes difficult to relate the measurable magnetic fields with specific brain elements as the neurons. Instead, the brain activity responsible for the magnetic fields generation is considered to be generated by synchronized bundle of neurons, which facilitate the brain understanding. Other assumption used to simplify the problem is the discarding of the effects of volume currents, or passive currents, in the generation of magnetic fields, which can increase the complexity of the brain understanding by adding the brain conductivities and more realistic brain volume models for the problem.

Chapter 3

Magnetoencephalography

Magnetoencephalography is a non-invasive technique that allows measurements of magnetic fields outside the head, generated by brain activity. This is possible using a special type of sensor capable of sensing very small magnetic fields (Clarke and Braginski, 2006). The measured magnetic fields, or MEG data, have a good time resolution and are almost undistorted by the different layers that compose the head. These properties allow its use for brain studies and give advantages compared against other non-invasive techniques such as Electroencephalograms and functional Magnetic Resonance Imaging, which are affected by the different layers of the head and have a low time resolution, respectively. It also has disadvantages, whereas its low spatial resolution and high sensitivity to neuronal currents tangential to the brain surface are some of the most critical ones (Niedermeyer and Silva, 2005).

In this chapter are presented the basis to study the brain from MEG data or recordings. The first section introduces the characteristics of the MEG acquisition system, while the second and the third sections explains the measurements of magnetic fields outside the head, and two of the most used techniques to estimate the brain activity responsible for the generation of the magnetic fields, respectively, the linearly constrained minimum variance (LCMV) beamformer and the minimum norm estimates (MNE) spatial filter. The last section presents some of the most known variations for the MNE spatial filter and for the LCMV beamformer, used to reduce their most characteristics problems.

3.1 MEG acquisition system

The measurements of magnetic fields generated by biochemical processes inside the brain have been studied since 1960s, when the first magnetic brain recording, or magnetoencephalograms, was published (Clarke and Braginski, 2006). However, it was not until the early 1970s when recordings with good signal quality were available (Malmivuo, 2000), those recordings were obtained using the Superconducting QUantum Interference Devices (SQUID). Since then, the number of SQUIDs used in the MEG acquisition system has increased considerable, to whole head system with more than 200 sensors (Clarke and Braginski, 2006; Baillet et al., 2001). Nevertheless, the cost of the system has also increased since the SQUID development, which required expensive and complex instrumentation components, such as flux transformers, a cryogenic block, and a shielded room (Clarke and Braginski, 2004), Figure 3.1.

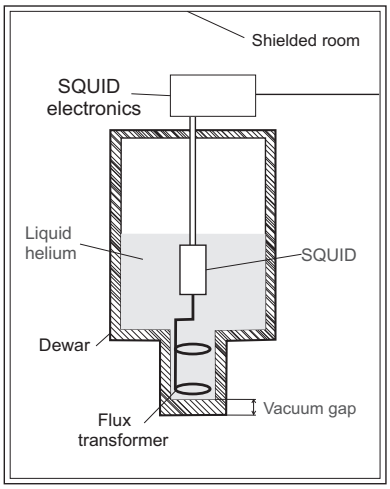

Figure 3.1: Single channel MEG acquisition system[1].

Most of the MEG acquisition system components are needed because of the SQUIDs characteristics, which require a cryogenic block to keep their temperatures, and the flux transformers temperatures, which are required to be superconductors. The shielding room is necessary to reduce the external interferences that have stronger signals than the magnetic fields generated by the brain activity. The MEG acquisition system components can be observed in Figure 3.1, where the dewar, or MEG flask, is the place where the SQUIDs, the flux transformers, and the cooling block are located. The flask has a vacuum gap that separate the coils from the scalp surface. The flux transformer can be found in the form of magnetometers, radial or planar gradiometers, or a combination of both (Clarke and Braginski, 2004).

[1] Figure adapted from (Pizzela et al., 2001)

The magnetic fields are measured on the SQUIDs in the form of electric currents induced on the flux transformers, which follows the right hand rule (Handy, 2009). The SQUIDs sensitivities to the magnetic fields generated from the brain activity depends on the configuration and design of the flux transformers, which pick up the magnetic fields components normal to its surface (Hämäläinen et al., 1993). This dependence on the flux transformer is because of their different configurations, which can reduce or cancel the effects that the external noise and background interferences have, while at the same time improve the accuracy of the measured magnetic fields (Hämäläinen et al., 1993). For example, the axial first order gradiometer composed of two coils is more sensitive to signals near the lower coil, while the upper coil is used to compensate the artefacts effects from distant sources (Handy, 2009). The magnetometer is another example of flux transformers, which consist of a single loop wire sensitive to the magnetic field components perpendicular to its area (Vrba and Robinson, 2001). In Figure 3.2 are presented some configurations for the flux transformers.

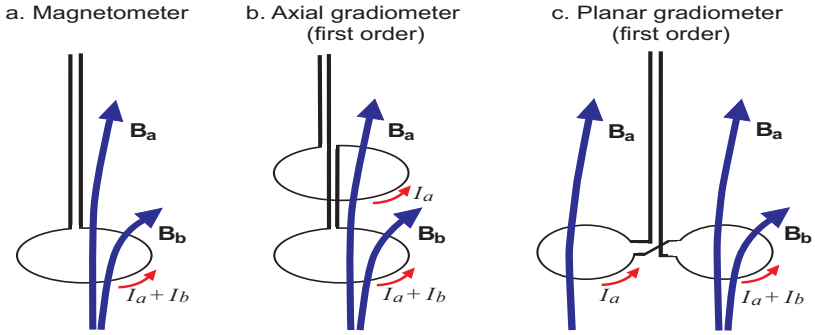

Figure 3.2: Magnetic flux transformers[2]. a) Magnetometer, b) Axial gradiometer, and c) planar gradiometer. In the figure are shown the magnetic fields effects from distant sources ($\mathbf{B_a}$) and for local sources ($\mathbf{B_b}$), which induce currents (I_a and I_b) on the flux transformers coils.

3.2 Magnetic forward problem

The forward problem in neuromagnetism consists in the measurement of magnetic fields outside the head, where the measured magnetic fields are obtained from the contribution of various magnetic fields generated from synchronous neural activity. This is possible because of the super imposable property that the magnetic fields have, which are additive and do not affect each other (Lu and Kaufman, 2003). The calculation of the magnetic fields outside the head generated by brain electrical currents is achieved using Maxwell equations in their quasi-static approximation form (Hämäläinen et al., 1993), which are listed below:

[2] Figure adapted from (Handy, 2009)

$$\nabla \cdot \mathbf{E} = \rho/\epsilon_o \tag{3.1}$$

$$\nabla \times \mathbf{E} = -\delta\mathbf{B}/\delta t \tag{3.2}$$

$$\nabla \cdot \mathbf{B} = 0 \tag{3.3}$$

$$\nabla \times \mathbf{B} = \mu_o(\mathbf{J} + \epsilon_o \delta\mathbf{E}/\delta t) \tag{3.4}$$

where $\mathbf{B}$ and $\mathbf{E}$ represent the magnetic and electric fields generated by neuronal currents $\mathbf{J}$, respectively. Moreover, μ_0, ϵ_0 and ρ represent the permeability of the free space, the permittivity of the free space, and the charge density, while $\nabla\cdot$, $\nabla\times$, and $\delta/\delta t$ represent the divergence, the curl, and the partial derivative operators, respectively. The Maxwell equations are the base for the magnetostatic, which is defined as the study of steady magnetic fields generated by steady currents, currents that do not have any variation in their charge, $\nabla\cdot\mathbf{J} = 0$ (Griffiths and College, 1999; Cheng, 1989). The use of the quasistatic approximation is justified because the electrical currents generated from brain activity oscillates in a range of frequencies below 1 Khz (Baillet et al., 2001; Hämäläinen et al., 1993).

3.2.1 Equivalent current dipoles

The synchronous neuronal activity can be represented as equivalent currents dipoles (ECD) (Hämäläinen et al., 1993), which generate electric and magnetic fields similar to the neuronal currents, Figure 3.3. This is under the assumption that the magnetic fields are generated by segment of currents that are relatively small compared with the distance from where the field is measured, and because of the super imposable magnetic fields property (Lu and Kaufman, 2003). Then, N equivalent current dipoles can be used to represent the brain activity generated by synchronous neuronal activity located on N different regions. This also helps to find a mathematical solution for the inverse problem, where the unknown locations are limited to specific positions in order to look for the brain activity (Papanicolaou, 2009).

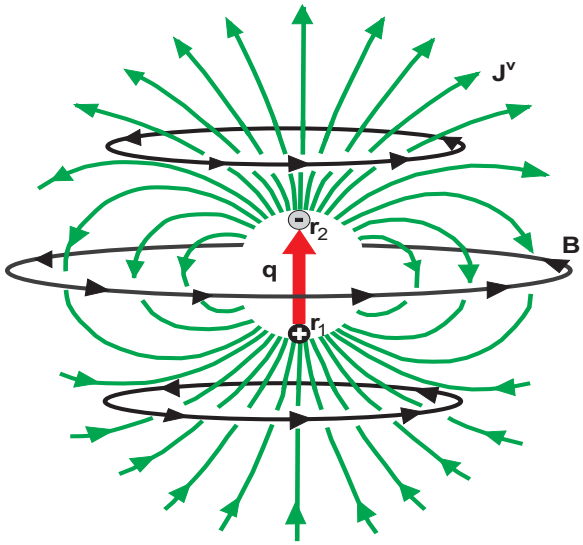

Figure 3.3: Magnetic fields produced by a current dipole[3]. The figure shows the magnetic fields produced by a current dipole immerse in homogeneous conducting medium. It can be observed that the magnetic fields $\mathbf{B}$ are due to the current dipole $\mathbf{q}$, not to the volume currents $\mathbf{J}^v$.

The neuronal currents can be divided into two components, the primary currents $\mathbf{J}^p$ and the volume current $\mathbf{J}^v$, as was explained in the previous chapter. At the macroscopic level the primary currents are the responsible for the generation of the magnetic fields. Then, the current dipole can be seen as a concentration of primary currents $\mathbf{J}^p$ to a single point (Hämäläinen et al., 1993). In Equation 3.5 is presented the expression for the current dipole, where $\mathbf{q} \in \mathbb{R}^3$ is a vector that represents the strength of the dipole and its direction, q is a scalar used for the magnitude of the positive and negative dipole charges, and $\mathbf{r}_2 \in \mathbb{R}^3$ and $\mathbf{r}_1 \in \mathbb{R}^3$ are the locations for the charges that create the current dipole, Figure 3.3.

$$\mathbf{q} = q(\mathbf{r}_2 - \mathbf{r}_1) \tag{3.5}$$

3.2.2 Biot-Savart law

The Biot-Savart law describes the relation between an electric current at position $\mathbf{r}_i \in \mathbb{R}^3$ and the magnetic field at position $\mathbf{r} \in \mathbb{R}^3$ generated by that current (Cheng, 1989). In the neuromagnetism problem context, the Biot-Savart law is used to describe the magnetic fields at position $\mathbf{r}$, $\mathbf{B(r)} \in \mathbb{R}^3$, generated by electrical currents located in the brain at positions $\mathbf{r}_i$, $\mathbf{J}(\mathbf{r}_i) \in \mathbb{R}^3$, Equation 3.6 (Baillet et al., 2001; Sarvas, 1987). These currents can be replaced, at the macroscopic level, by synchronous neural activity located on a specific brain region, or by an equivalent current dipole $\mathbf{q}$, which simplifies the expression for Equation

[3]Figure adapted from (Lu and Kaufman, 2003)

3.6 (Hämäläinen et al., 1993; Lu and Kaufman, 2003). However, the use of the Biot-Savart law in the neuromagnetism context depends on factors such as the shape of the volume that defines the head, and the consideration of homogeneous or non-homogeneous conductivities for the volume conductor, which increase the complexity for the solution of the Biot-Savart law. The density current $\mathbf{J}(\mathbf{r}_i)$ can be expressed by Equation 3.7, where $\mathbf{E}(\mathbf{r}_i) \in \mathbb{R}^3$ is the electric field generated in the membrane of the neuron, V is the scalar membrane potential, and σ is the brain region conductivity (Hämäläinen et al., 1993).

$$\mathbf{B}(\mathbf{r}) = \frac{\mu_0}{4\pi} \int \mathbf{J}(\mathbf{r}_i) \times \frac{\mathbf{r} - \mathbf{r}_i}{|\mathbf{r} - \mathbf{r}_i|^3} dv' \tag{3.6}$$

$$\mathbf{J}(\mathbf{r}_i) = \mathbf{J}^p(\mathbf{r}_i) + \mathbf{J}^v(\mathbf{r}_i) = \mathbf{J}^p(\mathbf{r}_i) + \sigma\mathbf{E}(\mathbf{r}_i) = \mathbf{J}^p(\mathbf{r}_i) - \sigma\nabla V \tag{3.7}$$

The inclusion of different conductivities for homogeneous brain regions requires the consideration of volume currents in the Biot-Savart law expression, as can be seen in Equation 3.8, where σ_j is used to express the different conductivities found in m brain regions G_j, while $\mathbf{B}_0(\mathbf{r}) \in \mathbb{R}^3$ are the magnetic field generate by the primary currents, or equivalent current dipoles, as can be seen in Equation 3.9. In the case of a infinite homogeneous conductor the magnetic fields are obtained only considering the primary current (Hämäläinen et al., 1993; Sarvas, 1987). Another important factor to consider in the measurements of the magnetic fields is the shape of the head, such as the case of a spherical symmetric conductor, where the magnetic fields are obtained without considering the volume currents (Sarvas, 1987; Hämäläinen et al., 1993).

$$\mathbf{B}(\mathbf{r}) = \mathbf{B}_0(\mathbf{r}) - \frac{\mu_0}{4\pi} \sum_{j=1}^{m} \sigma_j \int_{G_j} \nabla' V \times \frac{\mathbf{r} - \mathbf{r}_i}{|\mathbf{r} - \mathbf{r}_i|^3} dv' \tag{3.8}$$

$$\mathbf{B}_0(\mathbf{r}) = \frac{\mu_0}{4\pi} \int \mathbf{J}^p(\mathbf{r}_i) \times \frac{\mathbf{r} - \mathbf{r}_i}{|\mathbf{r} - \mathbf{r}_i|^3} dv' \tag{3.9}$$

Thus, the measurements of magnetic fields generated by synchronous activity located on a specific brain region, in a unbounded homogeneous medium, can be represented by Equation 3.10 (Sarvas, 1987), where t is the time instant when the magnetic fields are measured, while $\mathbf{r}_i$ is the average between distances $\mathbf{r}_1$ and $\mathbf{r}_2$, or the current dipole $\mathbf{q}(\mathbf{r}_i)$ location, Figure 3.4. Therefore, the magnetic fields can be calculated using Equation 3.11, where each of the

N brain sources, located in the unbounded homogeneous medium that define the brain, are considered for the generation of the measured magnetic fields (Hämäläinen et al., 1993).

$$\mathbf{B}(\mathbf{r},t) = \frac{\mu_0}{4\pi}\mathbf{q}(\mathbf{r}_i,t) \times \frac{\mathbf{r}-\mathbf{r}_i}{|\mathbf{r}-\mathbf{r}_i|^3} \tag{3.10}$$

$$\mathbf{B}(\mathbf{r},t) = \frac{\mu_0}{4\pi}\sum_{i=1}^{N}\mathbf{q}(\mathbf{r}_i,t) \times \frac{\mathbf{r}-\mathbf{r}_i}{|\mathbf{r}-\mathbf{r}_i|^3} \tag{3.11}$$

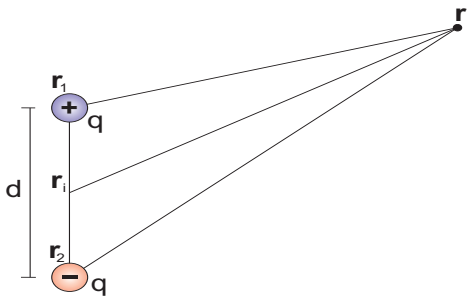

Figure 3.4: Equivalent current dipole representation[4]. The locations for the charges that generate the magnetic fields can be observed, the centre of the equivalent current dipole $\mathbf{r}_i$, and the location $\mathbf{r}$ where are measured the magnetic fields generated by the dipole activity.

3.2.3 Lead-fields

As was mention in the first chapter, the leadfields are defined as the sensitivities of the sensors to the brain sources responsible for the generation of the magnetic fields. These are found by calculating the output of the sensors when a unit-magnitude brain source is placed at a specific location and direction (Malmivuo, 2000). Then, the output of sensor m to a unit-magnitude brain source located at position $\mathbf{r}_i$ is defined as $l_m^x(\mathbf{r}_i)$, $l_m^y(\mathbf{r}_i)$, and $l_m^z(\mathbf{r}_i)$, when the source is oriented to the x, y and z directions, respectively (Sekihara and Nagarajan, 2008). Hence, the sensitivity of sensor m can be expressed by the 3×1 leadfield vector defined as $\boldsymbol{l}_m(\mathbf{r}_i) = [l_m^x(\mathbf{r}_i), l_m^y(\mathbf{r}_i), l_m^z(\mathbf{r}_i)] \in \mathbb{R}^3$. On the other hand, the sensitivity of M sensors to a source located at position $\mathbf{r}_i$ is described by the $M \times 3$ leadfield matrix $\boldsymbol{L}(\mathbf{r}_i) = [\boldsymbol{l}_x(\mathbf{r}_i), \boldsymbol{l}_y(\mathbf{r}_i), \boldsymbol{l}_z(\mathbf{r}_i)] \in \mathbb{R}^{M\times 3}$, composed by the sensitivities of the sensors to each of the unit-strength components of the brain source, Figure 3.5.

[4] Figure adapted from (Cheng, 1989)

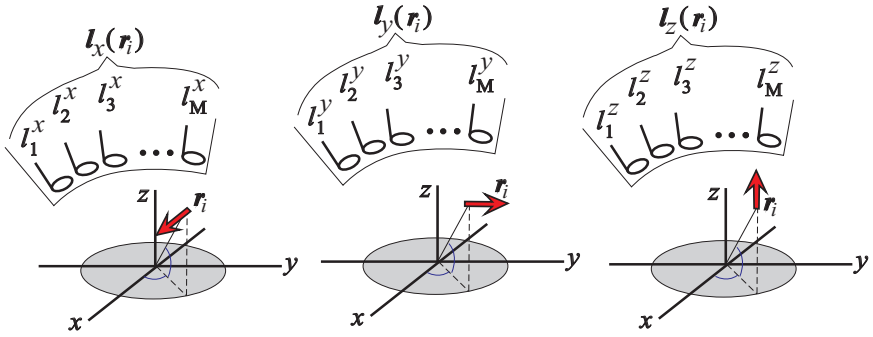

Figure 3.5: Sensitivity of M sensors to a unit-magnitude brain source located at position $\mathbf{r}_i$, and oriented in the x, y an z directions[5].

In the unbounded homogeneous conductor case, the lead-fields are obtained using the Biot-Savart law expressed in Equation 3.10. However, the flux transformer used to pick up the magnetic fields on the sensors are normally oriented tangentially with respect to the surface of the volume that defines the head (Lu and Kaufman, 2003), and therefore, the sensors are only sensitive to fields that are normal to the sensors surfaces (Lu and Kaufman, 2003; Hämäläinen et al., 1993). Thus, the magnetic field measured on the m sensor at position $\mathbf{r}$ can be expressed by equations 3.12 and 3.13, where the 3×1 vector $\mathbf{a}_m(\mathbf{r}) \in \mathbb{R}^3$ represents the unitary vector normal to the surface of the m sensor, as can be seen in Figure 3.6.

$$B_m(\mathbf{r}, t) = \frac{\mu_0}{4\pi}\mathbf{q}(\mathbf{r}_i, t) \times \frac{\mathbf{r} - \mathbf{r}_i}{|\mathbf{r} - \mathbf{r}_i|^3} \cdot \mathbf{a}_m(\mathbf{r}) \tag{3.12}$$

$$B_m(\mathbf{r}, t) = \boldsymbol{l}_m(\mathbf{r}_i) \cdot \mathbf{q}(\mathbf{r}_i, t) \tag{3.13}$$

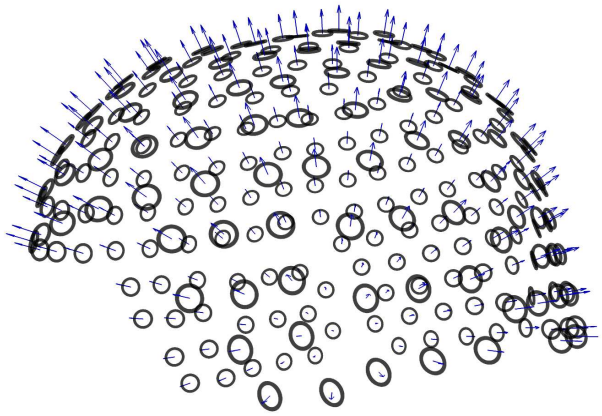

Figure 3.6: Sensors distribution for the York Neuroimaging Centre. 4D Neuroimaging Magnes 3600 Whole Head 248 Channel MEG scanner[6], represented as black rings. The orientation of the sensor was simulated to be radial to the surface of a sphere, represented by blue arrows on the figure.

[5] Figure adapted from (Sekihara and Nagarajan, 2008)
[6] *https://www.ynic.york.ac.uk/FrontPage*

3.2.4 Measuring the magnetic fields

The solution for the forward problem can be used to express the measurements of magnetic fields generated from N brain sources, or equivalent current dipoles, in a MEG acquisition system composed by M sensors. Then, the magnetic fields measured on the sensors can be represented by Equation 3.14, where $\mathbf{x} \in \mathbb{R}^M$ is a $M \times 1$ vector composed by the measurements obtained from the sampling of all the sensors on a single time instant t (Van Veen and Buckley, 1988), while $\mathbf{n} \in \mathbb{R}^M$ is a $M \times 1$ vector used to express the effects of the external noise in the measurements of the magnetic fields, which in some cases this can be treated as a zero mean and uncorrelated random process (Imada, 2010).

$$\mathbf{x} = \sum_{i=1}^{N} \boldsymbol{L}(\mathbf{r}_i)\mathbf{q}(\mathbf{r}_i, t) + \mathbf{n} \tag{3.14}$$

The solution for the forward problem can be expressed in the form of products between matrices and vectors using linear algebra identities (Mosher et al., 1999; Peraza R., 2012). Thus, Equation 3.12 can be represented as Equation 3.15, where $\mathbf{r}_s \in \mathbb{R}^3$ and $\mathbf{r}_i \in \mathbb{R}^3$ are the locations for the m sensor and the i brain source, respectively, while $\mathbf{r}_{si} = \mathbf{r}_s - \mathbf{r}_i = [r_x, r_y, r_z]$, $\mathbf{q}(\mathbf{r}_i, t) = [q_x, q_y, q_z]^T$, and $\mathbf{a}_m = [a_x, a_y, a_z]$.

$$B_m(\mathbf{r}_s, t) = \frac{\mu_0}{4\pi|\mathbf{r}_{si}|^3} \begin{bmatrix} a_x & a_y & a_z \end{bmatrix} \begin{bmatrix} 0 & r_z & -r_y \\ -r_z & 0 & r_x \\ r_y & -r_x & 0 \end{bmatrix} \begin{bmatrix} q_x \\ q_y \\ q_z \end{bmatrix} \tag{3.15}$$

The composite lead-field matrix $\mathbf{H} = [\boldsymbol{L}(\mathbf{r}_1), \boldsymbol{L}(\mathbf{r}_2), \ldots, \boldsymbol{L}(\mathbf{r}_N)] \in \mathbb{R}^{M \times 3N}$ is presented in Equation 3.16, where $\mathbf{R}_{si} \in \mathbb{R}^{3\times 3}$ is defined in Equation 3.17 (Peraza R., 2012).

$$\mathbf{H} = \frac{\mu_0}{4\pi} \begin{bmatrix} \mathbf{a}_1 & 0 & \ldots & 0 \\ 0 & \mathbf{a}_2 & \ldots & 0 \\ \vdots & \vdots & \ddots & \vdots \\ 0 & 0 & \ldots & \mathbf{a}_M \end{bmatrix} \begin{bmatrix} \mathbf{R}_{11} & \mathbf{R}_{12} & \ldots & \mathbf{R}_{1N} \\ \mathbf{R}_{21} & \mathbf{R}_{22} & \ldots & \mathbf{R}_{2N} \\ \vdots & \vdots & \ddots & \vdots \\ \mathbf{R}_{M1} & \mathbf{R}_{M2} & \ldots & \mathbf{R}_{MN} \end{bmatrix} \tag{3.16}$$

$$\mathbf{R}_{si} = \frac{1}{|\mathbf{r}_{si}|^3} \begin{bmatrix} 0 & r_z & -r_y \\ -r_z & 0 & r_x \\ r_y & -r_x & 0 \end{bmatrix} \tag{3.17}$$

Therefore, the summation in Equation 3.14 can be expressed as Equation 3.18, where the matrix $\mathbf{m} \in \mathbb{R}^{3N}$ is composed by the N dipole moments responsible for the generation of the magnetic fields at a specific time instant t, $\mathbf{m} = [q_{1x}, q_{1y}, q_{1z}, \ldots, q_{Nx}, q_{Ny}, q_{Nz}]^T$

$$\mathbf{x} = \mathbf{Hm} + \mathbf{n} \tag{3.18}$$

Measuring the magnetic fields in the sensors domain allows an estimation of the brain sources locations by identifying the characteristic pattern of the magnetic fields generated from equivalent current dipoles, Figure 3.3. These patterns can be identified using equations 3.14 or 3.18, for the magnetic fields generated by one and by multiple current dipoles. However, the magnetic fields detected on the sensors are affected by factors such as the external noise, the orientation of the sources and sensors, and by the magnetic fields spread effect (Schoffelen and Gross, 2009; Lu and Kaufman, 2003). In figures 3.7 and 3.8 are show the magnetic fields generated in the noiseless case by an equivalent current dipole, and by a combination of 7 equivalent currents dipoles, respectively. The magnetic fields are measured at the surface of a sphere, which represent the sensors domain, where only the orthogonal components of the fields with respect to the sphere surface are measured (Hämäläinen et al., 1993).

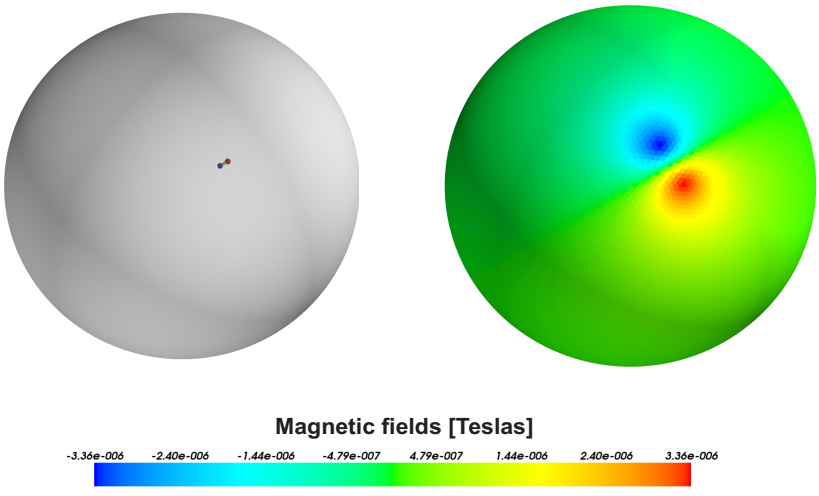

Figure 3.7: Magnetic fields generated by a tangentially oriented equivalent current dipole, with respect to a sphere surface that represents the cortex. The sphere on the left represents the brain, while the sphere on the right is the space where the fields were measured. The ECD location and orientation are represented by two points located on the brain volume. The simulation for the generated activity and the implementation of the Biot-Savar law were made using python, while the display of the volume and the measured magnetic field using Mayavi.

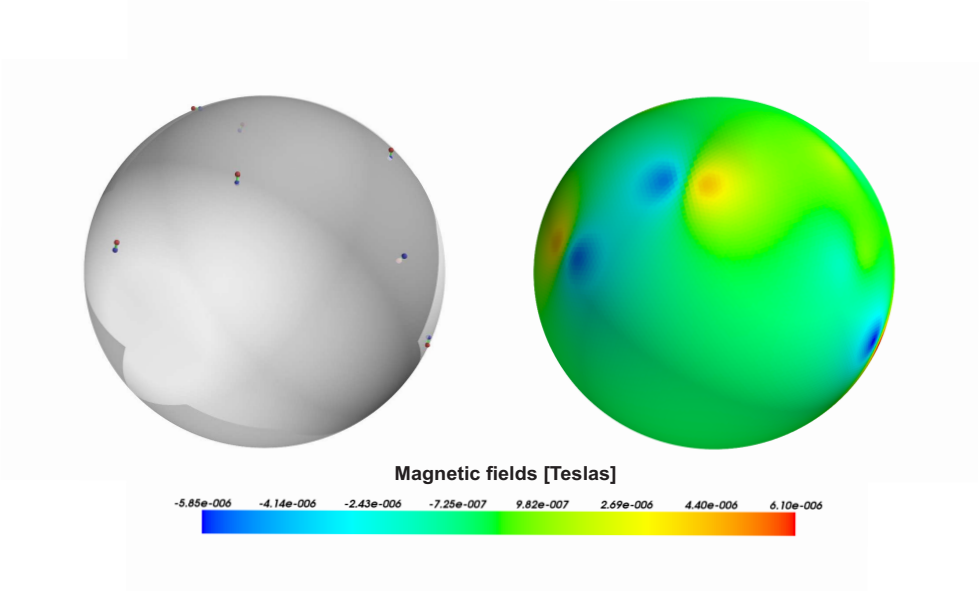

Figure 3.8: Magnetic fields measured on the surface of a sphere, generated from 7 ECDs. On the left is presented the sphere that defines the brain volume, and the locations and orientations for the simulated ECDs, as two points per ECD. On the right is presented the measured magnetic fields generated from the activity of the 7 ECDs.

3.3 Magnetic inverse problem

The magnetoencephalograms are used to study the brain in fields such as neuroimaging, where signal processing and regression techniques are applied to the measured data in order to understand the brain behaviour (Clarke and Braginski, 2006). However, as was mentioned before, the study of magnetic fields on the sensors domain is limited by factors like the fields spread effect (Schoffelen and Gross, 2009). This is one of the main reasons to use the solution of the neuromagnetism inverse problem for the study of the brain, rather than the measured magnetic fields. The inverse problem deals with the estimation of brain sources time series from measured magnetic fields, where the main difficulty for the finding of the time series is the non-unique solution characteristic for the problem (Hämäläinen et al., 1993; Sarvas, 1987). Thus, the common approach followed to solve the problem is by restricting the locations for the brain sources responsible for the generation of the magnetic fields, and then, by inverting the resulting set of constrained equations (Clarke and Braginski, 2006). Two of the most used techniques to estimate the solution of the inverse problem are the LCMV beamformer and the MNE spatial filter (Sekihara and Nagarajan, 2008), even when these are different spatial filters, they share similarities as was showed by Mosher (Mosher et al., 2003), appendix C.

3.3.1 Minimum Norm Estimate

Minimum Norm estimate is a spatial filter used in neuromagnetism to estimate the brain sources responsible for the generation of magnetic fields measurable outside the head. An important characteristic of this filter is its non-adaptive property related to the calculation of the filter weights, which depend only on the lead-field matrices $\boldsymbol{L}(\mathbf{r}_i)$ (Hämäläinen et al., 1993). This property helps the filter to not be affected by the presence of correlated brain activity, which is one of the main problems that the LCMV has (Van Veen et al., 1997). However, this property also affects the performance of the filter, making it more susceptible to the effects of the external noise. The MNE spatial filter is based on the regression from the forward problem using the least-squares method to build a constrained set of equations in order to solve the inverse problem (Sekihara and Nagarajan, 2008)

In minimum norm, the solution for the inverse problem is found searching for brain sources with the smallest amplitude that satisfy the magnetic fields measured outside the head (Hämäläinen et al., 1993). This search is made in all the square-integrable brain sources confined in the space spanned by the sensors (Hämäläinen et al., 1993), where the concept of norm is utilized to describe the amplitude of the sources as their lengths or sizes. The MNE mathematical problem is based on the expression for the forward problem, Equation 3.14, which is presented for the noiseless case in Equation 3.19. It can be observed in Equation 3.19 that the only unknown parameter are the brain sources $\mathbf{m}$, where the magnetic fields and the lead-fields are obtained from the MEG acquisition system.

$$\mathbf{x} = \mathbf{H}\mathbf{m} \tag{3.19}$$

The solution for the inverse problem can be estimated as the solution of the linear least squares inverse of Equation 3.19, defining the estimation of the unknown vector $\mathbf{m}$ as $\widehat{\mathbf{m}}$, for the least-square cost function presented in Equation 3.20 (Sekihara and Nagarajan, 2008). The solution for the least-square inverse function is shown in Equation 3.21, where $\mathbf{H}^{+} = \mathbf{H}^{T}[\mathbf{H}\mathbf{H}^{T}]^{-1}$ is used to express the generalized inverse of the composite lead field matrix $\mathbf{H}$ (Sekihara and Nagarajan, 2008). The inner products of the lead-fields matrices $[\mathbf{H}\mathbf{H}^{T}]$ is known as the gram matrix (Sekihara and Nagarajan, 2008), and its inverse can cause large computational errors because of the large eigenvalues that compose the matrix most of the times (Hämäläinen et al., 1993). Therefore, it is necessary to use regularization methods for the inverse problem, where some of the most used methods are the eigen-decomposition

truncation (Hämäläinen et al., 1993), the Singular Value Decomposition Truncation (SVDT) and the Tikhonov regularization (Sekihara and Nagarajan, 2008).

$$\mathcal{F} = ||\mathbf{x} - \mathbf{H}\widehat{\mathbf{m}}||^2 \tag{3.20}$$

$$\widehat{\mathbf{m}} = \mathbf{H}^{+}\mathbf{x} \tag{3.21}$$

The eigen-decomposition truncation regularization is implemented on the gram matrix by suppressing brain sources spanned by the lead-fields which have poor coupling to the sensors that measure the magnetic fields (Hämäläinen et al., 1993). Thus, it is necessary to express the inverse of the gram matrix as the eigen-decomposition of the matrix, as is presented in Equation 3.22, where $\mathbf{V}$ is used to express the eigenvectors, while $\mathbf{\Lambda}$ is used to express the diagonal matrix composed by the eigenvalues, such that $\mathbf{\Lambda}^{-1} = diag(\lambda_1^{-1}, \lambda_2^{-1}, \ldots, \lambda_N^{-1})$. Thereby, the regularization is achieved by replacing $\mathbf{\Lambda}$ with $\widehat{\mathbf{\Lambda}}$ in order to express the regularized diagonal matrix of eigenvalues, as can be seen in Equation 3.23. The k eigenvalue is selected to be equal or greater than the allowed tolerance value $\lambda_k \geq Tol$, whereas the smaller eigenvalues are suppressed (Hämäläinen et al., 1993).

$$[\mathbf{H}\mathbf{H}^T]^{-1} = \mathbf{V}\mathbf{\Lambda}^{-1}\mathbf{V}^T \tag{3.22}$$

$$\widehat{\mathbf{\Lambda}}^{-1} = diag(\lambda_1^{-1}, \ldots, \lambda_k^{-1}, 0, \ldots, 0) \tag{3.23}$$

The MNE filter weights $\mathbf{W}_{ls} \in \mathbb{R}^{3\times M}$ are calculated following Equation 3.24 and appendix A. The weights can be used to estimate the brain sources on locations $\mathbf{r}_i$ from the measured magnetic fields, as in equations 3.25 and 3.26. It is an estimate because the regularization method limits the number of eigenvalues used for the inverse of the gram matrix. The estimation will be more accurate when more eigenvalues are used, but then the filter will be more affected by the presence of the external noise. On the other hand, using few eigenvalues will increase the performance of the filter in terms of the noise, but the estimation of the brain sources will be poorer as a result (Hämäläinen et al., 1993; Sarvas, 1987).

$$\mathbf{W}_{ls}(\mathbf{r}_i) = \boldsymbol{L}^T(\mathbf{r}_i)[\mathbf{H}\mathbf{H}^T]^{-1} \tag{3.24}$$

$$\widehat{\mathbf{q}}(\mathbf{r}_i, t) = \mathbf{W}_{ls}^T(\mathbf{r}_i)\mathbf{x} \tag{3.25}$$

$$\widehat{\mathbf{m}} = \mathbf{W}_{ls}^T\mathbf{x} = \mathbf{H}^T[\mathbf{H}\mathbf{H}^T]^{-1}\mathbf{x} \tag{3.26}$$

The MNE non-adaptive spatial filter has advantages and disadvantages against other popular techniques used to estimate the solution for the inverse problem. The performance of the MNE is not affected by the presence of correlated brain activity, but its output is distorted and weighted to solutions closer to the sensors. These characteristics are related to the use of the least-squares method, which enhances and reduce the performance of the filter under specific conditions (Clarke and Braginski, 2006). The best performance of the filter can be found when the brain activity is located on the cortex and in the presence of a high signal to noise ratio, Figure 3.9, whereas one of the worst scenarios is on the presence of brain sources deeper than the cortex, Figure 3.10.

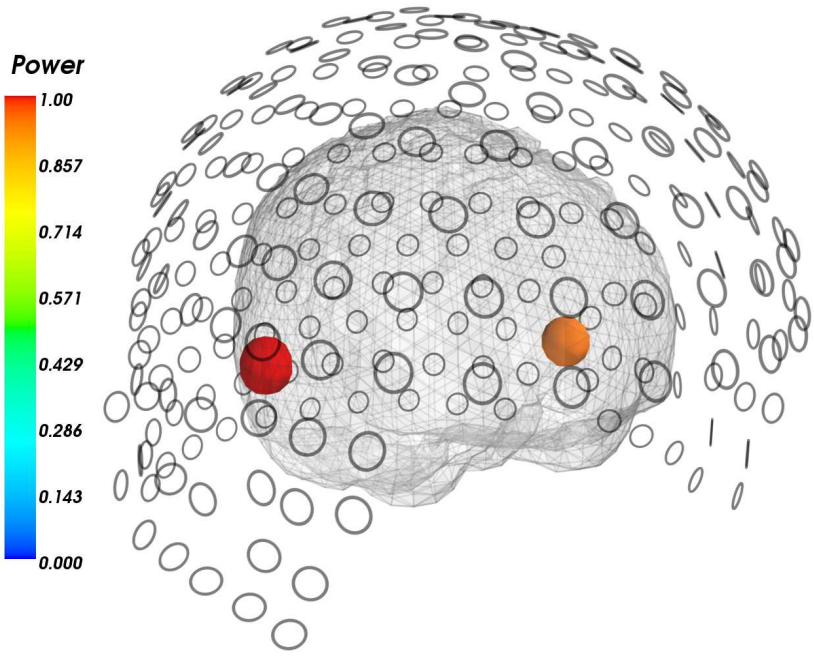

(a)

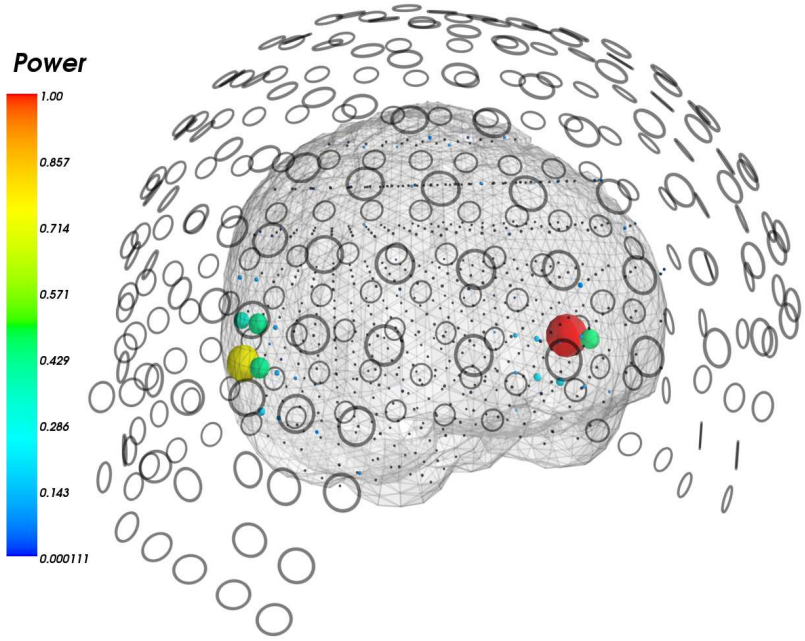

(b)

Figure 3.9: Performance of the MNE spatial filter in the finding of brain sources located near the cortex. In a) are presented the true locations for simulated brain sources, while on b) are presented the estimated locations of the sources using MNE, where the size of and colour of the spheres represent the power of the brain activity on those locations. The spatial filter was implemented in python. The brain sources were generated on different positions than the locations used to look for the brain activity. The sensor distribution, the mesh used to look for the brain activity, and the brain volume were obtained from the York Neuro Imaging Centre[7].

[7] *https://www.ynic.york.ac.uk/FrontPage*

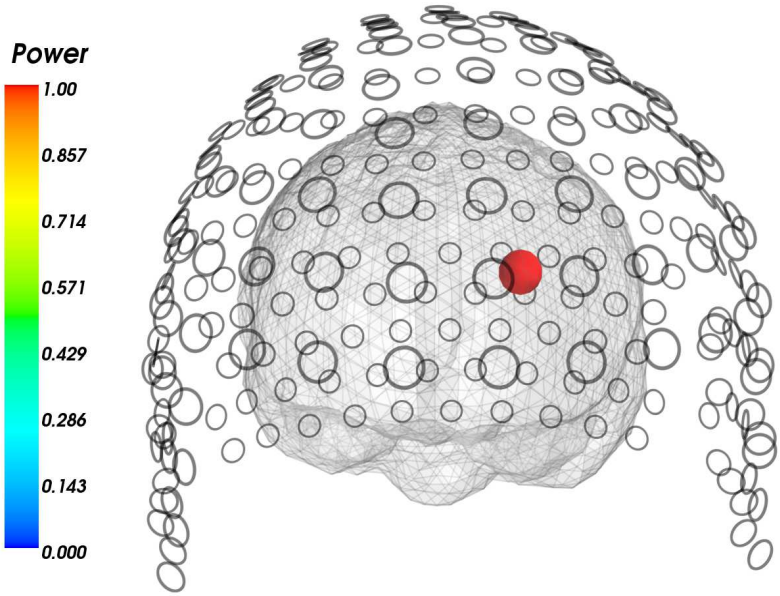

(a)

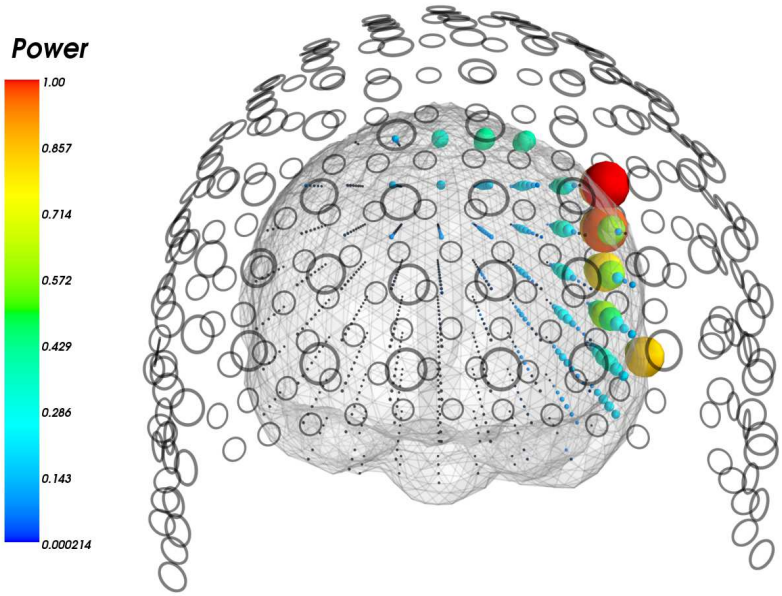

(b)

Figure 3.10: This figure shows the effects of a brain source located deeper than the cortex on the performance of the MNE spatial filter. In a) is presented the position of the brain source responsible for generation of magnetic fields, located deeper than the cortex. In b) can be observed the estimated locations for the brain source, which are near the sensors rather than in its true position.

3.3.2 Linearly Constrained Minimum Variance beamformer

The Linearly Constrained Minimum Variance beamformer is a spatial filter used to estimate the brain sources time series from measured magnetic fields (Van Veen et al., 1997). The LCMV is classified as an adaptive spatial filter, as its design relies on the covariance matrix for the measured magnetic fields (Van Veen et al., 1997). The LCMV is designed to allow the estimation of the brain activity located at location $\mathbf{r}_i$, while at the same time attenuate the contribution for the measured magnetic fields from brain sources at locations $\mathbf{r}_j$, where $\mathbf{r}_i \neq \mathbf{r}_j$. This estimation, or extraction, is implemented by the use of a set of weights $\mathbf{W}_b(\mathbf{r}_i) \in \mathbb{R}^{3\times M}$ that define the filter, as is shown in Equation 3.27 and appendix B. Unfortunately, the brain sources time series obtained with this technique are only estimates, because of factors that reduce the performance of the LCMV, factors such as the amount of correlation between the brain sources and the external noise (Sekihara and Nagarajan, 2008).

$$\widehat{\mathbf{q}}(\mathbf{r}_i) = \mathbf{W}_b^T(\mathbf{r}_i)\mathbf{x} \tag{3.27}$$

The LCMV beamformer was designed under the assumption that all brain sources are uncorrelated with each other (Sekihara and Nagarajan, 2008). This assumption allows the expression of the covariance matrix for the measured magnetic fields in terms of the auto-covariance matrices for the brain sources and the lead-fields matrices, as is shown in Equation 3.28, where $\mathbf{C}(\mathbf{x}) \in \mathbb{R}^{M\times M}$ is the $M \times M$ covariance matrix for the measured magnetic fields calculated over a time window containing P times samples, and $\langle\cdot\rangle$ is used to express the expectation operator. Moreover, the auto-covariance matrices for the brain sources on locations $\mathbf{r}_i$ are represented by the 3×3 matrices $\mathbf{C}(\mathbf{q}_i) \in \mathbb{R}^{3\times 3}$, as is shown in Equation 3.29, when the brain sources are modelled as random processes (Sekihara and Nagarajan, 2008). The effect of the noise is considered in Equation 3.28 in the form of the covariance matrix for the noise $\mathbf{Q}_\mathbf{n} \in \mathbb{R}^{M\times M}$, assuming that the noise is zero mean and uncorrelated on each of the sensors measurements (Van Veen et al., 1997).

$$\begin{aligned} \mathbf{C}(\mathbf{x}) &= \langle[\mathbf{x} - \langle\mathbf{x}\rangle][\mathbf{x} - \langle\mathbf{x}\rangle]^T\rangle \\ &= \sum_{i=1}^{N} \boldsymbol{L}(\mathbf{r}_i)\mathbf{C}(\mathbf{q}_i)\boldsymbol{L}^T(\mathbf{r}_i) + \mathbf{Q}_\mathbf{n} \end{aligned} \tag{3.28}$$

$$\mathbf{C}(\mathbf{q}_i) = \langle [\mathbf{q}(\mathbf{r}_i) - \langle \mathbf{q}(\mathbf{r}_i) \rangle][\mathbf{q}(\mathbf{r}_i) - \langle \mathbf{q}(\mathbf{r}_i) \rangle]^T \rangle \tag{3.29}$$

Then, it is necessary to design N sets of weights to extract the brain sources on N different locations, considering the $N/3 - 1$ degrees of freedom that the LCMV spatial filter has (Sekihara and Nagarajan, 2008; Van Veen et al., 1997). The pass and stop bands of the filter are characterized by the constraints presented in Equation 3.30, where $\mathbf{r} \in \Omega$, while Ω is used to represent the volume of the brain. The pass band of the filter define the spatial locations where the brain sources will be extracted, while the stop band is used to defines the spatial locations where the brain sources will be attenuated. Unfortunately, it is almost impossible to have a complete attenuation in the stop band (Van Veen et al., 1997). Hence, the trace of the covariance matrix for the brain sources $tr\{\mathbf{C}(\mathbf{q}_i)\}$ is used to minimize that problem, where the trace is used as a measure of the variance or strength of the sources (Van Veen et al., 1997).

$$\mathbf{W}_b^T(\mathbf{r}_i)\boldsymbol{L}(\mathbf{r}) = \begin{cases} \mathbf{I} & \mathbf{r} = \mathbf{r}_i \\ \mathbf{0} & \mathbf{r} \neq \mathbf{r}_i \end{cases} \tag{3.30}$$

The LCMV beamformer approach follows the idea to find the set of weights that minimize the variance of the extracted brain sources while the constraints presented in Equation 3.30 are fulfilled (Van Veen et al., 1997). This minimization of the variance optimizes the performance of the filter by reducing the contribution from sources located in the stop band (Van Veen et al., 1997). The LCMV mathematical problem is presented in Equation 3.31, where $\widehat{\mathbf{C}}(\mathbf{q}_i)$ is used to represent the estimated covariance matrix for the filter output $\widehat{\mathbf{q}}(\mathbf{r}_i)$, Equation 3.32. Thus, the solution for the constrained LCMV minimization problem is defined using the method of the Lagrange multipliers (Sekihara and Nagarajan, 2008). The solution for the LCMV problem is presented in Equation 3.33 (Van Veen et al., 1997).

$$\min_{\mathbf{W}_b(\mathbf{r}_i)} \quad tr\{\widehat{\mathbf{C}}(\mathbf{q}_i)\} \quad \text{subject to} \quad \mathbf{W}_b^T(\mathbf{r}_i)\boldsymbol{L}(\mathbf{r}_i) = \mathbf{I} \tag{3.31}$$

$$\widehat{\mathbf{C}}(\mathbf{q}_i) = \mathbf{W}_b^T(\mathbf{r}_i)\mathbf{C}(\mathbf{x})\mathbf{W}_b(\mathbf{r}_i) \tag{3.32}$$

$$\mathbf{W}_b^T(\mathbf{r}_i) = [\boldsymbol{L}^T(\mathbf{r}_i)\mathbf{C}^{-1}(\mathbf{x})\boldsymbol{L}(\mathbf{r}_i)]^{-1}\boldsymbol{L}^T(\mathbf{r}_i)\mathbf{C}^{-1}(\mathbf{x}) \tag{3.33}$$

Once the filter weights are obtained, the brain sources can be estimated from the measured magnetic fields. However, it is also necessary to find the brain locations $\mathbf{r}_i$ with enough activity to be considered as active, where the trace of the estimated covariance matrices for the brain sources can be used as a metric for their strength (Van Veen et al., 1997; Huang et al., 2004). Nevertheless, the trace of the filter output is not an accurate estimator, because of the LCMV weights design, which does not consider the external noise effect (Sekihara and Nagarajan, 2008). Then, a different metric is needed in order to considerer the effect of the external noise, this metric is known as the neural activity index (NAI), shown in Equation 3.34, where $\widehat{Var}(\mathbf{r}_i)$ is the estimated brain strength (Van Veen et al., 1997).

$$\text{NAI}(\mathbf{r}_i) = \widehat{Var}(\mathbf{r}_i) = \frac{tr\{[\boldsymbol{L}^T(\mathbf{r}_i)\mathbf{C}^{-1}(\mathbf{x})\boldsymbol{L}(\mathbf{r}_i)]^{-1}\}}{tr\{[\boldsymbol{L}^T(\mathbf{r}_i)\mathbf{Q}_\mathbf{n}^{-1}\boldsymbol{L}(\mathbf{r}_i)]^{-1}\}} \tag{3.34}$$

In Figure 3.11 is presented the estimation of brain activity using the LCMV beamformer, where the activity were simulated as uncorrelated AR processes, with a SNR of 20. In Figure 3.12 are presented the effects that correlated activity has on the performance of the LCMV beamformer, where two brain sources were simulated as correlated AR processes with a correlation coefficient factor of .5, while a third simulated source was uncorrelated with respect to the other two. The problem of correlated activity causes a decrease in the power of the estimated activity, which in some cases can make the estimated activity smaller than the effects of the external noise, making the filter estimate brain sources in the wrong locations (Sekihara et al., 2002). Moreover, even when this is the biggest weakness of the filter, its use for brain study has increased because it is not common to deal with highly correlated brain sources in most of brain studies, specially between distant brain regions (David et al., 2003).

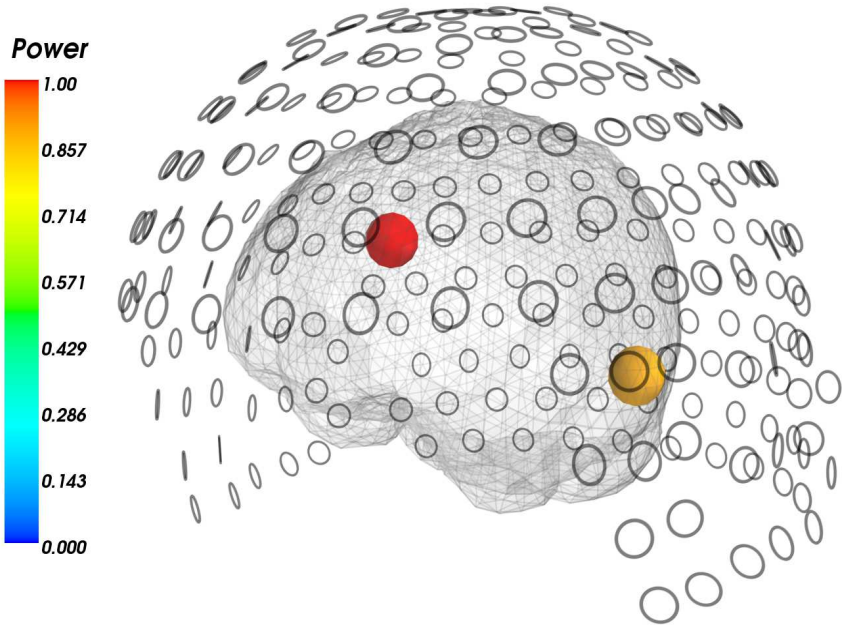

(a)

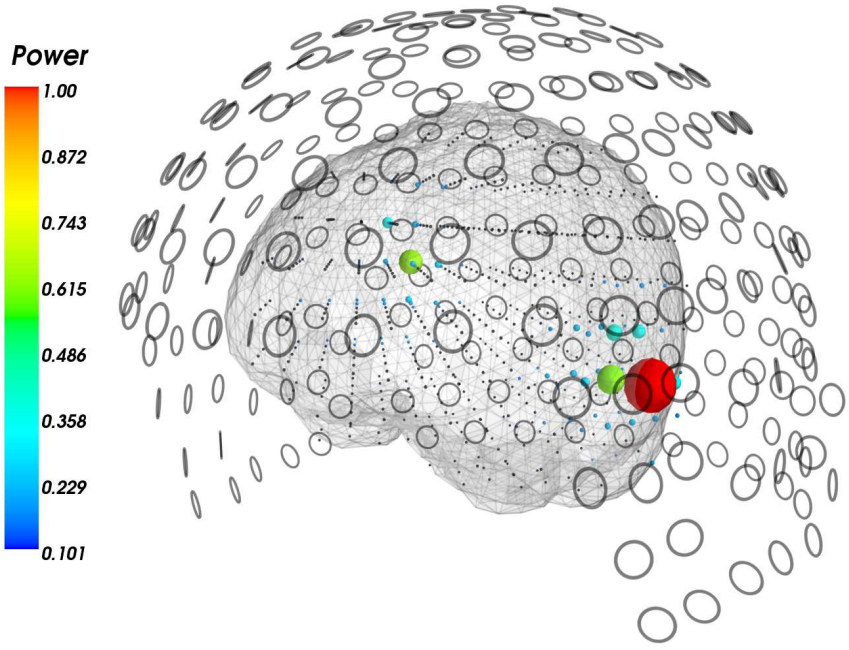

(b)

Figure 3.11: Estimation of simulated brain sources using the LCMV beamformer. In a) are presented the real locations for the simulated brain activity, while in b) are presented the estimated locations using the LCMV beamformer, where the size and colour of the spheres represent the power of the brain activity on those locations. The locations for the simulated brain sources do not match the locations used to look for the brain activity, which were based on the YNIC brain mesh[8].

[8] *https://www.ynic.york.ac.uk/FrontPage*

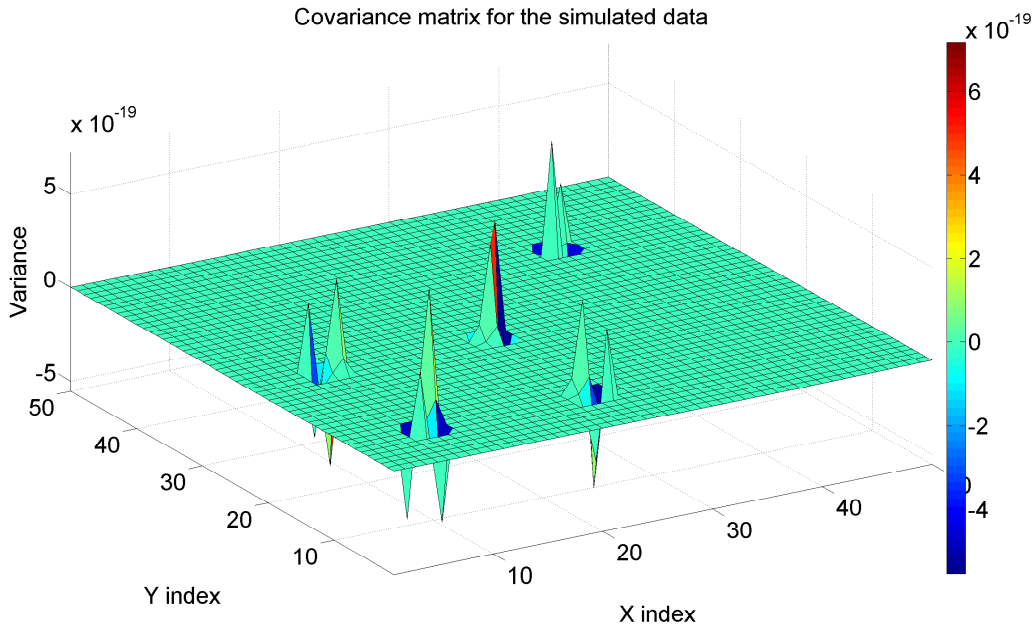

(a)

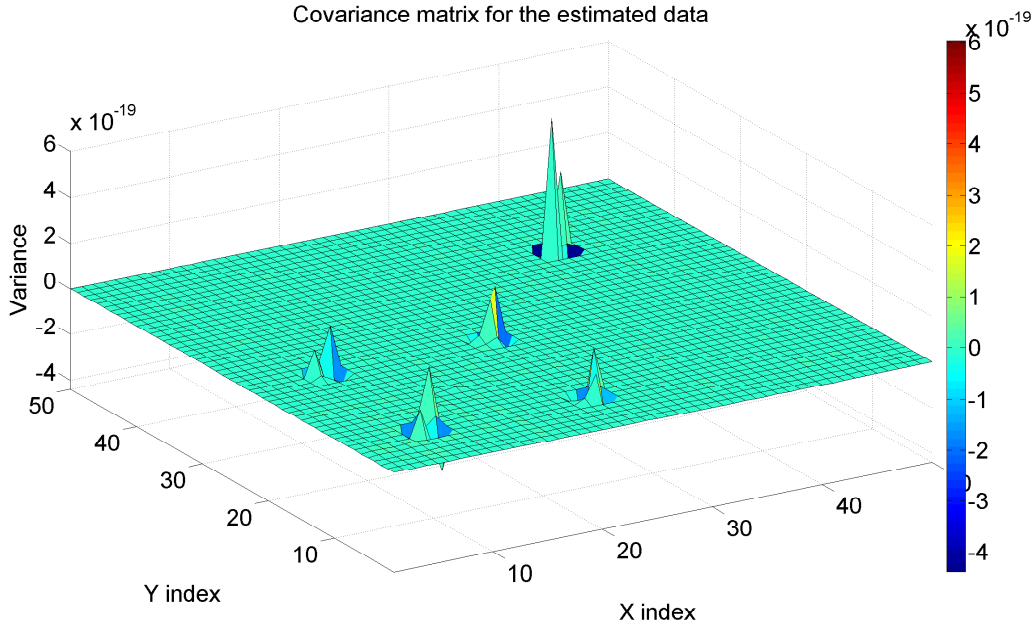

(b)

Figure 3.12: Effects of correlated activity on the performance of the LCMV beamformer. In a) is presented the covariance matrix composed by three simulated brain sources, its diagonals elements are composed by the variance of the brain sources components, while its off-diagonal elements are composed by the covariance between the brain sources components. In b) is presented the covariance matrix for the estimated brain activity, where their variances decrease in relation with the amount of correlation that exist between the simulated brain activity. The simulated brain activity match the positions used to solve the inverse problem.

3.4 Spatial filters variants

The previously mentioned spatial filters have advantages and disadvantages with respect to each other, which enhance their performances for specific scenarios while reducing their use for others. The main problem that the MNE non-adaptive spatial filter has is its distorted and weighted output characteristics, which is based on the least-squares method, but it also has advantages over the LMCV. On the other hand, the main problem related to the LCMV adaptive spatial filter is the assumption for the estimation of the weights that define the filter, the uncorrelated brain sources assumption. These problems have been the main focus of researches related to the design of spatial filters, where modifications to the MNE and the LCMV have been made to improve their weakness. Some of the most known algorithms used to improve MNE and the LCMV are the Unbiased Minimum Norm, the FOCal Undetermined System Solution (FOCUSS), the Dual-Core beamformer, and a beamformer that depends on the use of a higher order covariance matrix (Type-4).

3.4.1 Unbiased Minimum Norm

The unbiased MNE is a modification implemented on this filter to compensate for the bias to solutions for the inverse problem near the sensors. This compensation is implemented in the form of a matrix $\mathbf{W}_u \in \mathbb{R}^{3N\times 3N}$ composed by regularization parameters, Equation 3.35 and appendix A. These parameters are used to compensate for the problem of the use of the least-squares method, and for the fall-off over distance characteristic of the magnetic fields, which focus the filter on solutions near the sensors with more power in the field distributions with less currents (Clarke and Braginski, 2006). The compensation is introduced on the lead-fields, which cause the sensors to have a larger norm for brain locations near the sensors than for deeper sources.

$$\widehat{\mathbf{m}} = \mathbf{W}_u\mathbf{W}_u^T\mathbf{H}^T[\mathbf{H}\mathbf{W}_u\mathbf{W}_u^T\mathbf{H}^T]^{-1}\mathbf{x} \tag{3.35}$$

However, it is difficult to compensate for locations at different depths. The geometry of the shape of the volume conductor, and the location and orientations of the sensors complicate the finding of the parameters needed for the compensation. Thus, the compensation of the bias depends on the characteristics of the experiment implemented. One type of bias adjustment used is the normalization (Gorodnitsky et al., 1995), where each of the diagonal

elements of the matrix is defined as the reciprocal of the Euclidean norm of each of the $\boldsymbol{L}(\mathbf{r}_i)$ columns, Equation 3.36. Nevertheless, this regularization only works well on relatively small reconstruction spaces, or when sensors are close to the brain space (Gorodnitsky et al., 1995).

$$\mathbf{W}_u = \begin{bmatrix} 1/||\boldsymbol{l}_x(\mathbf{r}_1)|| & & & \\ & 1/||\boldsymbol{l}_y(\mathbf{r}_1)|| & & \\ & & \ddots & \\ & & & 1/||\boldsymbol{l}_z(\mathbf{r}_N)|| \end{bmatrix} \tag{3.36}$$

3.4.2 FOCUSS

The FOCal Undetermined System Solution algorithm is considered an improvement for the MNE distorted output, appendix D. Thus, the FOCUSS algorithm in combination with the unbiased implementation of the MNE enhances both of the main problems that the MNE has (Clarke and Braginski, 2006). FOCUSS uses the same approach as the unbiased minimum norm, but the regularized matrix is estimated through iterations. However, the starting point of the iteration is the main weakness that this implementation has. The solutions found will be undistorted, but the locations for the estimated brain sources will be wrong if the estimated locations for the brain activity are not properly bias compensated (Gorodnitsky et al., 1995). The FOCUSS algorithm is based on Equation 3.38, where the matrix of weights $\mathbf{W}_{F_k} \in \mathbb{R}^{3N\times 3N}$ is calculated over k iterations until a specified condition is fulfilled, appendix D. To avoid bad localization of the brain activity, the starting point of the iterations is normally defined as Equation 3.36.

$$\mathbf{W}_{F_k} = \begin{bmatrix} diag(\widehat{\mathbf{q}}_k(\mathbf{r}_1)) & & & \\ & diag(\widehat{\mathbf{q}}_k(\mathbf{r}_2)) & & \\ & & \ddots & \\ & & & diag(\widehat{\mathbf{q}}_k(\mathbf{r}_N)) \end{bmatrix} \tag{3.37}$$

$$\widehat{\mathbf{m}} = \mathbf{W}_{F_k}\mathbf{W}_{F_k}^T\mathbf{H}^T[\mathbf{H}\mathbf{W}_{F_k}\mathbf{W}_{F_k}^T\mathbf{H}^T]^{-1}\mathbf{x} \tag{3.38}$$

3.4.3 Dual-Core beamformer

A beamformer with a modified source model is one solution to reduce the effects of correlated brain sources on the performance of the LCMV beamformer (Brookes et al., 2007; Diwakar

et al., 2011). This modification to the well known LCMV beamformer is known as the Dual-Core beamformer, and is similar to the null-beamformer, which nullified the effects of brain sources at specific locations on other brain locations (Dalal et al., 2006). The difference with the Dual-Core beamformer is that the Dual-Core estimates the activity on two different locations at the same time, instead of reducing the effect of the second one. This is possible using the dual lead-fields concept presented on Equation 3.39, which defines the sensitive of the sensors for two different sources (Brookes et al., 2007). The Dual-Core beamformer design follows the LCMV approach based on the uncorrelated brain sources assumption, with the only difference that the Dual-Core beamformer uses the dual lead-fields, Equation 3.40.

$$\boldsymbol{L}_{DUAL} = \frac{1}{2}\boldsymbol{L}(\mathbf{r}_i) + \frac{1}{2}\boldsymbol{L}(\mathbf{r}_j) \tag{3.39}$$

$$\mathbf{W}_{DUAL}(\mathbf{r}_{ij}) = [\boldsymbol{L}_{DUAL}^T(\mathbf{r}_i)\mathbf{C}^{-1}(\mathbf{x})\boldsymbol{L}_{DUAL}(\mathbf{r}_i)]^{-1}\boldsymbol{L}_{DUAL}^T(\mathbf{r}_i)\mathbf{C}^{-1}(\mathbf{x}) \tag{3.40}$$

3.4.4 High order covariance matrix beamformer

The type 4 vectorized beamformer is a modified version of the LCMV beamformer, which deal with the effects of the external noise and correlated brain activity by using a higher order covariance matrix for the estimation of the filter weights (Huang et al., 2004). Then, the filter weights and the neural activity index can be expressed as Equation 3.41 and 3.42, respectively, where Equation 3.42 is the vectorized form of Equation 3.34 (Huang et al., 2004). The covariance matrix of higher order is expressed as $\mathbf{C}^n \in \mathbb{R}^{M\times M}$, where n is used to represent the order of the covariance matrix for the measured magnetic fields $\mathbf{C}(\mathbf{x})$, while $\mathbf{Q}_\mathbf{n}^n$ represent the n order covariance matrix for the external noise.

$$\mathbf{W}_{b4}^T(\mathbf{r}_i) = [\boldsymbol{L}^T(\mathbf{r}_i)\mathbf{C}^{-n}\boldsymbol{L}(\mathbf{r}_i)]^{-1}\boldsymbol{L}^T(\mathbf{r}_i)\mathbf{C}^{-n} \tag{3.41}$$

$$\mathrm{NAI}_4(\mathbf{r}_i) = \frac{(\boldsymbol{l}_x^T(\mathbf{r}_i)\mathbf{C}^{-n}\boldsymbol{l}_x(\mathbf{r}_i))^{-1}}{(\boldsymbol{l}_x^T(\mathbf{r}_i)\mathbf{Q}_\mathbf{n}^{-n}\boldsymbol{l}_x(\mathbf{r}_i))^{-1}} + \frac{(\boldsymbol{l}_y^T(\mathbf{r}_i)\mathbf{C}^{-n}\boldsymbol{l}_y(\mathbf{r}_i))^{-1}}{(\boldsymbol{l}_y^T(\mathbf{r}_i)\mathbf{Q}_\mathbf{n}^{-n}\boldsymbol{l}_y(\mathbf{r}_i))^{-1}} + \frac{(\boldsymbol{l}_z^T(\mathbf{r}_i)\mathbf{C}^{-n}\boldsymbol{l}_z(\mathbf{r}_i))^{-1}}{(\boldsymbol{l}_z^T(\mathbf{r}_i)\mathbf{Q}_\mathbf{n}^{-n}\boldsymbol{l}_z(\mathbf{r}_i))^{-1}} \tag{3.42}$$

3.5 Summary

In this chapter was introduced the use of magnetic fields generated from neuronal activity for the study of the brain. The magnetic fields generated from the brain activity are known as magnetoencephalograms, and their study can be implemented in two different domains or spaces, on the sensors used to measured the magnetic fields, and on the sources space using regression analysis to estimate where the brain signals were generated. The brain analysis on the sensors space depend on the solution of the forward problem, related to the measurements of the magnetic fields from the brain activity, where the Maxwells equations on their quasi static form are used. However, the study of the brain in the sensors domain generates problems related to the field spread effect, or with the reduction of the magnetic fields strength with respect to the distance from where the brain activity was generated.

The study of the brain in the sources space is possible by solving the neuromagnetism inverse problem, related to the estimation of the brain activity responsible for the generation of the magnetic fields. This approach is based on the Biot-Savart law, which is used to express the magnetic fields measured on the sensors. Thus, regression analysis are used to estimate the brain activity from the Biot-Savart law. Two of the most used techniques for this are the linearly constrained minimum variance beamformer, and the minimum norm estimates spatial filter. These techniques have advantages and disadvantages with respect to each other, such as been unaffected by the presence of correlated brain activity or by giving less distorted and unbiased solutions.

Chapter 4

Magnetoencephalography and functional brain connectivity

The study of brain dynamics using MEG signals requires signal processing techniques and statistical analysis to reduce the uncertainties related to the complexity of the brain. The accuracy of these techniques depends on factors such as the external noise, the sampling frequency, the geometry of the volume conductor used to represent the brain, and the smoothness of the brain signals spectrum in the frequency domain. The study of the brain dynamics can be implemented in the sensor domain (Smith, 1992; Zhongming et al., 2010) or in the source domain (Kujala et al., 2008; Gaetz and Cheyne, 2006), by measuring the magnetic fields generated by the brain activity or by solving the neuromagnetism inverse problem, respectively. However, as was mentioned before, the study of the brain dynamics in the sensor domain gives a non-accurate representation of the brain behaviour because of the magnetic field spread effects (Schoffelen and Gross, 2009; Brookes et al., 2011; Srinivasan et al., 2007), which increases the measuring of false brain interactions. On the other hand, brain studies in the source domain rely on the methods used for the solution of the inverse problem, where spurious findings of brain active regions could compromise the estimation of the brain interactions (David et al., 2006).

In this chapter are presented the most used techniques for the estimation of brain dynamics in the source domain, and one of the most used statistical analysis to reduce the finding of spurious brain connectivities. The techniques presented in this chapter are used on the two approaches to estimate the brain interactions using spatial filters, as is presented in Figure 4.1. The techniques presented in this chapter are focus on the estimation of the functional brain

interactions, without putting emphasis in their directions or causalities. It is also introduced in this chapter the required procedure for the use of the spatial filters in order to use their outputs for the measurements of the brain interactions, specially for the frequency domain implementation of the spatial filters, where the smoothness of the spectrum is important to reduce the measurements of false interactions.

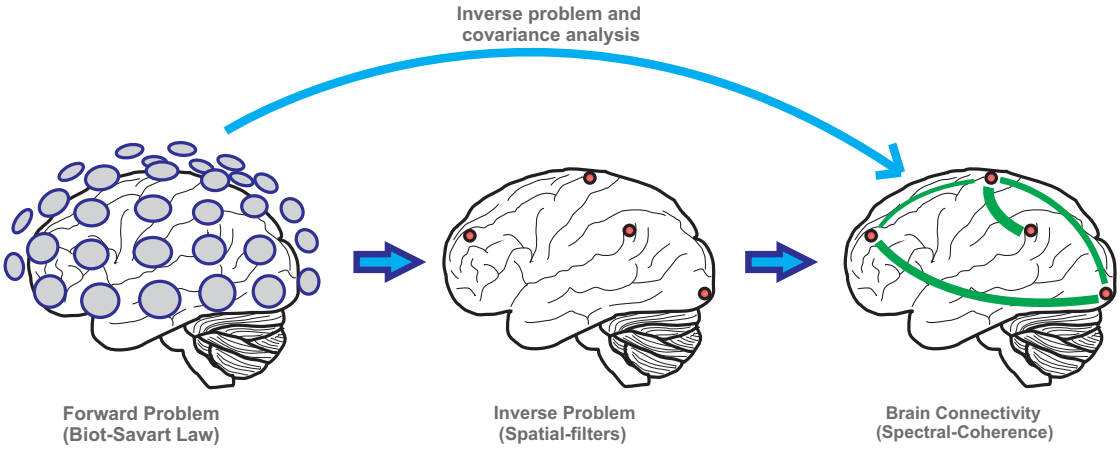

Figure 4.1: Approaches followed to estimate the brain dynamics using spatial filters.

4.1 Estimation of the brain activity

The brain activity responsible for the generation of the MEG data can be estimated as time series or as their spectrum. This is possible by using the spatial filters presented in Chapter 3 to solve the inverse problem in the time or in the frequency domain. The main difference between these two types of implementations is the use of the spectrum for the measured magnetic fields and its cross-spectral density matrix for the frequency domain implementation, instead of the measured magnetic fields time series and its covariance matrix for the time domain implementation (Sekihara and Nagarajan, 2008). The most common techniques used for the calculation of the spectrum and the cross-spectral density matrices are the fast Fourier transform, the Welch periodograms (Jensen and Vanni, 2002), and the multi-taper approach (Maris and Oostenveld, 2007). It is important to remark that the same results are obtained when the spatial filters are implemented in the time and in the frequency domain, by using the same time to frequency domain transformation techniques. The only difference is the increment of the computational processing.

The main advantage for the use of the frequency domain version of the spatial filters is the direct estimation of the brain interactions from the output of the filters, as was proved by Gross with the implementation of the Dynamic Imaging of Coherent Sources (Gross et al., 2001). Thus, it is also useful to reduce the computational cost for the calculation of the spectrum and the cross-spectral density matrices among different brain regions. This, as it is only needed the estimation of the spectrum and the cross-spectral density matrix for the measured magnetic fields, Section 4.1.2, while it is required the estimation of the spectrum and the cross-spectral density matrix for each of the time series obtained from the output of the time domain version of the spatial filters.

4.1.1 Spatial filters in the time domain

One way to calculate the brain interactions is with the use of the brain activity time series, which are obtained using the spatial filters implemented in the time domain, using Equation 3.25 or 3.27 from Chapter 3. The accuracy for the estimation relies on the characteristics of the spatial filters, and on external factors such as the amount of correlation present between different brain regions (Sekihara et al., 2002; Huang et al., 2004; Clarke and Braginski, 2006). For example, a brain study with expected highly correlated activity should use the MNE spatial filter for the estimation of the brain activity time series, as it is not affected by the presence of correlated brain activity. However, the performance of the LCMV beamformer is better than the MNE spatial filter in the presence of small correlated brain activity (Sekihara et al., 2002), as it does not have a significant bias to solutions near the sensors (Sekihara et al., 2005). Nevertheless, it is almost impossible to have complete certainty about the amount of correlation that exists among different brain regions, or to know that the brain activity responsible for the generation of the magnetic fields is located on the cortex or in deeper locations because of the complexity of the brain.

As was mentioned before, the performance of the LCMV beamformer is affected by the presence of correlated brain activity, which decreases the amplitude of the estimated activity depending on the amount of correlation (Sekihara and Nagarajan, 2008). Thus, in the presence of uncorrelated brain activity the estimation of the time series will be limited only by the SNR of the system. On the other hand, in the presence of highly correlated activity the estimated time series can be almost completed overlapped by the effects of the external noise, as their amplitudes are reduced by the amount of correlation. This reduces the possibilities to reconstruct the time series accurately.

The MNE spatial filter can estimate correctly the brain sources time series as long as the brain activity is located on the brain surface, otherwise the brain activity found will not match the correct locations (Clarke and Braginski, 2006). Another important problem that the MNE has is the effect of the external noise, which can decreases the performance of the filter because of the use of regularization techniques for the calculation of the weights that define the filter (Sarvas, 1987; Hämäläinen et al., 1993). This effect can be compensated by choosing a tolerance value for regularization techniques used for the inverse of the gram matrix. Nevertheless, if this value is not chosen correctly, the recovered time series will be mostly composed from the effects of the external noise instead of the brain activity.

The reconstruction of time series using the LCMV and MNE spatial filters for uncorrelated and correlated simulated brain activity is presented in figures 4.2 to 4.7. In Figures 4.2 and 4.5 can be observed the simulated activity locations and time series, for the uncorrelated and correlated cases, respectively. Moreover, Figures 4.3 and 4.4 show the reconstructed uncorrelated simulated activity using the LCMV and the MNE spatial filters, receptively. The effects of correlated activity on the reconstruction of brain activity can be observed in Figures 4.6 and 4.7, for the LCMV and the MNE spatial filter cases, respectively. The brain activity was simulated as AR processes of order 9, while the external noise was simulated as uncorrelated white noise for a SNR of 22. The selected locations used in Figures 4.2 to 4.7 for the LCMV and MNE time series reconstructions were chosen based on brain mesh locations with higher estimated activity, or power maps, for the uncorrelated brain activity case.

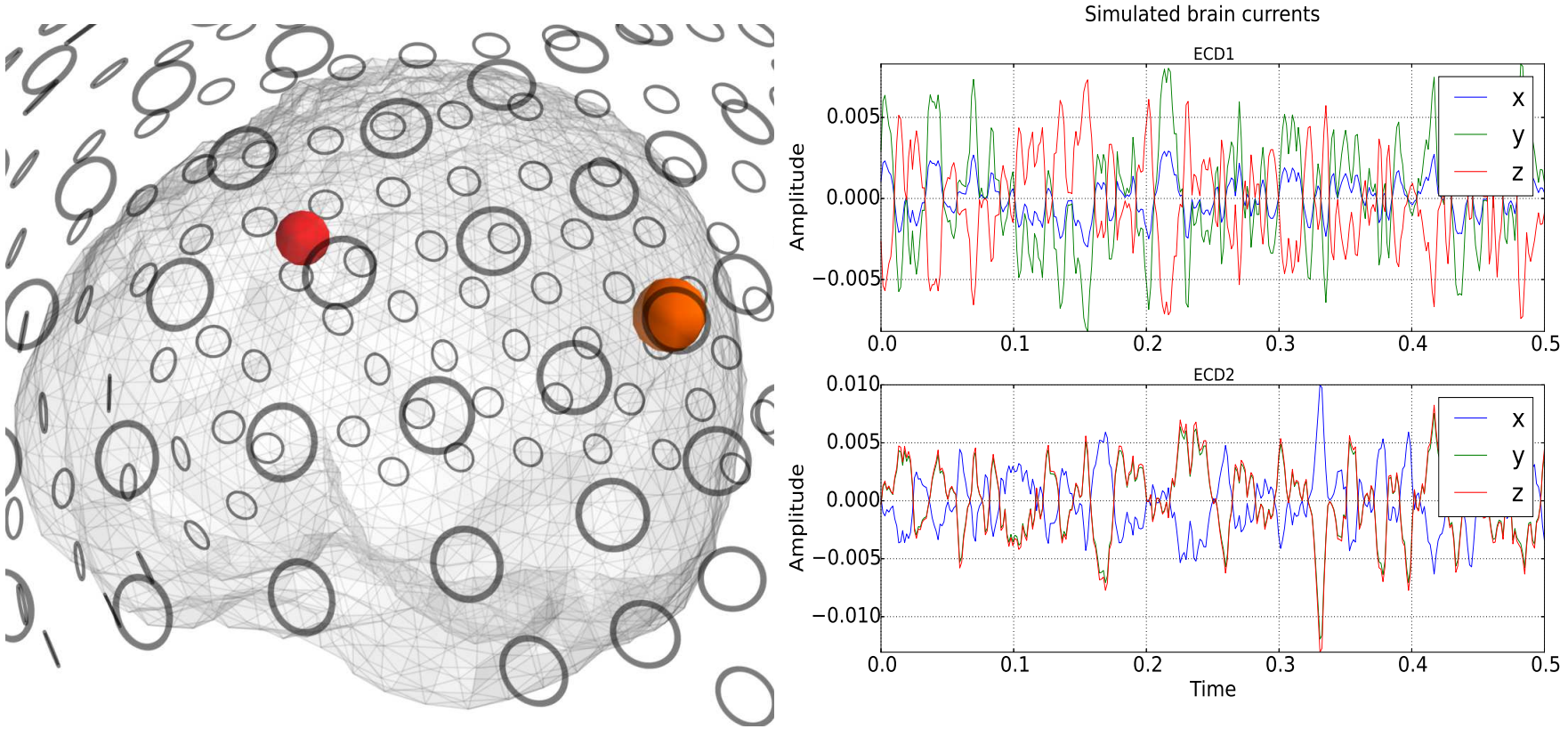

Figure 4.2: Simulation of uncorrelated brain activity. On the left can be observed the locations for the simulated brain activity, while on the right are presented the time series for the simulated activity. The sizes for the spheres represent the average power for the signals presented.

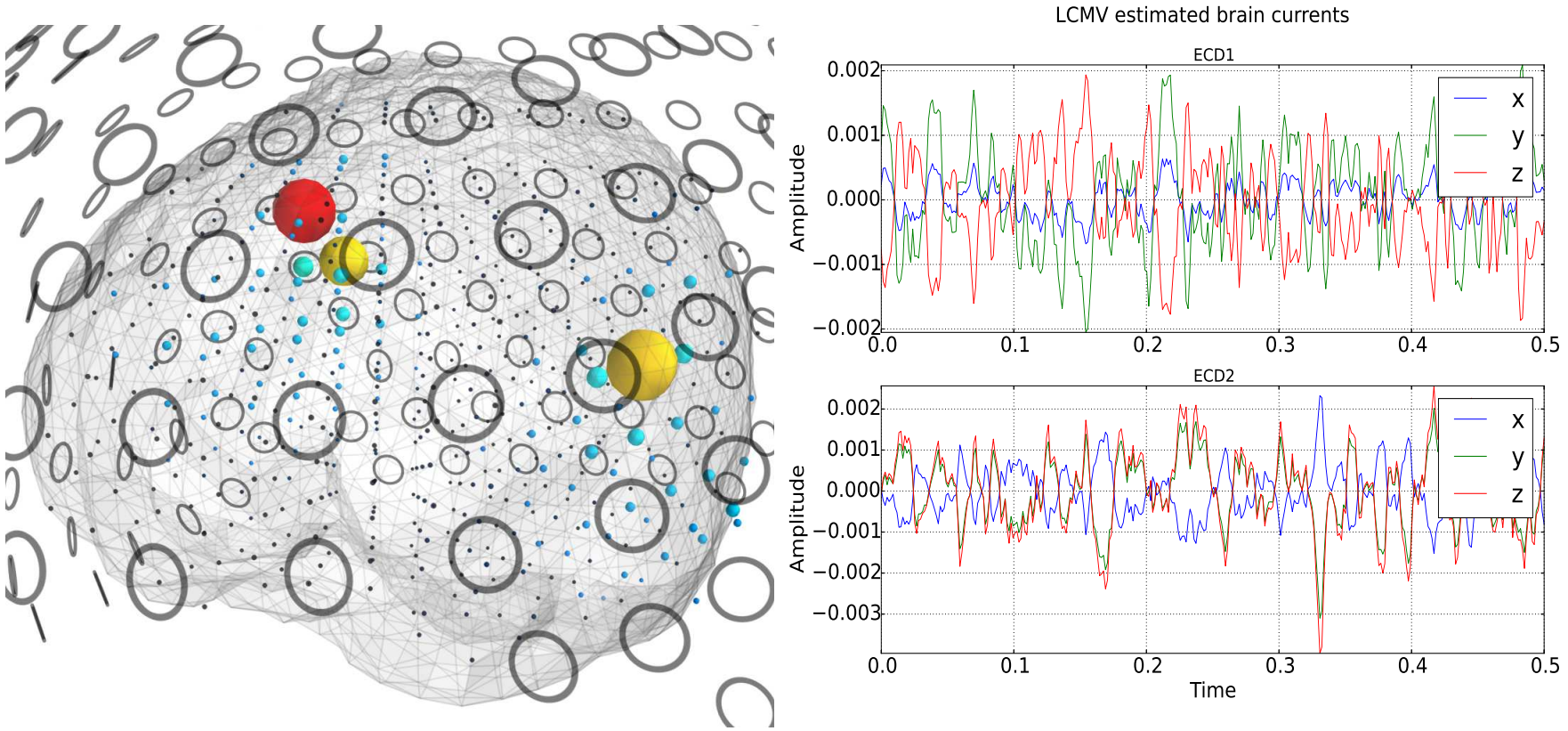

Figure 4.3: Reconstruction of uncorrelated simulated brain activity using the LCMV beamformer. On the left can be observed the locations for the reconstructed simulated brain activity, while on the right are presented the reconstructed time series for the simulated activity. The sizes for the spheres represent the average power for the signals presented.

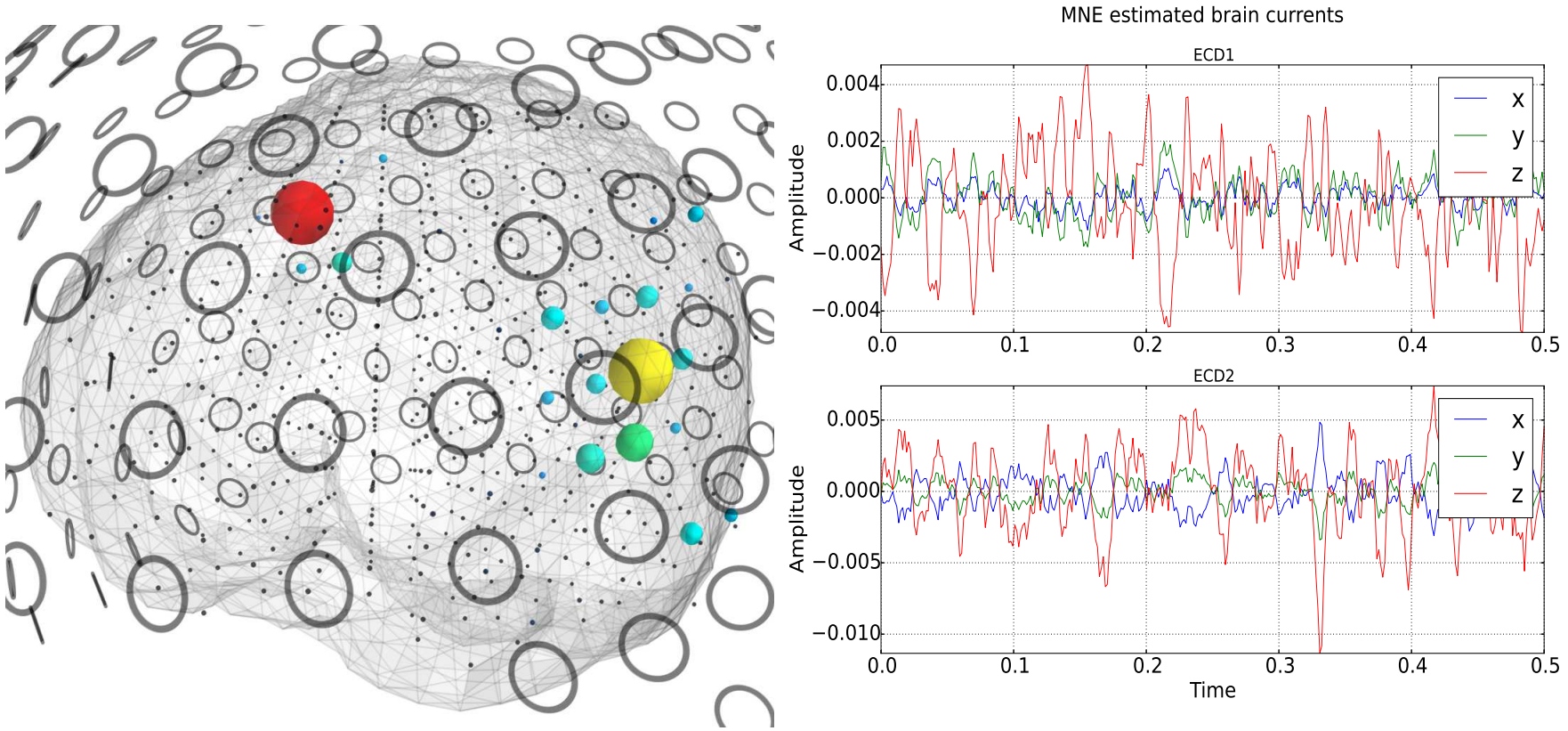

Figure 4.4: Reconstruction of uncorrelated simulated brain activity using the MNE spatial filter. On the left can be observed the locations for the reconstructed simulated brain activity, while on the right are presented the reconstructed time series for the simulated activity. The sizes for the spheres represent the average power for the signals presented.

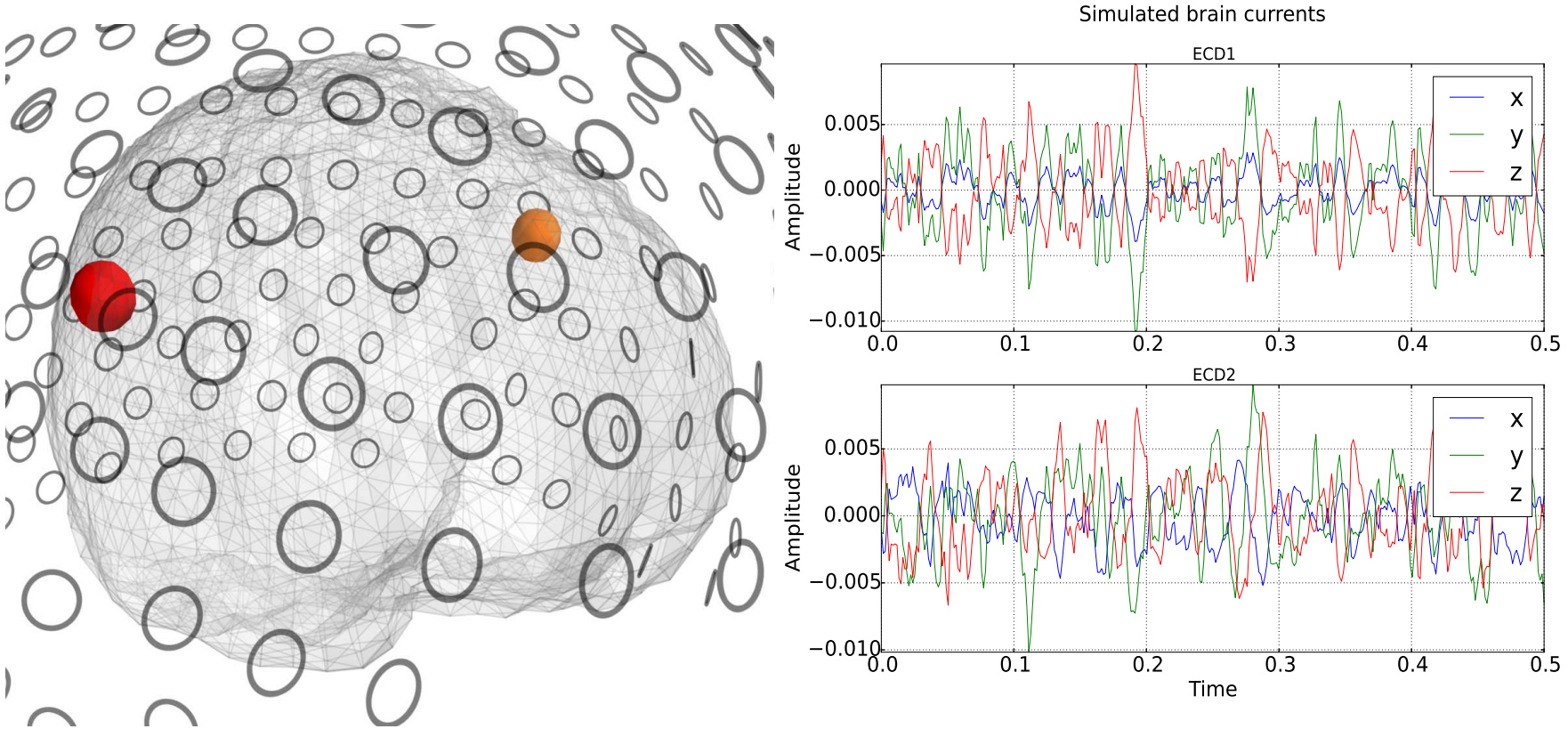

Figure 4.5: Simulation of correlated brain activity. On the left can be observed the locations for the simulated brain activity, while on the right are presented the time series for the simulated activity. The sizes for the spheres represent the average power for the signals presented.

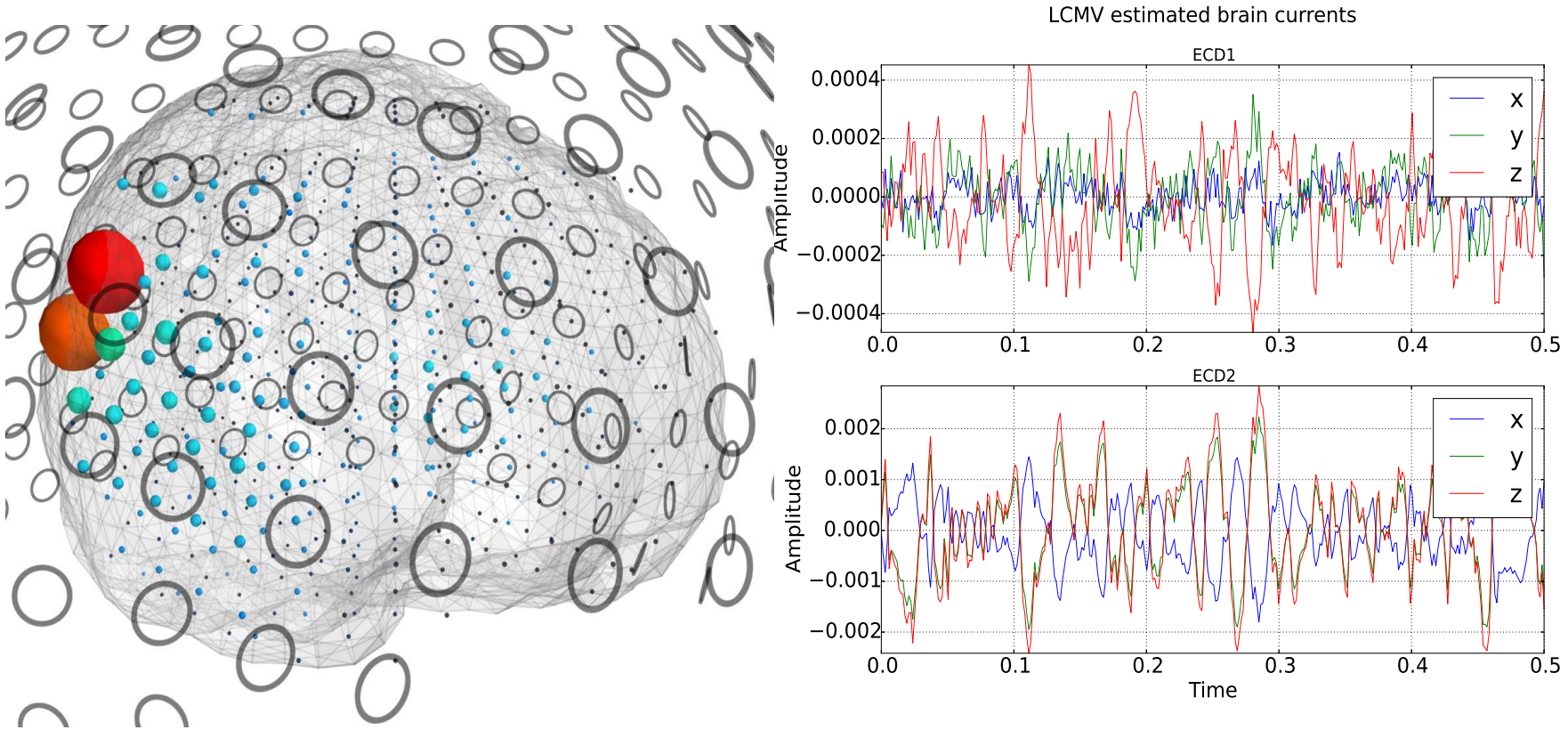

Figure 4.6: Reconstruction of correlated simulated brain activity using the LCMV beamformer. On the left can be observed the locations for the reconstructed simulated brain activity, while on the right are presented the reconstructed time series for the simulated activity. The sizes for the spheres represent the average power for the signals presented.

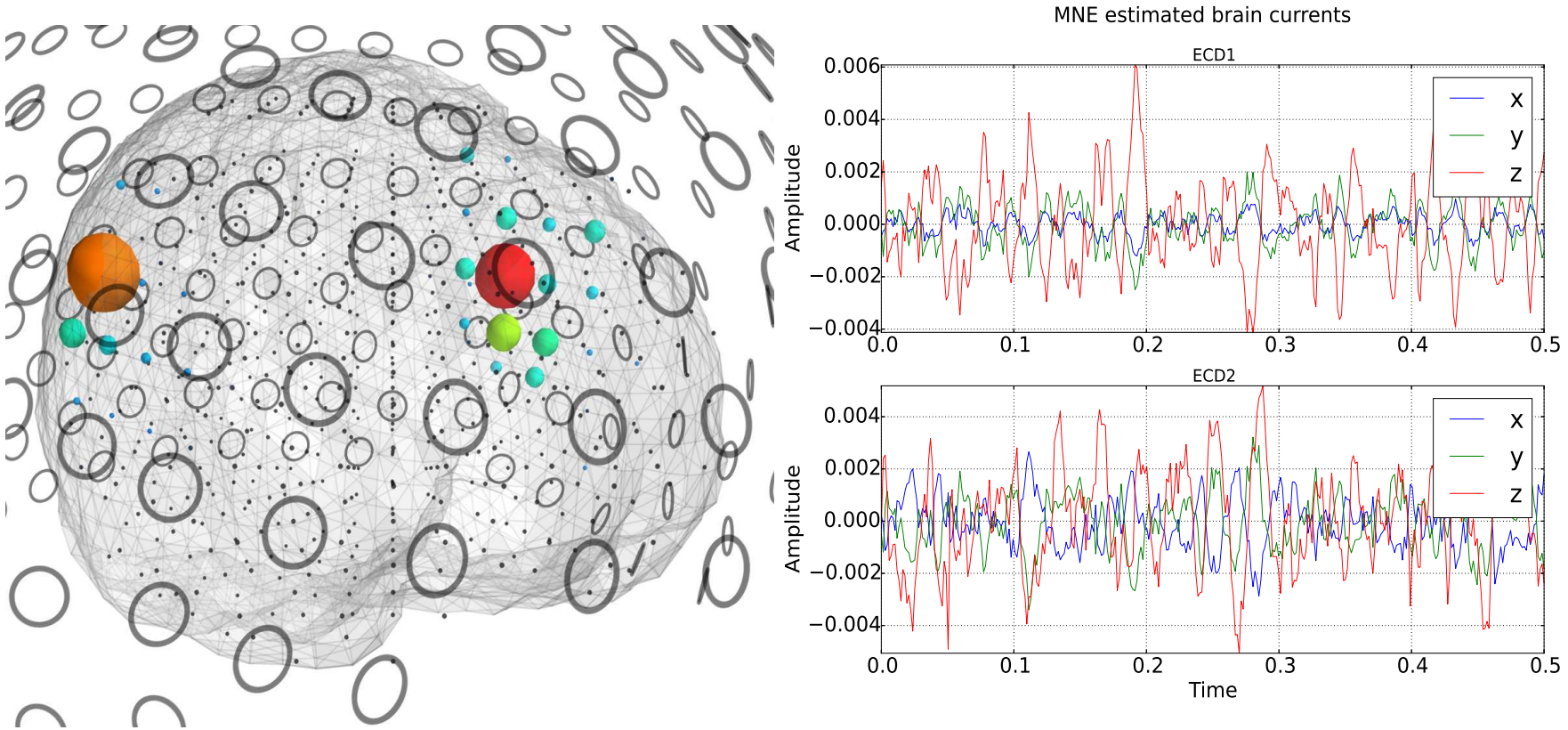

Figure 4.7: Reconstruction of correlated simulated brain activity using the MNE spatial filter. On the left can be observed the locations for the reconstructed simulated brain activity, while on the right are presented the reconstructed time series for the simulated activity. The sizes for the spheres represent the average power for the signals presented.

4.1.2 Spatial filters in the frequency domain

The use of the spatial filters in the frequency domain follows the same approach used for the implementation of the spatial filters in the time domain, with the exception that these versions of the filters use the Fourier transform for the MEG recordings as inputs to the filter, and the cross-spectral density matrix for the measured magnetic fields for the design of the filters weights (Sekihara and Nagarajan, 2008). The frequency domain versions of the filters present the same limitations as their time domain versions. The Fourier transform of the measured magnetic fields is defined in Equation 4.1, where $g_m(f)$ is the Fourier transform of channel m used in the measuring of the magnetic fields, Equation 4.2.

$$\mathbf{g}(f) = \begin{bmatrix} g_1(f) \\ g_2(f) \\ \vdots \\ g_M(f) \end{bmatrix} \tag{4.1}$$

$$g_m(f) = \int_{-\infty}^{\infty} b_m(t) e^{-2\pi f t} dt \tag{4.2}$$

The cross-spectral density matrix for the measured magnetic fields can be estimated using Equation 4.3 (Sekihara and Nagarajan, 2008), where the superscript H is used to represent the Hermitian transpose. However, in the use of the discrete Fourier transform, which is implemented in most of the software available to analyse data, the frequency resolution increases with the length of the data, while the accuracy for the estimation of the amplitude and phase of the spectrum does not (Jensen and Vanni, 2002). This can be improved using techniques such as the Welch periodograms (Welch, 1967) and the Multi-taper approach (Percival and Walden, 1998). The approach presented by Welch improves the estimation of the power spectra by dividing the signals into segments with the same length, and with specific overlapping among the segments. Then, the spectrum is found by averaging the estimated spectrum calculated for each of the segments. The multi-taper approach follows a different idea from the Welch periodograms, it is still based on spectrum averaging, but instead of the segmentation independent estimations are obtained for the same signal by using orthogonal tapers, which provides independent estimations for the underlying spectrum.

$$\mathbf{\Gamma}(f) = \langle \mathbf{g}(f) \mathbf{g}^H(f) \rangle \tag{4.3}$$

The frequency domain version of the spatial filters have the same design and characteristics as the spatial filters presented in equations 3.24 and 3.33. The difference between these version of the filters is how the filters weights are obtained, which for the frequency domain are calculated using equations 4.4 and 4.5, for the LCMV beamformer and the MNE spatial filter, respectively. It can be observed that there is no difference between the expressions used for the MNE spatial filter weights in the time and in frequency domain, this is because the filter is non-adaptive, and therefore, the filter does not rely on the measured magnetic fields, but on the characteristics of the MEG acquisition system. Thus, the estimated brain activity at location $\mathbf{r}_i$ for the f frequency is obtained using Equation 4.6.

$$\mathbf{W}_b^T(\mathbf{r}_i, f) = [\boldsymbol{L}^T(\mathbf{r}_i)\boldsymbol{\Gamma}^{-1}(f)\boldsymbol{L}(\mathbf{r}_i)]^{-1}\boldsymbol{L}^T(\mathbf{r}_i)\boldsymbol{\Gamma}^{-1}(f) \tag{4.4}$$

$$\mathbf{W}_{ls}(\mathbf{r}_i, f) = \boldsymbol{L}^T(\mathbf{r}_i)[\mathbf{H}\mathbf{H}^T]^{-1} \tag{4.5}$$

$$\mathbf{s}(\mathbf{r}_i, f) \approx \mathbf{W}_b^H(\mathbf{r}_i, f)\mathbf{g}(f) \approx \mathbf{W}_{ls}^H(\mathbf{r}_i, f)\mathbf{g}(f) \tag{4.6}$$

The use of the previously presented equations can be applied for specific frequencies f, or for a specific band of frequencies F_w (Sekihara and Nagarajan, 2008). Then, the cross spectral density matrix for the measured magnetic fields can be expressed as is presented in Equation 4.7, while the expression for the LCMV beamformer weights is expressed in Equation 4.8. In Figure 4.8 can be observed the effect of the use of the Welch periodograms compared with the use of the fast Fourier transform found in Matlab for the estimation of the power spectral density or raw periodograms.

$$\boldsymbol{\Gamma}(F_w) = \sum_{f \in F_w} \langle \mathbf{g}(f)\mathbf{g}^H(f) \rangle \tag{4.7}$$

$$\mathbf{W}_b^T(\mathbf{r}_i, F_w) = [\boldsymbol{L}^T(\mathbf{r}_i)\boldsymbol{\Gamma}^{-1}(F_w)\boldsymbol{L}(\mathbf{r}_i)]^{-1}\boldsymbol{L}^T(\mathbf{r}_i)\boldsymbol{\Gamma}^{-1}(F_w) \tag{4.8}$$

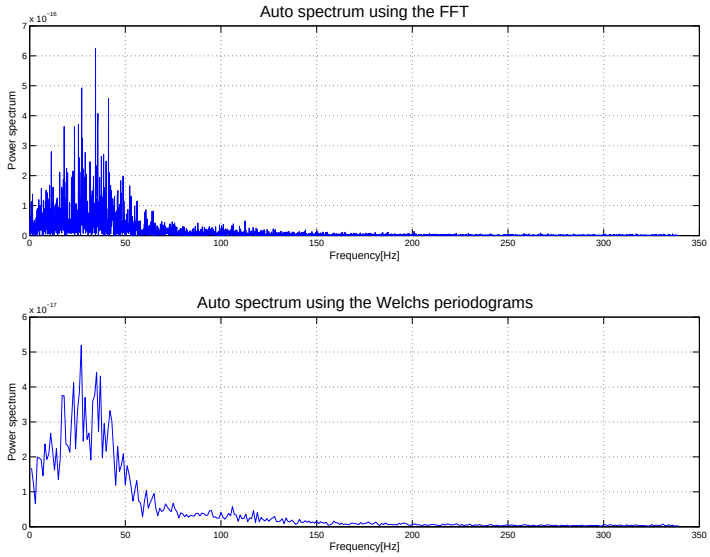

Figure 4.8: Spectrum for the brain activity using the FFT as the power spectral density, and the Welch periodograms, with 1 second non-overlapped segments. The Welch periodograms and the FFT were implemented on a 10 seconds length signal, sampled at 678.17 Hz.

4.2 MEG and functional brain interactions

Brain connectivity studies are being implemented using MEG data in order to find interactions between different brain regions and their causalities, where the properties of the MEG signals help to reduce some of the problems found in EEG and fMRI techniques. The brain interactions are classified into three different types, depending on the brain structure and functionality, as was explained in the previous chapters. Then, the brain interactions are obtained by analysing the spatial filters estimations of the brain activity with techniques such as correlation, spectral coherence, phase looking value, and mutual information, for the estimation of functional interactions, while methods like Granger causality and dynamical neural modelling are used to estimate the interactions directions (Srinivasan et al., 2007; David et al., 2004). The measurements of structural connectivities are found using anatomical approaches such as the Golgy stain method.

In the following subsections are presented some of the most used techniques based on MEG data to determine the functional brain interactions using time series analysis. The analysis are useful to quantify statistical dependencies between the found neuronal activity (Schoffelen and Gross, 2009), which are indicators of dynamical coupling between the estimated time series (Sporns, 2011). The techniques used to find these dependencies can be classified as linear and non-linear techniques, which are used to evaluate synchronous and non-synchronous brain

interactions (David et al., 2004).

4.2.1 Correlation analysis

Correlation analysis is one of the most commonly used techniques for the finding of relationships between the activity located on different brain regions. It is used to calculate the statistical dependencies between a pair of time series (Chatfield, 1995). These metrics are normally arranged into a $N \times N$ matrix known as the correlation matrix, composed by the interactions between N different time series. The diagonal elements of the matrix are known as the autocorrelation values, while the off-diagonal elements are used to express the amount of cross-correlation between the different time series. This method is widely used in neuroscience, and is defined as is presented in Equation 4.9 (David et al., 2004), where x and y represent the time series, and $\overline{x}$ and σ_x represent the mean and the standard deviation for the x time series, respectively. Thus, if c_{xy} has a value of 0 means that the two processes or time series do not have similarities, but the similarities between them increase as the value of $|c_{xy}|$ increases, having a maximum value of $|c_{xy}| = 1$, which means that those signals are entirely related (Leon Garcia, 1994).

$$c_{xy} = \left\langle \left(\frac{x - \overline{x}}{\sigma_x} \right) \left(\frac{y - \overline{y}}{\sigma_y} \right) \right\rangle \tag{4.9}$$

4.2.2 Spectral coherence

Another technique used for the measurements of functional brain interactions in neuroscience is the spectral coherence or coherency function, which is the normalized value of the cross-spectrum between the x and y signals $R_{xy}(f)$, Equation 4.10, defined as the Fourier transform of the cross-correlation function (David et al., 2004). The spectral coherence can take values between 0 and 1, where, as for the correlation case, 1 means that x and y signals are linearly dependent, while 0 means that there is no relationship between them. Many measurements of functional connectivity rely on this metric to determine interdependencies between different brain regions (Schoffelen and Gross, 2009). This metric is classified as a non-parametric technique, which uses the Fourier transform (Schoffelen and Gross, 2009). Both the cross-spectrum and the spectral coherences can be arranged intro matrices, known as the cross-spectral density matrix and the spectral coherence matrix, respectively.

$$R_{xy}(f) = \frac{|\gamma_{xy}(f)|^2}{|\gamma_{xx}(f)||\gamma_{yy}(f)|} \tag{4.10}$$

4.3 Brain connectivity and covariance analysis

The techniques presented in the previous sections are normally used, in the MEG context, on signals obtained from the outputs of the spatial filters. Some techniques, such as of the spectral coherence, require a lot of computational processing as it is necessary the spectrum of all possible locations where the brain activity is found, and is even more demanding when it is implemented in all-to-all pairwise analysis between the locations used to look for brain activity (Schoffelen and Gross, 2011). However, DICS is a different approach with advantages and disadvantages which rely on the analysis of the covariance matrices for the estimated activity in the time domain, or on the cross-spectral density matrices in the frequency domain. Its main disadvantage is that the information obtained is limited to information contained in the covariance matrix, while in the normal approach are also obtained the variations of the brain activity in the form of time series or as their spectrum.

The DICS approach reduce the computational cost for the study of brain dynamics, especially when it is implemented in the frequency domain. The computational cost is reduced as it is not necessary to calculate the cross-spectral density matrices used for the measurements of the brain dynamics. They are obtained directly from the output of the filter. In this section are presented the more representative technique for the approach based on the use of the spatial filters and the covariance analysis, the Dynamic Imaging of Coherent Sources (DICS) (Gross et al., 2001). It is also presented the permutation analysis used to reduce the findings of spurious interactions.

4.3.1 Dynamic imaging of coherent sources

DICS is based on the use of the LCMV beamformer to estimate the spectral power and the cross spectral density matrices for the brain activity directly from the outputs of the spatial filter (Gross et al., 2003). This is possible using the bases under which the LCMV beamformer was designed, Equation 3.31. This estimation for the spectral characteristics of the brain activity is obtained using Equation 4.11, where the weights of the filter are obtained using Equation 4.4, and can be obtained for a specific frequency f, or for frequencies averaged across a frequency band (Sekihara and Nagarajan, 2008). Thus, the spectral power

for brain locations is obtained when the weights used in Equation 4.11 are pointing to the same location $\mathbf{r}_i = \mathbf{r}_j$, while the cross-spectral density matrices are obtained when the filter weights are pointing to different locations $\mathbf{r}_i \neq \mathbf{r}_j$, where these locations determine the interaction between two different brain sources or regions (Gross et al., 2001). These metrics are obtained in the form of 3×3 matrices, as the brain activity is represented by equivalent current dipoles composed by their x, y and z components.

$$\mathbf{\Gamma}_{\mathbf{r}_i\mathbf{r}_j}(f) = \mathbf{W}_b(\mathbf{r}_i, f)\mathbf{\Gamma}(f)\mathbf{W}_b^H(\mathbf{r}_j, f) \tag{4.11}$$

The functional brain dynamics are found using the estimated cross-spectral density matrices in metrics such as the spectral coherence. DICS uses singular value decomposition (SVD) to find the characteristics singular values for $\mathbf{\Gamma}_{\mathbf{r}_i\mathbf{r}_j}(f)$, $\lambda_1, \lambda_2, \lambda_3$. This in order to find the dominant direction for the brain interactions (Gross et al., 2001), where, if the obtained singular values $\lambda_1 >> \lambda_2$ and $\lambda_1 >> \lambda_3$, then the cross-spectrum is attributed to sources with fixed orientations, determined by the singular vectors related to λ_1 (Gross et al., 2001). Thus, the strongest cross-spectrum, or strongest interaction, is defined by Equation 4.12. In the cases that brain sources do not have fixed orientations, the trace for the $\mathbf{\Gamma}_{\mathbf{r}_i\mathbf{r}_j}(f)$ matrix can be used as an indicator of the stronger direction (Gross et al., 2001). Once the strongest directions for the interactions are known, the brain dynamics can be estimated based on the spectral coherence, as is presented in Equation 4.13.

$$\gamma_{\mathbf{r}_i\mathbf{r}_j}(f) = \lambda_1\{\mathbf{\Gamma}_{\mathbf{r}_i\mathbf{r}_j}(f)\} \tag{4.12}$$

$$R_{\mathbf{r}_i\mathbf{r}_j}(f) = \frac{|\gamma_{\mathbf{r}_i\mathbf{r}_j}(f)|^2}{|\gamma_{\mathbf{r}_i\mathbf{r}_i}(f)||\gamma_{\mathbf{r}_j\mathbf{r}_j}(f)|} \tag{4.13}$$

The main problem found in DICS is the presence of correlated brain activity, which decreases its performance as result of the use of the LCMV beamformer (David et al., 2003). This problem is reduced using the method to estimate the brain activity among distant brain regions (David et al., 2003), as it is not common to find highly correlated brain activity between them. However, there exist other problems such as errors introduced by the linearly between the leadfields, errors in their calculations, and the effects of external noise, which can cause the finding of spurious brain interactions as a result (Schoffelen and Gross, 2011, 2009), especially for all-to-all pairwise brain dynamics measurements. These problems can be limited

following the strategies presented by Gross for the use of the DICS method (Gross et al., 2001), where peripheral signals, the magnetic fields measurements, and a priori information are used, to mention some of the proposed strategies. A complementary approach used to reduce the finding of false brain dynamics is the permutation analysis, which is introduced in the following subsection.

4.3.2 Permutation analysis

Permutation analysis has been used on MEG studies to reduce the finding of false active brain sources in the solution of the inverse problem (Nichols and Holmes, 2002; Pantazis et al., 2003). However, the same analysis has been also used to reduced the finding of spurious brain interactions and synchronizations (Singh and Barnes, 2003; Jerbi et al., 2007). This reduction is possible by comparing two different conditions, normally labelled as *active* and *rest* conditions. The active condition is related to experimental results obtained under specific circumstances, while the rest condition is used as a control case or as baseline (Pentazis et al., 2005). The comparisons are implemented using permutation analysis, significant tests, and *p-values*. These are used in order to find the probabilities of the different rearrangements, or permutations, of the data obtained from the experiments, to be classified as active or as rest conditions under the null-hypothesis (Nichols and Holmes, 2002).

The permutation analysis in the brain connectivity context has been used to find brain interactions between two different sources or regions, while reducing the finding of spurious connectivities. The analysis is implemented by rearranging the labels for the condition of interest and the baseline, and by estimating the probabilities of these new arrangements, or their p-values, in order to define the occurrence or surprise factor corresponding to them. Then, the probabilities obtained for the different arrangements, the *p-values*, are compared against a significant value α in order to determine if they are significant, or if the null hypothesis is rejected (Nichols and Holmes, 2002). If the *p-values* are significant, then the interactions found are classified as active, while they will be classified with the rest label (condition) if the null-hypothesis is valid (Pentazis et al., 2005). The null hypothesis is used to establish the conditions that allow the rearrangements of the data obtained from the experiments, under two different conditions or labels.

Thus, the permutation analysis has been used for brain connectivity studies to reveal statistically significance coupling between different brain sources, or between group of brain sources (Jerbi et al., 2007). In the permutation analysis any statistic measure can be used for the

significance test, even when the distribution for the data is unknown (Singh and Barnes, 2003; Chau et al., 2004). However, the analysis has different factors that can increase or decrease its performance, especially for the multiple comparison permutation test, where N different brain interactions are evaluated at the same time using N *p-value*s (Gaetz and Cheyne, 2006). The most known problem on this approach are the number of permutations used in order to find their distributions, and the correction of *p-values* to control the Family Wise Error Rate (FWER) (Pantazis et al., 2003; Nichols and Holmes, 2002). The family wise error rate is present when the probability of falsely declared brain interactions as significant is equal or higher than the α value (Nichols and Holmes, 2002), where the family concept is defined as the collections of statistical tests performed over all possible interactions.

For brain connectivity studies, the permutation analysis is usually implemented among specific selected voxels or between all-to-all pairwise voxels, where sometimes the voxels are seen as group of voxels (Satoru and Nichols, 2004; Jerbi et al., 2007). However, the computational cost for all-to-all pairwise voxels analysis can be too demanding, depending on how many voxels are used to look for the brain activity, as it will be necessary to calculate the spectral coherence for all interactions between those points, which are arranged in a matrix. Normally in MEG source-space coherence analysis a voxel is used as a reference, known as the seed voxel, and then the coherence is estimated between the seed and the rest of the voxels to look for the brain activity (Sekihara and Nagarajan, 2013). It provides a three dimensional mapping of source coherence called a source coherence image, with respect to the seed voxel. This map is represented as one of the columns or rows of the matrix obtained in all-to-all pairwise voxels analysis (Schoffelen and Gross, 2011), is a particular case of all possible brain interactions happening in the brain.

4.4 Summary

Functional brain interactions based on MEG data are normally estimated in two different ways, both of them using the previously mentioned spatial filters. The first approach estimates the brain activity in the time or in the frequency domain to be used on metrics such as correlation and coherence in order to estimate the amount of relationship between different brain regions. The second approach uses the LCMV beamformer to estimate the covariance matrices, or the cross spectral density matrices in the frequency domain, from the covariance, or cross-spectral density matrix, for the measured magnetic fields. The use of one approach over the other depends on the information required from the estimation, and on the amount

of interactions to estimate.

The first approach gives more information about the brain as it requires the estimation of the brain activity time series or frequency behaviour, while the second approach only requires the covariance or cross-spectral density matrix, which limit the information that can be obtained. Nonetheless, the computational cost required for the methods is an important issue when all-to-all pairwise brain interactions are estimated, especially for the first approach, as it require to estimate the brain activity for all possible locations used to look for the brain activity. On the other hand, the second approach only requires the estimation of the LCMV filter weights to filter the required data from the covariance matrix, or cross-spectral density matrix, for the measured magnetic fields.

Thus, DICS is a useful method for all-to-all pairwise brain interactions estimation, however, as been based on the use of the LCMV beamformer, it has the same limitation in the presence of correlated brain activity. In the next two chapters are presented two different approaches to deal with this problem, the Bilinear Constraint Minimum Variance (BCMV) beamformer, which modifies the design of the LCMV beamformer, and the Linearly Constrained Minimum Norm Estimates (LCMNE), which uses the MNE spatial filter as DICS uses the LCMV beamformer, as it is not affected by the presented of correlated brain activity.

Chapter 5

The LCMV and estimation of brain interactions

The Linearly Constrained Minimum Variance beamformer, based on the use of the Lagrange multipliers, has proved to be, in general terms, a more reliable technique than the Minimum Norm spatial filter, which relies on the least-squares method. A more reliable technique in terms of its implementation simplicity and on the results obtained when the amount of correlation between different brain regions is not too high. This has been one of the main reasons for the development of techniques to improve the performance of the LCMV beamformer in the presence of highly correlated brain activity. However, most of these techniques improve the performance of the filter without modifying its core, but by modifying the implementation of the filter to reduce the effects of the correlated activity (Diwakar et al., 2011; Dalal et al., 2006; Brookes et al., 2007; Huang et al., 2004; Gross et al., 2001). Therefore, the main assumption used to find the weights that define the filters has not been changed.

In this chapter are presented the LCMV beamformer uncorrelated brain sources assumption, and a new approach based on the design of the LCMV spatial filter, where the new approach considers the effects of correlated brain activity on its design. However, this new approach presents problems, and its solution may not be as elegant as the LCMV beamformer. The most important problem found on this new approach is the finding of solutions to a system of bilinear equations, which may lead to solutions that do not satisfy all conditions used as constraints based on the Lagrange multipliers method. This, because is difficult to find solutions since there is not warranty to find critical points with the constraints used. It is also difficult because of the nature of the problem, as in practice systems of bilinear equations are

normally overdetermined and inconsistent (Cohen and Tomasi, 1997). This new approach will be called the Bilinear Constraints Minimum Variance beamformer (BCMV).

5.1 Effects of correlated brain activity

As is presented by Kensuke Sekihara (Sekihara and Nagarajan, 2008), and by Van Veen (Van Veen et al., 1997), the main assumption used in the design of the LCMV spatial filter is located on the structure of the covariance matrix for the activity of the brain sources responsible for the generation of the magnetic fields. The assumption assumes that the matrix is composed only of the diagonal elements, while the off-diagonal elements have zero values. The covariance matrix of the measured magnetic fields, or the data covariance matrix, is presented in Equation 5.1, it is also presented the covariance matrix for the brain activity in Equation 5.2. In both expressions, the magnetic fields and the sources activity are averaged over time t. The expression 5.1 is different from Equation 3.28, as the relationship $\langle \mathbf{x}(t) \rangle \approx 0$ holds for many applications (Sekihara and Nagarajan, 2008).

$$\mathbf{C}(\mathbf{x}) = \langle \mathbf{x}(t)\mathbf{x}^T(t) \rangle = \begin{bmatrix} \langle x_1(t)^2 \rangle & \langle x_1(t)x_2(t) \rangle & \cdots & \langle x_1(t)x_M(t) \rangle \\ \langle x_2(t)x_1(t) \rangle & \langle x_2(t)^2 \rangle & \cdots & \langle x_2(t)x_M(t) \rangle \\ \vdots & \vdots & \ddots & \vdots \\ \langle x_M(t)x_1(t) \rangle & \langle x_M(t)^2 x_1(t) \rangle & \cdots & \langle x_M(t)^2 \rangle \end{bmatrix} \tag{5.1}$$

$$\mathbf{C}(\mathbf{m}) = \langle \mathbf{m}\mathbf{m}^T \rangle = \begin{bmatrix} \langle \mathbf{q}(\mathbf{r}_1, t)^2 \rangle & \langle \mathbf{q}(\mathbf{r}_1, t)\mathbf{q}(\mathbf{r}_2, t) \rangle & \cdots & \langle \mathbf{q}(\mathbf{r}_1, t)\mathbf{q}(\mathbf{r}_N, t) \rangle \\ \langle \mathbf{q}(\mathbf{r}_2, t)\mathbf{q}(\mathbf{r}_1, t) \rangle & \langle \mathbf{q}(\mathbf{r}_2, t)^2 \rangle & \cdots & \langle \mathbf{q}(\mathbf{r}_2, t)\mathbf{q}(\mathbf{r}_N, t) \rangle \\ \vdots & \vdots & \ddots & \vdots \\ \langle \mathbf{q}(\mathbf{r}_N, t)\mathbf{q}(\mathbf{r}_1, t) \rangle & \langle \mathbf{q}(\mathbf{r}_N, t)^2 \mathbf{q}(\mathbf{r}_2, t) \rangle & \cdots & \langle \mathbf{q}(\mathbf{r}_N, t)^2 \rangle \end{bmatrix} \tag{5.2}$$

Using Equation 3.18, presented again as Equation 5.3, it is possible to find the relationship that exist between the data covariance matrix and the covariance matrix for the brain sources, as is presented in Equation 5.4, where $\mathbf{C_n}$ is the noise covariance matrix .

$$\mathbf{x} = \mathbf{H}\mathbf{m} + \mathbf{n} \tag{5.3}$$

$$\mathbf{C}(\mathbf{x}) = \langle \mathbf{x}(t)\mathbf{x}^T(t) \rangle = \mathbf{H}\mathbf{C}(\mathbf{m})\mathbf{H}^T + \mathbf{C_n} \tag{5.4}$$

One of the most common assumptions made in MEG studies is the presence of zero mean white Gaussian noise, uncorrelated between the MEG acquisition sensor channels (Sekihara and Nagarajan, 2008; Imada, 2010). This assumption allows to express the external noise as is presented in Equation 5.5, which changes Equation 5.4 to Equation 5.6, where σ_0^2 is the variance of the noise.

$$\mathbf{C_n} = \sigma_0^2 \boldsymbol{I} \tag{5.5}$$

$$\mathbf{C}(\mathbf{x}) = \mathbf{H}\mathbf{C}(\mathbf{m})\mathbf{H}^T + \sigma_0^2 \boldsymbol{I} \tag{5.6}$$

The uncorrelated brain sources assumption used to calculate the LCMV beamformer weights implies that the product $\langle \mathbf{q}(\mathbf{r}_p, t)\mathbf{q}^T(\mathbf{r}_i, t) \rangle = 0$ for $p \neq i$, and $\sigma_p^2 = \langle \mathbf{q}(\mathbf{r}_p, t)^2 \rangle$, where σ_p^2 represents the power of the source p (Van Veen et al., 1997). Then, the matrix 5.2 can be represented as matrix 5.7, which is the base for Equation 3.28, used to estimate the LCMV filter weights (Sekihara and Nagarajan, 2008).

$$\mathbf{C}(\mathbf{m}) = \begin{bmatrix} \sigma_1^2 & 0 & \cdots & 0 \\ 0 & \sigma_2^2 & \cdots & 0 \\ \vdots & \vdots & \ddots & \vdots \\ 0 & 0 & \cdots & \sigma_N^2 \end{bmatrix} \tag{5.7}$$

The uncorrelated brain sources assumption simplifies the use of the Lagrange multipliers, as there is needed only one main constraint for its solution. This helps to maintain the degrees of freedom for the solution, as it was defined by Van Veen (Van Veen et al., 1997). The constraint works relatively well, with the exception when the amount of correlation between different brain sources is high, as explained by Sekihara (Sekihara et al., 2002).

5.1.1 Effects of correlated activity on LCMV performance

The LCMV uncorrelated brain sources assumption is almost impossible to achieve, as the brain sources are inevitably correlated to some degree (Sekihara and Nagarajan, 2008). This relation between the brain sources affects the performance of the spatial filter depending on

the amount of correlation, as the assumption used to design the filter is not fulfilled. This means that, the blocking capability of the LCMV beamformer will be limited depending on the amount of correlation present between the brain sources. Thus, the best blocking capability of the spatial filter will be achieved in the presence of uncorrelated brain sources, as is presented in Equation 5.8 (Sekihara and Nagarajan, 2008).

$$\mathbf{W}_b^T(\mathbf{r}_p)\boldsymbol{L}(\mathbf{r}_p) = \boldsymbol{I} \tag{5.8}$$

The reduction of the blocking capability of the LCMV beamformer weights can be represented, in the general case, by Equation 5.9 (Sekihara and Nagarajan, 2008), where $[\mathbf{C}^{-1}(\mathbf{m})]_{p,q}$ is used to represent the (p,i) element of the inverted $\mathbf{C}(\mathbf{m})$ matrix.

$$\mathbf{W}_b^T(\mathbf{r}_p)\boldsymbol{L}(\mathbf{r}_p) = \frac{[\mathbf{C}^{-1}(\mathbf{m})]_{p,i}}{[\mathbf{C}^{-1}(\mathbf{m})]_{p,p}} \tag{5.9}$$

Thus, the brain activity generated by a target source located at position $\mathbf{r}_p$, correlated with N_I different brain sources located at positions $\mathbf{r}_i$, where $i = 1, 2, \cdots, N_I$, is expressed as is show in Equation 5.10. Equation 5.10 shows that there exist leakage from the correlated sources on the activity generated from the target source. This leakage causes problems in the estimation of the brain sources time-series.

$$\widehat{\mathbf{q}}(\mathbf{r}_p, t) = \mathbf{q}(\mathbf{r}_p, t) + \sum_{i=1}^{N_I} \frac{[\mathbf{C}(\mathbf{m})]_{p,i}^{-1}}{[\mathbf{C}(\mathbf{m})]_{p,p}^{-1}} \mathbf{q}(\mathbf{r}_i, t) \tag{5.10}$$

The effect of correlated sources in the estimation of brain sources time-series using the LCMV spatial filter can be observed better with the case where only two sources are correlated, while the rest are not. The correlation coefficient between the correlated sources is denoted as μ, following Sekihara's notation (Sekihara and Nagarajan, 2008). Then, the covariance matrix for the brain activity can be expressed as follows:

$$\mathbf{C}(\mathbf{m}) = \begin{bmatrix} \begin{bmatrix} \sigma_1^2 & \mu\sigma_1\sigma_2 \\ \mu\sigma_2\sigma_1 & \sigma_2^2 \end{bmatrix} & 0 & \cdots & 0 \\ 0 & \sigma_3^2 & \cdots & 0 \\ \vdots & \vdots & \ddots & \vdots \\ 0 & 0 & \cdots & \sigma_N^2 \end{bmatrix} \tag{5.11}$$

and the inverse of the covariance matrix for the brain activity as follows:

$$\mathbf{C}^{-1}(\mathbf{m}) = \begin{bmatrix} \frac{1}{\sigma_1^2\sigma_2^2(1-\mu^2)} \begin{bmatrix} \sigma_2^2 & -\mu\sigma_1\sigma_2 \\ -\mu\sigma_2\sigma_1 & \sigma_1^2 \end{bmatrix} & 0 & \cdots & 0 \\ 0 & 1/\sigma_3^2 & \cdots & 0 \\ \vdots & \vdots & \ddots & \vdots \\ 0 & 0 & \cdots & 1/\sigma_N^2 \end{bmatrix} \tag{5.12}$$

Then, the effects that correlated activity has on the performance of the filter weights can be found combining equations 5.9 and 5.12, as is shown in the followings expressions:

$$\begin{aligned} \mathbf{W}_b^T(\mathbf{r}_1)\boldsymbol{L}(\mathbf{r}_1) &= \boldsymbol{I} & \mathbf{W}_b^T(\mathbf{r}_1)\boldsymbol{L}(\mathbf{r}_2) &= -\tfrac{\sigma_1}{\sigma_2}\mu\boldsymbol{I} \\ \mathbf{W}_b^T(\mathbf{r}_2)\boldsymbol{L}(\mathbf{r}_1) &= -\tfrac{\sigma_2}{\sigma_1}\mu\boldsymbol{I} & \mathbf{W}_b^T(\mathbf{r}_2)\boldsymbol{L}(\mathbf{r}_2) &= \boldsymbol{I} \end{aligned} \tag{5.13}$$

$$\mathbf{W}_b^T(\mathbf{r}_1)\boldsymbol{L}(\mathbf{r}_i) = \mathbf{0} \quad \mathbf{W}_b^T(\mathbf{r}_2)\boldsymbol{L}(\mathbf{r}_i) = \mathbf{0} \quad for \quad i = 3, \cdots, N \tag{5.14}$$

Therefore, when the LCMV spatial filter is used to estimate the brain activity generated by any of the sources located at positions $\mathbf{r}_1$ and $\mathbf{r}_2$, it lets pass the signals from the second source with a gain factor of $-\sigma_1\mu/\sigma_2$, while blocking the rest of the uncorrelated brain signals (Sekihara and Nagarajan, 2008). These leakages can be observed better in equations 5.15 and 5.16, where are presented the estimated activity for those locations. The gain factor reduces the power of the reconstructed, or estimated, signals. This effect is known as signal cancellation, and is the main reason for the decrease in the performance of the LCMV spatial filter. The amount of cancellation depends on the amount of correlation between sources, where N brain sources can be correlated (Sekihara and Nagarajan, 2008).

$$\widehat{\mathbf{q}}(\mathbf{r}_1, t) = \mathbf{q}(\mathbf{r}_1, t) - (\frac{\sigma_1}{\sigma_2}\mu)\mathbf{q}(\mathbf{r}_2, t) \tag{5.15}$$

$$\widehat{\mathbf{q}}(\mathbf{r}_2, t) = \mathbf{q}(\mathbf{r}_2, t) - (\frac{\sigma_2}{\sigma_1}\mu)\mathbf{q}(\mathbf{r}_1, t) \tag{5.16}$$

5.2 Bilinear constraints for a minimum variance beamformer

It is proposed in this section the use of constraints as in the LCMV case for a modified version of the filter, where the constraints are used to avoid the uncorrelated brain sources assumption. This proposal is motivated to improve the performance of the LCMV spatial filter in order to be more robust when used in brain connectivity studies, where the uncorrelated brain sources assumption creates reasonable doubts about the accuracy of the results obtained. The idea is similar to the dynamic imaging of coherent sources, but in this case the brain interactions are found by changing the LCMV design instead of changing its application. This modified version of the LCMV is designed in the time domain, nevertheless, its main application will be in the frequency domain, implemented in the same way as DICS, presented in Chapter 4.

This new approach is based on the solution of a bilinear system of equations used to express the covariance matrix for the measured magnetic fields. The main objective of the filter is to extract the covariance matrix corresponding to the $[\mathbf{C}(\mathbf{m})]_{p,i}$ element, or $\mathbf{C}(\mathbf{q}_p, \mathbf{q}_i)$, which expresses the covariance matrix between the three components of the sources on those locations (Gross et al., 2001; Mignerey, 1989). It is proposed to extract the brain sources covariance matrices by using two set of weights per location, or per interaction between the brain sources, expressed as $\mathbf{W}_{1b}(\mathbf{r}_p) \in \mathbb{R}^{3\times M}$ and $\mathbf{W}_{2b}(\mathbf{r}_i) \in \mathbb{R}^{3\times M}$ for locations $\mathbf{r}_p$ and $\mathbf{r}_i$. The design of the filter weights uses the same procedure as the LCMV beamformer, but in this case there will be N^2 bilinear equations to estimate all possible interactions between the brain sources. This is possible by defining the covariance matrix for the measured magnetic fields as is presented in Equation 5.17, which consider the correlated brain activity.

$$\mathbf{C}(\mathbf{x}) = \sum_{p=1}^{N}\sum_{i=1}^{N} \boldsymbol{L}(\mathbf{r}_p)\mathbf{C}(\mathbf{q}_p, \mathbf{q}_i)\boldsymbol{L}^T(\mathbf{r}_i) + \mathbf{C}_\mathbf{n} \tag{5.17}$$

Thus, the modified version of the spatial filter is proposed to estimate the brain activity as is presented in Equation 5.18, which is a similar expression as the one presented in Equation 4.11, but in the time domain.

$$\mathbf{C}(\mathbf{q}_p, \mathbf{q}_i) = \mathbf{W}_{1b}^T(\mathbf{r}_p)[\sum_{p=1}^{N}\sum_{i=1}^{N} \boldsymbol{L}(\mathbf{r}_p)\mathbf{C}(\mathbf{q}_p, \mathbf{q}_i)\boldsymbol{L}^T(\mathbf{r}_i)]\mathbf{W}_{2b}(\mathbf{r}_i) \tag{5.18}$$

5.2.1 Bilinear constraints

The main idea is to use defined constraints that let pass the activity on specific locations, or by specific brain interactions, whenever any of the conditions used for them are present, while nullifying the brain activity generated on different locations, or by different brain interactions. It is the same idea used as in the LCMV beamformer, but using a bilinear set of equations, where each of the bilinear variables are used to select specific locations for the interactions. Thus, as a brief description, the constraints are used to fulfil the conditions present in Equation 5.19, as in Equation 3.30 for the LCMV case. However, the bilinear form of the equations for the problem imply that their solutions may not fulfil all the constraints used, independently of the conditions related with the constraints, as is proved in this, and the following section.

$$\mathbf{W}_{1b}^T(\mathbf{r}_p)\boldsymbol{L}(\mathbf{r}) = \begin{cases} \mathbf{I} & \mathbf{r} = \mathbf{r}_p \\ \mathbf{0} & \mathbf{r} \neq \mathbf{r}_p \end{cases} \qquad \mathbf{W}_{2b}^T(\mathbf{r}_i)\boldsymbol{L}(\mathbf{r}) = \begin{cases} \mathbf{I} & \mathbf{r} = \mathbf{r}_i \\ \mathbf{0} & \mathbf{r} \neq \mathbf{r}_i \end{cases} \tag{5.19}$$

It is possible to use the LCMV filter weights in a way that the conditions present in Equation 5.19 are fulfilled. However, the LCMV weights will generate uncertainties in the presence of correlated brain activity. The main idea is to find the set of weights that satisfy the conditions presented using the Lagrange multipliers in the same way as is done for the LCMV beamforming, without relying on the uncorrelated brain sources assumption. The proposed problem is presented in Equation 5.20, similarly to Equation 3.31, where $\mathbf{r}_p$ can be a different or the same location as $\mathbf{r}_i$. Then, as in the LCMV case, the idea is to find the set of weights that minimize the variance of the filter output, where the variance can be generated from the power of a brain source or by the interactions between them.

$$\begin{aligned} &\min(tr\{\widehat{\mathbf{C}}(\mathbf{q}_p, \mathbf{q}_i)\}) \quad \text{subject to} \quad \mathbf{W}_{1b}^T(\mathbf{r}_p)\boldsymbol{L}(\mathbf{r}_p) = \mathbf{I}; \quad \mathbf{W}_{2b}^T(\mathbf{r}_i)\boldsymbol{L}(\mathbf{r}_i) = \mathbf{I} \\ &\mathbf{W}_{1b}(\mathbf{r}_p), \mathbf{W}_{2b}(\mathbf{r}_i) \end{aligned} \tag{5.20}$$

Bilinear equation using one constraint

It is presented an example of the bilinear problem using only one constraint. The condition used in this case may not be the most appropriate, as there is not possible to find a critical point in the space defined by the magnetic fields measured. However, it works as an example

of the bilinear approach, which is solved in the same way as the LCMV spatial filter case, with the use of the Lagrange multipliers (Ito and Kunisch, 2008). The bilinear function to minimize $f(\mathbf{W}_{1b}, \mathbf{W}_{2b})$ is presented in Equation 5.21, along with the constraint function $g(\mathbf{W}_{1b}, \mathbf{W}_{2b})$.

$$\begin{aligned} f(\mathbf{W}_{1b}, \mathbf{W}_{2b}) &= \mathbf{W}_{1b}^T(\mathbf{r}_p)\mathbf{C}(\mathbf{x})\mathbf{W}_{2b}(\mathbf{r}_i) \\ g(\mathbf{W}_{1b}, \mathbf{W}_{2b}) &= \mathbf{W}_{1b}^T(\mathbf{r}_p)\boldsymbol{L}(\mathbf{r}_p) + \mathbf{W}_{2b}^T(\mathbf{r}_i)\boldsymbol{L}(\mathbf{r}_i) = 2\boldsymbol{I} \end{aligned} \tag{5.21}$$

The use of the Lagrange multipliers to solve for $\mathbf{W}_{1b}$ and $\mathbf{W}_{2b}$ is presented in the following equations, where λ_{LM} is used to represent the Lagrange multiplier.

$$\begin{aligned} f(\mathbf{W}_{1b}, \mathbf{W}_{2b}, \lambda_{LM}) &= \mathbf{W}_{1b}^T(\mathbf{r}_p)\mathbf{C}(\mathbf{x})\mathbf{W}_{2b}(\mathbf{r}_i) + \lambda_{LM}(\mathbf{W}_{1b}^T(\mathbf{r}_p)\boldsymbol{L}(\mathbf{r}_p) + \mathbf{W}_{2b}^T(\mathbf{r}_i)\boldsymbol{L}(\mathbf{r}_i) - 2\boldsymbol{I}) \\ \tfrac{\delta f(\mathbf{W}_{1b}, \mathbf{W}_{2b}, \lambda_{LM})}{\delta \mathbf{W}_{1b}} &= \mathbf{C}(\mathbf{x})\mathbf{W}_{2b}(\mathbf{r}_i) + \lambda_{LM}\boldsymbol{L}(\mathbf{r}_p) \\ \tfrac{\delta f(\mathbf{W}_{1b}, \mathbf{W}_{2b}, \lambda_{LM})}{\delta \mathbf{W}_{2b}} &= \mathbf{W}_{1b}^T(\mathbf{r}_p)\mathbf{C}(\mathbf{x}) + \lambda_{LM}\boldsymbol{L}(\mathbf{r}_i)^T \end{aligned} \tag{5.22}$$

Then, $\mathbf{W}_{1b}$ and $\mathbf{W}_{2b}$ expressions in terms of λ_{LM} are presented as:

$$\begin{aligned} \mathbf{W}_{2b}(\mathbf{r}_i) &= -\lambda_{LM}\mathbf{C}^{-1}(\mathbf{x})\boldsymbol{L}(\mathbf{r}_p) \\ \mathbf{W}_{1b}^T(\mathbf{r}_p) &= -\lambda_{LM}\boldsymbol{L}^T(\mathbf{r}_i)\mathbf{C}^{-1}(\mathbf{x}) \end{aligned} \tag{5.23}$$

Plugging $\mathbf{W}_{1b}$ and $\mathbf{W}_{2b}$ in $g(\mathbf{W}_{1b}, \mathbf{W}_{2b})$ to solve for λ_{LM}:

$$\lambda_{LM} = -[\boldsymbol{L}^T(\mathbf{r}_i)\mathbf{C}^{-1}(\mathbf{x}))\boldsymbol{L}(\mathbf{r}_p)]^{-1} \tag{5.24}$$

Finding the expression for $\mathbf{W}_{1b}$ and $\mathbf{W}_{2b}$ by using the expression for λ_{LM}:

$$\mathbf{W}_{1b}^T(\mathbf{r}_p) = \frac{\boldsymbol{L}^T(\mathbf{r}_i)\mathbf{C}^{-1}(\mathbf{x})}{\boldsymbol{L}^T(\mathbf{r}_i)\mathbf{C}^{-1}(\mathbf{x})\boldsymbol{L}(\mathbf{r}_p)} \qquad \mathbf{W}_{2b}(\mathbf{r}_i) = \frac{\mathbf{C}^{-1}(\mathbf{x})\boldsymbol{L}(\mathbf{r}_p)}{\boldsymbol{L}^T(\mathbf{r}_i)\mathbf{C}^{-1}(\mathbf{x})\boldsymbol{L}(\mathbf{r}_p)} \tag{5.25}$$

However, the expressions found for $\mathbf{W}_{1b}$ and $\mathbf{W}_{2b}$ do not fulfil the constraints presented on Equation 5.19 in most of the cases, only when their expressions match the same expression as for the LCMV filter weights presented in Equation 3.33. The proposed spatial filter was tested using simulated brain activity in order to illustrate its characteristics problems. The brain activity was simulated as correlated autoregressive processes (AR) for a SNR of 20, located

on three specific locations of a brain mesh composed by 62 elements located on a predefined brain volume. Table 5.1 shows the correlation matrix among the simulated brain activity, where their locations are represented considering the brain sources components. Therefore, a simulated brain source located at position 12 will be represented by elements 34 to 36 of the correlation matrix.

Location	12(34-36)	40(118-120)	58(172-174)
12(34-36)	1	0	.5
40(118-120)	0	1	.2
58(172-174)	.5	.2	1

Table 5.1: Correlation matrix for simulated brain activity used for the BCMV test.

The covariance matrix among the elements that compose the brain mesh used to solve the inverse problem is composed by 62 elements, and then, it has a 186×186 dimension since each element consider the three brain sources components. The LCMV and the BCMV spatial filters are used to estimate this covariance matrix in order to show the performance of the filters in functional brain dynamic studies, presented on figures 5.1 and 5.2, respectively. It can be observed that using the LCMV gives almost an accurate representation of the brain activity power and covariances, with some reductions on their amplitudes because of the uncorrelated brain sources assumption. On the other hand, the estimations accuracy using the BCMV spatial filter is not good, as it does not estimate the brain activity power and their interactions on the correct locations.

It can also be observed on figures 5.1 and 5.2 that the estimate activity and interactions have different range of amplitudes for both figures. This difference in amplitudes makes difficult the comparison betwen the matrices diagonal elements, which have the same values since the BCMV expressions match the LCMV filter weights for those cases. However, the scenario is different for the off-diagonal elements, as the constraints are not fulfilled. Thus, the off-diagonal elements estimated values do not make sense, as their amplitudes are to high to be considered as valid estimations.

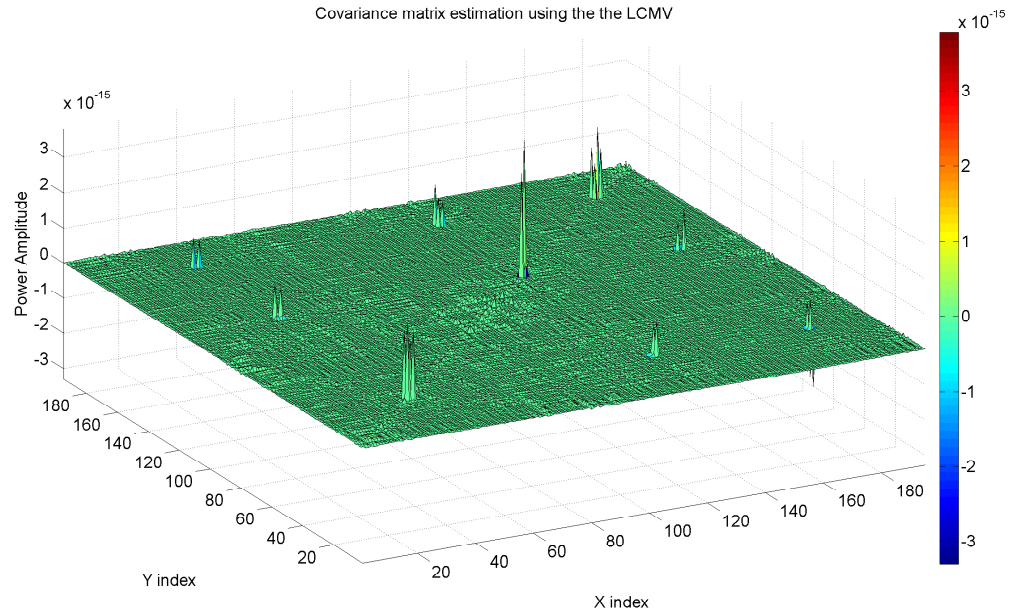

Figure 5.1: Estimated covariance matrix for simulated brain activity using the LCMV beamformer. The characteristics for the simulated activity are presented in Table 5.1.

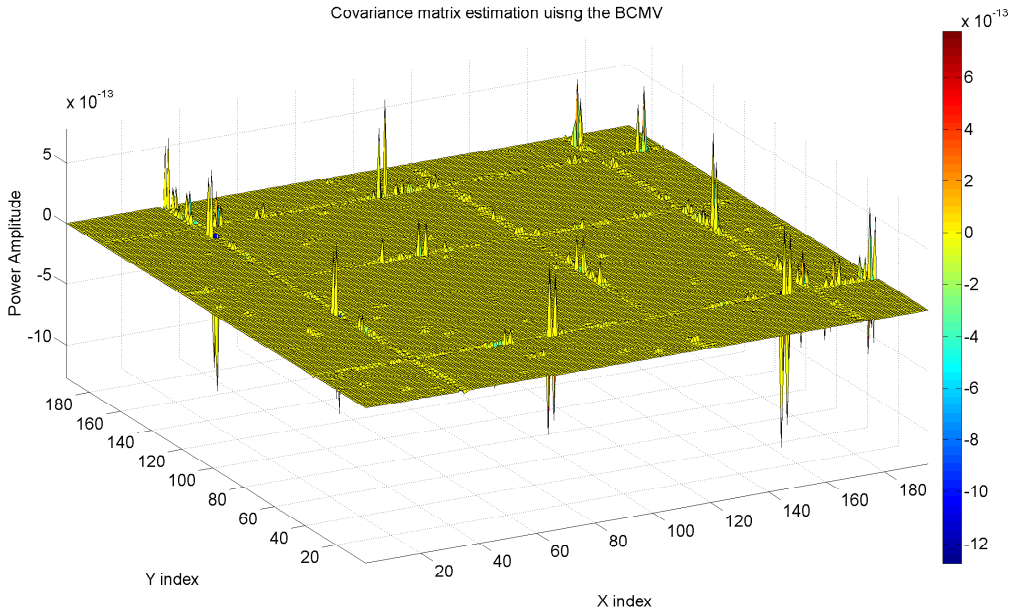

Figure 5.2: Estimated covariance matrix for simulated brain activity using the BCMV spatial filter. The characteristics for the simulated activity are presented in Table 5.1.

Comparison between DICS and the BCMV spatial filter

The problems related with the obtained solution for the BCMV proposed spatial filter can be observed with more detail in the following example, where the BCMV is used to estimate the spectral coherence between simulated brain activity. The results obtained are compared against results obtained using DICS. For this comparison brain activity was simulated in order to have complete certainty of where the brain sources locations are, and to know the amount of correlation present between them. The brain activity was simulated as autoregressive processes (AR) of order 9, for a SNR of 22. The locations and the amount of correlation among the simulated brain sources are presented in Table 5.2.

Brain source(x,y,z)	A(35,182,190)	B(35,100,190)	C(140,100,190)	D(140,182,190)
A(35,182,190)	1	.2	0.0	0.0
B(35,100,190)	.2	1	0.0	.4
C(140,100,190)	0.0	0.0	1	0.0
D(140,182,190)	0.0	.4	0.0	1

Table 5.2: The matrix shows the correlation coefficients among simulated brain activity located on specific x, y, and z positions. The locations for the brain sources are presented in millimetres.

In Figure 5.3 are presented the locations for the simulated brain activity, with respect to a brain volume used to solve the inverse problem, highlighted by red circles, and represented for labels A, B, C and D. The description for the simulated activity are presented in Table 5.2. Then, the LCMV and the BCMV spatial filters were used to estimated the brain activity from the simulated magnetic fields, as can be seen in Figure 5.4. It can be observed how the estimated power is identical for both estimations. This is because the BCMV spatial filter has the same filter weights expressions as the LCMV beamformer for this case, Equation 3.33. However, this is not the case for the estimation of the brain activity interactions, as is shown later on this section.

In Figure 5.4 specific locations are selected for the study of the functional brain dynamics using both spatial filters. These locations were selected from the brain mesh elements with enough estimated power to be considered as active brain regions. Thus, the functional brain dynamics are estimated for this locations following the DICS approach and using the BCMV spatial filter for the estimation of the cross-spectral density matrices, using the singular value decomposition truncation to find the strongest interactions among the brain mesh elements used to solve the inverse problem, section 4.3.1 .

The estimated functional brain dynamoics obtained using DICS and the BCMV following the DICS approach are presented in figures 5.5, 5.6, 5.7 and 5.8. Figures 5.5 and 5.7 present the estimated functional brain dynamics using both spatial filters between the seed voxels located at position 408 and 451 and the rest of the brain mesh elements, respectively. On the other hand, Figure 5.6 and 5.8 present the same interactions as the previous figures but inly considering the brain mesh elements located on the cortex.

It can be observed in the figures that the functional brain dynamics estimation using DICS are more accurate than the ones obtained using the BCVM spatial filter. The BCMV has a bad performance because of the amplification of specific interactions that make impossible the finding of anything else. The brain interactions found with the BCMV spatial filter are located on positions that do not match the expected ones. On the other hand, the LCMV beamformer, or DICS, has a moderate performance, as the amount correlation between the brain sources reduce it. However, it is possible to have an idea of where the brain interactions are using the DICS approach, while it is impossible to make any valid assumption using the BCMV spatial filter results.

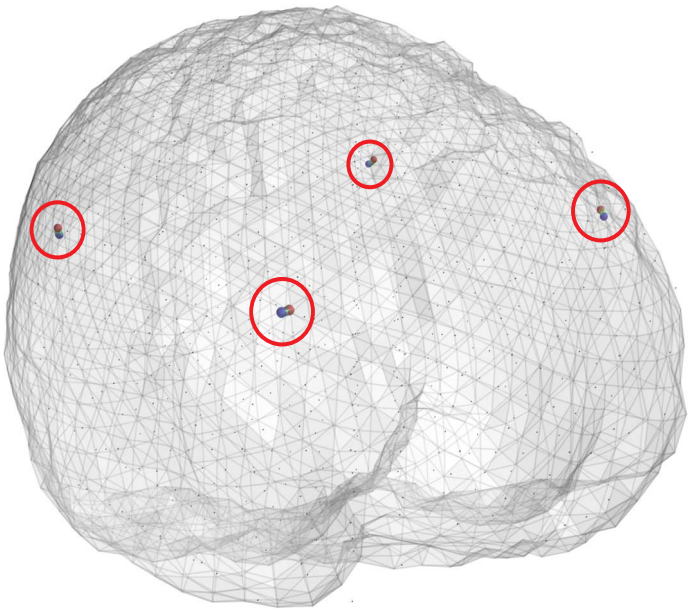

(a)

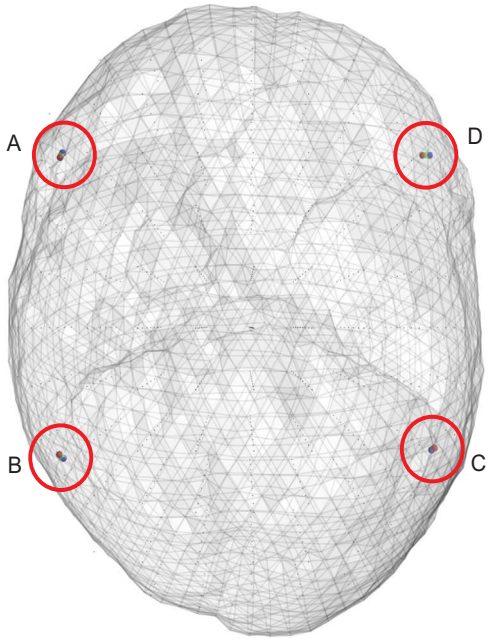

(b)

Figure 5.3: Locations for simulated correlated and uncorrelated brain activity, highlighted by red circles and identified using the labels A, B, C and D.

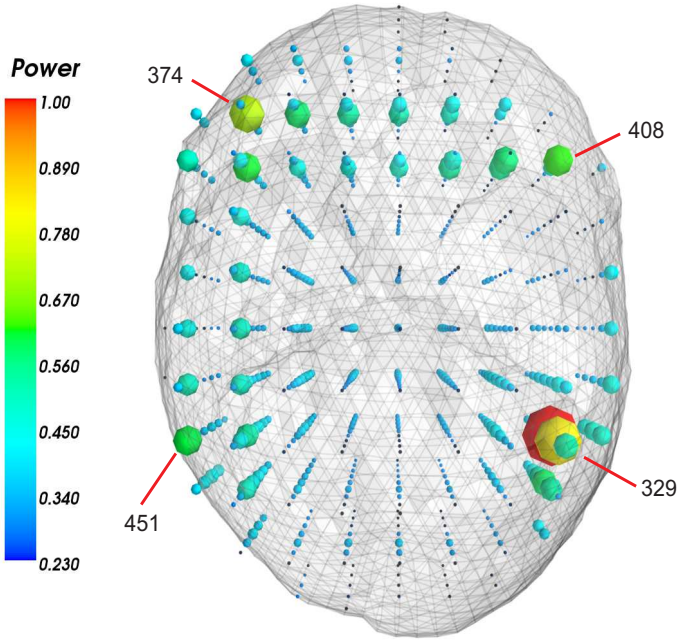

(a)

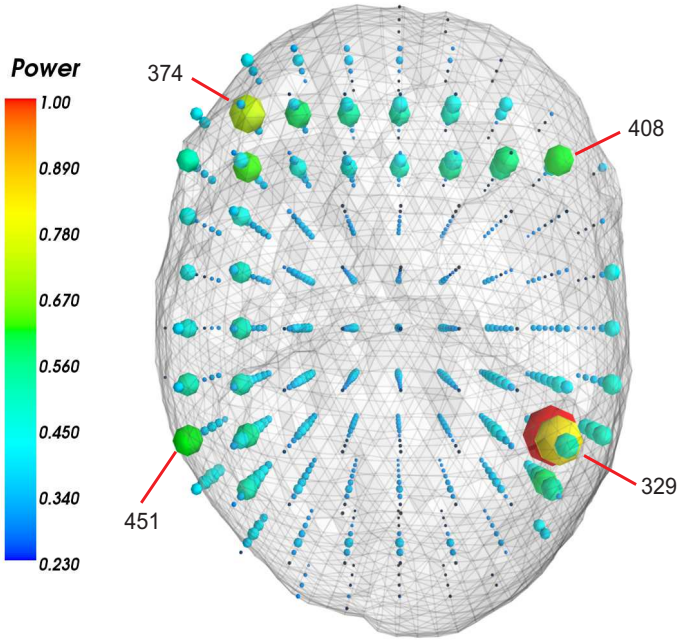

(b)

Figure 5.4: Estimated brain power using the LCMV and BCMV spatial filters, with normalized values to have a maximum value of one for plotting reasons. In a) is presented the estimated brain power using the LCMV beamformer, while in b) is the estimated brain power using the BCMV spatial filter. The size and colours of the spheres represent the amount of power estimated on each of the elements that compose the brain mesh used to solve the inverse problem.

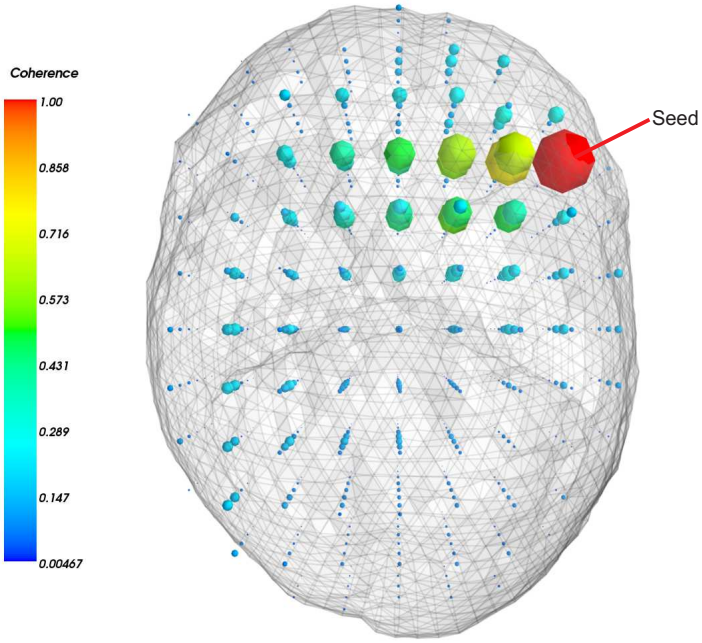

(a)

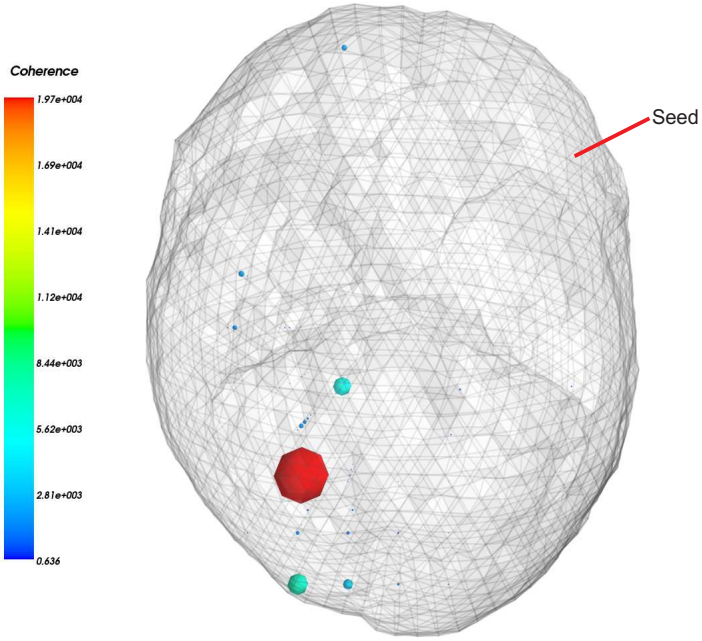

(b)

Figure 5.5: Estimated brain coherence using a seed voxel located at position 408. In a) are presented the estimated functional brain dynamics obtained using DICS. In b) are presented the functional brain interactions obtained using the BCMV spatial filter.

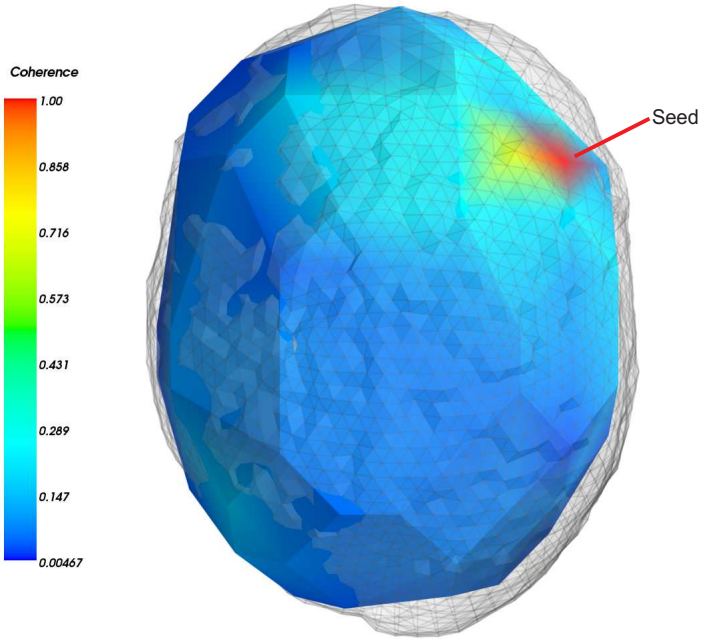

(a)

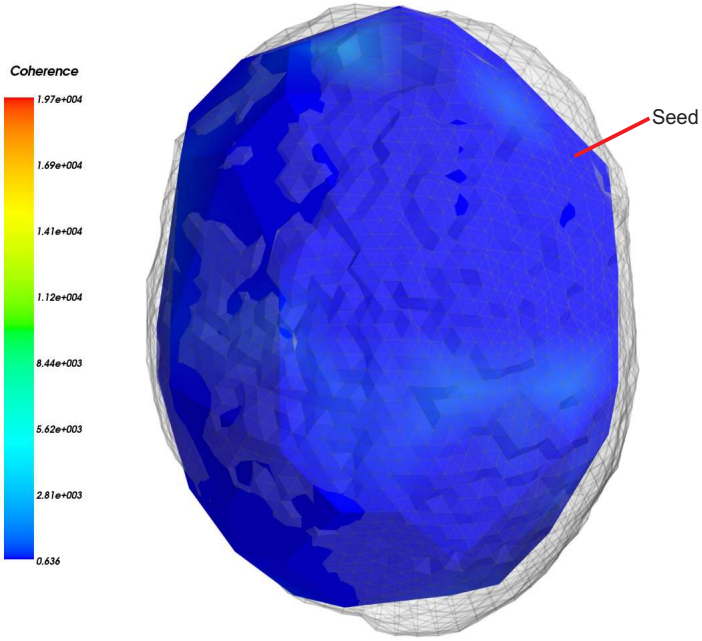

(b)

Figure 5.6: Estimated cortical brain coherence using a seed voxel located at position 408. In a) are presented the estimated cortical functional brain dynamics obtained using DICS. In b) are presented the cortical functional brain interactions obtained using the BCMV spatial filter.

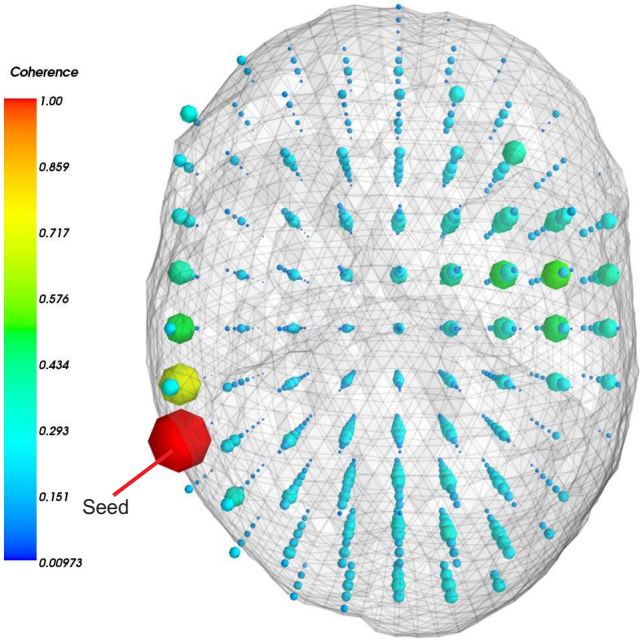

(a)

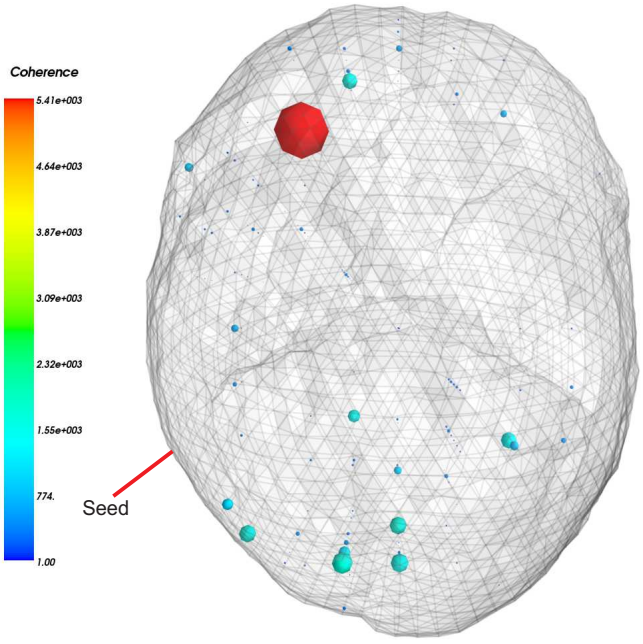

(b)

Figure 5.7: Estimated brain coherence using a seed voxel located at position 451. In a) are presented the estimated functional brain dynamics obtained using DICS. In b) are presented the functional brain interactions obtained using the BCMV spatial filter.

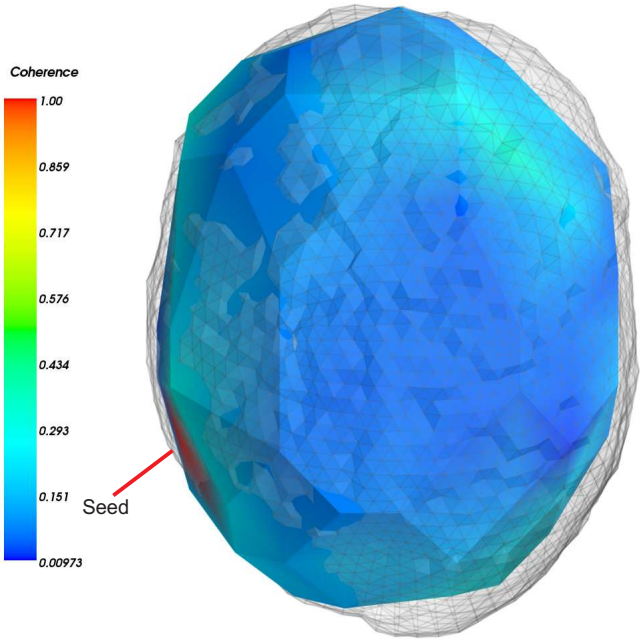

(a)

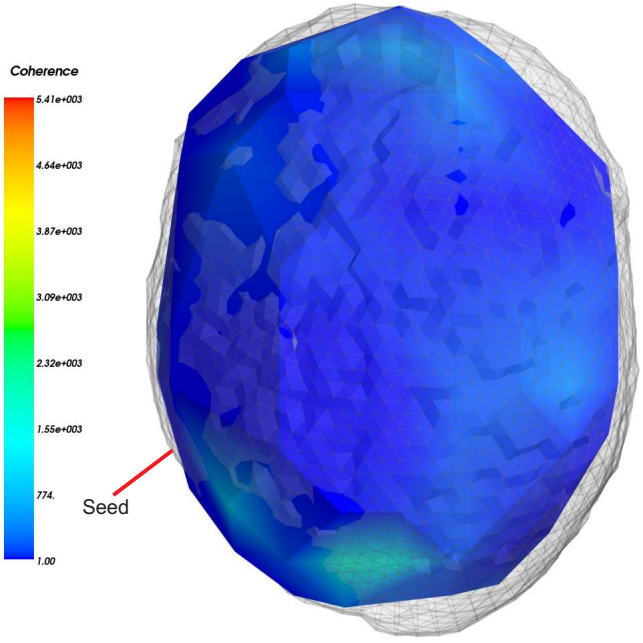

(b)

Figure 5.8: Estimated cortical brain coherence using a seed voxel located at position 451. In a) are presented the estimated cortical functional brain dynamics obtained using DICS. In b) are presented the cortical functional brain interactions obtained using the BCMV spatial filter.

Bilinear equation using more than one constraint

The complexity for the filter weights expressions increase considerable when more than one constraint is used. This is because of the need to solve higher order equations: second, third, fourth order equations, depending on the number of constraints used. This implies the use of methods such as the quadratic formula to find the roots for the second order equations, which can give imaginary results. Nevertheless, the solution for the problem using more constraints may have the same issues as the case when only one constraint is used. Another possible problem is related with the type of constraints used, some of them can generate results that rely on the inversion of a non-invertible matrix, as is for example the product $\boldsymbol{L}(\mathbf{r}_i)\boldsymbol{L}^T(\mathbf{r}_p)$, present when constraints similar as Equation 5.26 are used. It is a complex problem, which solution may requires the use of alternative methods in order to reduce the uncertainties and complexities related with a system of bilinear equations.

$$g(\mathbf{W}_{1b}, \mathbf{W}_{2b}) = \mathbf{W}_{1b}^T(\mathbf{r}_p)\boldsymbol{L}(\mathbf{r}_p)\boldsymbol{I}\,\boldsymbol{L}(\mathbf{r}_i)^T\mathbf{W}_{2b}(\mathbf{r}_i) = \boldsymbol{I} \tag{5.26}$$

5.2.2 Characteristics of a system of bilinear equations

In contrast with the solution for linear systems, the solution for bilinear systems and models are not well understood, even when they are used in science and engineering fields (Abrahamsson et al., 2007; Bai and Liu, 2005). A bilinear system of equations is characterized by $\mathbf{yTz} = \mathbf{d}$, expressed as a summation in Equation 5.27, where t_{ijk} and d_i are known real numbers (Cohen and Tomasi, 1997). The system consist of l equations and $m+n$ unknowns, such that $y_1, \cdots, y_m$ and $z_1 \cdots, z_n$. However, the bilinear system can be ever more complex as is presented in Equation 5.21, where $\mathbf{W}_{1b}$ and $\mathbf{W}_{2b}$ have a $N \times 3$ dimension. The bilinear systems can be divided into homogeneous and non-homogeneous systems, where the homogeneous case is present when $\mathbf{d} = 0$.

$$\sum_{j=1}^{m}\sum_{k=1}^{n} t_{ijk}y_j z_k = d_i \qquad for \quad i = 1, \cdots, l \tag{5.27}$$

There exists different established approaches to solve a bilinear system of equations depending on the dimensions of y and z. The case of a homogeneous bilinear system with $m = 1$ or $n = 1$ is reduced to solving a linear system, while the generalized eigenvalue method can be used to solve the problem when $m = 2$ or $n = 2$ (Cohen and Tomasi, 1997). However, the

cases when $m, n \geq 3$ remain unsolved (Cohen and Tomasi, 1997). One way to solve these problems is by treating them as optimization problems, where techniques such as the least squares method are used (VanAntwerp and Braatz, 2000; Bai and Liu, 2006).

5.3 Summary

In this chapter was presented an idea to modify the linearly constrained minimum variance beamformer in order to improve its performance in the presence of correlated brain activity. However, the proposed approach presents problems that make difficult its implementation using the Lagrange multipliers method. This, because it is difficult to find constraints that allow solutions for the problem. For this reason a different approach is proposed in the next chapter, which uses a different spatial filter to improve the finding of correlated brain activity using MEG data.

5.4 Discussion

The results obtained with the proposed BMCV spatial filter generates more issues than possible solutions. This, because of the structure of the proposed problem, which involves the solution of a bilinear set of equations to find the functional brain dynamics using two set of filter weights. The generated issues are not only about the complexity finding solutions for the bilinear equations using the Lagrange multipliers, but because the characteristics of a system of bilinear equations, presented in section 5.2.2. Another issue generated from the proposed idea is the possible reduction of the degrees of freedom, as there will be more equations to be solved than in the LCMV beamformer case, using the same sensors.

In this chapter was presented an example that shows the feasibility of the proposed approach for the estimation of the functional brain dynamics. The results obtained show inconsistent estimations because of the BCMV filter weights expressions, as their gains did not fulfil the constraints used for its design based on the Lagrange multipliers. The problem arises from the constraints used, since it is not possible to find critical points within the plane of the problem defined by the system of bilinear equations. Nevertheless, the use of more complex of higher number of constraints does not warranty the finding of critical points, and additional problems may appear with them. Problems such as the finding of solutions to quadratic, cubic or higher order problems, and the inclusion of complex numbers are some of them. The

constraints can also generate solutions with almost singular products, as is the case of the gram matrix, which require the use of regularization techniques for its inverse.

Thus, functional brain dynamics were estimated using different set of weights for the proposed idea, by using different constraints following the procedure presented in this chapter for the case of a single constraint. The estimated spectral coherences did not match the locations for the simulated activity interactions, showing less performance that the LCMV beamformer in all the different implementations. The LCMV only presented its characteristic power reduction of the estimated brain activity because of the uncorrelated brain sources assumption. The BMCV issues increase with the reduction of the SNR, since the filter weights increase its amplitude, overlapping the estimation of the brain activity interactions.

5.5 Conclusion

The LCMV beamformer has proved to be a robust and easy to be implemented technique, where its adaptability increases its performance compared with other approaches such as the MNE spatial filter. However, in the presence of correlated brain activity, those important properties that characterize the LCMV beamformer are reduced proportionally to the amount of correlation present. This reduce the robustness of the spatial filter, as there is impossible to have absolute certainty of where and how correlated are the generated brain activity. There has been different proposed solutions for the reduction of the uncorrelated brain sources assumption problem. Some of the proposed solutions involve smart changes to the LCMV implementation (Huang et al., 2004; Brookes et al., 2007; Gross et al., 2001; Dalal et al., 2006), while others rely on reducing the brain regions relationships by using only part of the sensors that measures the brain activity, or by using the LCMV to analyse distant brain regions, as is unusual for distant brain regions to be highly correlated (David et al., 2003).

However, the presented ideas deal with the uncorrelated brain sources assumption problem by improving the implementation of the spatial filter, rather than solving the problem present on the design of the LCMV, which was no built specifically for its use on MEG studies. In this chapter was proposed an idea to modify the design of the LCMV to reduce this problem, being the main motivation the LCMV performance improvement for the estimation of the functional brain dynamics. The proposed idea uses two set of weights to estimate the functional brain interactions from the magnetic fields covariance matrix, where its solution involve a bilinear set of equations that contains all possible brain interactions to be estimated.

Unfortunately the proposed idea generated additional problems that makes difficult its implementation or solution by using the Lagrange multipliers as in the LCMV beamformer case. The main problem is the complexity related with the finding of solution to the system of bilinear equations. Unfortunately the use of the Lagrange multipliers generated inconsistent solution for the constraint used to solve the problem. It may be possible to find valid solutions using different constraints, however, the complexity of the solution may increases, generating additional problems such are the use of complex numbers and large expressions almost impossible to implement. Moreover, even with all the mentioned problems, the proposed idea allows a different approach for the reduction of the uncorrelated brain sources assumption problem for the LCMV beamformer. It presents an alternative approach to deal with this problem without loosing the adaptability property of the LCMV beamformer, which it will gives some advantages over non-adaptive spatial filters as the MNE, which performance and implementation requires a more complicated selection of parameters.

Chapter 6

The MNE and the estimation of brain interactions

In this chapter is presented an approach inspired by DICS to estimate the functional brain interactions using a spatial filter based on the least-squares method, instead of the LCMV beamformer. The purpose of this change is to increase the accuracy for the estimation of interactions between brain activity sources following the DICS approach. This increase in the performance is possible as the proposed filter is not highly affected by the amount of correlation present among the brain sources. However, as this approach is based on the use of the least-squared method, it has the same limitations as the MNE spatial filter (Clarke and Braginski, 2006), a distorted and weighted output to solutions near the sensors. The proposed spatial filter is designed in the time domain to estimate the covariance matrices for the brain sources directly from the measured magnetic fields. Nevertheless, its implementation in the frequency domain is possible as it was presented in Chapter 4, where the filter is used to estimate the cross-spectral density matrices for the brain sources.

Thus, the cross-spectral density matrices estimated using the proposed spatial filter can be used to calculate the functional brain dynamics between the brain activity in the form of spectral coherences. The estimated brain interactions are obtained for the three components of the brain sources following the equivalent current dipole model. This can be reduced to have a metric of the strength of relationship between two different brain sources using the singular value decomposition to find the stronger direction for the relationship, as it was shown in Chapter 4 for the DICS method. In this chapter is explained the mathematics behind the proposed method, also its advantages and disadvantages with respect to DICS, and

therefore, with respect to the LCMV beamformer. In this chapter are also presented examples for the applications of the proposed method that helps understanding its performance and limitations in the estimation of the functional brain interactions.

6.1 Linearly Constrained Minimum Norm spatial filter

The proposed filter is based on two widely used methods for brain sources localization and reconstruction, the Linearly Constrained Minimum Variance beamformer (Van Veen and Buckley, 1988), and the Minimum Norm Estimates non-adaptive spatial filter (Hämäläinen et al., 1993), Section 3.3. The method was designed following the LCMV idea, but using the least-squares method to find the set of weights that define the filter, as in the MNE case. The Linearly Constrained Minimum Norm Estimates (LCMNE) non-adaptive spatial filter has been used before to reconstruct the time series for brain activity (Kumihashi and Sekihara, 2010). In this occasion is proposed its use for the estimation of the brain sources cross-covariance matrices directly from the measured magnetic fields, without being affected by the presence of correlated brain activity (Sanchez and Halliday, 2013).

The LCMNE spatial filter shows similar behaviour with respect to the MNE spatial filter when both of them are used to estimate the brain sources time series from the measured magnetic fields, which is expected as both of them share similar expressions in their designs. However, the approach used to calculate the weights that define the LCMNE spatial filter is similar to the LCMV, but using the least-squares method instead of the Lagrange multipliers.

The LCMNE filter design allows the estimation of the covariance matrices between the brain sources at locations $\mathbf{r}_i$ and $\mathbf{r}_j$, $\mathbf{C}(\mathbf{q}_i, \mathbf{q}_j)$, from the covariance matrix of the measured magnetic fields, $\mathbf{C}(\mathbf{x})$, using a $M \times 3$ matrix of filter weights for each location, as is presented in Equation 6.1, where $\widehat{\mathbf{C}}(\mathbf{q}_i, \mathbf{q}_j)$ is used to represent the estimated covariance matrices. The extraction is established from the representation of $\mathbf{C}(\mathbf{x})$ as the double summation of the product between the covariance matrices among the brain sources at locations $\mathbf{r}_i$ and $\mathbf{r}_j$, and the leadfields matrices for the same locations as is presented in Equation 6.2, where $\mathbf{C}_n$ is used to represent the covariance matrix for the external noise, as was previously introduced in Equation 5.17.

$$\widehat{\mathbf{C}}(\mathbf{q}_i, \mathbf{q}_j) = \mathbf{W}^T(\mathbf{r}_i)\mathbf{C}(\mathbf{x})\mathbf{W}(\mathbf{r}_j) \tag{6.1}$$

$$\mathbf{C}(\mathbf{x}) = \sum_{i=1}^{N}\sum_{j=1}^{N} \boldsymbol{L}(\mathbf{r}_i)\mathbf{C}(\mathbf{q}_i, \mathbf{q}_j)\boldsymbol{L}^T(\mathbf{r}_j) + \mathbf{C}_n \tag{6.2}$$

The estimation is implemented by constraining the product between the leadfield matrices $\boldsymbol{L}(\mathbf{r})$ and the filter weights for a specific location $\mathbf{r}_i$ to be equal to the identity matrix $\mathbf{I}$, while the product for different locations $\mathbf{r}_j$ is equal to zero, for $i \neq j$, as in the LCMV case. The constraints are used to define the stop and pass bands of the filter, as can be observed in Equation 3.30. However, it is almost impossible to have complete attenuation in the stop band (Van Veen et al., 1997). Nevertheless, the attenuations are enough to allow good estimations for the covariance matrices between different brain sources. The constraints shown in Equation 3.30 for a specific location $\mathbf{r}_i$ can be rearranged in order to express the $3 \times 3N$ matrix of constraints $\mathbf{D}(\mathbf{r}_i) = [\mathbf{I}_{\mathbf{r}_1=\mathbf{r}_i}, \mathbf{0}_{\mathbf{r}_2\neq\mathbf{r}_i}, \ldots, \mathbf{0}_{\mathbf{r}_N\neq\mathbf{r}_i}]$ as the product between the composite leadfield matrix $\mathbf{H}$ and the LCMNE filter weights designed for the same location $\mathbf{W}(\mathbf{r}_i) \in \mathbb{R}^{3\times M}$, as is presented in Equation 6.3.

$$\mathbf{W}^T(\mathbf{r}_i)\mathbf{H} = \mathbf{D}(\mathbf{r}_i) \tag{6.3}$$

The filter weights are found by solving the least-squares inverse for the cost function presented in Equation 6.4 (Sekihara and Nagarajan, 2008). The least-squares method is used over the Lagrange multipliers to avoid the complexity of the problem due to a bilinear system of equations with inconsistent solutions, chapter 5. Also, because of the degrees of freedom which can be reduced in the case of a bilinear system of equations. The solution for the least-square function is shown in Equation 6.5, where the generalized inverse $\mathbf{H}^+$ is expressed as the product between the composite leadfield matrix, or gram matrix, and its inverse, such that $\mathbf{H}^+ = \mathbf{H}^T[\mathbf{H}\mathbf{H}^T]^+$.

$$\mathcal{F}_{LM} = ||\mathbf{D}(\mathbf{r}_i) - \mathbf{W}^T(\mathbf{r}_i)\mathbf{H}||^2 \tag{6.4}$$

$$\mathbf{W}^T(\mathbf{r}_i) = \mathbf{D}(\mathbf{r}_i)\mathbf{H}^+ \tag{6.5}$$

As in the MNE spatial filter, the use of a regularization technique is needed in order to estimate the inverse of the gram matrix. In the proposed approach is used the singular value decomposition truncation (SVDT) (Sekihara and Nagarajan, 2008; Hansen, 1987; Golub and

Van Loan, 2012) for the pseudo inverse. The reason for the use of the SVDT is to follow the same decomposition used in DICS for the finding of the strongest interactions presented in Chapter 4. SVDT is show in equations 6.6 and 6.7, where $\mathbf{U}$, and $\mathbf{V}$ are used to represent the singular left and right matrices, while $\mathbf{\Sigma}$ represents the singular values diagonal matrix. As in the MNE case, the regularization is implemented by suppressing the singular values smaller than a predefined threshold. The filter performance presents the same problems as the MNE, problems related to the external noise, and with the regularization technique, explained in Section 3.3.1. Thus, the filter weights can be obtained using Equation 6.8.

$$\begin{aligned} \boldsymbol{SVD}(\mathbf{H}\mathbf{H}^T) &= \mathbf{U}\mathbf{\Sigma}\mathbf{V}^T \\ \left[\mathbf{H}\mathbf{H}^T\right]^{-1} &= \mathbf{V}\mathbf{\Sigma}^{-1}\mathbf{U}^T \end{aligned} \tag{6.6}$$

$$\begin{aligned} \left[\mathbf{H}\mathbf{H}^T\right]^{+} &= \mathbf{V}\mathbf{\Sigma}^{+}\mathbf{U}^T \\ \mathbf{\Sigma}^{+} &= diag(\lambda_1^{-1}, \ldots, \lambda_k^{-1}, 0, \ldots, 0)T \end{aligned} \tag{6.7}$$

$$\mathbf{W}^T(\mathbf{r}_i) = \mathbf{D}(\mathbf{r}_i)\mathbf{H}^T[\mathbf{V}\mathbf{\Sigma}^{+}\mathbf{U}^T] \tag{6.8}$$

The cross-spectral density matrix for the spectrum of the measured magnetic fields can be expressed for specific frequencies f, or for a specific frequency window band F_w, Equation 6.9, where the subscript H indicates the Hermitian transpose and $\langle . \rangle$ indicates the expectation operator, while $\mathbf{g}(f)$ is the Fourier transform for the measured magnetic fields, as was mentioned in chapter 4. The cross-spectral density matrix $\mathbf{\Gamma}(F_w)$ is defined for the LCMNE spatial filter as it can be observed in Equation 6.10, which is an expression similar to the one used in the LCMV beamformer, but considering all possible interactions among the different brain sources responsible for the generation of the magnetic fields cross-spectral density matrix. In Equation 6.10 the 3×3 matrices $\mathbf{\Gamma}_{\mathbf{r}_i\mathbf{r}_j}(F_w)$ are used to represent the cross-spectral density matrices between the brain sources at positions $\mathbf{r}_i$ and $\mathbf{r}_j$, while $\mathbf{Q}$ is used to represent the cross-spectral density matrix for the external noise.

$$\mathbf{\Gamma}(F_w) = \sum_{f \in F_w} \langle \mathbf{g}(f)\mathbf{g}^H(f) \rangle \tag{6.9}$$

$$\mathbf{\Gamma}(F_w) = \sum_{i=1}^{N}\sum_{j=1}^{N} \boldsymbol{L}(\mathbf{r}_i)\mathbf{\Gamma}_{\mathbf{r}_i\mathbf{r}_j}(F_w)\boldsymbol{L}^T(\mathbf{r}_j) + \mathbf{Q} \tag{6.10}$$

The implementation of the LCMNE in the frequency domain allows the estimation of the cross-spectral density matrices $\mathbf{\Gamma}_{\mathbf{r}_i\mathbf{r}_j}(F_w)$ from the cross-spectral density matrix $\mathbf{\Gamma}(F_w)$, by using the $3\times M$ matrices of filter weights $\mathbf{W}(\mathbf{r}_i)$ to estimate the spectrum of the brain sources responsible of the generation of the $\mathbf{\Gamma}_{\mathbf{r}_i\mathbf{r}_j}(F_w)$ matrices, Equation 6.11.

$$\widehat{\mathbf{\Gamma}}_{\mathbf{r}_i\mathbf{r}_j}(F_w) = \mathbf{W}(\mathbf{r}_i)\mathbf{\Gamma}(F_w)\mathbf{W}^T(\mathbf{r}_j) \tag{6.11}$$

Once the cross-spectral density matrices for the brain sources are obtained, it is possible the use of their elements to measure the brain dynamics in the form of the spectral coherences (Baccalá and Sameshima, 2001). The 3×3 estimated cross-spectral density matrices $\widehat{\mathbf{\Gamma}}_{\mathbf{r}_i\mathbf{r}_j}(F_w)$ are composed of the estimated interactions between the spectral densities of the x, y and z components of the brain sources at positions $\mathbf{r}_i$ and $\mathbf{r}_j$, as can be seen in the matrix presented in Equation 6.12. The spectral coherences among the different components of the brain sources $R_{i_xj_y}(f)$ are calculated based on $\widehat{\mathbf{\Gamma}}_{\mathbf{r}_i\mathbf{r}j}(F_w)$, Equation 6.13. However, the estimation of the spectral coherence can be calculated in the same way as is calculated in DICS, by finding the stronger brain sources interaction in $\widehat{\mathbf{\Gamma}}_{\mathbf{r}_i\mathbf{r}j}(F_w)$, as was presented in chapter 4. The expressions for the estimation of the brain dynamics using the DICS approach are shown in equations 6.14 and 6.15, where λ_a is the strongest brain source interaction.

$$\widehat{\mathbf{\Gamma}}_{\mathbf{r}_i\mathbf{r}_j}(F_w) = \begin{bmatrix} F_{i_xj_x}(F_w) & F_{i_xj_y}(F_w) & F_{i_xj_z}(F_w) \\ F_{i_yj_x}(F_w) & F_{i_yj_y}(F_w) & F_{i_yj_z}(F_w) \\ F_{i_zj_x}(F_w) & F_{i_zj_y}(F_w) & F_{i_zj_z}(F_w) \end{bmatrix} \tag{6.12}$$

$$R_{i_xj_y}(F_w) = \frac{|F_{i_xj_y}(F_w)|^2}{F_{i_xj_x}(F_w)F_{i_yj_y}(F_w)} \tag{6.13}$$

$$\gamma_{\mathbf{r}_i\mathbf{r}_j}(F_w) = \lambda_a\{\mathbf{\Gamma}_{\mathbf{r}_i\mathbf{r}_j}(F_w)\} \tag{6.14}$$

$$R_{\mathbf{r}_i\mathbf{r}_j}(F_w) = \frac{|\gamma_{\mathbf{r}_i\mathbf{r}_j}(F_w)|^2}{|\gamma_{\mathbf{r}_i\mathbf{r}_i}(F_w)||\gamma_{\mathbf{r}_j\mathbf{r}_j}(F_w)|} \tag{6.15}$$

Thus, it is mathematically possible to estimate the cross-spectral density matrices using the proposed spatial filter, and therefore, it can be used for the estimation of the functional brain dynamics. However, because the filter is based on the least-squares method, the results tend to be distorted and weighted to solutions closer to the sensors, as in the MNE case. This does not affect its suitability to be used for the estimation of the brain dynamics, but other techniques are needed to be used together with the proposed method to minimize those problems (Gorodnitsky et al., 1995; Clarke and Braginski, 2006). Other factors that affect the performance are the signal to noise ratio (SNR) and the tolerance value used for the inversion of the gram matrix, the regularization method.

6.1.1 Focal Undetermined System Solution and the Linearly Constrained Minimum Norm Estimates

The results obtained estimating the functional brain dynamics using the LCMNE spatial filter are distinct from the estimation obtained using DICS. The main reason for this is the distorted output characteristics of the least-squares method, which, in brain connectivity studies, generates a lot of spurious interactions, as can be seen on the examples presented in the next section. This problem is present even when the brain sources responsible for the generation of the brain activity are uncorrelated. The distorted output generates spurious interactions as the activity estimated in most of the points on the mesh grid, used to solve the inverse problem, have signals with similar behaviour between them, which gives as a result highly correlated estimated coherence matrices.

The FOCUSS algorithm was designed to reduce the distortion generated on solutions given by the MNE spatial filter (Gorodnitsky et al., 1995), as it was explained in Section 3.4.2. This characteristic of the algorithm can be applied for the estimation of the functional brain dynamics by using the LCMNE spatial filter using Equations 6.11 and 6.15. The use of the FOCUSS algorithm does not change the proposed approach, as FOCUSS uses the estimation obtained from the spatial filters to reduce the distortion. The FOCUSS weights design also remains without any important changes, as they allow the estimation of the cross-spectral density matrices for the brain sources by using the LCMNE spatial filter, as is presented in Equations 6.16 and 6.17, where the sub index k is used to express number of iteration for the algorithm. Section 3.4.2 offers more information about this.

$$\mathbf{W}_{F_k} = \begin{bmatrix} diag(\sqrt{\widehat{\mathbf{\Gamma}}_{\mathbf{r}_1\mathbf{r}_1}(F_w)}) & & & \\ & diag(\sqrt{\widehat{\mathbf{\Gamma}}_{\mathbf{r}_2\mathbf{r}_2}(F_w)}) & & \\ & & \ddots & \\ & & & diag(\sqrt{\widehat{\mathbf{\Gamma}}_{\mathbf{r}_N\mathbf{r}_N}(F_w)}) \end{bmatrix} \tag{6.16}$$

$$\mathbf{W}^T(\mathbf{r}_i) = \mathbf{D}(\mathbf{r}_i)\mathbf{W}_{F_k}\mathbf{W}_{F_k}^T\mathbf{H}^T[\mathbf{H}\mathbf{H}^T]^+ \tag{6.17}$$

The main problem applying FOCUSS to the LCMNE spatial filter functional brain dynamics estimations are the use of the tolerance value for the inversion of the gram matrix in the iterations, and the number of iterations for the algorithm. If the tolerance value is not choose correctly, the obtained brain dynamics can be only generated because of the effect of the external noise, as in the MNE case. On the other hand, if the number of iterations is not enough, the results obtained will be highly correlated, while if the number of steps are too many, the result obtained will lose most of the brain interactions. Unfortunately, there is not a specific method defined to select the tolerance value or to select the number of iterations. The results presented in this chapter were obtained using trial and error implementations.

6.1.2 Spurious brain dynamics generated by the leadfields linearity

Combining the LCMNE spatial filter with the FOCUSS algorithm gives as a result an improvement of the functional brain dynamics estimation compared with the single LCMNE case. It is an estimation that gives similar results as using the DICS approach, as both spatial filters are related (Mosher et al., 2003), but at the same time the estimations of each method are characterized different, as can be seen in the next section. One of the most noticeable issues present in both approaches is the finding of spurious interactions from the linearity between the leadfields matrices. The linearity is generated from the symmetry of the geometry used to build the brain mesh in order to solve the inverse problem. The linearity can be observed as spurious connectivity patterns on the estimated coherences matrices in both, the DICS and the combination of the LCMNE and FOCUSS approaches.

One way to reduce the spurious connectivities induced by the leafields patterns is by contrasting the connectivity maps, or the coherence matrices, for two different conditions, normally labelled as active and control conditions (Nichols and Holmes, 2002). The *active* conditions

are present when a specific stimulus is used to obtain the maps, while the *control* conditions acts as baselines for experimental contrast (Schoffelen and Gross, 2011). The pattern can be found easily when the connectivity maps are obtained from the activity of uncorrelated brain sources, or when the solutions are estimated using the spatial filters in the presence of the external uncorrelated Gaussian noise. Therefore, the connectivity maps, or estimated coherence matrices, can be found by subtracting the connectivity maps found using the control conditions from the active conditions (Schoffelen and Gross, 2011).

Thus, the spurious connectivity patterns depend on the geometries used to build the brain mesh needed to solve the inverse problem, where different geometries give different patterns that can be seen in the estimated coherences matrices. In Figures 6.2, 6.4, and 6.6, are presented the characteristic patterns for three different brain mesh geometries, the estimated coherence maps for each brain mesh, between all brain mesh elements in the presence of uncorrelated white noise. In Figure 6.2 is presented the spectral coherence map for a brain mesh formed from three concatenate spherical shells, where the points are located radially one shell over the other, Figure 6.1. In Figure 6.4 is presented the spectral coherence map obtained with a similar mesh as on Figure 6.1, but using the points of 4 layers of half spheres that are not distributed radially one over the other, Figure 6.3. Figure 6.6 shows the coherence map obtained with the brain mesh used in the York Neuroimaging Centre, for the case when the points on the mesh are separate by 15 $[mm]$, Figure 6.5.

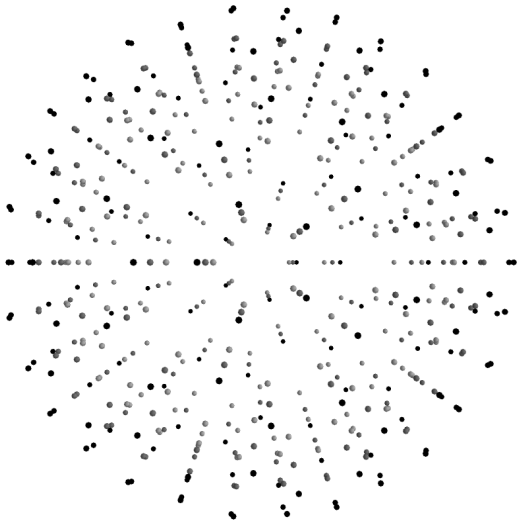

Figure 6.1: Spherical concentric shells used to solve the inverse problem. The points on each of the shells are radially aligned. The shells are represented by points, where different grey intensities are used to distinguish each of the shells.

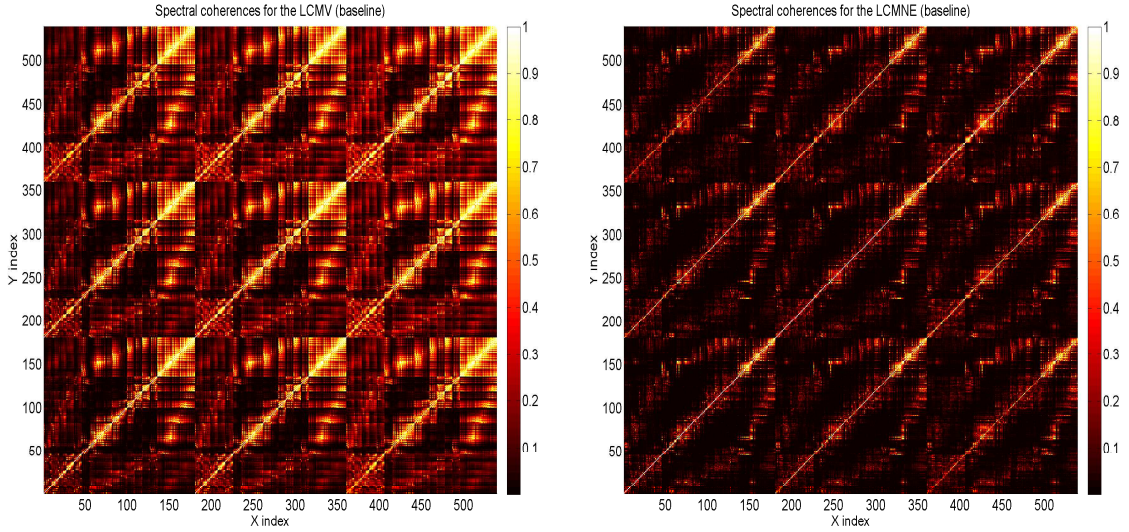

Figure 6.2: Coherence map patterns from a brain mesh built with radially aligned spherical shells, Figure 6.1. On the right side is presented the pattern obtained using the LCMNE spatial filter implemented in the same way DICS uses the LCMV beamformer. On the left side is presented the pattern obtained using DICS, or the LCMV beamformer.

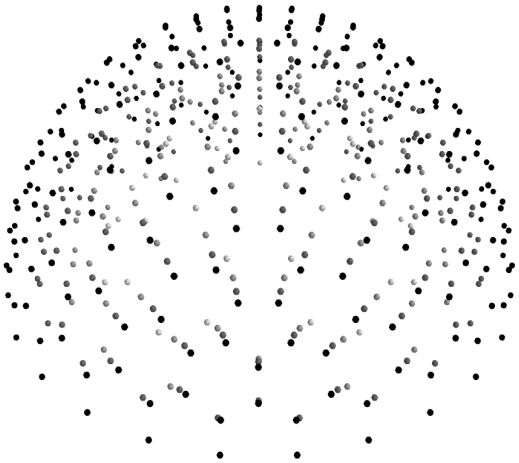

Figure 6.3: Not aligned spherical concentric shells used to solve the inverse problem. This brain mesh was built from four spherical shells, were each shell is composed of a different number of points, which are not aligned with other spherical shells points. The shells are represented by points, where different grey intensities are used to distinguish each of the shells.

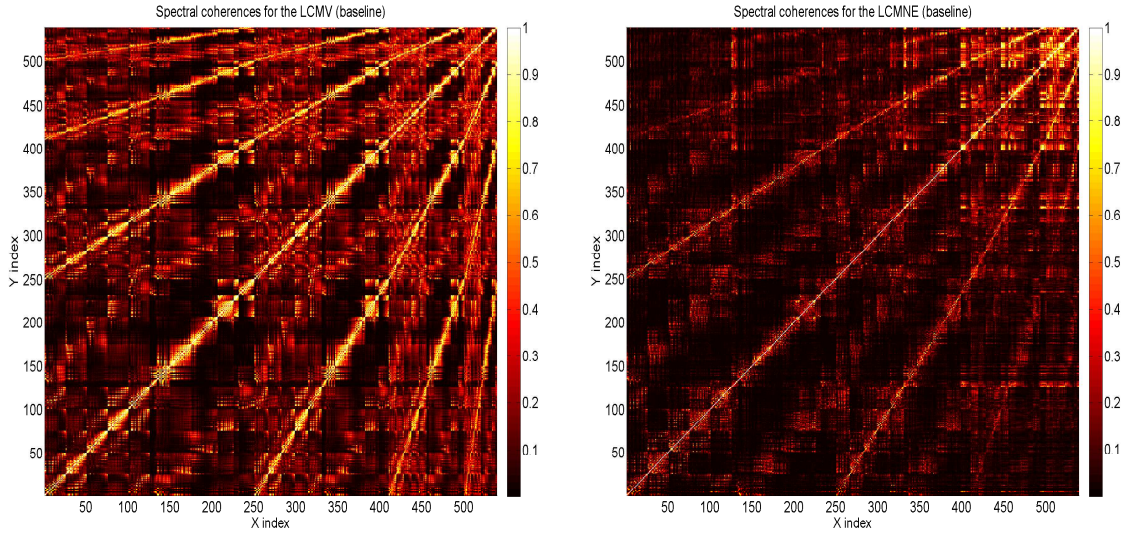

Figure 6.4: Coherence map patterns for a brain mesh built with no aligned spherical shells, Figure 6.3. On the right side is presented the pattern obtained using the LCMNE spatial filter implemented in the same way DICS uses the LCMV beamformer. On the left side is presented the pattern obtained using DICS, or the LCMV beamformer.

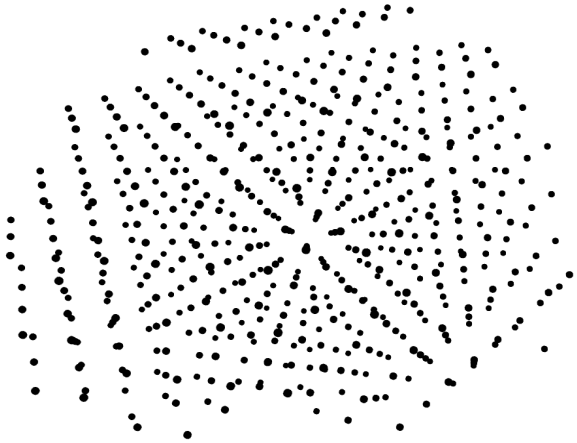

Figure 6.5: York Neuroimaging Centre[1] brain mesh used to solve the inverse problem. The points on the brain mesh are separated by a distance of 15 [mm] with each other.

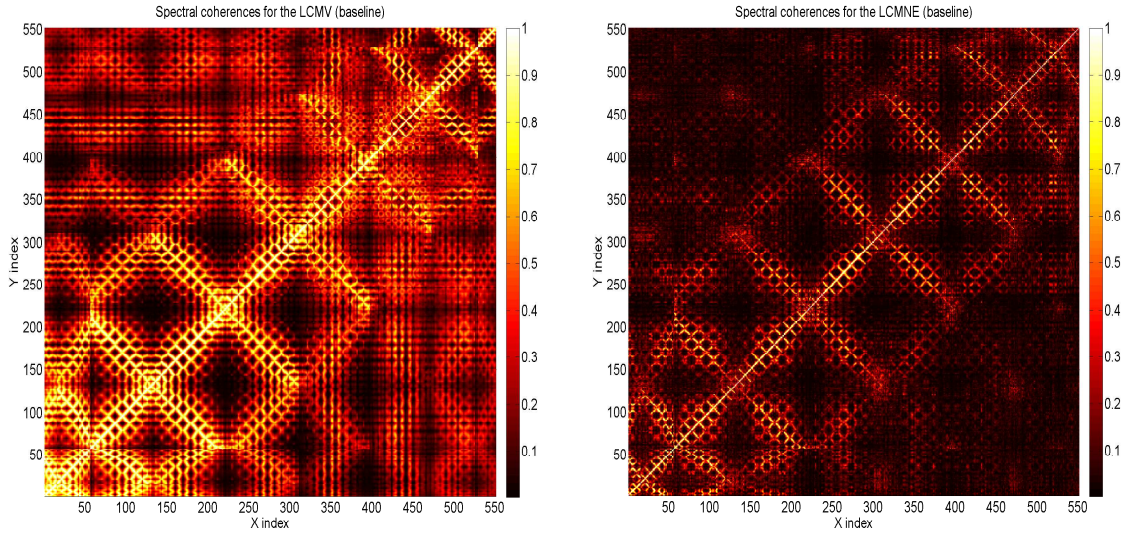

Figure 6.6: Coherence map patterns obtained using the YNIC brain mesh, Figure 6.5. On the right side is presented the pattern obtained using the LCMNE spatial filter implemented in the same way DICS uses the LCMV beamformer. On the left side is presented the pattern obtained using DICS, or the LCMV beamformer.

[1] *https://www.ynic.york.ac.uk/FrontPage*

6.2 Estimation of simulated brain interactions.

The feasibility of the LCMNE spatial filter in combination with the FOCUSS algorithm was tested with computational simulations in order to understand its behaviour when used for brain dynamics estimations. The results obtained show that it is possible to use the LCMNE in combination with the FOCUSS algorithm for the estimations of the functional brain dynamics, however, there exist factors that complicates the analysis of the results obtained, as is explained later on this section. The results obtained are compared against results obtained using DICS as a well established technique, comparison implemented in order to validate the use of the LCMNE with the FOCUSS algorithm. The scenarios used to test the proposed method are characterized by the number of simulated brain sources, the amount of correlation between them, their locations with respect to the brain mesh used to solve the inverse problem, and by the SNR ratio of the simulated MEG acquisition system.

The brain activity was simulated following the equivalent dipole model, while the inverse problem was solved using the York NueroImaging Centre brain mesh. Thus, the neuronal currents used to drive the equivalent current dipoles were generated as AR processes of order 9 with 10 seconds length (Angelidou et al., 1992), located on specific positions within the brain mesh used to solve the inverse problem. The amount of correlation between the simulated ECDs was generated using the Cholesky decomposition, and the external noise was simulated as Gaussian white uncorrelated noise for a specific SNR, calculated as the ratio of the Frobenius norm for the simulated brain activity covariance matrix and the simulated external noise (Sekihara et al., 2001). On the other hand, the implementation of the spatial filters in the frequency domain was limited to a specific frequency band from 1 to 50 [Hz], as the used MEG data for the AR modelling was previously filtered for those frequencies.

The simulated MEG acquisition system consist of 248 SQUIDs sensors, and their locations match the YNIC MEG acquisition system sensors distribution[1]. Moreover, the leadfields matrices used to solve the forward and inverse problems were obtained as it was presented by Sarvas and Mosher (Sarvas, 1987; Mosher et al., 1999). Then, the feasibility of the LCMNE spatial filter in combination with the FOCUSS algorithm was tested by simulating three main scenarios. The first scenario is used to introduce the ideal case for the use of the LCMNE with FOCUSS method, while the second and third are used to introduce a realistic example and the worst scenario for the use of the proposed method, respectively.

[1] *https://www.ynic.york.ac.uk/FrontPage*

6.2.1 Interactions between two brain sources located on the cortex.

The ideal case for the use of the LCMNE spatial filter in combination with the FOCUSS algorithm for the estimation of functional brain dynamics is present when the brain activity is located on the cortex and when their locations match the brain mesh used to solve the inverse problem, also in the presence of a high SNR. This, since the weighted and distorted characteristic effects of the filter output are reduced to their minimums for this case. Then, in this first introduced scenario is presented this ideal case, where the functional brain dynamics are simulated as pairs of correlated and correlated brain sources located on the cortex, for a SNR of 22, where the brain sources locations match the brain mesh used to solve the inverse problem. The simulated MEG acquisition system used for this scenario, and the following examples is presented in Figure 6.7, while the brain mesh used on this first example is presented in appendix G.

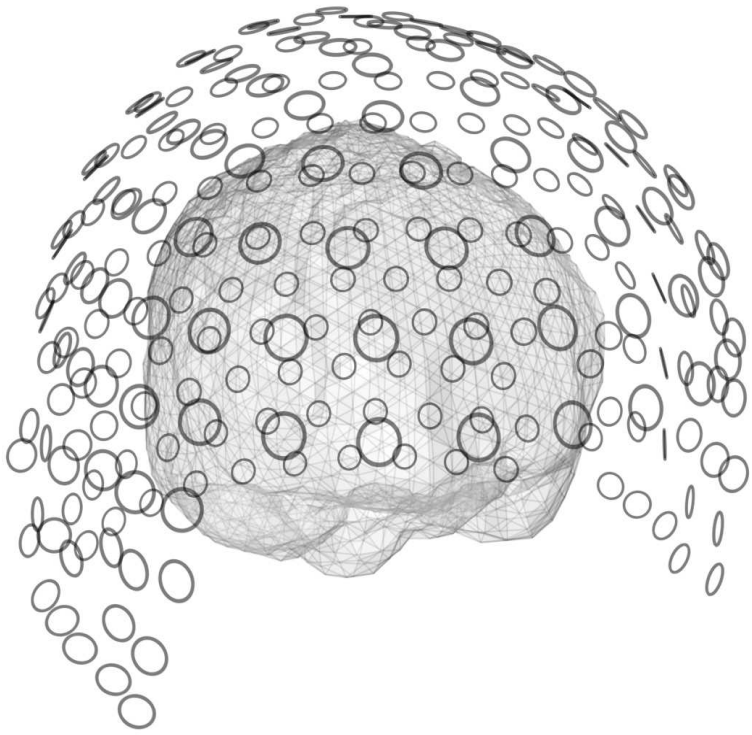

Figure 6.7: YNIC MEG acquisition system. The figure shows the distribution of sensors used to measure the simulated brain activity, represented as black rings surrounding the brain.

Uncorrelated brain activity

The simulation of uncorrelated brain activity is used to present the case when there are not brain interactions. It is introduced as the ideal case for the LCMNE with FOCUSS and the DICS approaches, since the LCMV is affected by the presence of correlated brain activity. It is an ideal case not only in terms of the spatial filters, but also in the sense that the brain activity is always correlated at some degree. This scenario is generated by simulating a pair of uncorrelated brain sources positioned as presented in Figure 6.8, where it can be seen the match between the brain sources locations and the brain mesh used to solve the inverse problem, specifically with brain mesh elements 263 and 346.

In the Figure 6.9 are also presented the estimated solutions for the inverse problem using the LCMV and the MNE spatial filters in the time domain, represented as estimated power on each of the brain mesh elements, where the colour and size of the spheres represent the amount of power on each location. The estimations are presented to have an idea of where to look for the brain activity, even when the simulated brain sources match the locations of the brain mesh. The estimations obtained using the MNE shows more distortion compared with the LCMV estimations. The same behaviour can be found in the frequency domain implementation of the spatial filters, where the distorted MNE output generates spurious connections in brain dynamics studies.

Thus, the brain dynamics are estimated implementing the spatial filters in the frequency domain as presented in Sections 4.3 and 6.1. The brain dynamics are estimated in the form of coherence matrices, or maps, for conditions used to estimate the functional brain interactions as presented in Section 4.3. Therefore, the active coherence matrices are estimated from the reconstructed simulated brain activity, while the control coherence maps are obtained in the presence of white noise without the presence of simulated brain activity. The estimated coherence matrices for the active and control conditions are presented in figures 6.10 and 6.11, for the LCMNE with FOCUSS and DICS methods, respectively.

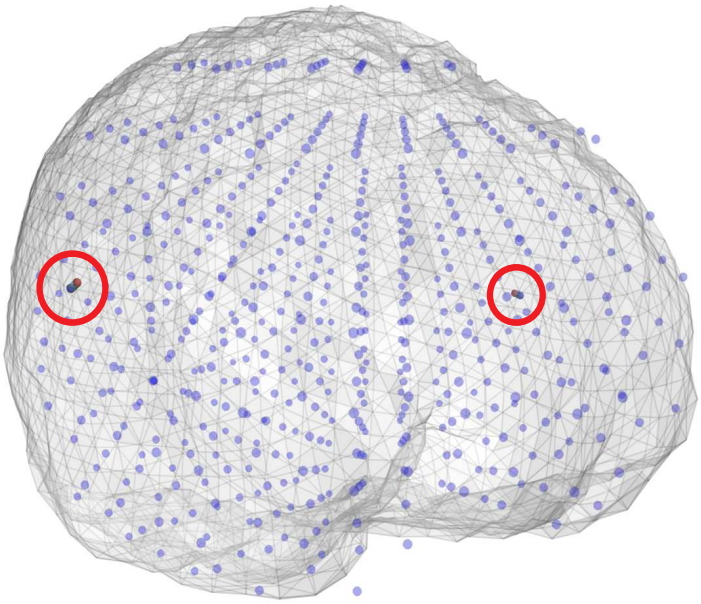

(a)

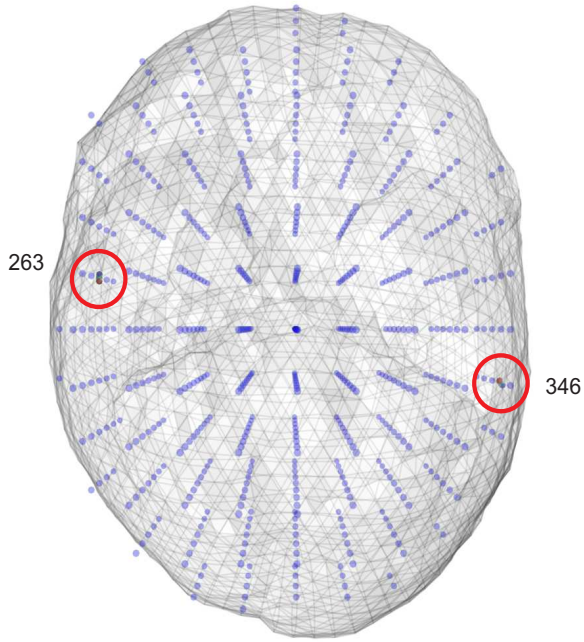

(b)

Figure 6.8: Locations for simulated uncorrelated brain sources. In a) and b) are presented the location for the simulated uncorrelated brain activity on two different perspectives. It can be observed the match between the locations for the simulated activity and the brain mesh used to solve the inverse problem. The locations are highlighted by red circles, while the brain mesh used to solve the inverse problem is presented as small blue spheres.

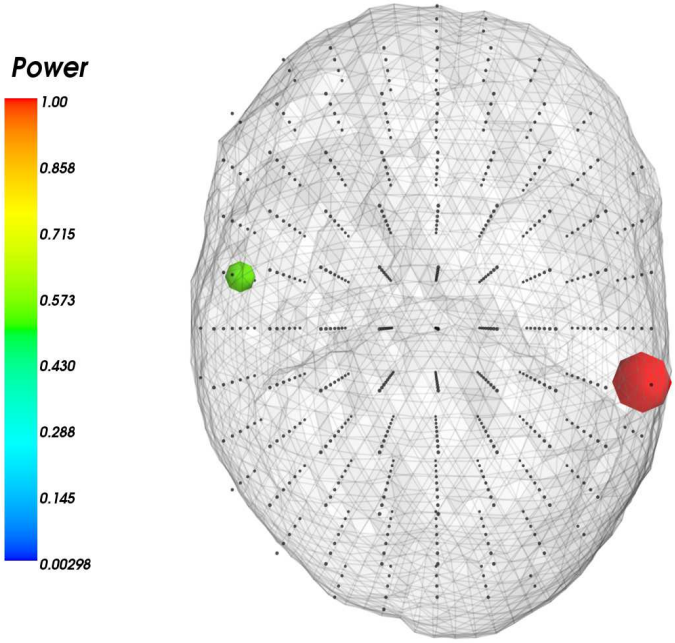

(a)

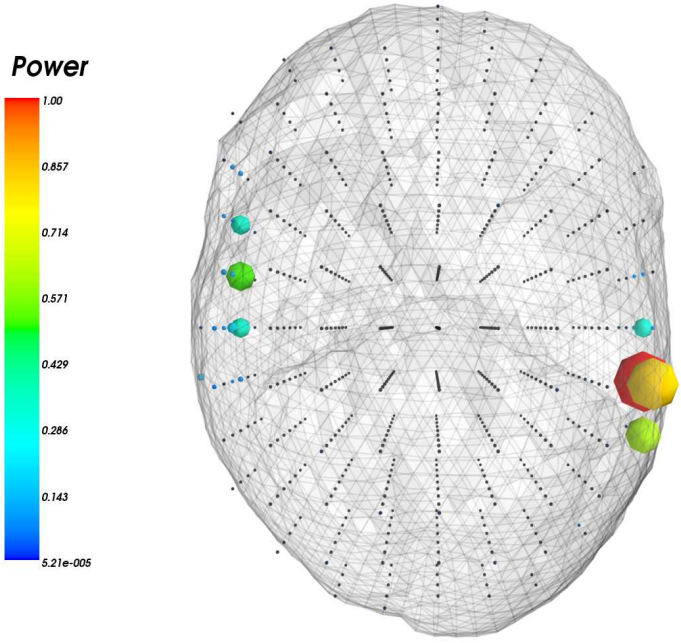

(b)

Figure 6.9: Power for reconstructed simulated uncorrelated brain activity using the LCMV and the MNE spatial filters. The power is presented as normalized values for plotting reasons. In a) is presented the LCMV estimated power for the simulated activity, while in b) are presented the estimated power using the MNE spatial filter. The colour and size of the spheres represent the amount of estimated power on each of the locations used to solve the inverse problem, appendix G.

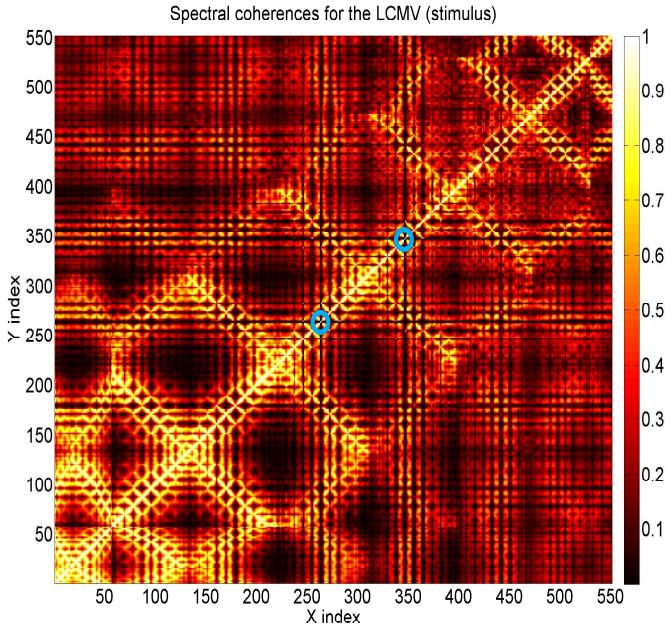

(a)

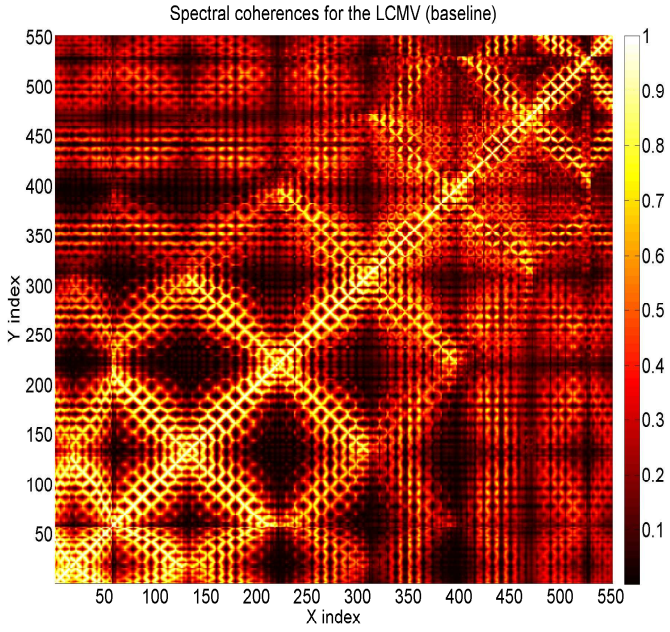

(b)

Figure 6.10: Estimated coherence matrices using DICS. On the top, estimated active condition coherence matrix, while on the bottom is presented the estimated control condition coherence matrix. Locations for the simulated activity are highlighted by blue circles.

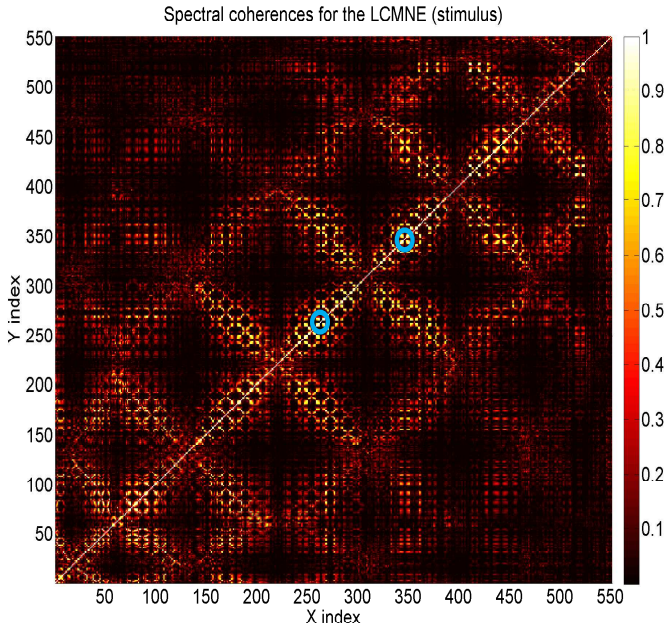

(a)

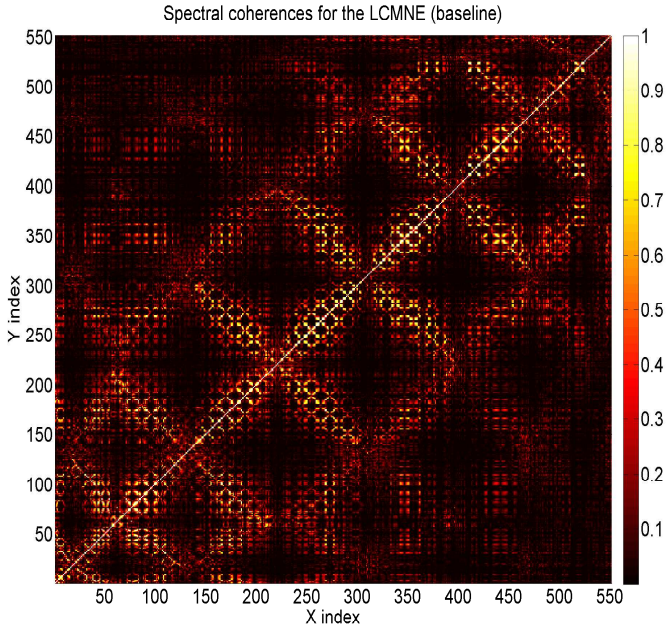

(b)

Figure 6.11: Estimated coherence matrices using the LCMNE with the FOCUSS algorithm. On the top, estimated active condition coherence matrix, while on the bottom is presented the estimated control condition coherence matrix. Locations for the simulated activity are highlighted by blue circles.

It can be observed that there does not appear to be great differences between the two conditions in both cases. However, it is possible to use the estimated coherence matrices for the estimation of the functional brain dynamics by contrasting the conditions, or by calculating the difference between them. The differences can be observed in figures 6.12 and 6.13, for DICS and for the use of the LCMNE spatial filter with the FOCUSS algorithm method, respectively. It can be observed that DICS gives an idea of the sources locations and their interactions, however, it looks like it is very sensitive to brain sources activity, as it presents high coherence even when the sources are uncorrelated. On the other hand, the use of the LCMNE spatial filter with the FOCUSS algorithm shows that it is possible its use to estimate the functional brain dynamics, however, there exist spurious interactions related to its characteristic distorted output, even with simulated activity located in positions that match the brain mesh and with a high SNR.

The coherence matrices presented in figures 6.12 and 6.13 can be used to estimate the functional connections between the different brain locations. In figures 6.14 and 6.15 are presented the interactions with enough intensity to be considered as brain connections, or estimated links between the elements that form the brain mesh used to solve the inverse problem. Figure 6.14 shows the brain connections obtained using DICS for the estimation of the coherence map, using a threshold value of .4. The brain connections estimated using the LCMNE with the FOCUSS method are presented in Figure 6.15, using a threshold value of .3. The threshold values used were selected in order to reduce the finding of spurious connections.

It can be observed in figures 6.12 and 6.13 that DICS gives a higher number of brain interactions estimations, all of them spurious brain connections. Thus, the uncorrelated simulated activity, the match between locations for the simulated activity and the brain mesh used and a SNR of 22 were not enough to obtain good estimations, even when these parameters characterize the ideal scenario for the use of both spatial filters. Therefore, the estimation of brain interactions between all-to-all brain locations are affected by other factors such as the leadfileds linearity, Section 6.1.2. Then, it can be concluded that, for this first introduced case, the LCMNE with FOCUSS method has a better performance than DICS for the estimation of the brain connections.

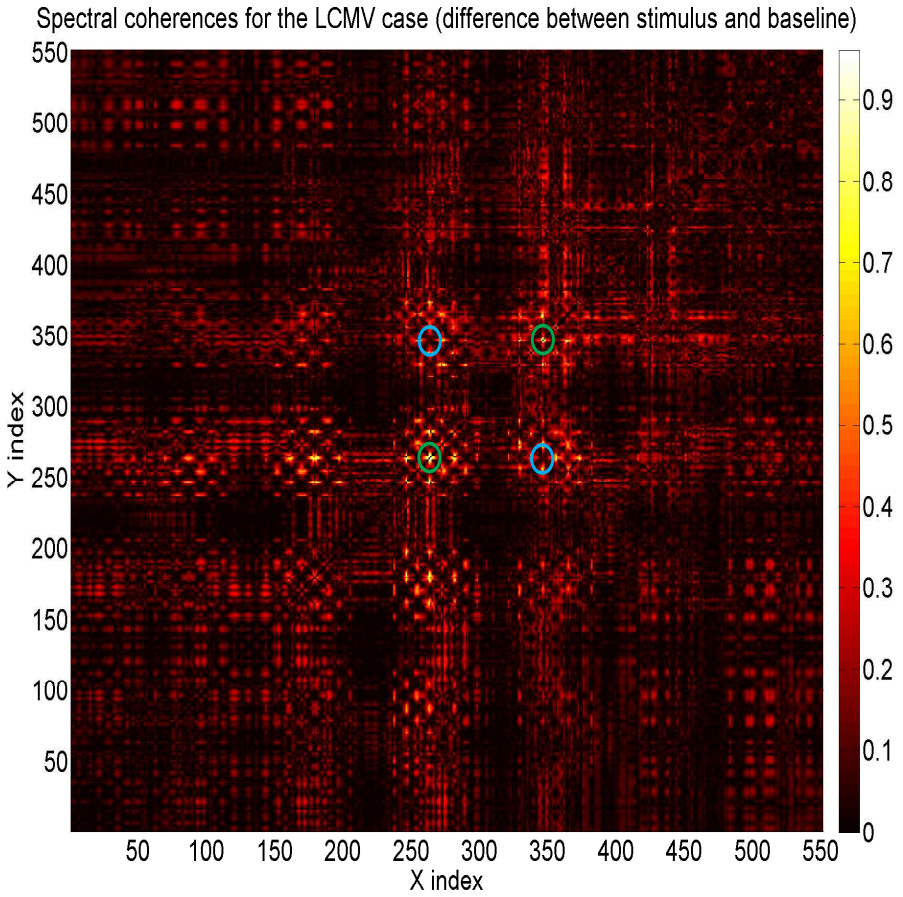

Figure 6.12: Estimated coherence map using DICS. It was calculated as the difference between the active and control conditions presented in Figure 6.10. It can be observed spurious brain interactions as the simulated brain activity was uncorrelated. The simulated brain sources are located at positions 263 and 346. The locations for the simulated activity are highlighted by green circles, while their possible interactions locations by blue circles.

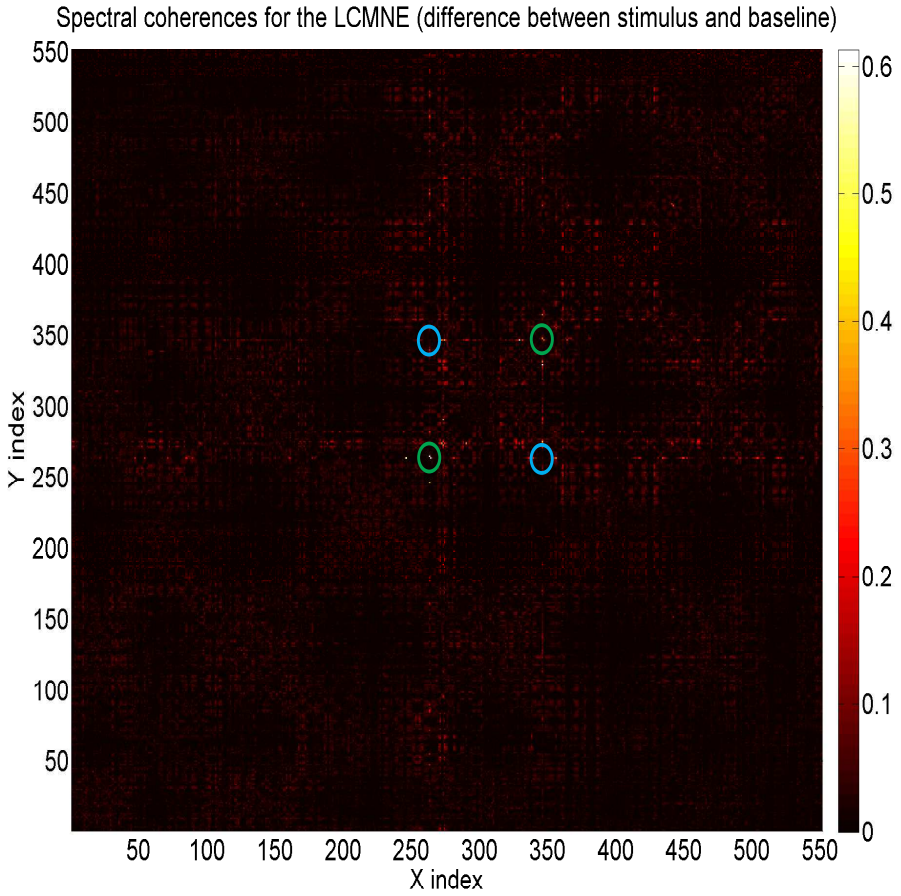

Figure 6.13: Estimated coherence map using the LCMNE spatial filter in combination with the FOCUSS algorithm. It was calculated as the difference between the active and control conditions presented in Figure 6.11. The simulated brain sources are located at positions 263 and 346, represented by the X and Y indexes in the figure. The locations for the simulated activity are highlighted by green circles, while their possible interactions locations by blue circles.

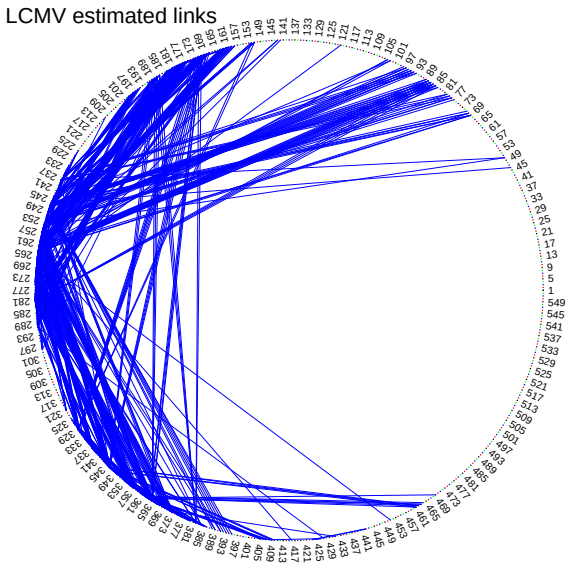

Figure 6.14: Brain connections estimated using DICS. The links between the different points represent the existence of functional interactions between sources located on different locations. The locations can be observed in Figure 6.8, and a detailed representation of the 15 [mm] brain mesh used is presented in appendix G.

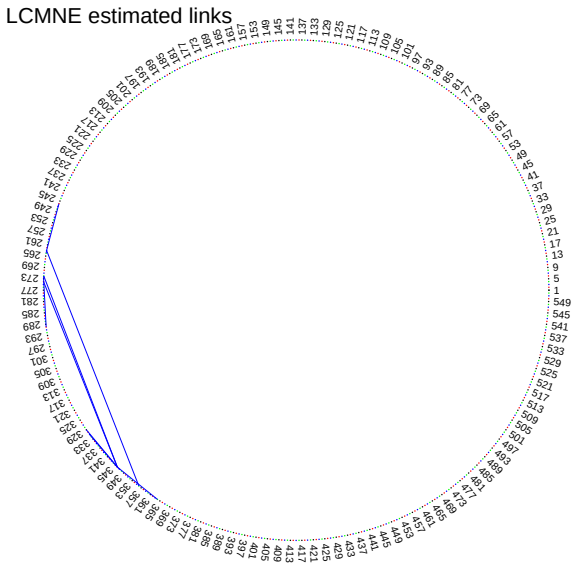

Figure 6.15: Brain connections estimated using the proposed method. The links between the different points represent the existence of functional interactions between sources located on different locations. The locations can be observed in Figure 6.8, and a detailed representation of the 15 [mm] brain mesh used is presented in appendix G.

Correlated brain activity

This scenario is used to present the estimation of functional brain interactions from correlated simulated activity, using the same SNR, locations and brain mesh as in the previous example. The locations can be observed in Figure 6.8. The brain activity was correlated with a correlation factor of .7, value selected to compare the performance of DICS and the LCMNE with FOCUSS method estimating high correlated brain activity. The effects that correlated activity has on the LCMV beamformer and the MNE spatial filter for the brain sources power estimations can be observed in Figure 6.16. The reduction of the estimated power in the LCMV beamformer case is due to the uncorrelated brain sources assumption, explained in Chapter 5. On the other hand, the MNE spatial filter is not affected by the presence of correlated brain activity.

As in the previous case, the functional brain interactions were estimated using DICS and the LCMNE with FOCUSS methods. The estimated active and control coherence matrices using both methods are not presented, as there are not too many differences with respect to the coherence matrices presented in Figures 6.10 and 6.11. There exist small differences, but on the matrices can be mainly observed the leadfields linearly pattern that generates spurious connections. As in the previous example, the brain interactions are found by calculating the difference between the active and control conditions as is presented in Figures 6.17 and 6.18, for DICS and for the LCMNE with FOCUSS methods, respectively.

In Figure 6.17 can be observed that it is possible to have an idea about where the brain connections are, but the locations with higher coherence values are not matching the locations related with the simulated activity, which is located on elements 263 and 346 of the brain mesh, represented as indexes in the figure. On the other hand, in Figure 6.18, the estimated brain dynamics obtained using the LCMNE in combination with the FOCUSS algorithm shows less number of locations with higher coherence values in the connectivity map. Some of those locations match the locations where the simulated activity was generated, showing a better performance than DICS for this specific scenario.

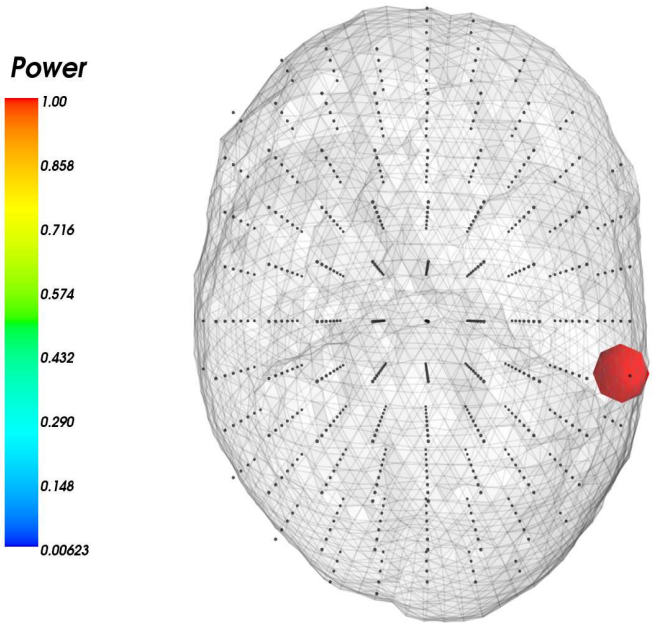

(a)

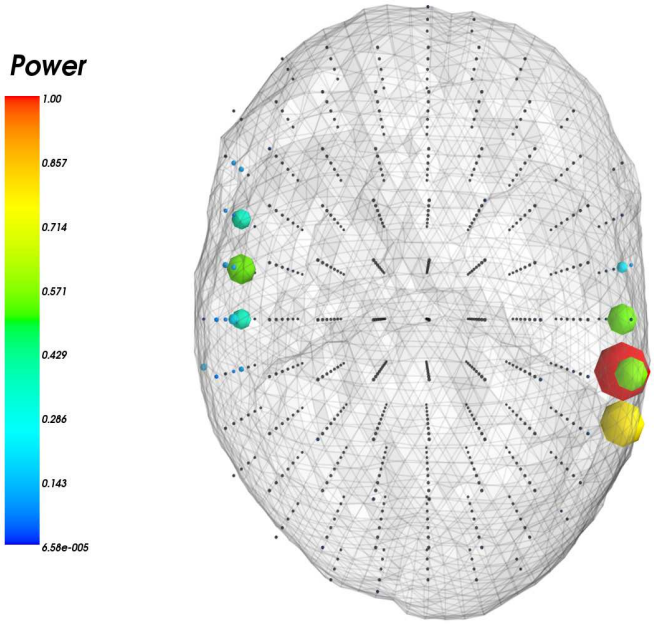

(b)

Figure 6.16: Estimated brain power using the LCMV and MNE in the time domain, with normalized values to have a maximum equals to one for plotting reasons. On the top is presented the estimated brain activity using the LCMV beamformer, while on the bottom is presented the estimated activity using the MNE spatial filter.

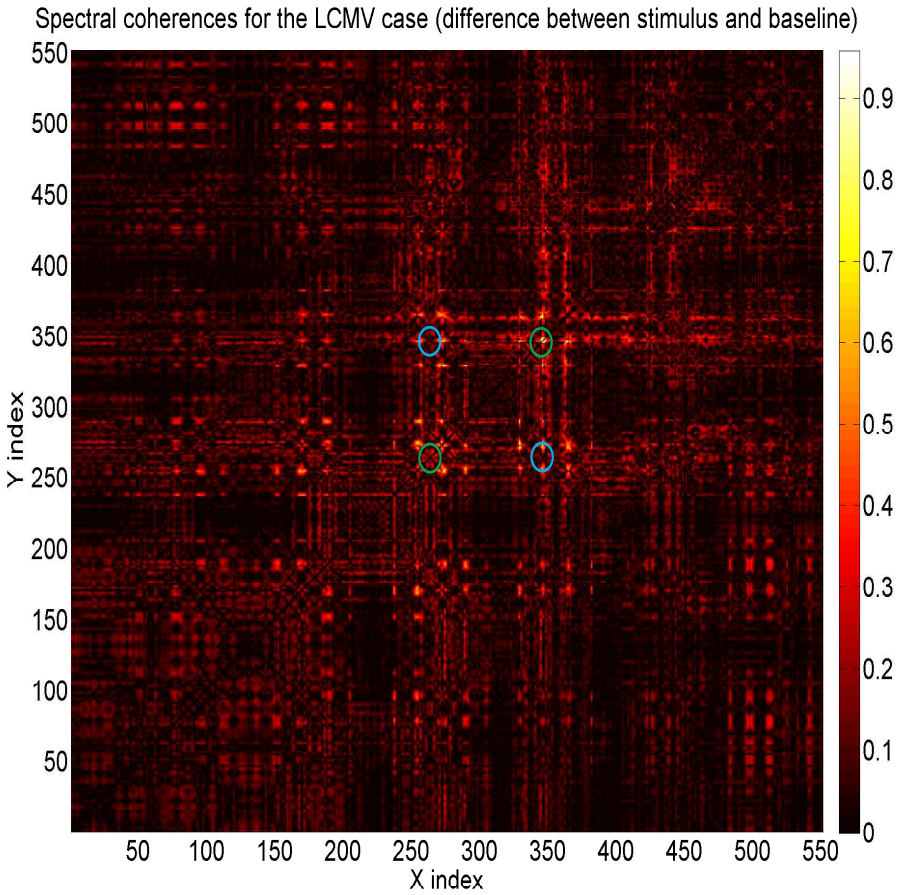

Figure 6.17: Estimated coherence map using DICS. The map was calculated as the difference between the active and control conditions obtained using DICS. The locations for the simulated activity are highlighted by green circles, while locations for the expected interactions are highlighted with blue circles.

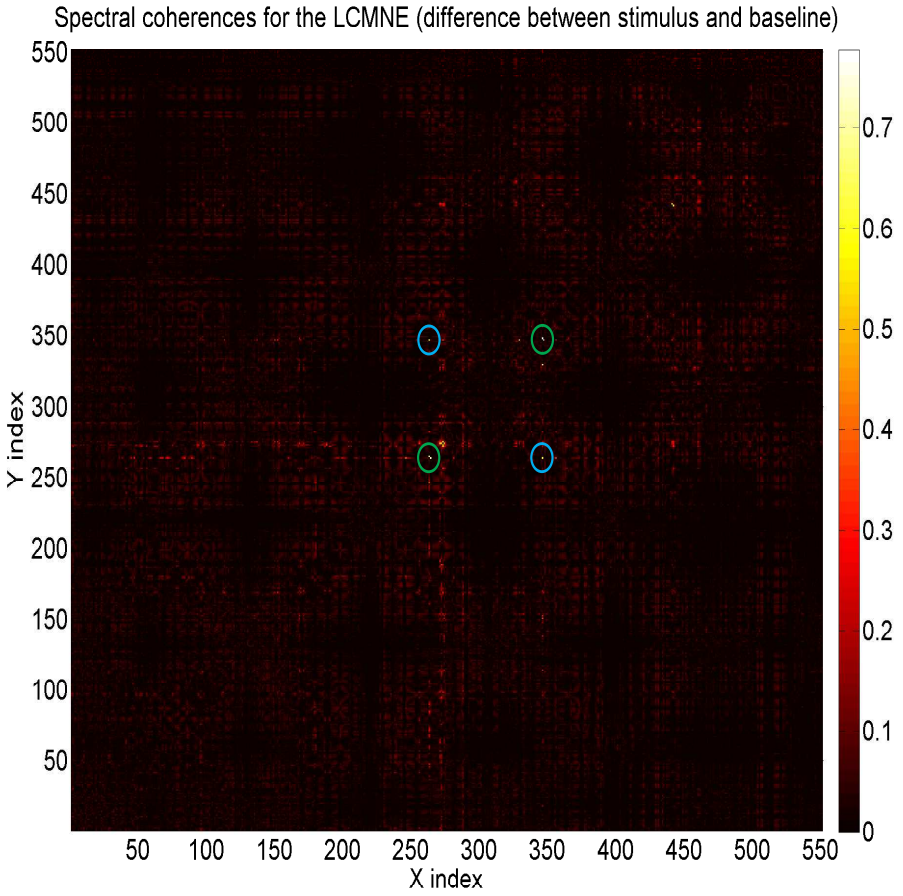

Figure 6.18: Estimated coherence map using the LCMNE with FOCUSS method. The map was calculated as the difference between the active and control conditions obtained using the LCMNE with FOCUSS. The locations for the simulated activity are highlighted by green circles, while locations for the expected interactions are highlighted with blue circles.

Thus, the estimated coherence values obtained using the LCMNE spatial filter with the FOCUSS algorithm are better estimations for the true coherence value between the simulated brain activity, .49 ($.7^2$), than the ones obtained using DICS, which estimates high coherence values for many of the locations used to solve the inverse problem and almost zero coherence between brain locations used to simulate the brain activity. This, because the uncorrelated brain activity assumption, which is not fulfilled reducing the power for the estimated brain activity. In Table 6.1 are presented the coherence values estimated using the two methods for the active condition and for the difference between conditions, for locations where the brain activity was simulated.

a) LCMNE/DICS	263	346
263	1	.58/.01
346	.58/.01	1

b) LCMNE/DICS	263	346
263	0.0	.57/.02
346	.57/.02	0.0

Table 6.1: Estimated coherence matrices for the active condition and for the difference between the active and control conditions. The matrices show the estimated coherence values using DICS and the LCMNE with FOCUSS method. In a) and b) can be observed the coherence values estimated for the active conditions and for the differences between the conditions, respectively.

Estimated connections between brain mesh elements can be observed in figures 6.19 and 6.20, for DICS and for the LCMNE with FOCUSS method, respectively, where the links are obtained from the off-diagonal elements of the coherence matrices presented in figures 6.17 and 6.18. To be more specific, the links are selected as those which have stronger intensity than the threshold values used to reduce the finding of spurios connections. Thus, a threshold value of .4 is used in Figure 6.19, while a threshold value of .3 is used in Figure 6.20.

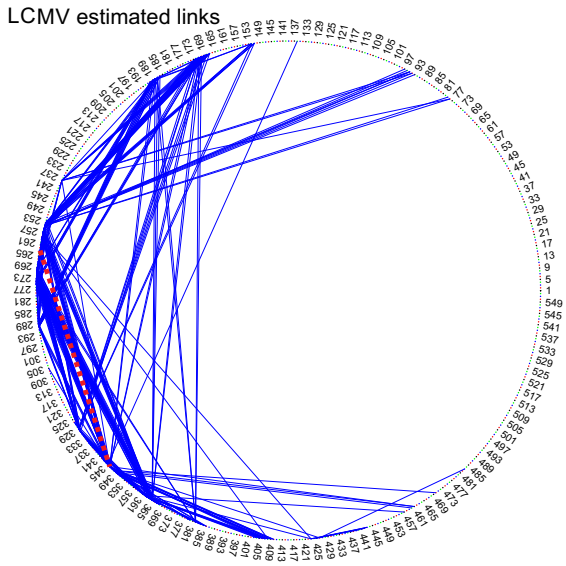

Figure 6.19: Brain connections estimated using DICS. The links between the different points represent the existence of functional interactions between different brain locations. The locations can be observed in Figure 6.8. The expected link generated with the simulated correlated activity is represented by a red dashed line.

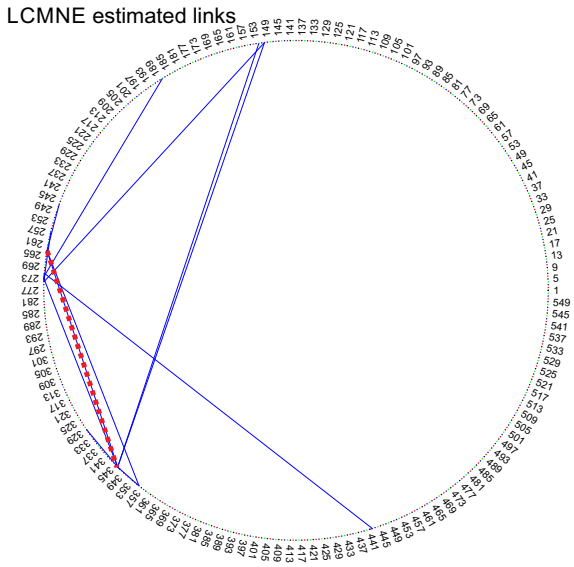

Figure 6.20: Brain connections estimated using the LCMNE with FOCUSS method. The links between the different points represent the existence of functional interactions between different brain locations. The locations can be observed in Figure 6.8. The expected link generated with the simulated correlated activity is represented by a red dashed line.

Brain coherence without FOCUSS and using FOCUSS with 5 iterations

In the previous presented examples the functional brain dynamics estimations were obtained using the LCMNE spatial filter in combination with the FOCUSS algorithm, which was used in four iterations. The number of iterations is an important issue that need to be introduced, as there is not a defined approach to select how many of those are required. In the previous examples, and on the following ones, the number of iterations used is the same, as it shows a good performance for the estimation of the brain dynamics using the simulated data. Altough, different values would be required for diffeernt scenarios, since the use of FOCUSS is affected by the SNR and the tolerance value used for the inversion of the gram matrix, Section 6.1

Thus, the number of iterations is normally selected using a try and error approach. This uncertainty about the number of iterations is one of the main problems that the proposed method has, as if the number of iterations is not enough then the findings of spurious interactions could be very high, and therefore, almost impossible to estimate the real brain connections. On the other hand, if the number of iterations are too many, then, there is the possibility that the estimated activity has less power or smaller intensities than the expected, because of the excess of iterations. In the worst case, the brain interactions can be lost from the estimations because of this problem.

These issues are presented in figures 6.21 and 6.22, where the previous experiment is repeated without using the FOCUSS algorithm, and when the method is implemented using 5 iterations of FOCUSS, respectively. Figure 6.21 shows how problematic is the implementation of the LCMNE spatial filter for the brain dynamics estimations without the use of FOCUSS. This, since it is almost impossible to know where the brain interactions are located, as most of the possible interactions present high values. On the other hand, Figure 6.22 shows some decrease on the estimated brain interactions when compared against Figure 6.18, because of the more iterations used. This loss in intensity increases if more iterations are used.

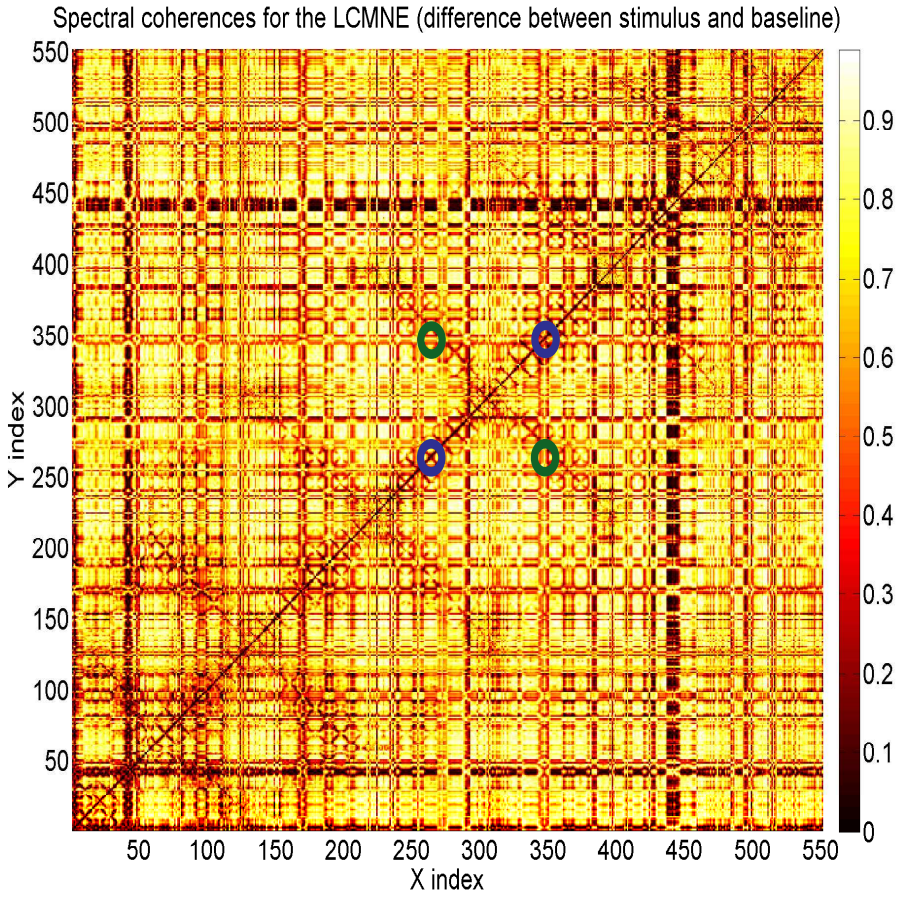

Figure 6.21: Implementation of the LCMNE spatial filter without the use of FOCUSS for the estimation of functional brain dynamics using the simulated data generated on the last example. It can be observed that most of the estimated coherence present high values, which makes difficult to find the real brain connections. The locations where the activity were generated are highlighted by blue circles, while interactions locations are highlighted by green circles.

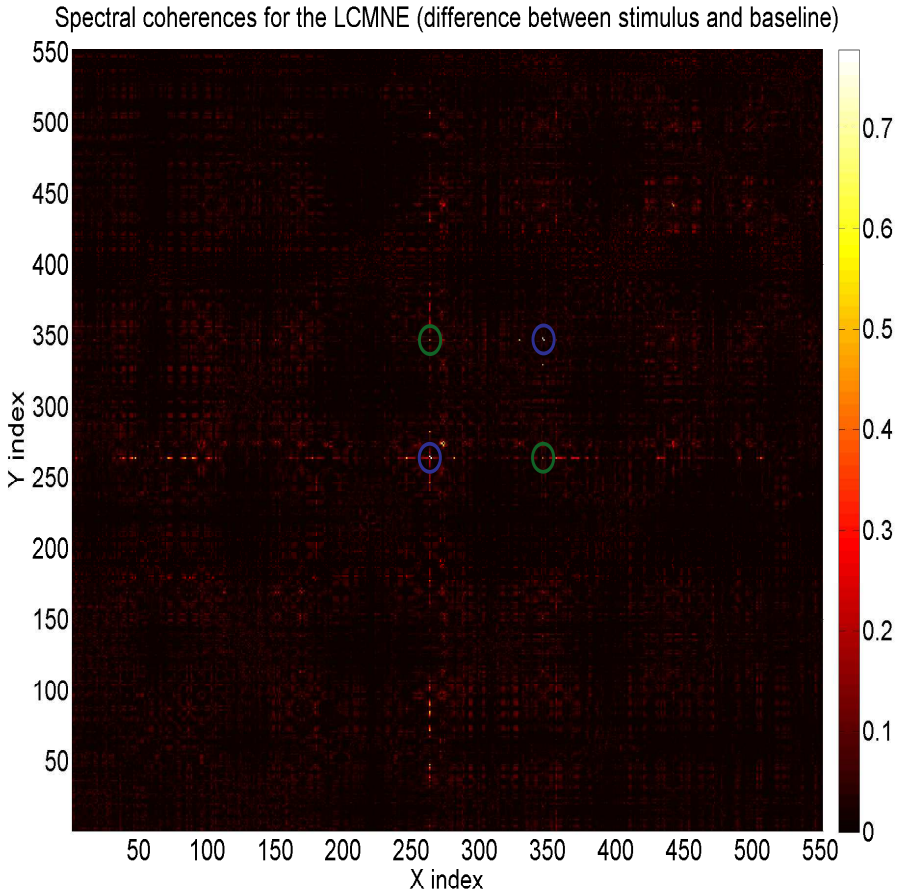

Figure 6.22: Implementation of the LCMNE spatial filter method using 5 iterations of the FOCUSS algorithm for the estimation of functional brain dynamics using the simulated data generated on the last example. It can be observed the lost of the expected connection compared with Figure 6.18. The locations where the simulated activity were generated are highlighted by blue circles, while interactions locations are highlighted by green circles.

6.2.2 Estimation of simulated brain interactions from correlated and uncorrelated brain cortical activity

In this example are introduced realistic scenarios for the functional brain dynamics estimations, using the LCMNE with FOCUSS and the DICS methods. The scenarios used on this example consider two different SNR values, and the presence of correlated and uncorrelated cortical brain activity. Moreover, the locations for the simulated activity do not match the brain mesh used to solve the inverse problem. These parameters values were selected in order to show the distorted output characteristic of the proposed method, which in functional brain dynamics studies generate the finding of spurious interactions. The results obtained using the LCMNE with FOCUSS method are compared against results obtained using DICS, which as being based on the LCMV it presents an undistorted output, but because of the correlated activity some of the brain interactions are reduced in intensity.

The following examples use a brain mesh composed of 1848 elements, separated by 10 [mm] with each other, appendix G. Using this brain mesh allows to show better how the distortion is generated compared with the 15 [mm] brain mesh used in the previous examples. The locations for the simulated brain sources and the correlation coefficients used to generate the brain activity are presented in Table 6.2, where the locations are presented considering their x, y an z Cartesian coordinate system components. The brain activity was simulated as AR processes of order 9 as in the previous examples. The selected amount of correlation is used to understand the behaviour of DICS and the LCMNE with FOCUSS methods in the presence of high correlated and uncorrelated brain activity.

Brain source(x,y,z)	1(35,182,190)	2(35,100,190)	3(140,100,190)	4(140,182,190)
1(35,182,190)	1	0.7	0.0	0.0
2(35,100,190)	0.7	1	0.0	0.7
3(140,100,190)	0.0	0.0	1	0.0
4(140,182,190)	0.0	0.7	0.0	1

Table 6.2: Correlation matrix for the simulated brain activity. The matrix shows the correlation coefficients between the simulated brain activity and their locations, Figure 6.23. The positions of the brain sources are presented in millimetres.

Correlated and uncorrelated activity with a SNR of 22.

The first scenario is characterized by the brain activity simulated as described in Table 6.2, for a SNR of 22. This scenario is used to present the use of the LCMNE with the FOCUSS algorithm for the estimation of brain connections in a more realistic scenario than in the previous examples. However, the value for the SNR used is not too realistic, but later on the same example will be introduced considering a more realistic SNR. The SNR of 22 is used only to show the feasibility of the method for the brain dynamics estimations. Thus, in Figure 6.23 are presented the locations for the simulated activity, represented in the same way as in Table 6.2 and highlited by red circles. In the figure is also presented the brain mesh used for the solution of the inverse problem.

In Figure 6.24 are presented the simulated sources estimated power using the LCMV beamformer, which shows a distorted output because of the presence of high correlated brain activity, it can also be observed that brain mesh elements close to the simulated uncorrelated brain source are the brain locations with more estimated power. Moreover, the estimated power for the simulated brain activity using the MNE spatial filter is also presented in the figure, where a distorted estimation can be observed. In the figure some locations were selected based on the estimated amount of power present on them. This, in order to analyse the functional brain dynamics using the LCMNE with FOCUSS and the DICS methods as presented in sections 4.2 and 6.1. In Table 6.3 are presented the expected coherence values for the selected locations, Figure 6.24, where .49 is obtained from $.7^2$.

Brain Mesh(MNE/LCMV)	1325/1324	1431/1430	1420/1420	1313/1314
1325/1324	1	0.49	0.0	0.0
1431/1430	0.49	1	0.0	0.49
1420/1420	0.0	0.0	1	0.0
1313/1314	0.0	0.49	0.0	1

Table 6.3: Expected coherence matrix for selected brain mesh locations. The matrix shows expected coherence values for the LCMV and MNE active locations shown in Figure 6.23.

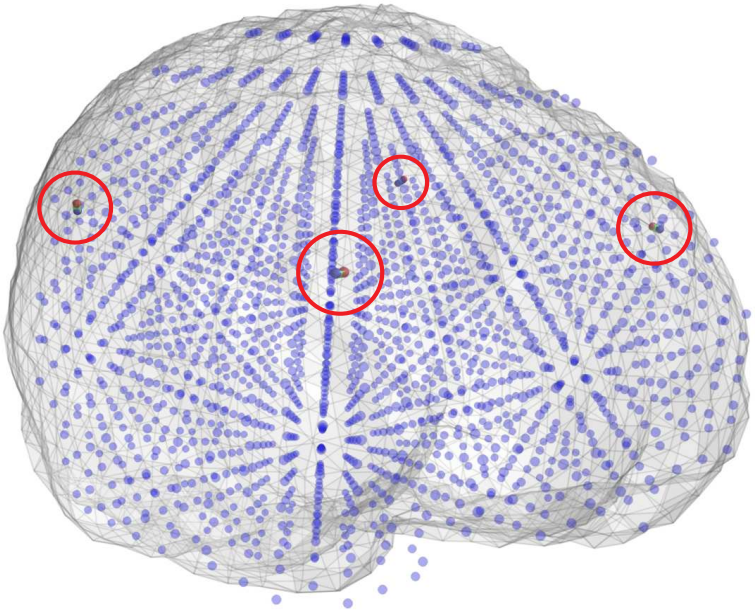

(a)

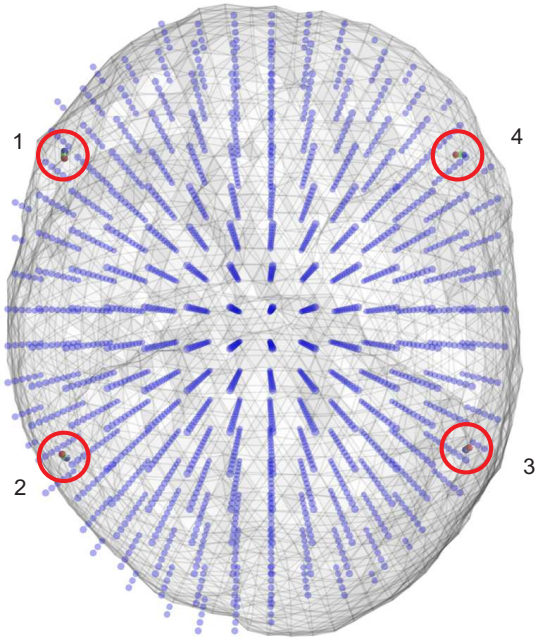

(b)

Figure 6.23: Simulated correlated and uncorrelated cortical brain activity locations, presented on a 10 mm brain mesh used to solve the inverse problem. In a) and b) are presented the locations for the simulated activity, highlighted by red circles. It can also be observed the brain mesh used to solve the inverse problem, composed by blue spheres that represented their elements.

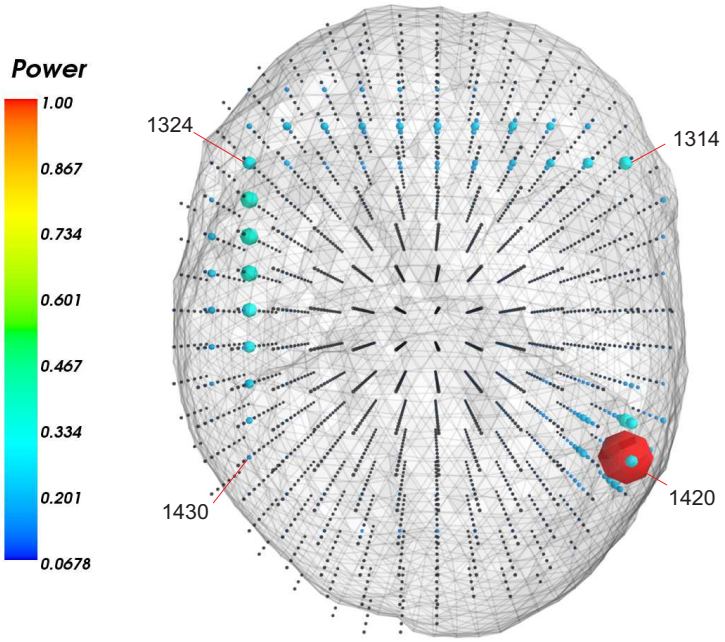

(a)

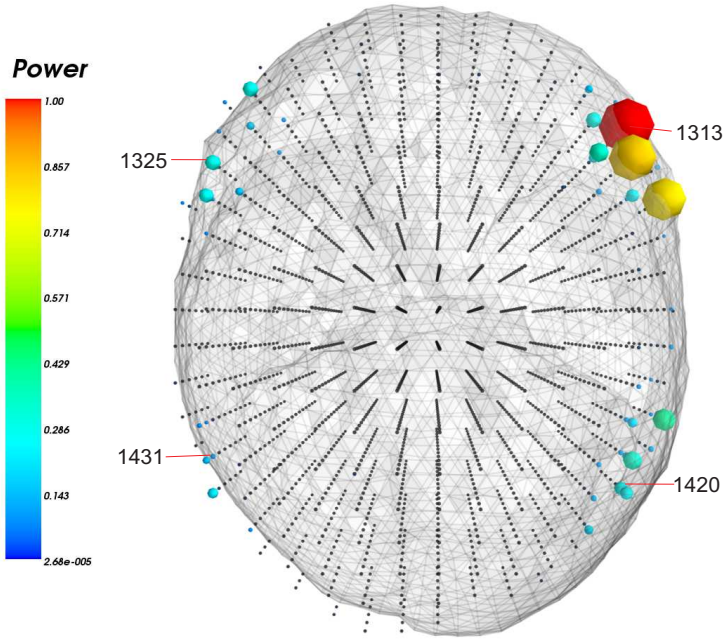

(b)

Figure 6.24: Locations for estimated simulated activity power using the LCMV and the MNE in the time domain, with normalized values to have a maximum value of one for plotting reasons. In a) are presented the estimated power for each of the locations used to solve the inverse problem using the LCMV beamformer, while on b) are presented the estimated power using the MNE spatial filter.

Implementing DICS and the LCMNE spatial filter with the FOCUSS algorithm using 4 iterations for the estimation of simulated functional brain interactions give as a result figures 6.25 and 6.26, which show the coherence matrices for the active and control conditions. It can be observed that it is almost impossible to find the correct locations for the simulated brain interactions due to very large coherence values in many elements of the matrices. However, the characteristic pattern from the leadfields is more clear than in the previous cases, as the used brain mesh is composed by more voxels. In Table 6.4 are shown the coherence values obtained from the active condition using DICS and the LCMNE with FOCUSS methods for the locations selected in Figure 6.24, which represent the estimated brain activity.

Brain Mesh(LCMNE/DICS)	1325/1324	1431/1430	1420/1420	1313/1314
1325/1324	0.0	.58/.33	.00/.00	.03/.01
1431/1430	.58/.33	0.0	.01/.01	0.45/.04
1420/1420	.00/.00	.01/.01	0.0	.02/.00
1313/1314	.03/.01	.45/.04	.02/.00	0.0

Table 6.4: Coherence values obtained from the active condition using DICS and the LCMNE with FOCUSS, arranged in a matrix for the locations presented in Figure 6.24.

Thus, the functional brain interactions are obtained by contrasting the two conditions for both methods, as presented in figures 6.27 and 6.28 for DICS and for the LCMNE with FOCUSS method, respectively. The obtained differences for the coherence maps can be observed better in figures 6.29 and 6.30, where only few elements of the matrices are shown, elements related with locations presented in Figure 6.24. The coherence values for the difference between conditions using the two methods are presented in a matrix form in Table 6.5. It can be seen that most of the coherence values obtained using the proposed method match the values obtained in the active condition coherence matrix, while for the LCMV case do not.

Brain Mesh(LCMNE/DICS)	1325/1324	1431/1430	1420/1420	1313/1314
1325/1324	0.0	.57/.30	.00/.00	.00/.00
1431/1430	.57/.30	0.0	.01/.01	0.41/.01
1420/1420	.00/.00	.01/.01	0.0	.01/.00
1313/1314	.00/.00	.41/.01	.01/.00	0.0

Table 6.5: Estimated coherences values obtained as the difference between conditions. The matrix shows the coherence values obtained from the coherence matrices presented in figures 6.29 and 6.30, for the locations presented in Figure 6.24.

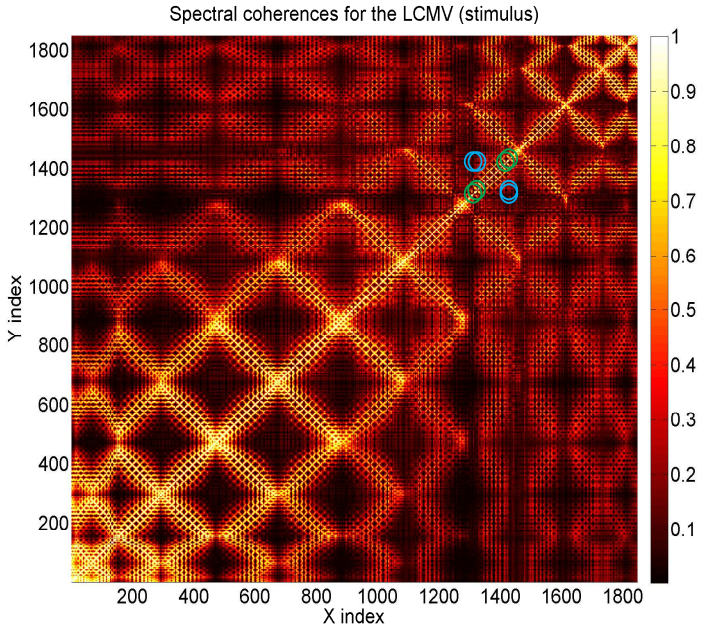

(a)

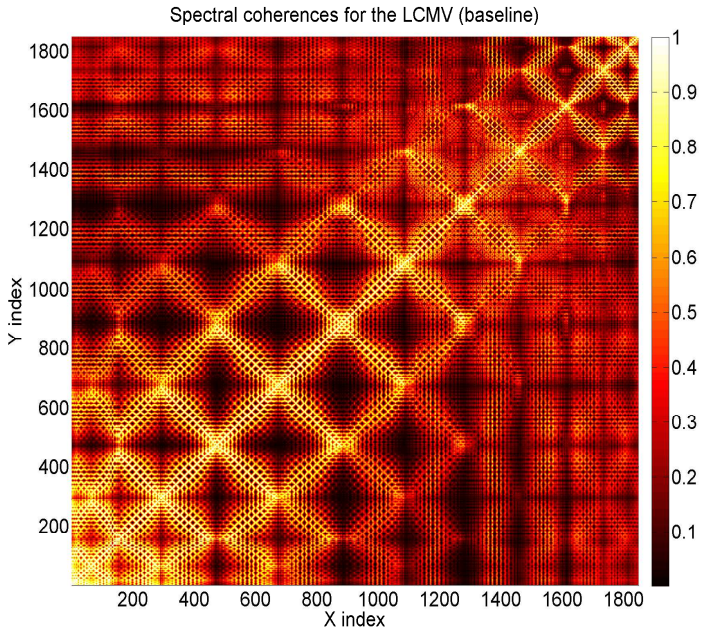

(b)

Figure 6.25: Active and control conditions coherence matrices for the simulated activity, estimated using the DICS method. On the top is show the coherence matrix for the active condition, while on the bottom is presented the control case. The simulated brain activity is related with locations presented in Figure 6.23. Selected locations for the brain sources dynamics estimations are highlighted by green circles, while their interactions are highlighted by blue circles.

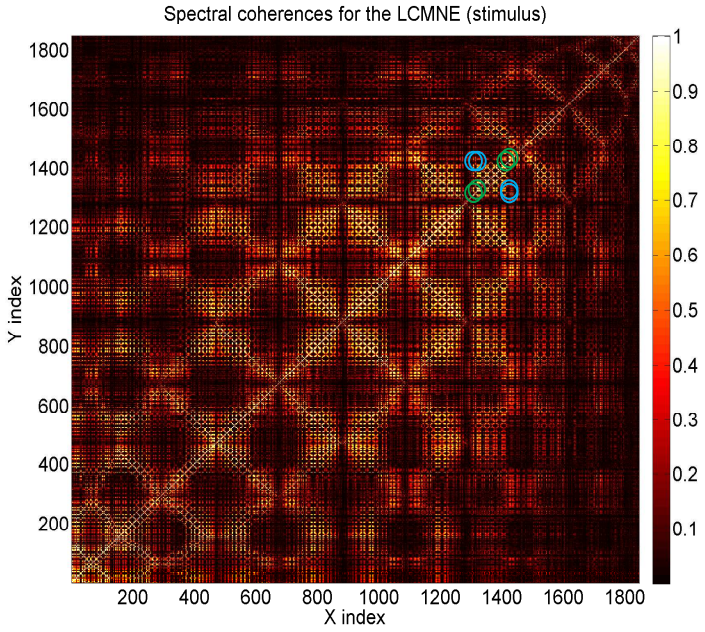

(a)

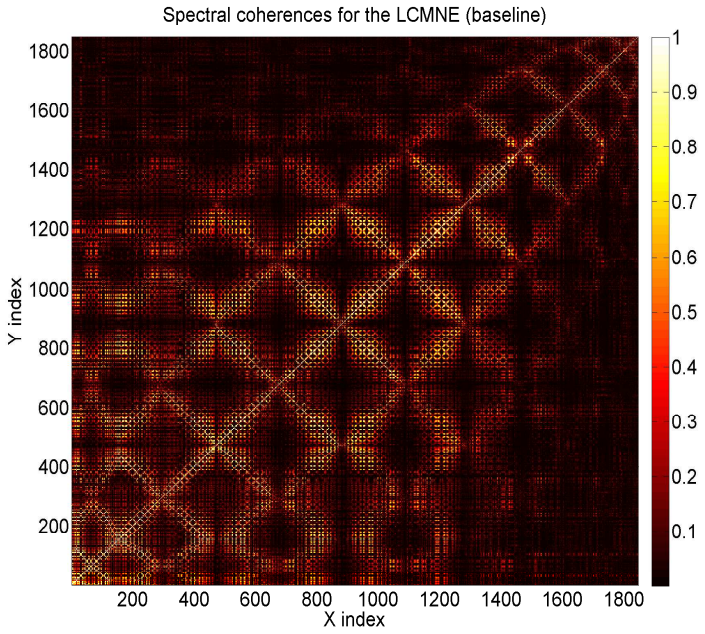

(b)

Figure 6.26: Active and control conditions coherence matrices for the simulated activity, estimated using the LCMNE spatial filter with the FOCUSS method. On the top is show the coherence matrix for the active condition, while on the bottom is presented the control case. The simulated brain activity is related to locations presented in Figure 6.23. The axis indexes are used to locate the brain mesh elements. Selected locations for the brain sources dynamics estimations are highlighted by green circles, while their interactions are highlighted by blue circles.

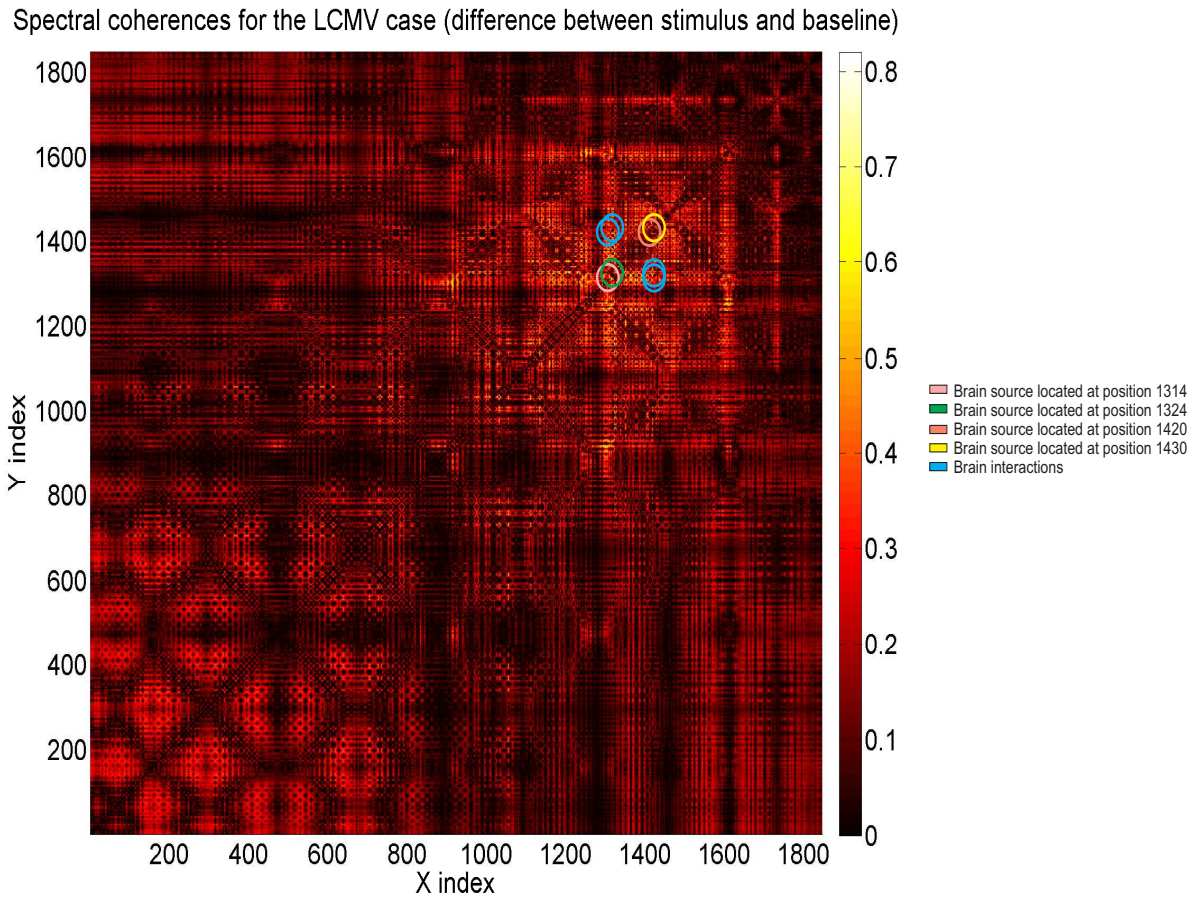

Figure 6.27: Estimated coherence map using DICS. The map was calculated as the difference between the active and control conditions presented in Figure 6.25. The locations for the simulated activity and their interactions are highlighted by circles of different colours.

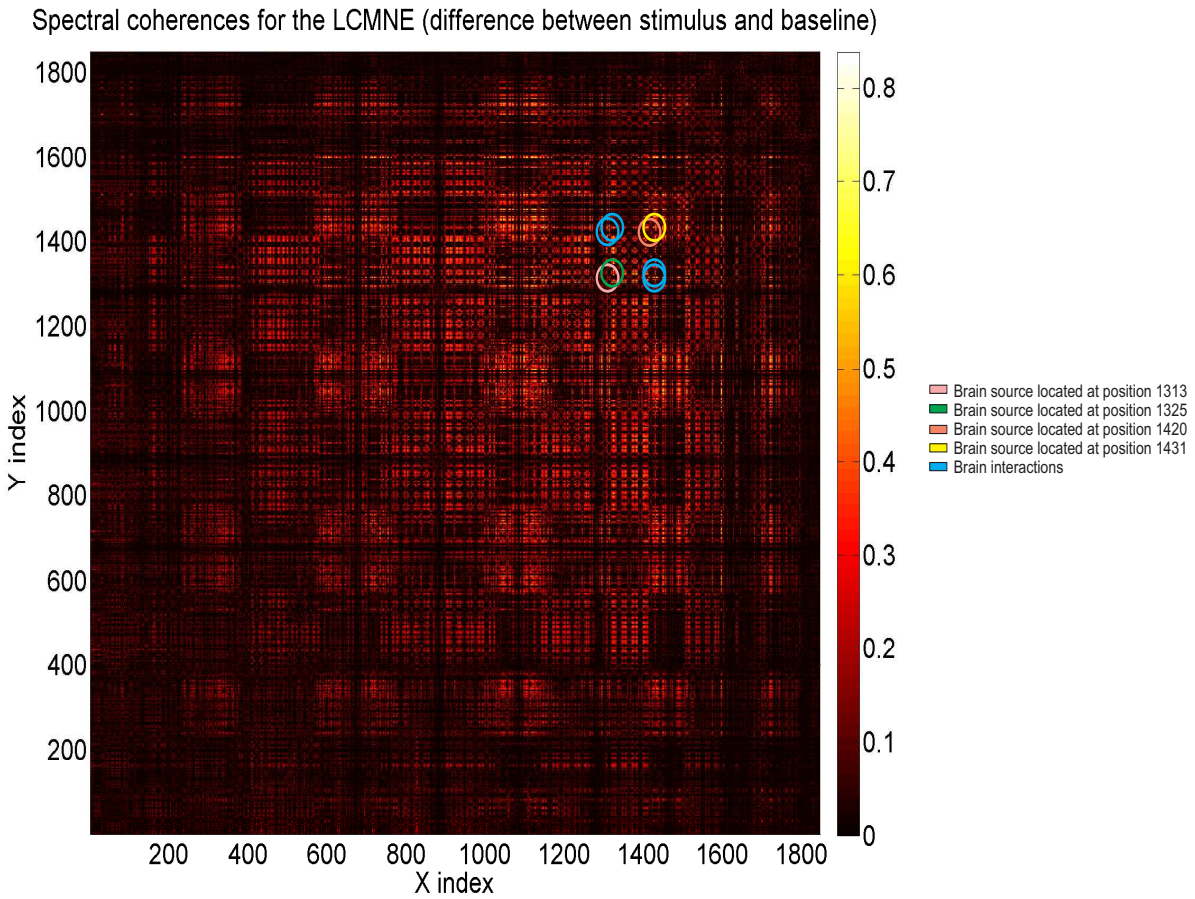

Figure 6.28: Estimated coherence map using the LCMNE with FOCUSS method. The map was calculated as the difference between the active and control conditions presented in Figure 6.26. The locations for the simulated activity and their interactions are highlighted by circles of different colours.

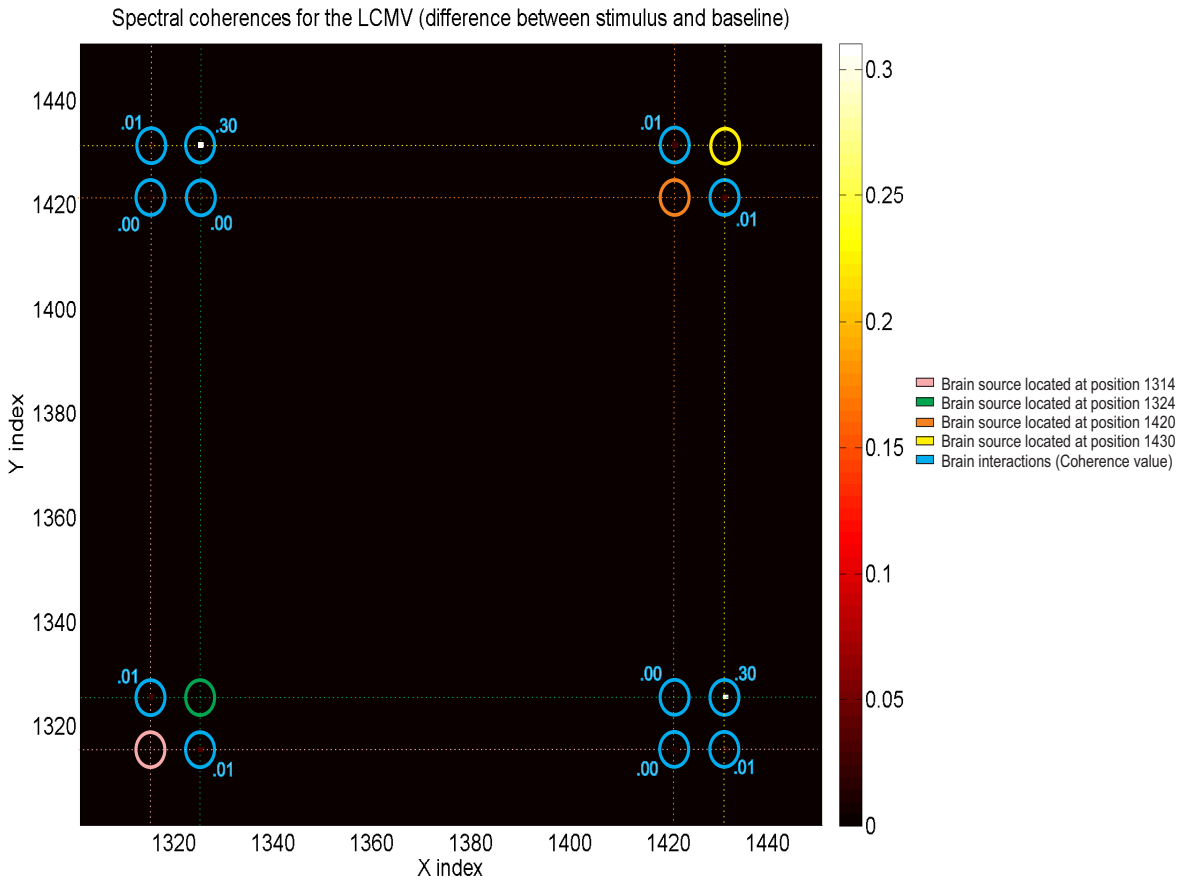

Figure 6.29: Estimated coherence map using DICS for specific elements. This matrix is based on the coherence matrix shown in Figure 6.27, but only shows few elements related with the interactions of locations presented in Figure 6.24, while the rest of locations are omitted. This, in order to have a closer and clear view for the estimated brain interactions.

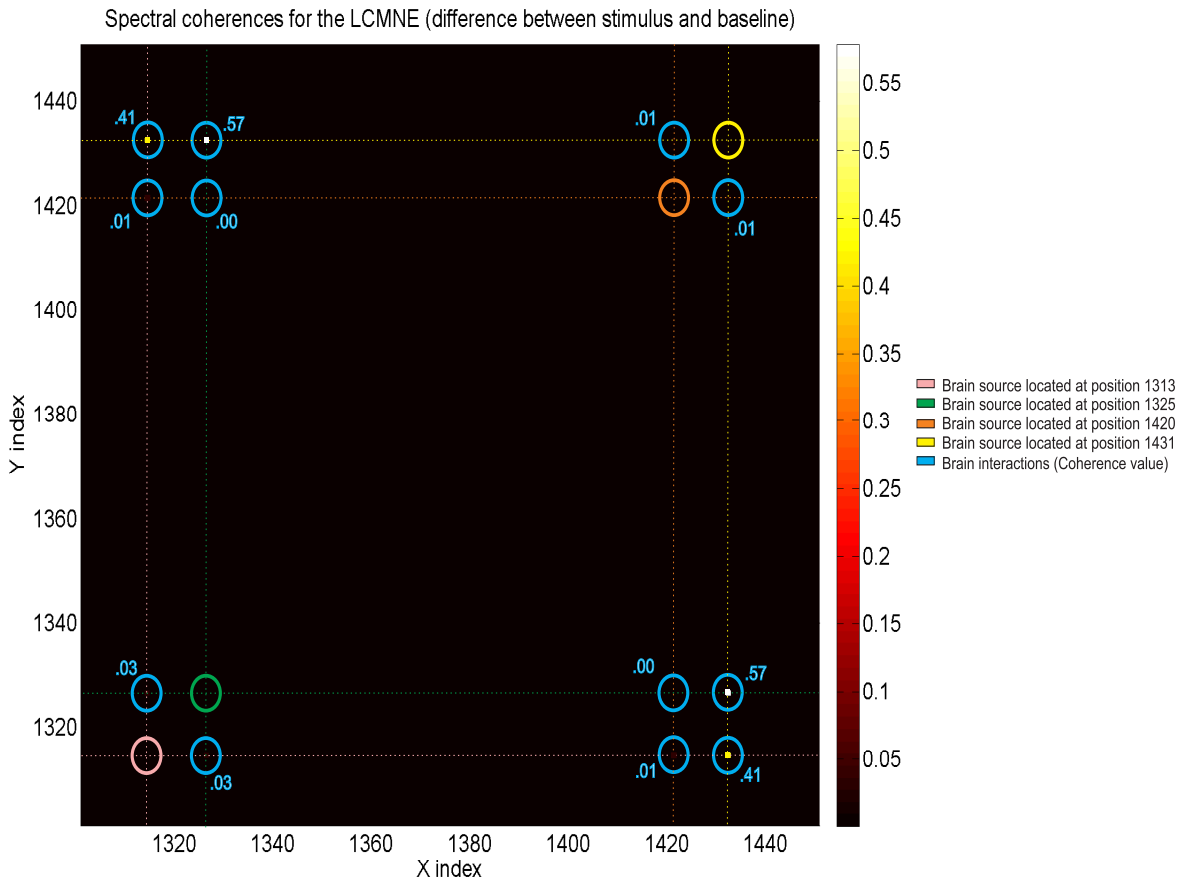

Figure 6.30: Estimated coherence map using the LCMNE with FOCUSS method for specific elements. This matrix is based on the coherence matrix shown in Figure 6.28, but only shows few elements related with the interactions of locations presented in Figure 6.24, while the rest locations are omitted. This, in order to have a closer and clear view for the estimated brain interactions.

Therefore, functional brain interactions can be estimated from the active condition coherence matrices or from the difference between the active and control conditions. However, the use of all the matrices elements increase the finding of false brain connections, since most of their elements have a coherence value higher than 0. This means that all locations used to solve the inverse problem are connected at some degree, even when we know from the simulations that this is not the case. Thus, specific locations need to be selected in order to estimate the functional brain interactions. The most common criteria used is based on the power maps presented in Figure 6.24, selecting the locations with enough estimated power to be considered as brain active regions. However, this is also a problem, as the weighted and distorted output characteristic of the LCMNE spatial filter generates spurious brain active regions.

The coherence matrices obtained from the active condition and from the difference between the active and control conditions can be also used to represent the brain connections as brain images, where one row or column of the matrices is used to represent the functional brain dynamics between one location, known as seed voxel, and the rest of them. Figure 6.31 shows the brain connections between a seed voxel located at position 1430 and the rest of the brain mesh when DICS is used to estimate the brain connections. A different representation for the brain connections can be observed in Figure 6.32, where the brain surface interactions obtained from the same seed voxel are presented.

On the other hand, figures 6.33 and 6.34 present images for the estimated brain connections obtained using the LCMNE with the FOCUSS method, obtained from figures 6.26 and 6.28. The connections are presented for the seed voxel located on the element 1431 of the brain mesh used to solve the inverse problem. Figure 6.33 shows the functional brain connections between the seed voxel and all the elements of the brain mesh used, while Figure 6.34 shows only the brain connections located on the cortex.

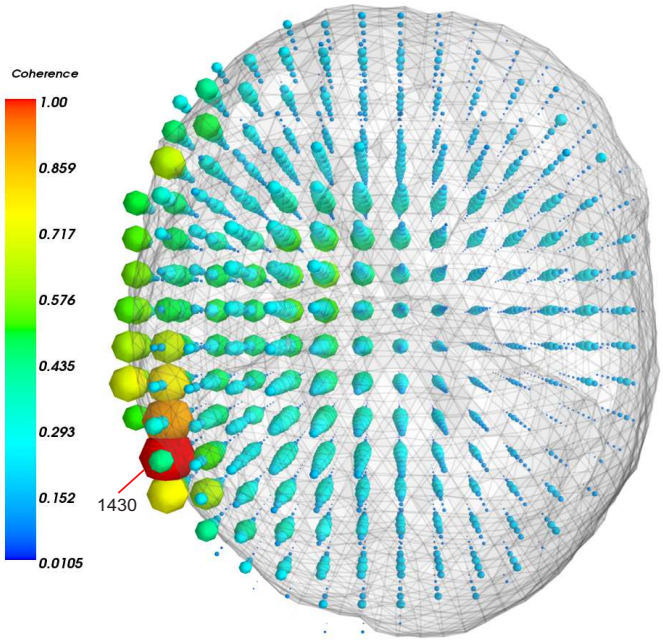

(a)

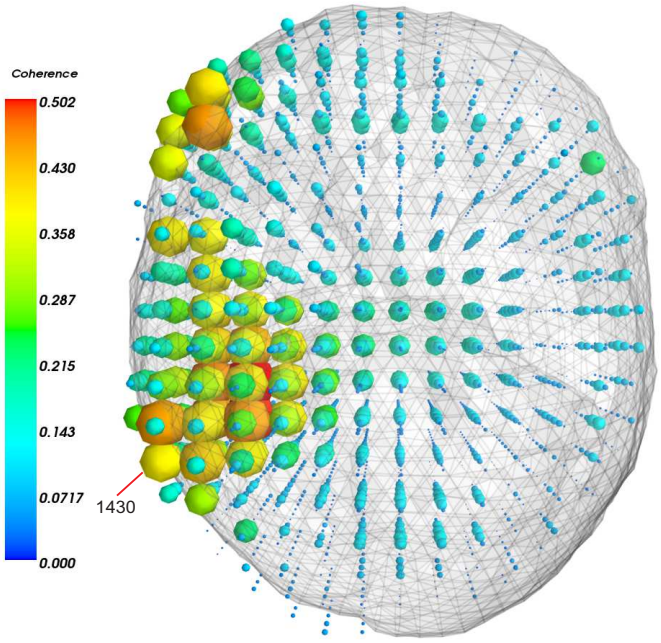

(b)

Figure 6.31: In a) are presented the brain connections obtained from the active condition among the seed voxel and all locations used to solve the inverse problem, while on b) are presented the brain connections obtained as the difference between the active and control conditions. In both cases the brain connections were obtained using DICS. The sizes and colours of the spheres represent the intensity of the connections between the seed voxel and the brain mesh elements.

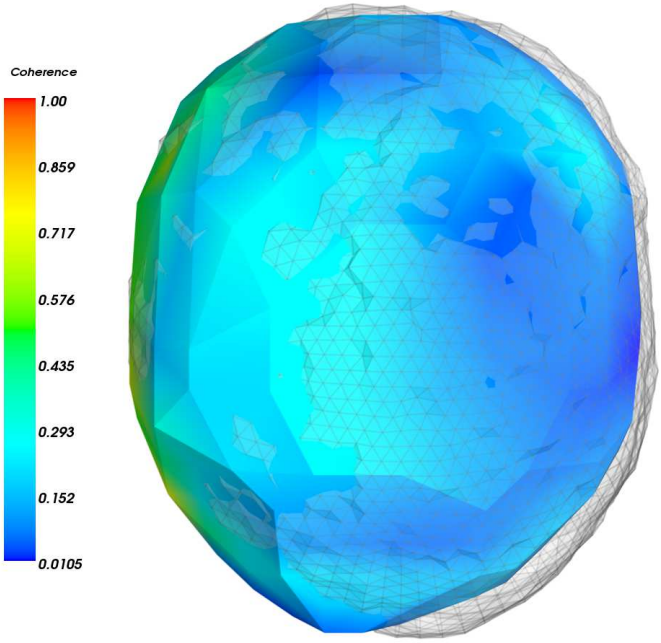

(a)

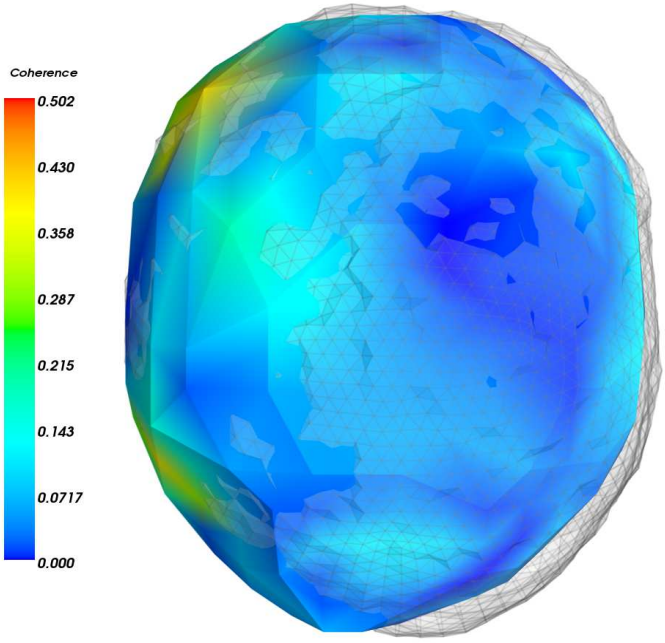

(b)

Figure 6.32: In a) and b) are presented the brain cortical connections obtained from the active and from the difference between the active and control conditions, respectively. Interactions estimated using DICS, where the different colours on the brain surface represent the intensity of the connections between the seed voxel located at position 1430 and the rest of the cortex.

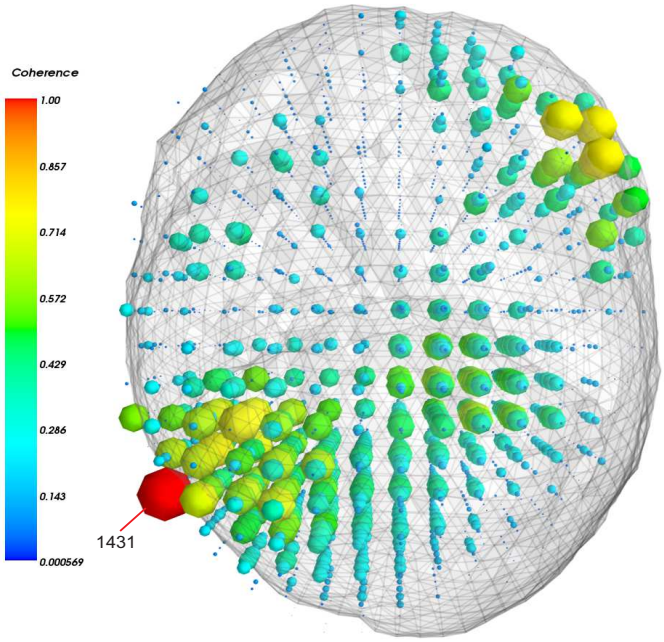

(a)

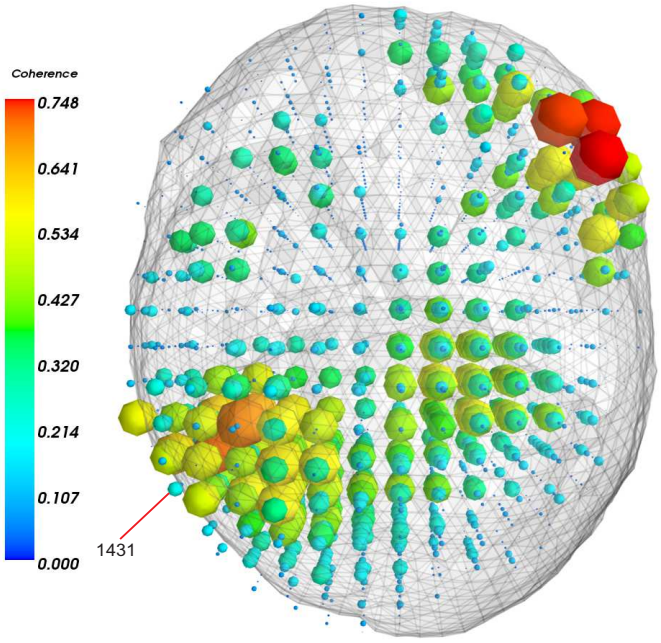

(b)

Figure 6.33: In a) are presented the brain connections obtained from the active condition among the seed voxel and all locations used to solve the inverse problem, while on b) are presented connections obtained as the difference between the active and control conditions. In both cases, connections were obtained using the LCMNE with FOCUSS method. The sizes and colours of the spheres represent the intensity of the connections between the seed voxel and the brain mesh elements.

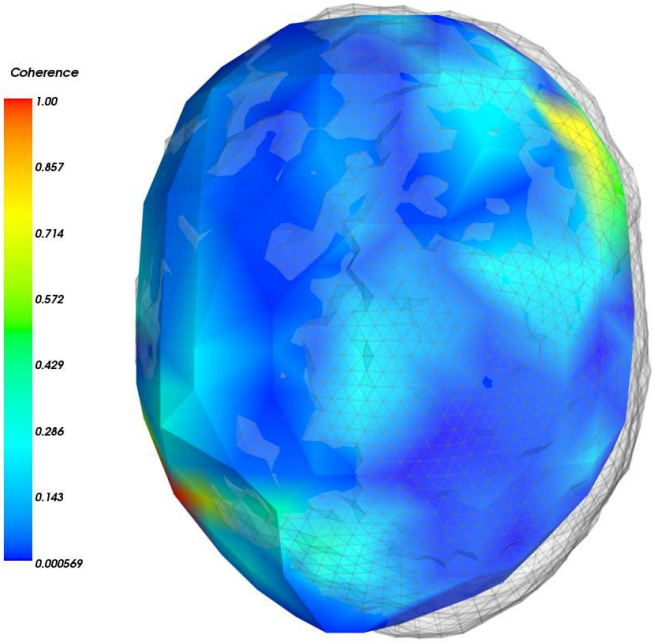

(a)

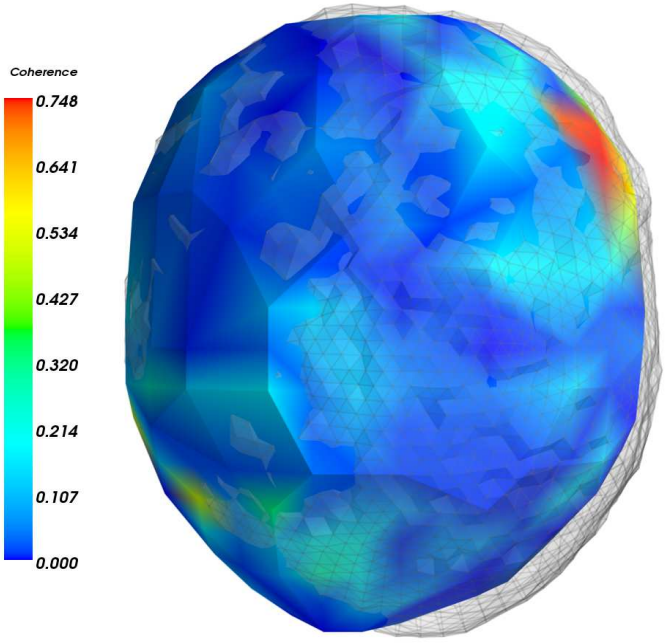

(b)

Figure 6.34: In a) and b) are presented the brain cortical connections obtained from the active and from the difference between the active and control conditions, respectively. Interactions estimated using LCMNE with FOCUSS method, where the different colours on the brain surface represent the intensity of the connections between the seed voxel located at position 1431 and the rest of the cortex.

Correlated and uncorrelated activity with a SNR of 11.

The previous example shows an increment in the finding of spurious connections using DICS and the LCMNE with FOCUSS algorithm for the estimation of functional brain dynamics, compared with the first two presented examples. This increment was due the locations of the simulated activity, which did not match the brain mesh used to solve the inverse problem increasing the distortion of the LCMNE spatial filter. This distortion can increases more if a smaller SNR is used, as is presented in this example using a SNR of 11.

In this new example the locations and the characteristics for the simulated activity are the same as the ones used in the previous scenario. The locations for the simulated brain activity presented in Figure 6.23. However, the estimation of the brain activity localization is different, as can be seen in Figure 6.35, obtained using the LCMV and the MNE spatial filters implemented in the time domain. The figure also shows the estimated locations of the brain mesh with enough power to be considered as active locations near the real locations of the simulated activity. In Table 6.3 are presented the expected coherence values between the selected locations considering the simulated brain activity, where .49 is obtained from $.7^2$.

The estimated coherence matrices for the active and control conditions using DICS and the LCMNE beamformer are not presented, as they are very similar to the ones presented in figures 6.25 and 6.26, where it is impossible to make any assumption about the brain interactions. The LCMNE spatial filter is implemented using a smaller tolerance value for the inverse of the gram matrix compared with previous examples. This, in order to reduce the effects of the external noise without changing the number of iterations for the implementation of the FOCUSS algorithm. In the previous example was used a threshold value of $1e^{-10}$ for the TSVD with a SNR of 22, while in this case the threshold value used is $1e^{-8}$, which gave the results presented on this section. If the tolerance value is not changed, the increment in the number of iterations helps to reduce the effects of the external noise, but some of the simulated brain interactions may be lost because of the increment. This is one of the main problems that the proposed method has.

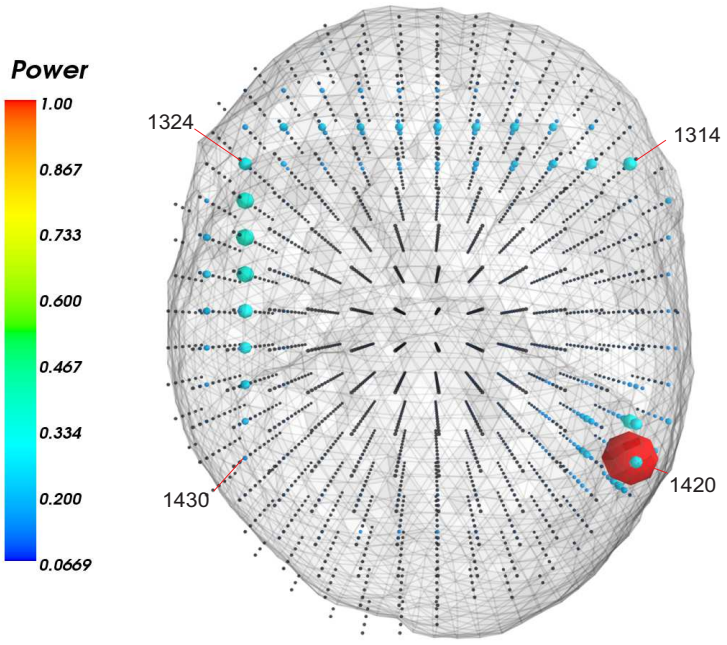

(a)

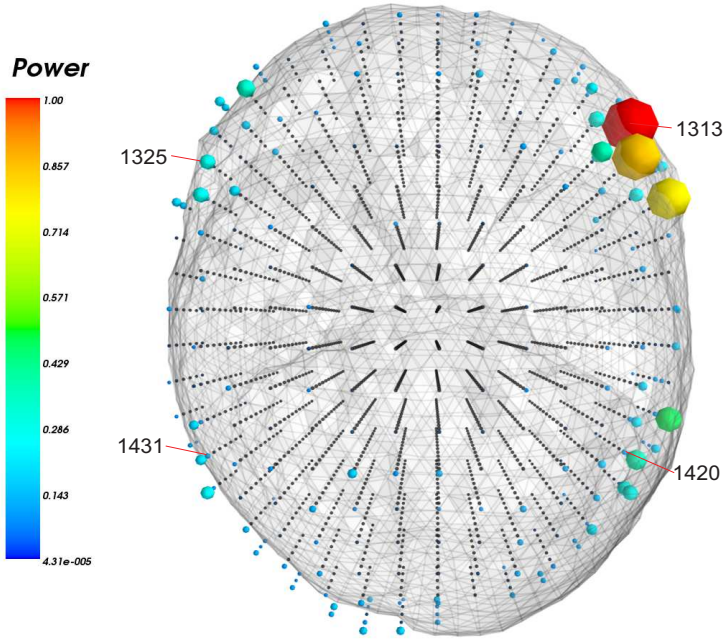

(b)

Figure 6.35: Estimated brain power using the LCMV and MNE in the time domain, with normalized values to have a maximum of one for plotting reasons. On the top is presented the estimated brain activity using the LCMV beamformer, while on the bottom is presented the estimated activity using the MNE spatial filter. It is presented the estimated locations near the simulated activity which will be used as references for the generated brain activity.

The difference between the estimated interactions for the active and control conditions are presented in figures 6.36 and 6.37, for DICS and the LCMNE with FOCUSS methods, respectively. It can be observed on those figures that the amount of information that can be obtained is limited, as there is not clear where the real connections are. Therefore, it is necessary the use of metrics to define locations with enough activity to be considered as active locations. One of the most used metrics is the estimated brain power presented in Figure 6.35. Figures 6.38 and 6.39 present the estimated spectral coherence for those locations only.

Figure 6.38 shows the obtained spectral coherences between elements $1314, 1324, 1420, 1430$ of the brain mesh used to solve the inverse problem using DICS, while in Figure 6.39 are presented the estimated spectral coherences between brain mesh elements $1313, 1325, 1420, 1431$ using the LCMNE with FOCUSS method. In those figures only interactions among the specified locations are presented, while the rest of the elements present coherence values equals to zero in order to highlight better the estimated coherences between the selected locations.

In Table 6.6 are presented the estimated coherence values for locations presented in figures 6.38 and 6.39. It can be observed the decrease of intensity for the estimated connections when compared against tables 6.4 and 6.5. This loss of intensity is due the smaller SNR used for the simulated brain activity. However, even when their intensities are smaller, it can be observed the same behaviour in terms of connectivity among the defined locations.

Brain Mesh(LCMNE/DICS)	1325/1324	1431/1430	1420/1420	1313/1314
1325/1324	0.0	.15/.25	.00/.00	.00/.16
1431/1430	.15/.25	0.0	.00/.02	0.21/.00
1420/1420	.00/.00	.00/.02	0.0	.01/.01
1313/1314	.00/.16	.21/.00	.01/.01	0.0

Table 6.6: Estimated coherence values obtained as the difference between conditions. The matrix shows the coherence values obtained from the coherence matrices presented in Figures 6.38 and 6.39, for the locations presented in Figure 6.35.

Brain images corresponding to the estimated brain dynamics for this example are presented in Figures 6.40, 6.41, 6.42 and 6.43, for brain seed voxels located on brain mesh elements 1430 and 1431 for DICS and the LCMNE with FOCUSS method, respectively. In Figures 6.40 and 6.42 are presented the brain dynamics obtained in all the brain mesh elements used, while in figures 6.41 and 6.43 are presented the brain dynamics found on the cortex.

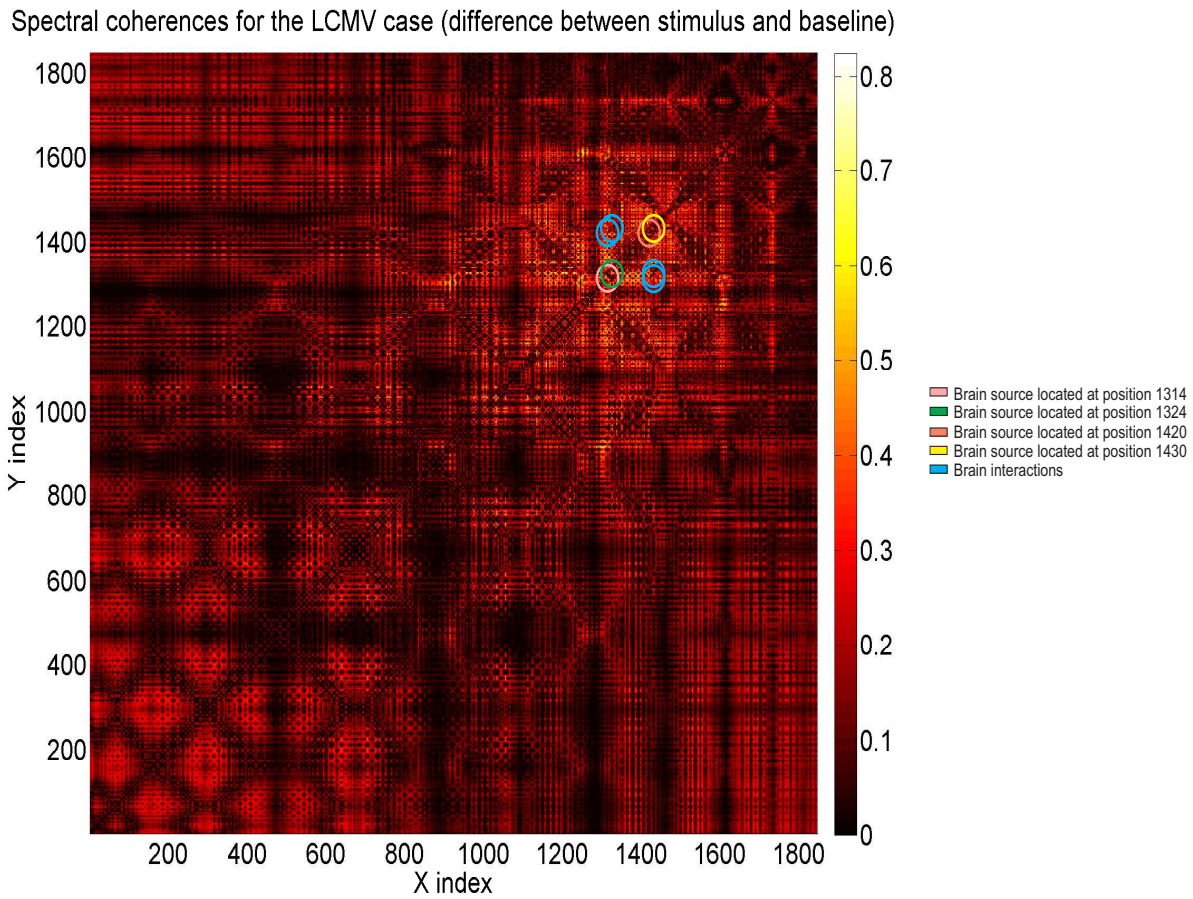

Figure 6.36: Estimated coherence map using DICS. The map was calculated as the difference between the active and control conditions coherence values. The locations for the simulated activity and their interactions are highlighted by circles of different colours.

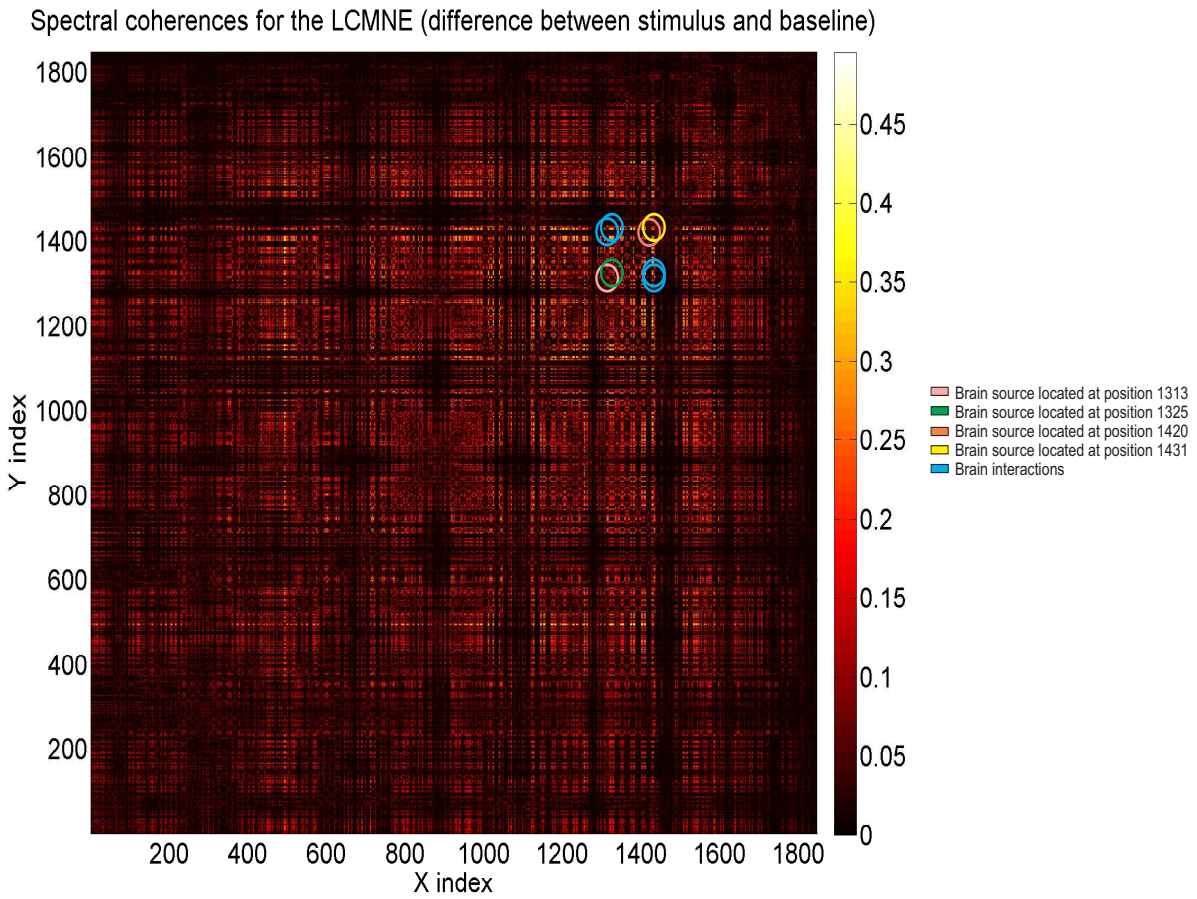

Figure 6.37: Estimated coherence map using the LCMNE with FOCUSS method. The map was calculated as the difference between the active and control conditions coherence values. The locations for the simulated activity and their interactions are highlighted by circles of different colours.

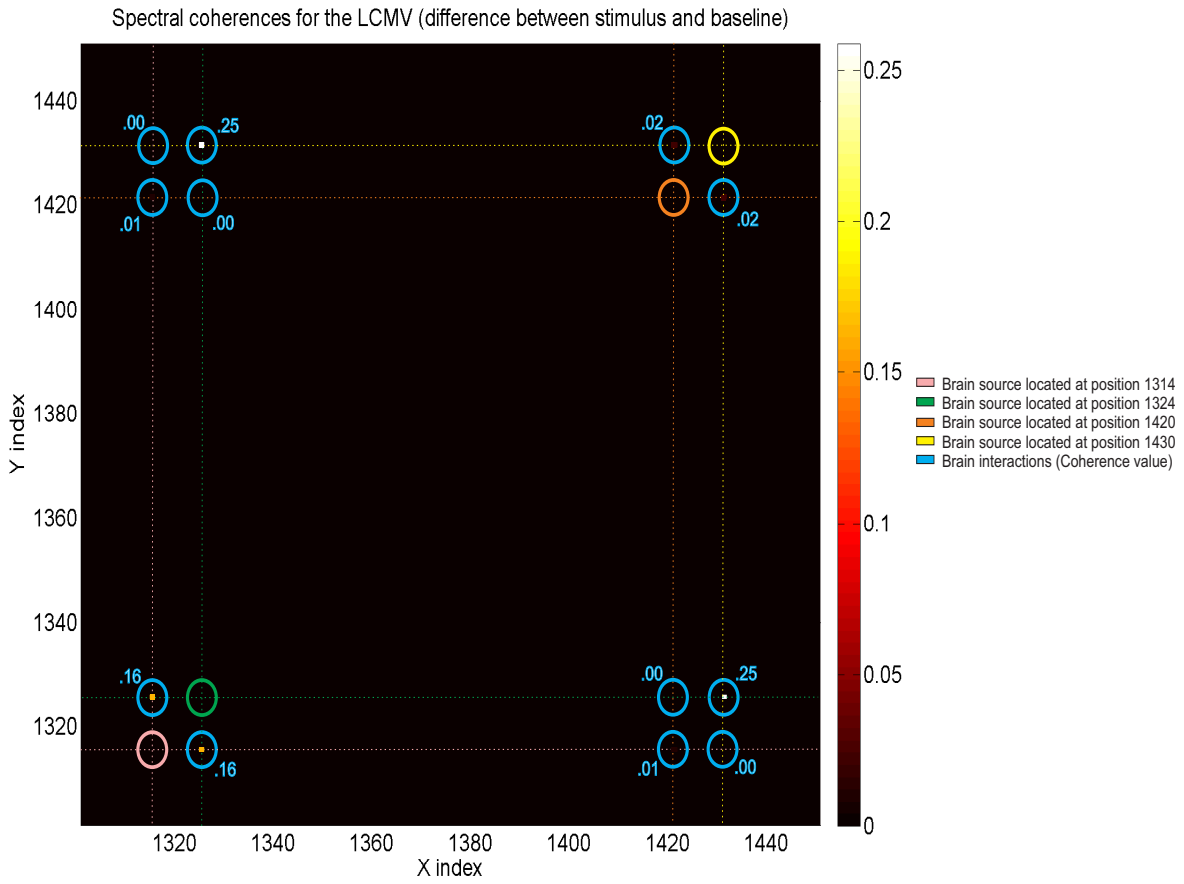

Figure 6.38: Estimated coherence map using DICS for few elements. This matrix is based on the coherence matrix shown in Figure 6.36. The locations for the simulated activity and their interactions are highlighted by circles of different colours, while the rest of the interactions are omitted by representing them with zero coherence values.

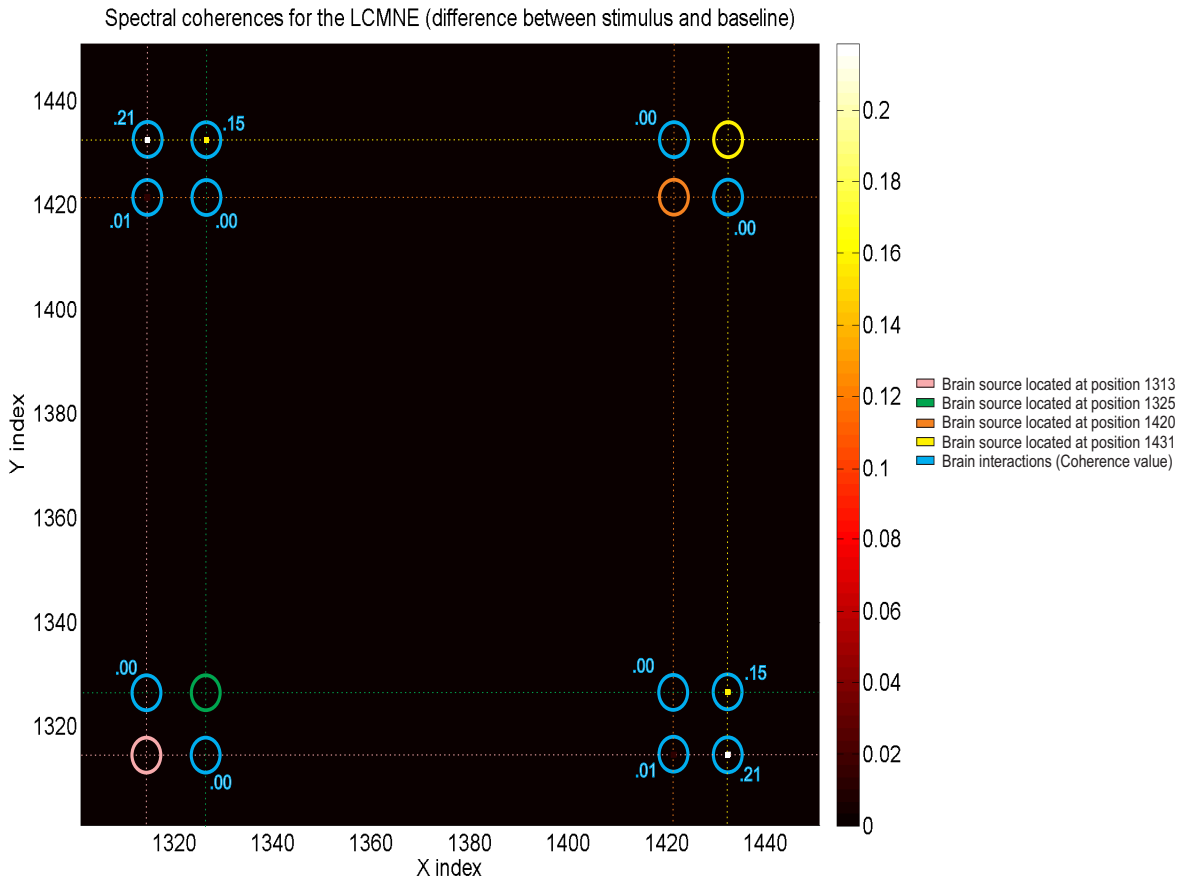

Figure 6.39: Estimated coherence map using the the LCMNE with FOCUSS method for few elements. This matrix is based on the coherence matrix shown in Figure 6.37, showing only few elements. The locations for the simulated activity and their interactions are highlighted by circles of different colours, while the rest of the interactions are omitted by representing them with zero coherence values.

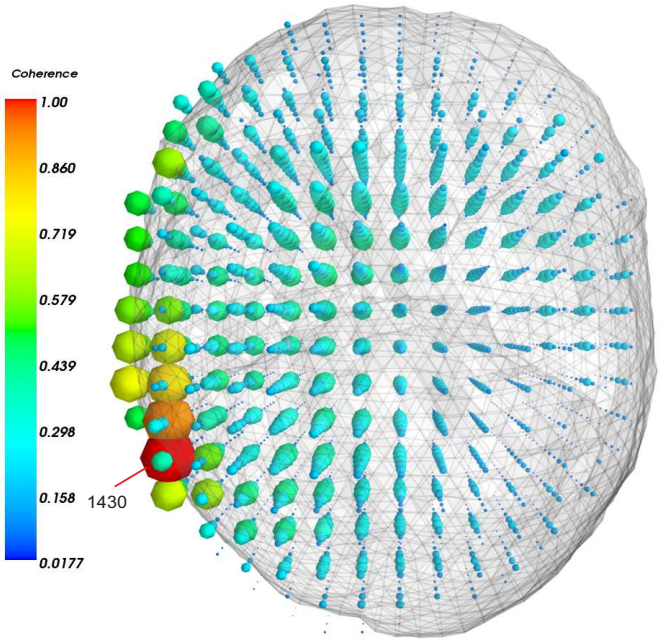

(a)

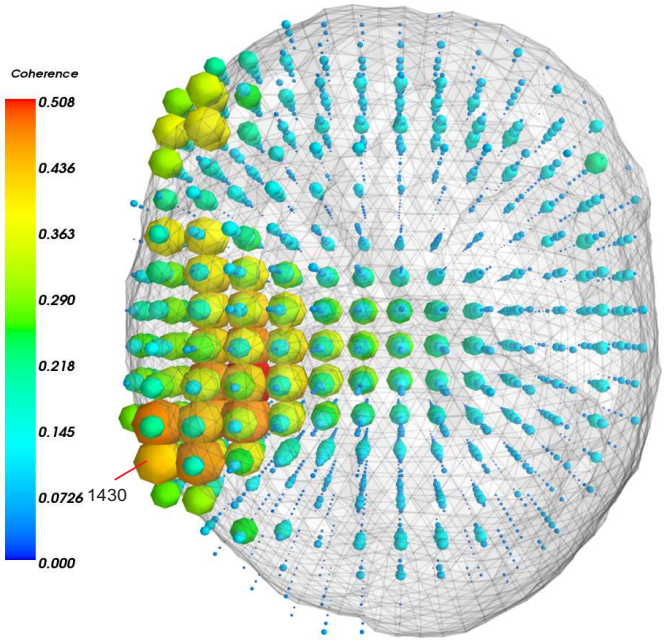

(b)

Figure 6.40: In a) are presented the brain connections obtained from the active condition among the seed voxel and all locations used to solve the inverse problem, while on b) are presented the brain connections obtained as the difference between the active and control conditions. In both cases the brain connections were obtained using DICS. The sizes and colours of the spheres represent the intensity of the connections between the seed voxel and the brain mesh elements.

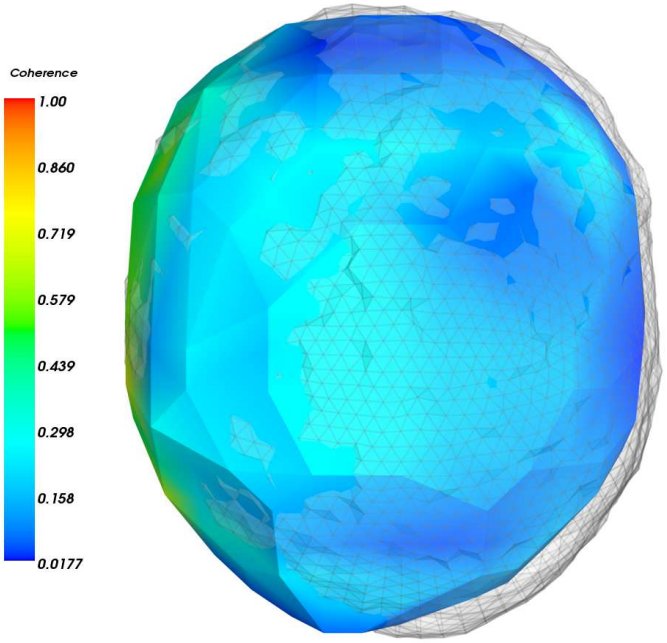

(a)

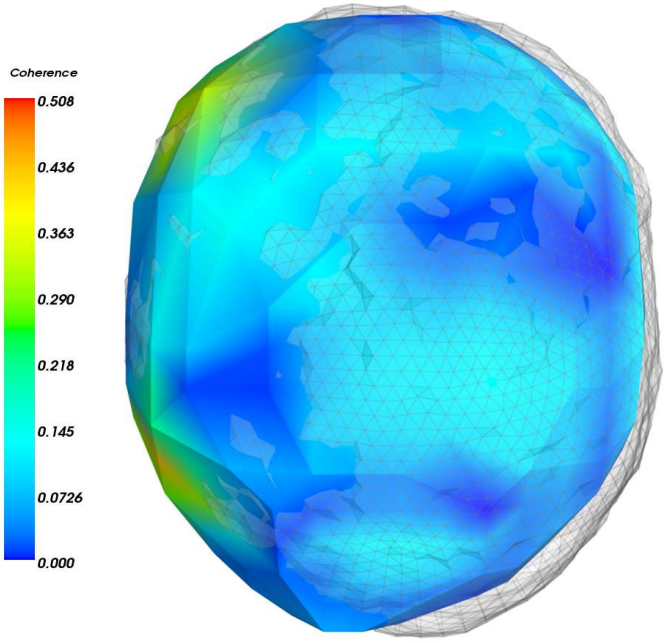

(b)

Figure 6.41: In a) and b) are presented the brain cortical connections obtained from the active and from the difference between the active and control conditions, respectively. Interactions were estimated using DICS, where the different colours on the brain surface represent the intensity of the connections between the seed voxel located at position 1430 and the rest of the cortex.

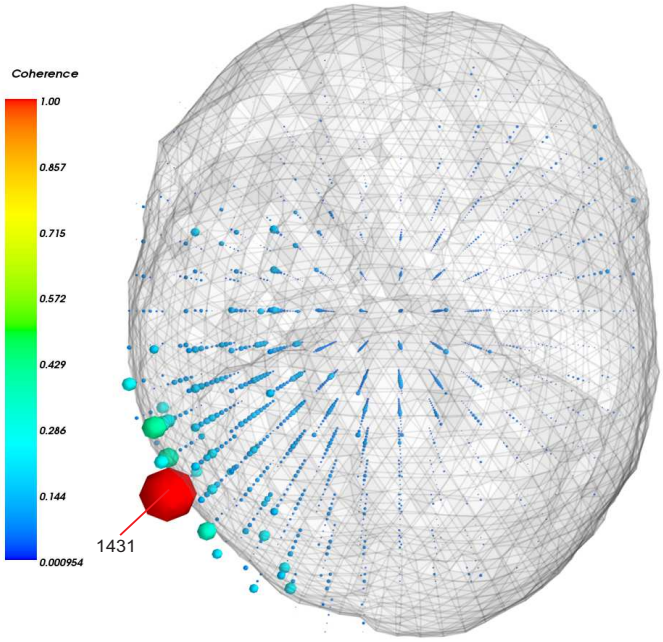

(a)

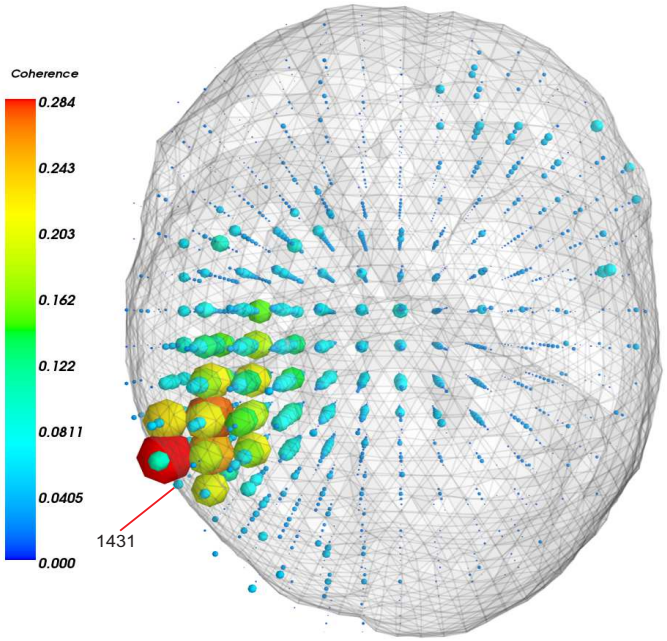

(b)

Figure 6.42: In a) are presented brain connections obtained from the active condition among the seed voxel and all brain mesh locations, while on b) are presented the brain connections obtained as the difference between the active and control conditions. In both cases the brain connections were obtained using the LCMNE with FOCUSS method. The sizes and colours of the spheres represent the intensity of the connections between the seed voxel and the brain mesh elements.

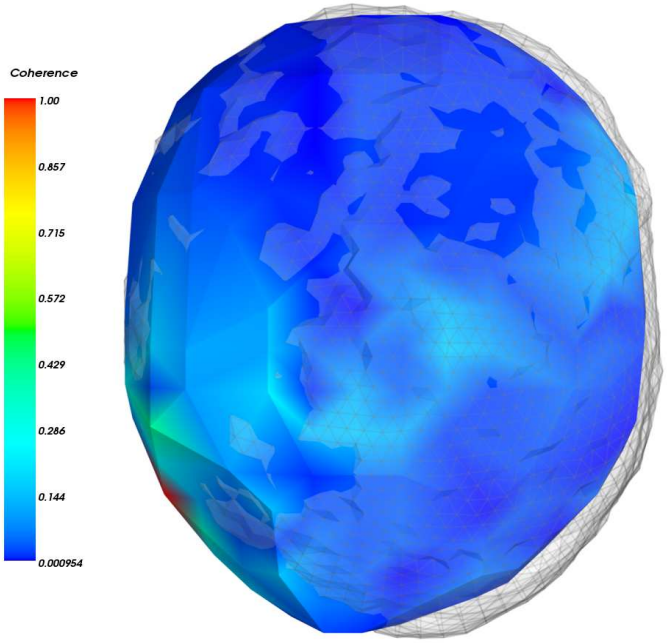

(a)

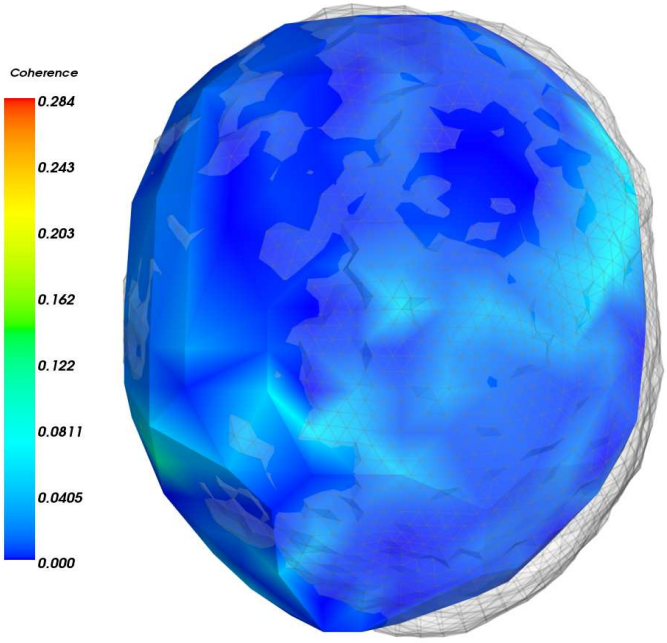

(b)

Figure 6.43: In a) and b) are presented the brain cortical connections obtained from the active and from the difference between the active and control conditions, respectively. Interactions were estimated using LCMNE with FOCUSS method, where different colours on the cortex represent the intensity of the connections between the seed voxel located at position 1431 and the rest of the cortex.

6.2.3 Estimation of simulated brain interactions from correlated and uncorrelated non cortical brain activity.

In the previous presented estimations of functional brain dynamics, the LCMNE spatial filter in combination with FOCUSS and DICS were implemented with simulated brain activity generated on the brain surface. The constraint of cortical simulated activity has been used because of the LCMNE spatial filter limitation, which gives a weighted estimation, or solution, to interactions on brain mesh locations near the sensors used to measure the brain activity, in comparison with deeper locations. The effects of non cortical simulated brain activity, correlated and uncorrelated, are presented in this subsection. Thus, the brain activity is generated in the same way as in the previous examples, but are not located on the cortex.

Using a brain mesh with 10 mm distance between its elements.

The brain activity was simulated on locations that match the brain mesh used to solve the inverse problem, specifically on locations 329, 374, 408, and 451, as is presented in Figure 6.44. The brain activity was simulated as AR processes of order 9, while the external noise was simulated as an uncorrelated Gaussian process, as in the previous examples. The SNR for this simulation is 22, to focus the results on the weighted solution characteristic of the LCMNE spatial filter, rather than on the distortion effect. The correlation coefficients used for the simulation of the brain activity are presented in Table 6.7 in a matrix form for locations where the activity were generated.

Brain source(Location)	374	451	329	408
374	1	0.7	0.0	0.0
451	0.7	1	0.0	0.7
329	0.0	0.0	1	0.0
408	0.0	0.7	0.0	1

Table 6.7: Correlation matrix for the simulated data. The matrix shows the correlation coefficients between the simulated brain activity, where their locations can be observed in Figure 6.44. The positions of the brain sources match the brain mesh used to solve the inverse problem.

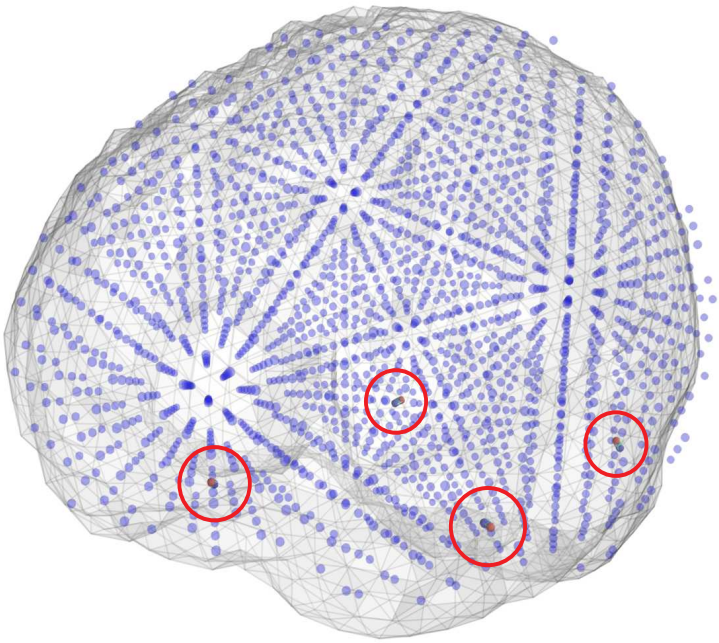

(a)

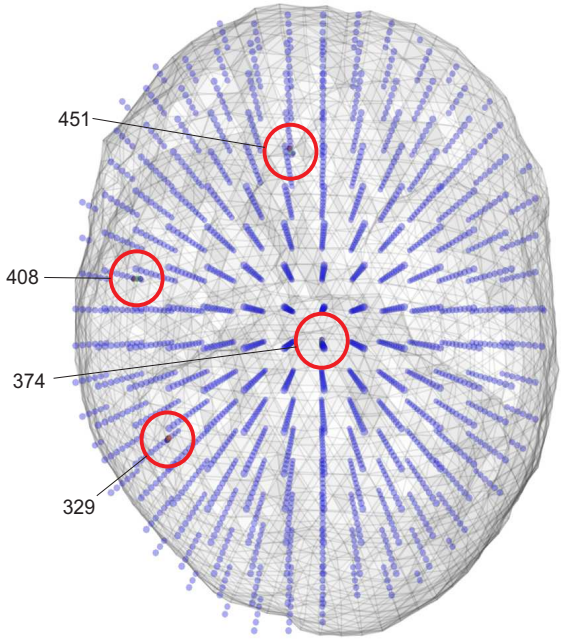

(b)

Figure 6.44: Locations for the simulated activity and the estimated brain power using the LCMV and MNE in the time domain, with normalized values to have a maximum value of one for plotting reasons. On a) and b) are presented the locations for the simulated activity on two different perspectives. The locations are highlighted by red circles and by labels related with the brain mesh elements where the activity was located.

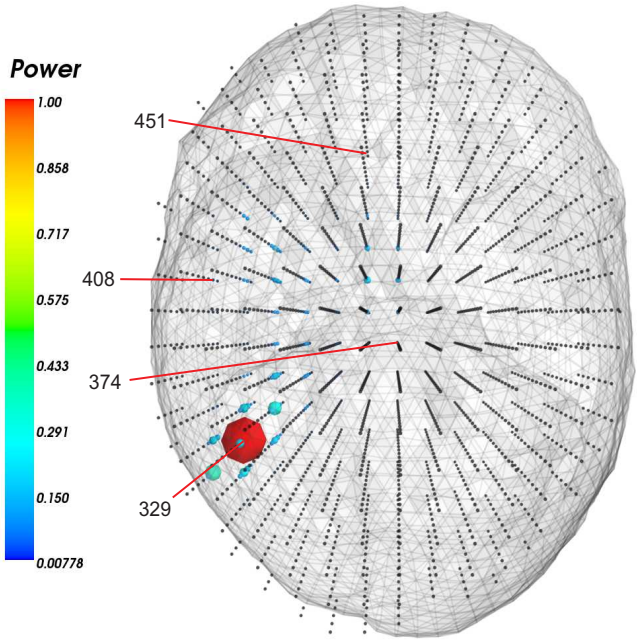

(a)

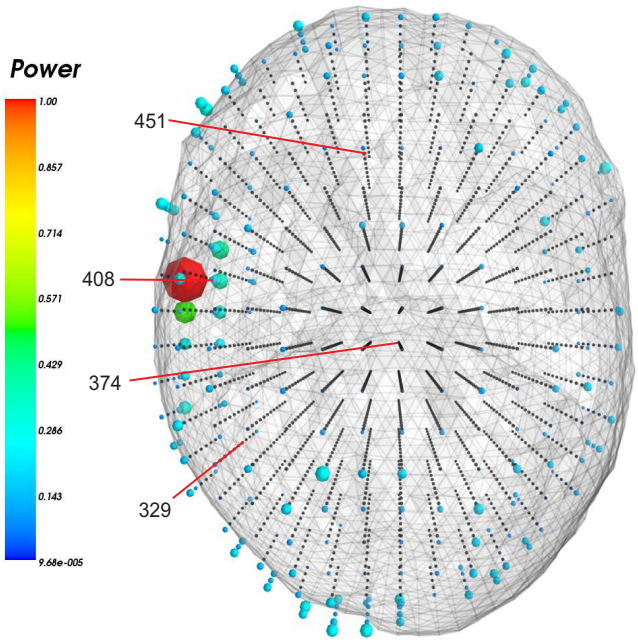

(b)

Figure 6.45: Locations for the estimated simulated brain power using the LCMV and MNE in the time domain, with normalized values to have a maximum value of one for plotting reasons. On a) are presented the estimated brain activity using the LCMV beamformer, while on b) the estimated power using the MNE spatial filter. In the figure are shown the brain mesh locations used to simulated the brain activity.

The coherence matrices obtained using DICS and the LCMNE with FOCUSS method from the simulated activity are presented in figures 6.46 and 6.47, while the difference between conditions matrices are presented in figures 6.50 and 6.51. In the DICS estimations can be observed that there is not too much difference from coherence matrices obtained in the previous examples. However, in the LCMNE with FOCUSS estimations the patterns have some changes, because of the LCMNE weighed solution. The obtained coherence values for the active conditions are presented in Table 6.8, while in Table 6.9 are presented the coherence values for the difference between the conditions, for locations where the activity was simulated.

Brain source(LCMNE/DICS)	374	451	329	408
374	1	.20/.63	.07/.00	.61/.00
451	.20/.63	1	.00/.00	.22/.00
329	.07/.00	.00/.00	1	.17/.00
408	.61/.00	.22/.00	.17/.00	1

Table 6.8: Estimated coherence values for the non cortical simulated data. The matrix shows the estimated coherence values between the simulated activity for the active condition using DICS and the proposed method. The locations for the simulated activity can be observed in Figure 6.44.

Brain source(LCMNE/DICS)	374	451	329	408
374	0.0	.02/.26	.05/.56	.07/.36
451	.02/.26	0.0	.00/.14	.02/.19
329	.05/.56	.00/.14	0.0	.06/.59
408	.07/.36	.02/.19	.06/.59	0.0

Table 6.9: Estimated coherence values for non cortical simulated data. The matrix shows the coherence values between the non cortical simulated brain activity obtained as the difference between the active and control conditions using DICS and the proposed method. The brain sources locations can be observed in Figure 6.44.

The brain connections are also presented as brain images for a seed voxel located on the brain mesh element 451, as presented in figures 6.52, 6.53, 6.54 and 6.55 for DICS and for the LCMNE with FOCUSS methods. It can be observed on the figures that the estimated brain dynamics are better represented when are estimated using DICS, as it was expected because of the weighted output characteristic of the LCMNE spatial filter.

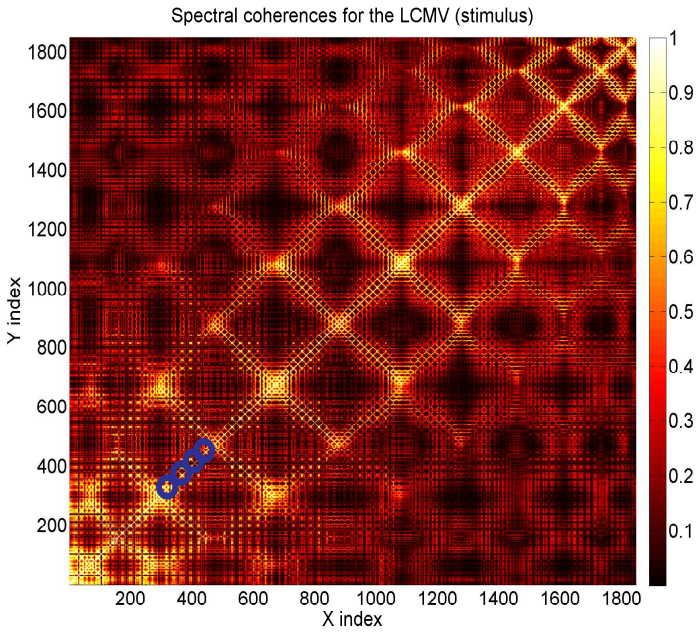

(a)

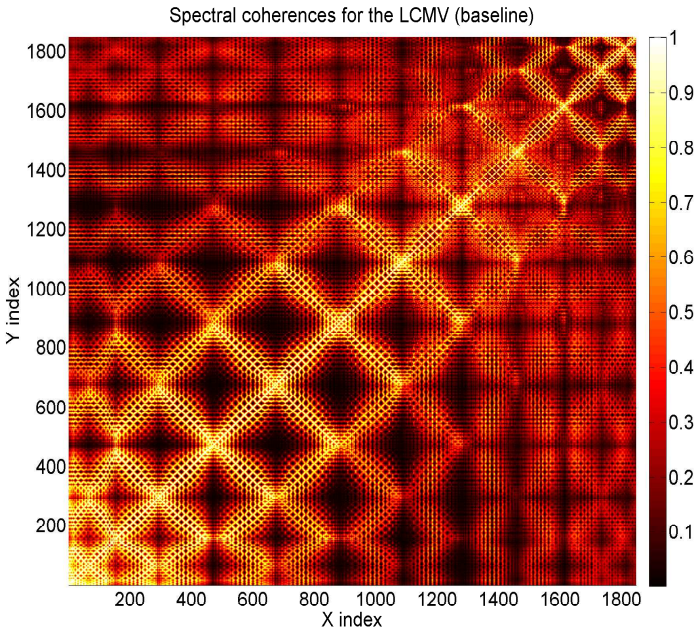

(b)

Figure 6.46: Estimated active and control conditions coherence matrices for the simulated activity estimated using DICS. On the top is show the coherence matrix for the active condition, while on the bottom is presented the estimated matrix for the control condition. The locations for the simulated activity are highlights by blue circles.

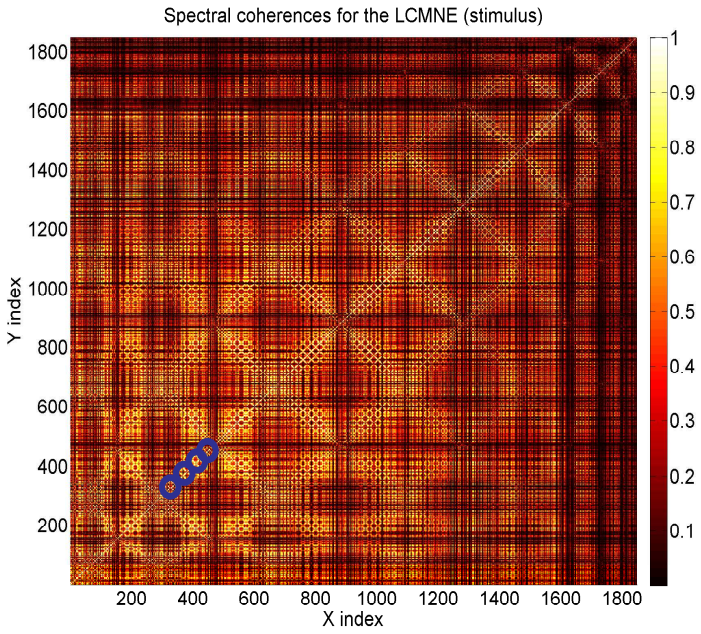

(a)

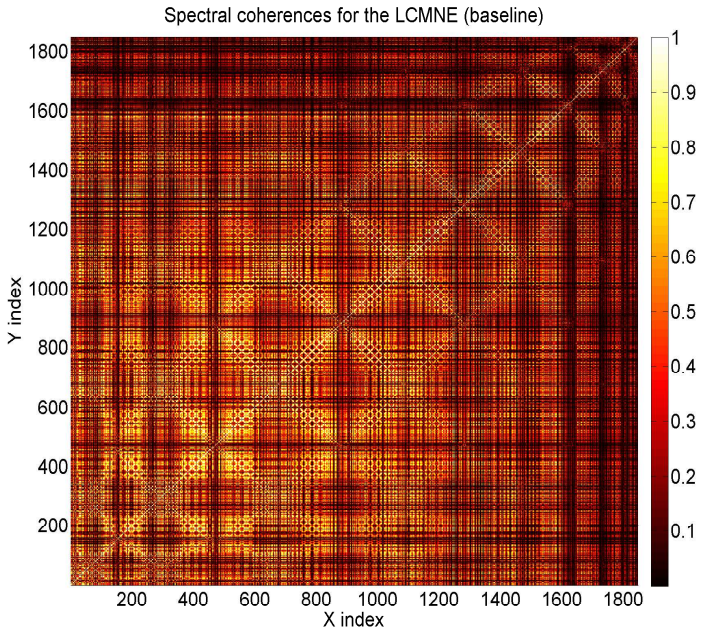

(b)

Figure 6.47: Estimated active and control conditions coherence matrices for the simulated activity estimated using the LCMNE with FOCUSS method. On the top is show the coherence matrix for the active condition, while on the bottom is presented the estimated matrix for the control condition. The locations for the simulated activity are highlights by blue circles.

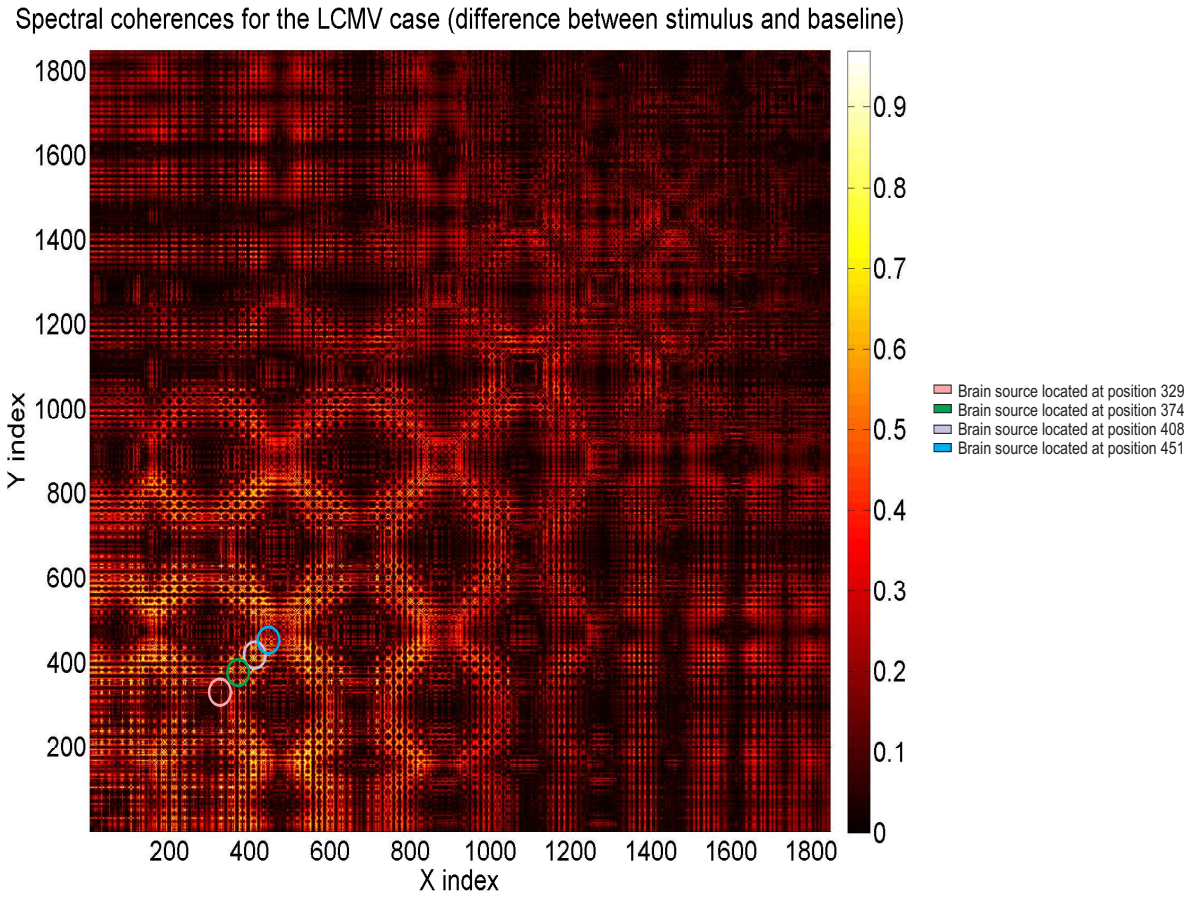

Figure 6.48: Estimated coherence map using DICS for non cortical brain activity. Calculated as the difference between the active and control conditions presented in Figure 6.46. The locations for the simulated activity are highlighted by circles of different colours.

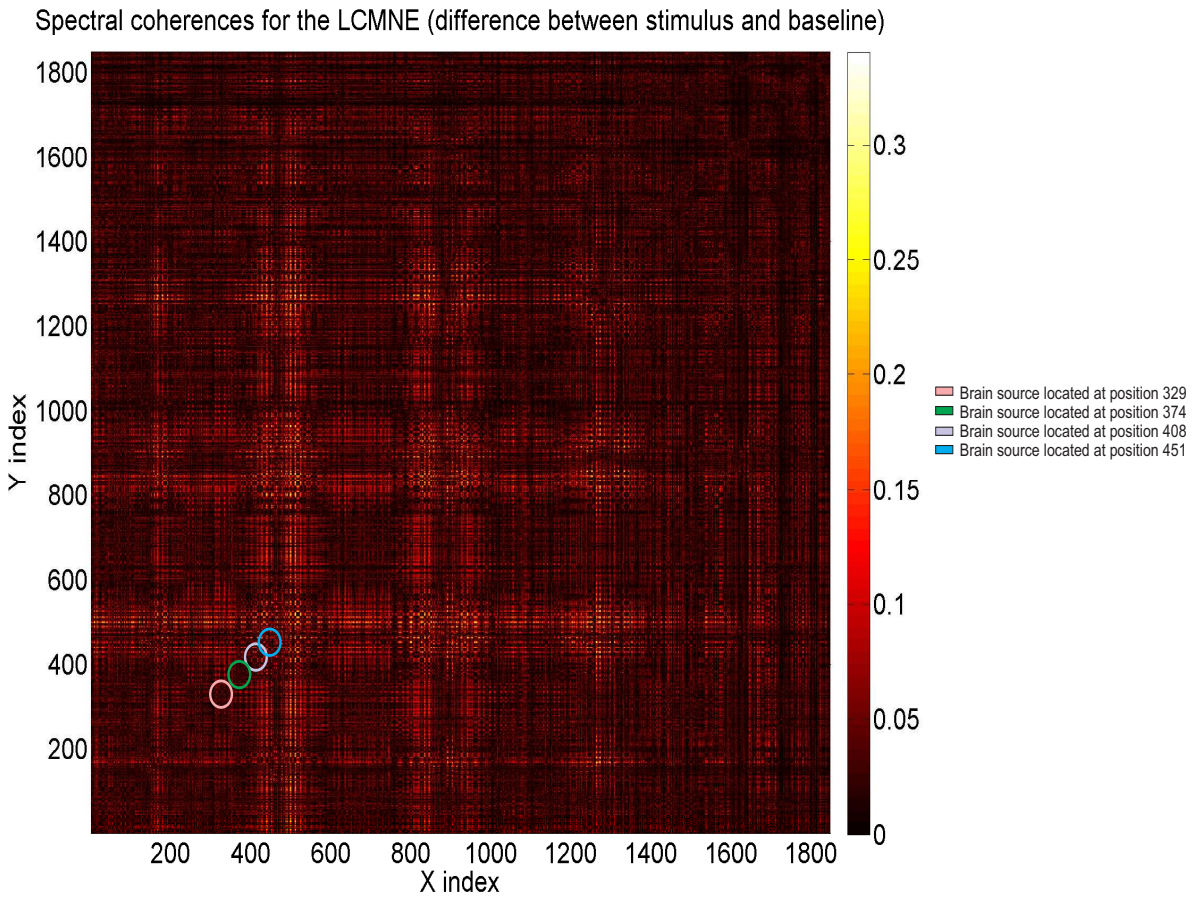

Figure 6.49: Estimated coherence map using the LCMNE with FOCUSS approach for non cortical brain activity. Calculated as the difference between the active and control conditions presented in Figure 6.47. The locations for the simulated activity are highlighted by circles of different colours.

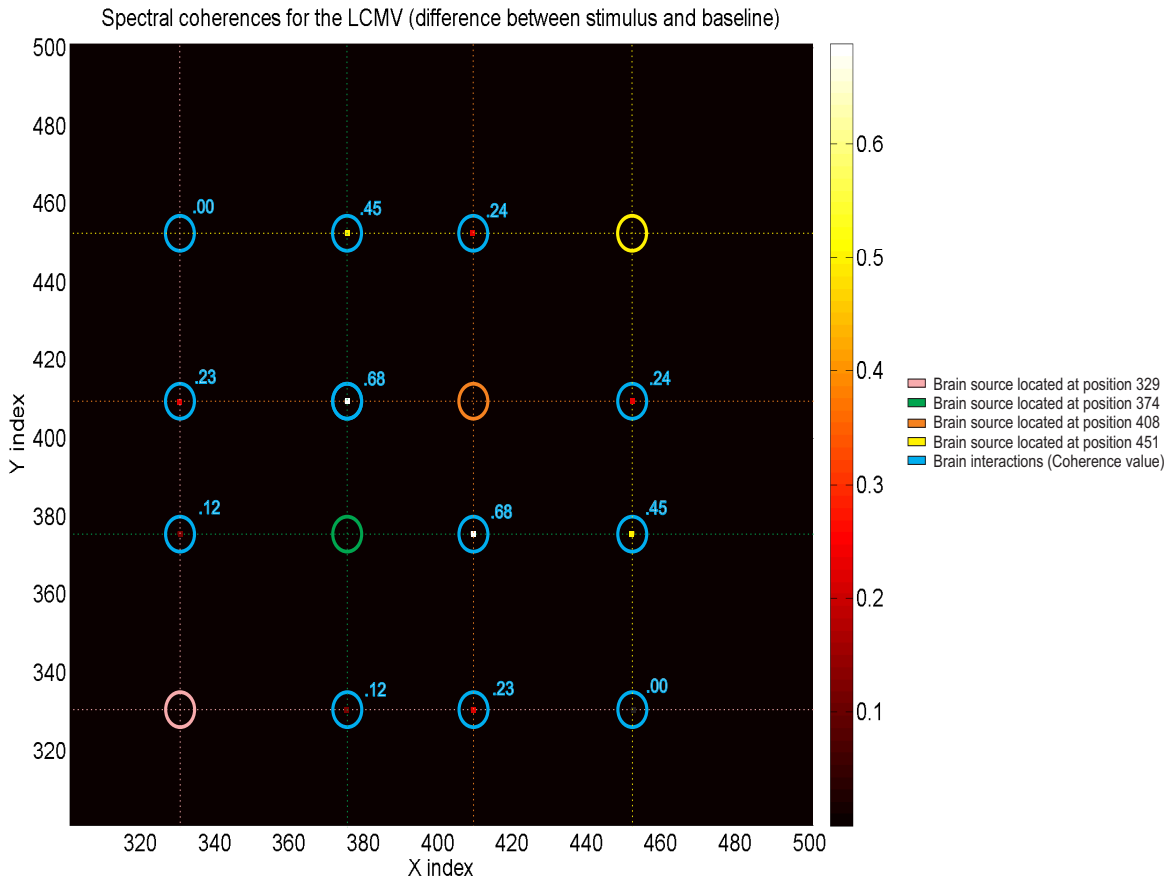

Figure 6.50: Estimated coherence map using DICS for specific non cortical brain locations, selected accordingly to Figure 6.44. The coherence map was calculated as the difference between the active and control conditions presented in Figure 6.46. The locations for the simulated activity are highlighted by circles, while the rest of locations are omitted.

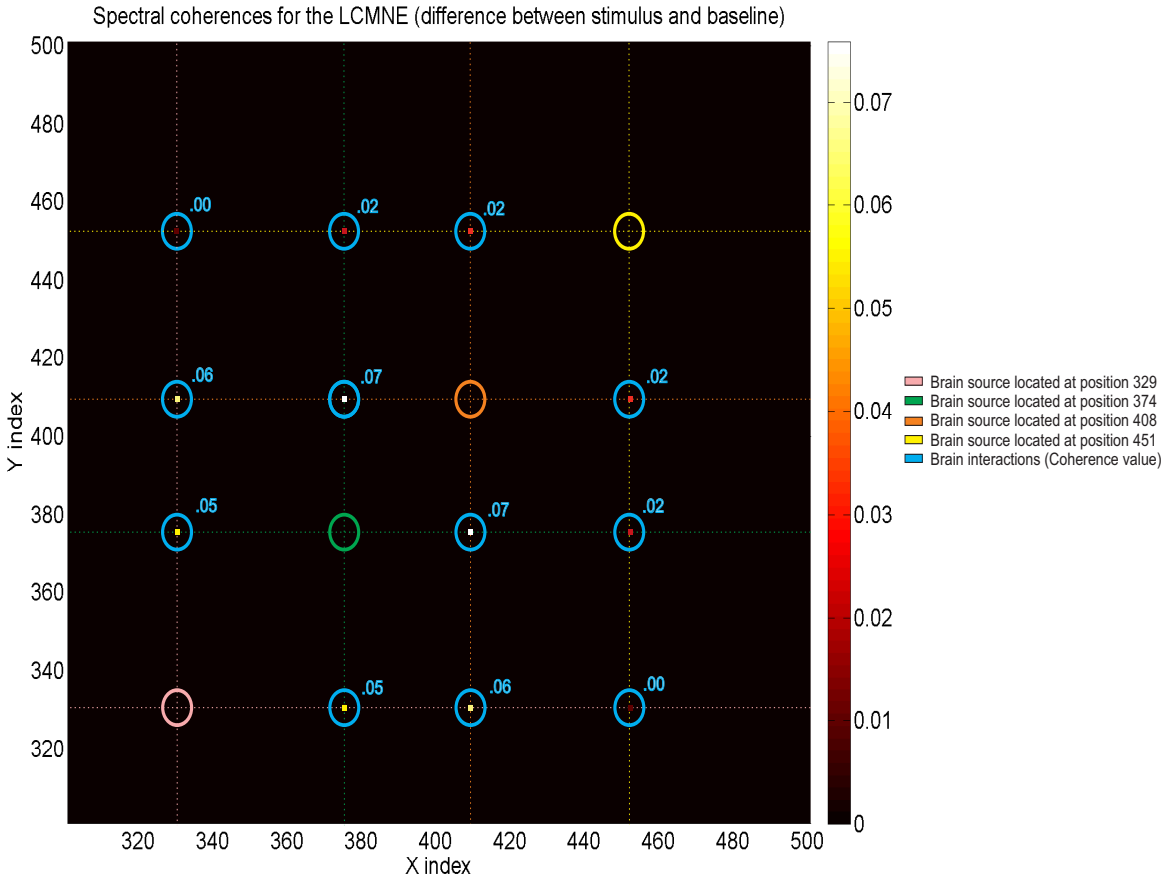

Figure 6.51: Estimated coherence map using the LCMNE with FOCUSS approach for specific non cortical brain locations, selected accordingly to Figure 6.44. The coherence map was calculated as the difference between the active and control conditions presented in Figure 6.47. The locations for the simulated activity are highlighted by circles, while the rest of locations are omitted.

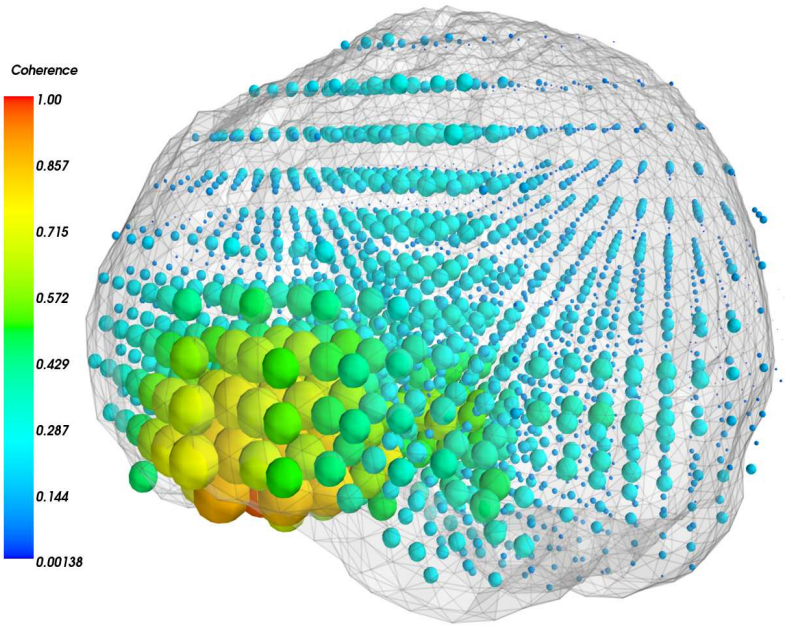

(a)

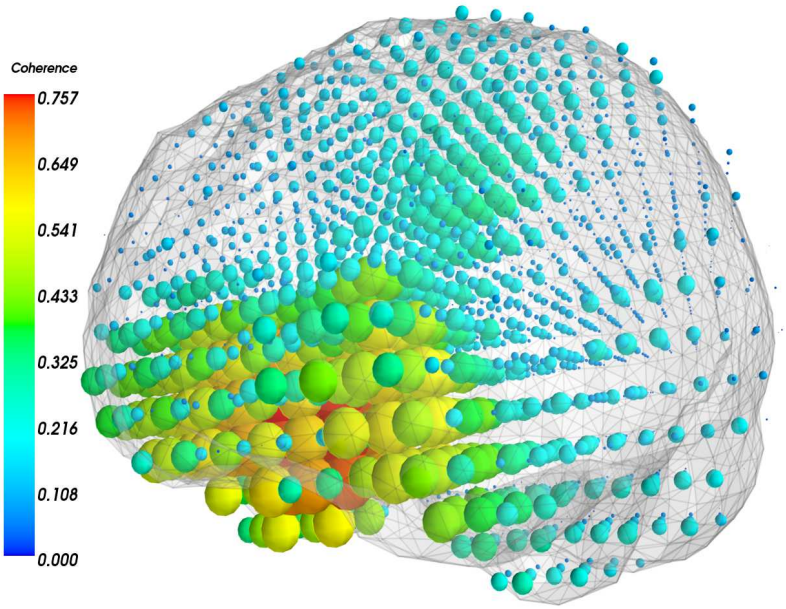

(b)

Figure 6.52: Estimated brain coherence using a seed voxel located at position 451. The brain dynamics are presented among all the points used to look for the brain activity and the seed voxel. In a) can be observed the brain dynamics for the active condition, while on b) are presented the brain interactions for the difference between the active and control conditions, using DICS.

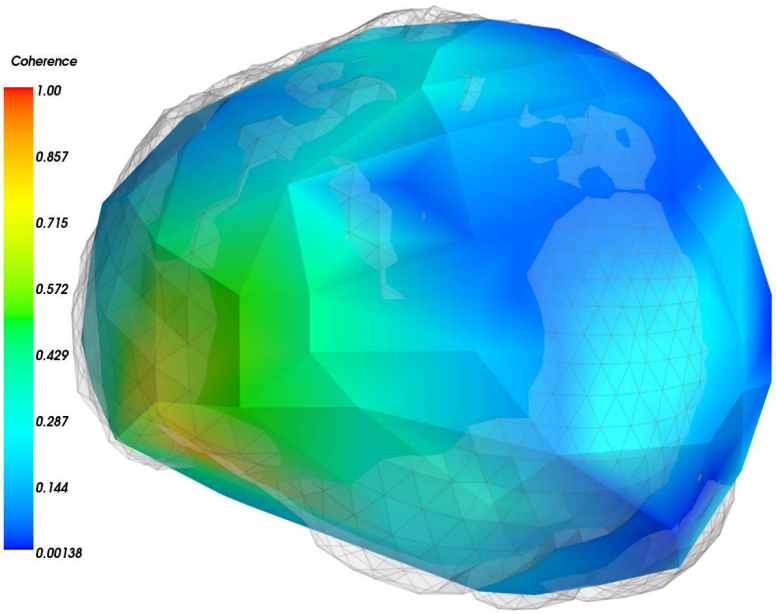

(a)

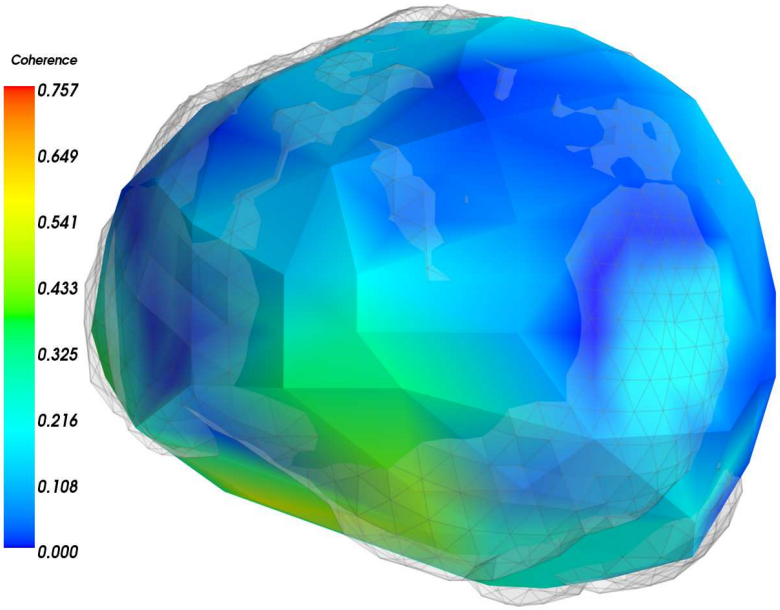

(b)

Figure 6.53: Estimated brain coherence using a seed voxel located at position 451. The brain dynamics are presented among the brain mesh elements located on the cortex. In a) can be observed the cortical brain dynamics obtained using DICS, while on b) are presented the estimated cortical brain dynamics using DICS for the difference between the active and control conditions.

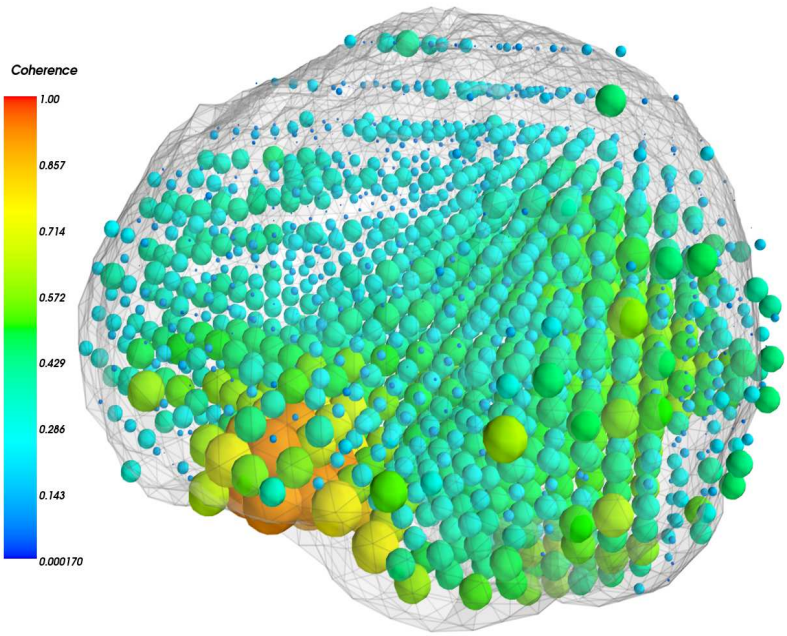

(a)

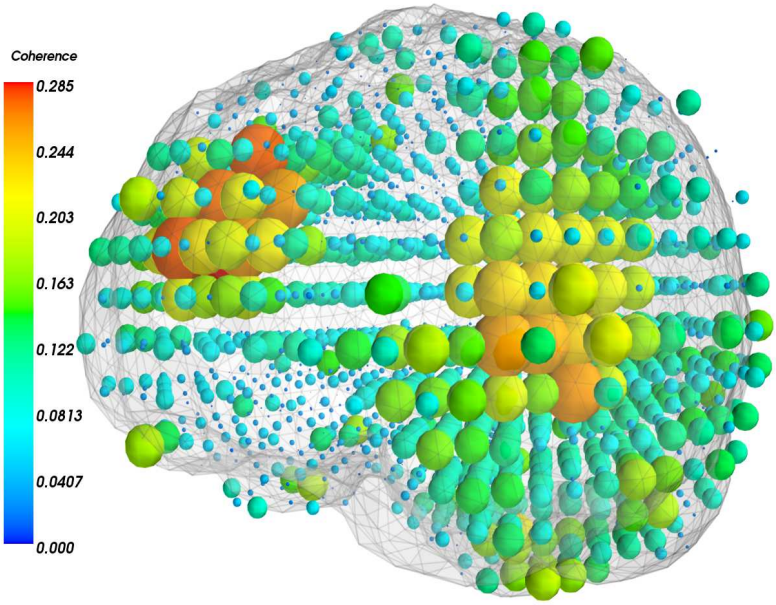

(b)

Figure 6.54: Estimated brain coherence using a seed voxel located at position 451. The brain dynamics are presented among all the points used to look for the brain activity and the seed voxel. In a) can be observed the brain dynamics for the active condition, while on b) are presented the brain interactions for the difference between the active and control conditions, using the LCMNE with FOCUSS method.

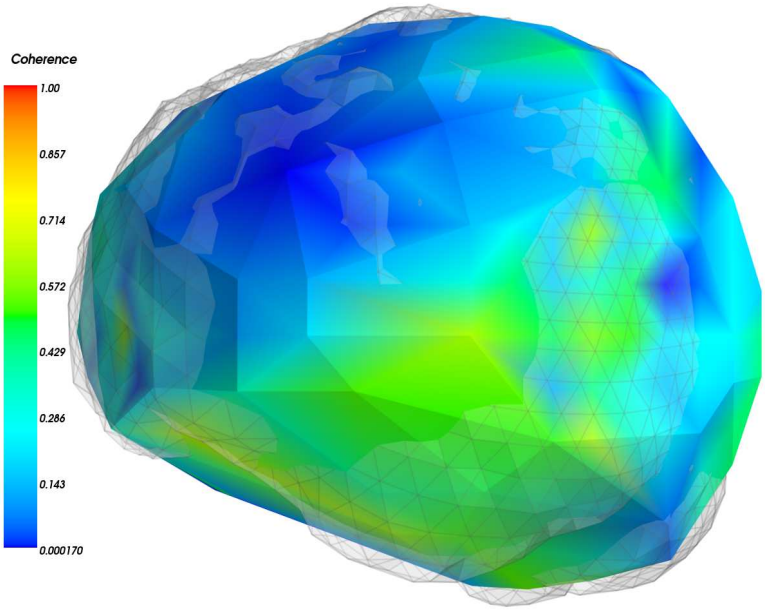

(a)

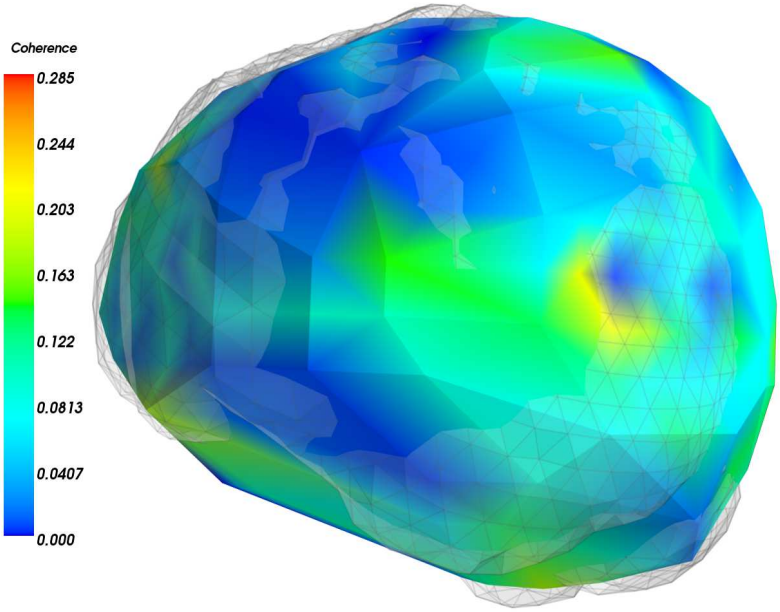

(b)

Figure 6.55: Estimated brain coherence using a seed voxel located at position 451. The brain dynamics are presented among the brain mesh elements located on the cortex. In a) can be observed the cortical brain dynamics obtained using the LCMNE with FOCUSS, while on b) are presented the estimated cortical brain dynamics using the LCMNE with FOCUSS for the difference between the active and control conditions.

6.3 Validation and discussion.

It was proved with simulations the reliability of the LCMNE spatial filter in combination with the FOCUSS algorithm for the estimation of functional brain dynamics, having a similar motivation as DICS has by using the LCMV beamformer. However, the observed performance of the proposed method is not perfect. There exist a number of issues related to the use of the LCMNE that FOCUSS cannot totally eliminate, specially those related to the distorted and weighted output to solutions near the sensors, characteristics of the MNE spatial filter, which is the base for the LCMNE filter together with the least-squares method. Nevertheless, this is not the only problem, as spurious interactions generated from the linearity related to the leadfields creates patterns that make difficult to analyse the estimated brain dynamics using the proposed method. The last mentioned problem also applied to DICS.

A comparison between two different conditions helps reducing the spurious interactions, following the same principle applied in the permutation analysis, without applying the permutations but by contrasting the conditions. The control condition coherence maps were obtained using DICS and the LCMNE together with FOCUSS to estimate spurious interactions in the presence of uncorrelated white noise without any brain activity, while the active conditions were obtained in the presence of brain activity. DICS is implemented as a benchmark for the estimation of the brain dynamics, as a well established technique.

The contrasted results obtained in the previously presented examples shown that both approaches offers similarities and differences on their brain dynamics estimations. In one side DICS gives a scattered representation of the functional brain dynamics around the real brain interactions, while the LCMNE in combination with FOCUSS gives a focused solution to the real interactions, in addition with spurious brain dynamics found using both techniques. Then, for the scenarios presented where the brain activity was correlated with coefficients factors higher or equal than .4, the use of the LCMNE with FOCUSS gave better estimations for the simulated brain dynamics than DICS.

It is important to remark that the uncorrelated brain sources assumption for the LCMV beamformer, according to the obtained results, reduces the spectral power of correlated activity on locations related to the simulated activity. However, it allows brain mesh elements with relative distance, but still close, to the generated activity to give an estimation of the brain interactions, Figures 6.17, 6.27, 6.36 and 6.50. On the other hand, the LCMNE spatial filter in combination with the FOCUSS algorithm gives correct estimations for the expected

coherence values when the FOCUSS algorithm allows the pass of activity from those locations. Unfortunately, its characteristic distorted output generates spurious interactions that makes difficult to have an idea of where the real brain interactions are.

A decrease in the performance of the proposed method occurs when it is used to estimate brain interactions between non cortical brain sources, as the method presents a weighted output to solutions near the sensors, Section 6.2.3. This is one of the reasons for the use of simulations to test the reliability of the proposed method. In Section 7.2.2 are presented some methods that may decrease or compensate the weighted solution. The examples presented so far in this chapter have been used to understand the reliability and the issues that characterize the proposed method, however, more repetitions of the experiments are required to asses its performance. Therefore, 100 repetitions were implemented for 3 different experiments, where the locations and the correlation coefficients used to simulated the brain activity on each of them are presented in Table 6.10, where a brain mesh with 15 [mm] of distance between elements was used for the experiments, appendix G.

The simulated brain activity did not match the brain mesh used, and therefore, the locations to look for the brain interactions were selected based on the spectral power implementing the LCMV beamformer and the LCMNE with FOCUSS method in the frequency domain, using the trace for the results obtained from equations 4.11 and 6.11. The implementation of the spatial filters in the time domain can also be used for that, Section 3.3. In Table 6.11 can be observed the mean for the obtained coherence values for the simulated activity, which is different from the expected, because of the variance for the spectral simulated activity estimation using the Welchs periodograms for 10 segments used on 10 seconds length signals.

Brain source(x,y,z)	A(35,182,190)	B(35,100,190)	C(140,100,190)	D(140,182,190)
A(35,182,190)	1	.9/.7/.5	0.0	0.0
B(35,100,190)	.9/.7/.5	1	0.0	.4/.7/.4
C(140,100,190)	0.0	0.0	1	0.0
D(140,182,190)	0.0	.4/.7/.4	0.0	1

Table 6.10: Correlation matrix used to generate 100 repetitions of simulated data for different strength of correlations. The matrix shows the correlation coefficients used to simulate the brain activity located on specific x, y, and z locations, for different experiments (experiment1/experiment2/experimentnt3). The locations for the brain sources are presented in millimetres.

Brain source(x,y,z)	A(35,182,190)	B(35,100,190)	C(140,100,190)	D(140,182,190)
A(35,182,190)	1	.94/.65/.30	0.0	0.0
B(35,100,190)	.94/.65/.30	1	0.0	.21/.70/.24
C(140,100,190)	0.0	0.0	1	0.0
D(140,182,190)	0.0	.21/.70/.24	0.0	1

Table 6.11: The matrix shows the mean coherence values obtained from the 100 repetitions of simulated activity located on specific x, y, and z locations, for different experiments (experiment1/experiment2/experimentnt3). The locations for the brain sources are presented in millimetres.

Thus, DICS and the LCMNE in combination with the FOCUSS algorithm were applied to 100 repetitions of three different experiments for the estimation of simulated functional brain dynamics with averaged SNR values of 22 and 11. Then, the brain coherence values were estimated between brain mesh locations 415, 451, 329 and 408 for the LCMNE case, and between brain mesh locations 414, 451, 458 and 408 for the DICS case. These are brain mesh locations near the generated activity from the A, B, C and D simulated brain sources, respectively, with enough estimated power to be considered as active. Tables 6.12 and 6.13 show the mean estimated coherence values for the simulated experiments using DICS and the LCMNE in combination with FOCUSS methods for an averaged SNR of 22. In Figure 6.56 can be observed the statistic characteristics for the estimated coherence values using the LCMNE spatial filter in combination with the FOCUSS algorithm, while in Figure 6.57 are presented the statistic characteristics of the estimated brain interactions obtained using the DICS approach. The statistic of the data are shown in the form of boxplots[2].

It can be observed with the tables and figures presented in the last paragraph that the LCMNE in combination with the FOCUSS algorithm gives more significant results compared with the use of DICS for the estimation of the same simulated brain interactions. The significant of the estimated coherence values were obtained based on t-tests for the Fisher's transform of the estimated coherences values presented in Tables 6.12 and 6.13. In Table 6.14 can be observed the obtained p-values for an averaged SNR of 22. The distribution for the estimated activity for the active condition and for the difference between the conditions obtained using DICS and the LCMNE with FOCUSS method are presented in appendix H.0.3. It is also presented in the same appendix the distribution obtained for the simulated brain activity for the 100 repetitions of the three experiments.

[2] *http://uk.mathworks.com/help/symbolic/mupad_ref/plotboxplot.html*

Brain source	$\widehat{A}(415)$	$\widehat{B}(451)$	$\widehat{C}(329)$	$\widehat{D}(408)$
$\widehat{A}(415)$	1	$.76^{[*]}/.59^{[*]}/.36^{[*]}$ $.74^{[\dagger]}/.55^{[\dagger]}/.33^{[\dagger]}$	0.0	0.0
$\widehat{B}(451)$	$.76^{[*]}/.59^{[*]}/.36^{[*]}$ $.74^{[\dagger]}/.55^{[\dagger]}/.33^{[\dagger]}$	1	0.0	$.05^{[*]}/.19^{[*]}/.25^{[*]}$ $.02^{[\dagger]}/.14^{[\dagger]}/.20^{[\dagger]}$
$\widehat{C}(329)$	0.0	0.0	1	0.0
$\widehat{D}(408)$	0.0	$.05^{[*]}/.19^{[*]}/.25^{[*]}$ $.02^{[\dagger]}/.14^{[\dagger]}/.20^{[\dagger]}$	0.0	1

Table 6.12: Mean for estimated coherence values among specific brain mesh elements using the LCMNE with FOCUSS for the simulated experiments (*experiment1/experiment2/experiment3*).

Brain source	$\widehat{A}(414)$	$\widehat{B}(451)$	$\widehat{C}(458)$	$\widehat{D}(408)$
$\widehat{A}(414)$	1	$.11^{[*]}/.12^{[*]}/.11^{[*]}$ $.10^{[\dagger]}/.09^{[\dagger]}/.09^{[\dagger]}$	0.0	0.0
$\widehat{B}(451)$	$.11^{[*]}/.12^{[*]}/.11^{[*]}$ $.10^{[\dagger]}/.09^{[\dagger]}/.09^{[\dagger]}$	1	0.0	$.09^{[*]}/.09^{[*]}/.12^{[*]}$ $.10^{[\dagger]}/.09^{[\dagger]}/.07^{[\dagger]}$
$\widehat{C}(458)$	0.0	0.0	1	0.0
$\widehat{D}(408)$	0.0	$.09^{[*]}/.09^{[*]}/.12^{[*]}$ $.10^{[\dagger]}/.09^{[\dagger]}/.07^{[\dagger]}$	0.0	1

Table 6.13: Mean for estimated coherence values among specific brain mesh elements using DICS for the simulated experiments (*experiment1/experiment2/experiment3*).

Experiment(Interaction)	LCMNE$^{[*]}$	LCMNE$^{[\dagger]}$	LCMV$^{[*]}$	LCMV$^{[\dagger]}$
$E1(\widehat{A}/\widehat{B})$	$7.57e^{-54}$	$1.28e^{-69}$	$2.51e^{-222}$	$1.98e^{-252}$
$E1(\widehat{B}/\widehat{D})$	$2.25e^{-125}$	$9.90e^{-127}$	$2.73e^{-118}$	$1.08e^{-103}$
$E2(\widehat{A}/\widehat{B})$	$4.14e^{-13}$	$1.67e^{-34}$	$1.19e^{-177}$	$1.17e^{-198}$
$E2(\widehat{B}/\widehat{D})$	$3.46e^{-186}$	$8.81e^{-202}$	$2.71e^{-197}$	$2.94e^{-196}$
$E3(\widehat{A}/\widehat{B})$	$8.84e^{-15}$	$9.25e^{-6}$	$5.15e^{-134}$	$4.81e^{-116}$
$E3(\widehat{B}/\widehat{D})$	$1.68e^{-4}$	$8.57e^{-7}$	$9.19e^{-86}$	$1.15e^{-105}$

Table 6.14: Obtained p-values using t-tests for the simulated and estimated interactions using the LCMNE with FOCUSS method and the DICS method(LCMV) for specific brain mesh elements.

[*] Estimated coherence values obtained from the active condition

[†] Estimated coherence values obtained from the difference between the active and the control conditions

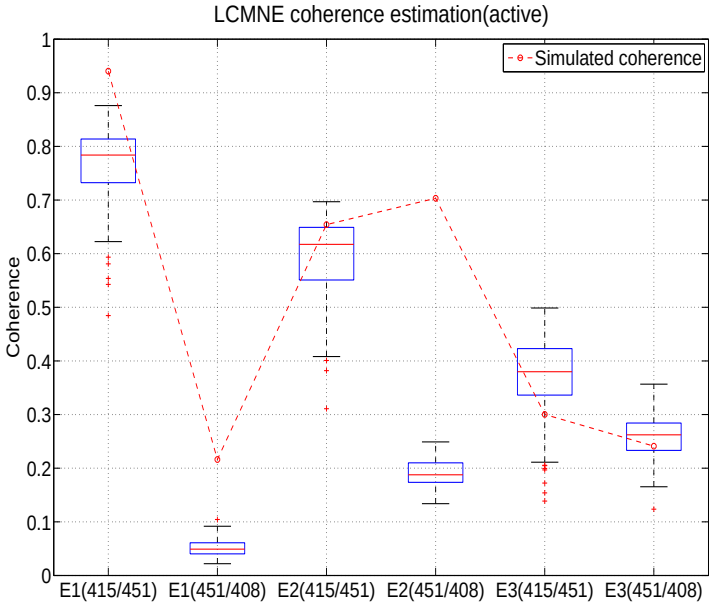

(a)

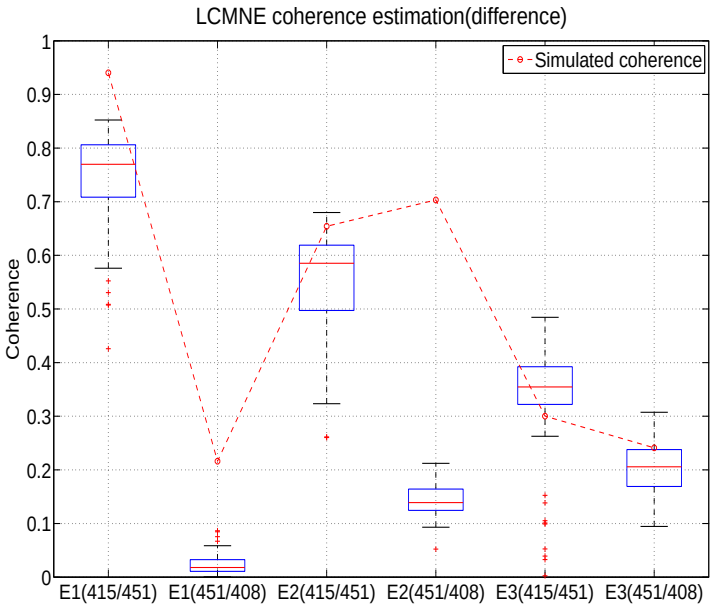

(b)

Figure 6.56: Estimated coherence values for 100 trials using the LCMNE with FOCUSS method, for a SNR of 22. On the top the estimated coherence values obtained from the active condition, while on the bottom the estimated coherence values obtained as the difference between the active and control conditions. The experiments and the interactions between specific brain sources are presented as E1(A/B), which means the interaction between source A and B in the first experiment.

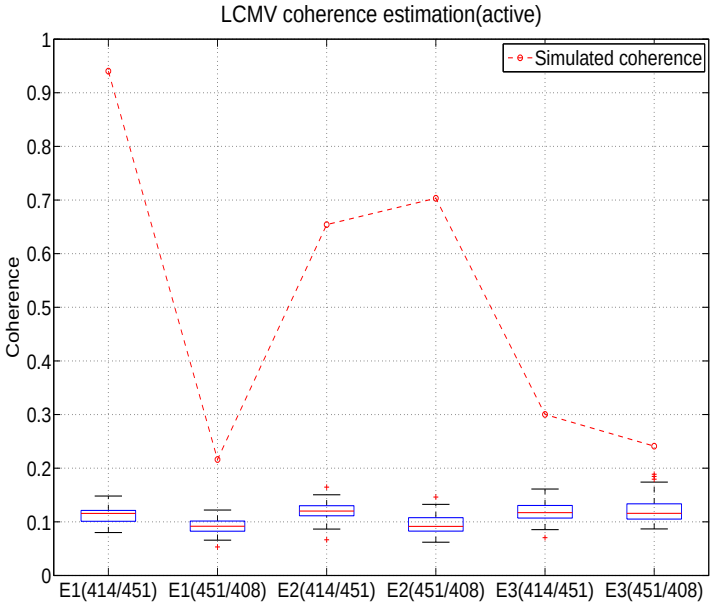

(a)

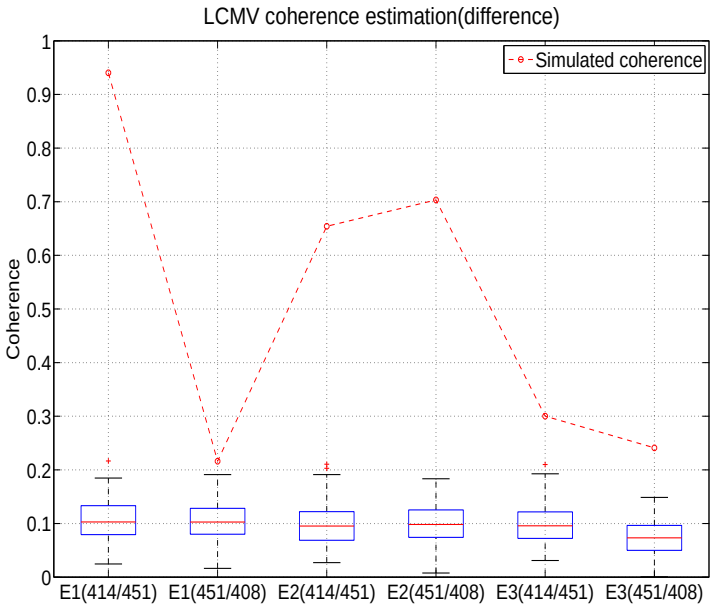

(b)

Figure 6.57: Estimated coherence values for 100 trials using DICS, for a SNR of 22. On the top the estimated coherence values obtained from the active condition, while on the bottom the estimated coherence values obtained as the difference between the active and control conditions. The experiments, and the interactions between specific brain sources are presented as E1(A/B), which means the interaction between source A and B in the first experiment.

Same number of experiments repetitions were implemented to show the external noise effects in the performance of DICS and the LCMNE with the FOCUSS methods. In these new set of experiments an averaged SNR of 11 was used for the MEG system, using the same characteristics for the simulated activity as in Table 6.10. The obtained results are presented in Figures 6.58 and 6.59 for the LCMNE with FOCUSS method, and for DICS, respectively, in the form of boxplots[2]. In Tables 6.15 and 6.16 can be observed the mean coherence values estimated using the active condition and the difference between the active and control conditions, while in Table 6.17 can be observed the p-values obtained using t-tests for the simulated and estimated activity, the distributions used for the t-tests are presented in appendix H.0.4.

Brain source	$\widehat{A}(415)$	$\widehat{B}(451)$	$\widehat{C}(329)$	$\widehat{D}(408)$
$\widehat{A}(415)$	1	$.28^{[*]}/.15^{[*]}/.08^{[*]}$ $.20^{[\dagger]}/.10^{[\dagger]}/.03^{[\dagger]}$	0.0	0.0
$\widehat{B}(451)$	$.28^{[*]}/.15^{[*]}/.08^{[*]}$ $.20^{[\dagger]}/.10^{[\dagger]}/.03^{[\dagger]}$	1	0.0	$.02^{[*]}/.07^{[*]}/.07^{[*]}$ $.01^{[\dagger]}/.05^{[\dagger]}/.05^{[\dagger]}$
$\widehat{C}(329)$	0.0	0.0	1	0.0
$\widehat{D}(408)$	0.0	$.02^{[*]}/.07^{[*]}/.07^{[*]}$ $.01^{[\dagger]}/.05^{[\dagger]}/.05^{[\dagger]}$	0.0	1

Table 6.15: Mean for estimated coherence values among specific brain mesh elements using the LCMNE with FOCUSS for the simulated experiments (*experiment1/experiment2/experiment3*).

Brain source	$\widehat{A}(414)$	$\widehat{B}(451)$	$\widehat{C}(458)$	$\widehat{D}(408)$
$\widehat{A}(414)$	1	$.10^{[*]}/.11^{[*]}/.11^{[*]}$ $.10^{[\dagger]}/.10^{[\dagger]}/.10^{[\dagger]}$	0.0	0.0
$\widehat{B}(451)$	$.10^{[*]}/.11^{[*]}/.11^{[*]}$ $.10^{[\dagger]}/.10^{[\dagger]}/.10^{[\dagger]}$	1	0.0	$.08^{[*]}/.09^{[*]}/.11^{[*]}$ $.10^{[\dagger]}/.10^{[\dagger]}/.08^{[\dagger]}$
$\widehat{C}(458)$	0.0	0.0	1	0.0
$\widehat{D}(408)$	0.0	$.08^{[*]}/.09^{[*]}/.11^{[*]}$ $.10^{[\dagger]}/.10^{[\dagger]}/.08^{[\dagger]}$	0.0	1

Table 6.16: Mean for estimated coherence values among specific brain mesh elements using DICS for the simulated experiments (*experiment1/experiment2/experiment3*).

[2] *http://uk.mathworks.com/help/symbolic/mupad_ref/plotboxplot.html*

[*] Estimated coherence values obtained from the active condition

[†] Estimated coherence values obtained from the difference between the active and the control conditions

Experiment(Interaction)	LCMNE[*]	LCMNE[†]	LCMV[*]	LCMV[†]
$E1(\widehat{A}/\widehat{B})$	$5.76e^{-99}$	$8.44e^{-111}$	$1.77e^{-230}$	$3.87e^{-264}$
$E1(\widehat{B}/\widehat{D})$	$8.68e^{-109}$	$5.22e^{-194}$	$1.16e^{-123}$	$4.91e^{-103}$
$E2(\widehat{A}/\widehat{B})$	$6.07e^{-90}$	$3.03e^{-103}$	$2.66e^{-165}$	$2.80e^{-205}$
$E2(\widehat{B}/\widehat{D})$	$1.01e^{-174}$	$1.74e^{-188}$	$1.37e^{-168}$	$3.15e^{-213}$
$E3(\widehat{A}/\widehat{B})$	$1.69e^{-88}$	$5.40e^{-116}$	$3.83e^{-146}$	$1.10e^{-110}$
$E3(\widehat{B}/\widehat{D})$	$3.26e^{-83}$	$1.51e^{-118}$	$3.70e^{-121}$	$8.55e^{-116}$

Table 6.17: Obtained p-values using t-tests for the simulated and estimated interactions using the LCMNE with FOCUSS method and the DICS method(LCMV) for specific brain mesh elements.

The results presented in Figures 6.56 to 6.59 show that the proposed method gets closer values from those expected from the simulated activity when it is compared with estimates obtained using the DICS method, even in the presence of low SNR. One of the main reasons for this is the uncorrelated brain sources assumption used in the LCMV beamformer design, which is the base for the DICS approach. As was presented in Chapter 5, the uncorrelated brain sources assumption reduces the power for the correlated brain sources, and therefore, the interactions estimations. The LCMNE in combination with the FOCUSS algorithm shows closer values for the coherence expected, however, the estimation are closer to the expected values only when the FOCUSS algorithm allows the brain activity to pass. Otherwise, the estimated coherence values will be too small to be considered as functional brain interactions. In the presence of a small SNR the estimated coherence values are reduced as is shown in Figure 6.58, but the estimated values keep a similar behaviour as the one obtained using a SNR of 22. The estimated coherence values using DICS for a SNR of 11 do not show many differences from the coherence obtained using a SNR of 22.

It can be observed in the previously presented tables and figures in this chapter that the estimated coherence values obtained for the active condition, and for the difference between the active and the control conditions, shows similar values even if there exist a mismatch between the positions of the simulated activity and the brain mesh used. This suggests that the characteristic pattern generated by the leadfields linearity is present only on locations where there is not brain activity, or when the power of the generated brain activity is not enough to reduce it. This scenario is presented in the estimations obtained using DICS and the LCMNE with the FOCUSS algorithm method.

[*] Estimated coherence values obtained from the active condition

[†] Estimated coherence values obtained from the difference between the active and the control conditions

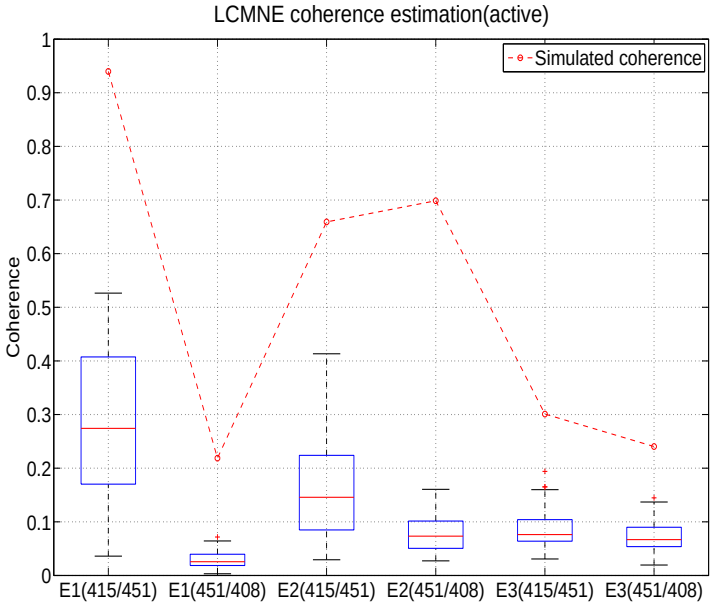

(a)

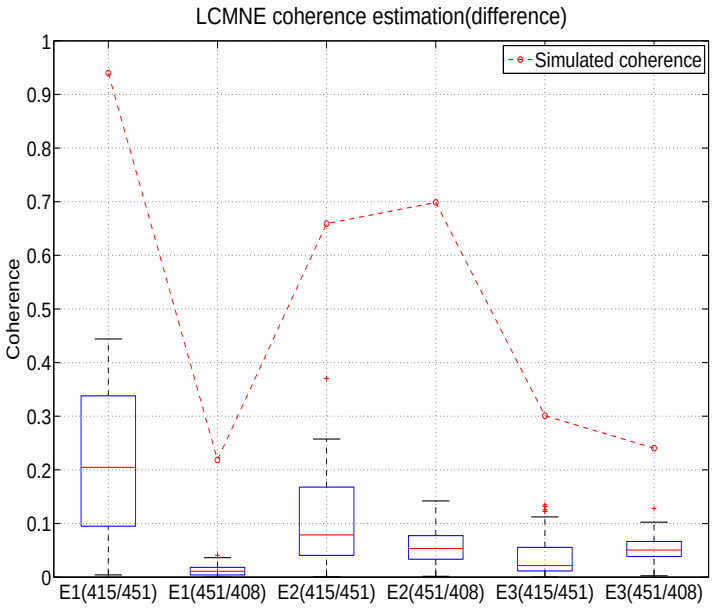

(b)

Figure 6.58: Estimated coherence values for 100 trials using the LCMNE with FOCUSS method, for a SNR of 11. On the top the estimated coherence values obtained from the active condition, while on the bottom the estimated coherence values obtained as the difference between the active and control conditions. The experiments and the interactions between specific brain sources are presented as E1(A/B), which means the interaction between source A and B in the first experiment.

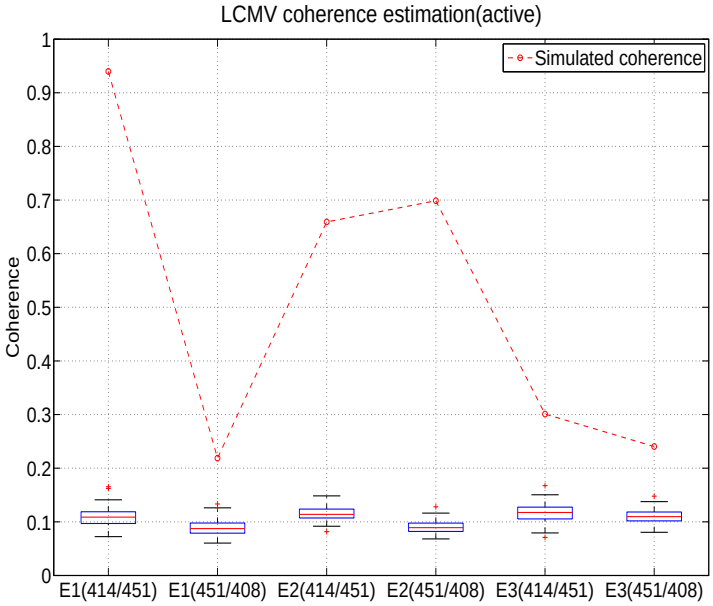

(a)

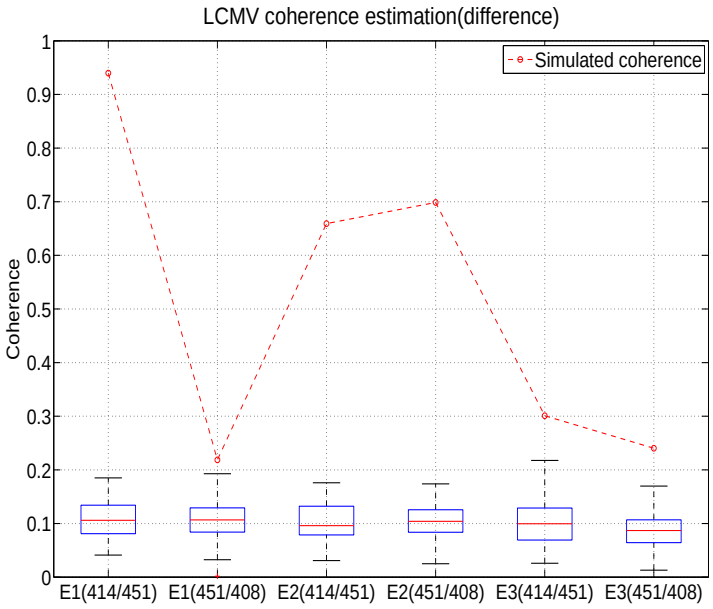

(b)

Figure 6.59: Estimated coherence values for 100 trials using DICS, for a SNR of 11. On the top the estimated coherence values obtained from the active condition, while on the bottom the estimated coherence values obtained as the difference between the active and control conditions. The experiments, and the interactions between specific brain sources are presented as E1(A/B), which means the interaction between source A and B in the first experiment.

Then, it is possible the use of DICS and the LCMNE with FOCUSS method for the estimation of the functional brain dynamics based on the estimation of the cross-spectral matrices. However, the metric of how good a technique is over the other depends on the use of them, as the techniques have their best performances on specific scenarios, as was mentioned before in this chapter. In one side DICS always gives an estimation of where the correlated activity is, even in the presence of highly correlated activity, but the obtained coherence values are not similar to the real brain interactions values. In the other side the LCMNE in combination with the FOCUSS algorithm gives good estimations for cortical simulated coherence values, but it is hard to identify the locations where the simulated activity is, situation that gets worst in case that the simulated activity is not located on the surface of the brain. This type of analysis would have better results if a combination of both techniques is used, as DICS can be used to located the positions for the simulated brain interactions, while the LCMNE with FOCUSS can be used to estimate the coherence values for those locations.

6.4 Conclusion.

In this chapter was presented the estimation of the functional brain interactions using a Linearly Constrained Minimum Norm spatial filter in combination with the Focal Undetermined System Solution algorithm. The estimation was also implemented using the Dynamic Imaging of Coherent Sources to compare the performance of the proposed approach. The estimation of the brain dynamics was implemented to understand the behaviour of both methods, especially for the LCMNE case, and to know their limitations under different scenarios. The scenarios were defined by simulating brain activity using different correlation coefficients, and by changing their locations on the space used to solve the inverse problem. The correlation between the simulated brain sources was used to measure the performance under difference brain relationships, while the change of positions was used to see the effects of the weighted and distorted solution of the LCMNE spatial filter.

The use of the LCMNE spatial filter in the same way DICS uses the LCMV beamformer for the estimation of brain interactions, based on the cross-spectral density matrices, gives highly correlated estimations among all possible brain interactions used to form the brain dynamics coherence matrix. This is reduced with the use of FOCUSS, as was presented in this chapter. DICS, on the other hand, is affected by the use of the LCMV beamformer uncorrelated brain sources assumption, which decreases the brain interactions amplitudes in relation with the amount of correlation between the brain activity. The DICS and the LMNE with FOCUSS

approaches are also affected by spurious interactions generated from the linearity between the leadfields matrices used to map the brain activity from the source space to the sensor space, and vice-versa for the solution of the inverse problem.

One solution to decrease the leadfields linearity effect is by calculating the difference between the active and control conditions, or by contrasting the conditions. The contrasted matrices obtained using the LCMNE spatial filter in combination with the FOCUSS algorithm allows a better estimation of where the brain interactions are, but the spurious interactions generated by the distorted characteristic of the spatial filter remains on the estimated coherence matrices. The coherences obtained with DICS after the conditions contrast give an idea about where the real brain coherences are. Unfortunately, the coherences values for locations where the brain activity were simulated are normally different from the expected.

The implemented simulations gives encouraging results for the use of the LCMNE in combination with the FOCUSS algorithm for the estimation of cortical brain dynamics, in the same way DICS uses the LCMV beamformer. Nevertheless, the performance of the filter is not perfect, because the approach is not robust enough to be used with real data, where the characteristic weighted output of the LCMNE spatial filter limit its use for the estimation of brain activity located on the cortex. If the brain sources are located on deeper locations, then the estimation of the functional brain interactions will mismatch the locations for the real, or for the simulated brain activity.

Then, the proposed method has some problems that need to be solved before being applied to real MEG data, if not a priori information is used to analyse the brain interactions between brain surface locations. In this case the estimated interactions obtained from those locations, using the LCMNE with FOCUSS method, should give similar values as the real brain interactions, as was observed with the implementation of the simulations, especially in the presence of high correlated brain activity as the leadfields linearity pattern decreases according to the activity present on those locations. However, this only gives similar values for the real interactions, but the estimated coherence matrices will gave spurious interactions that makes difficult the finding of real brain dynamics using the matrix. The LCMNE in combination with DICS can be used if not a priori information is available, but it needs to exist the certainty that the brain activity is generated from cortical brain sources, where DICS can be used to estimate the locations for the real brain interactions, while the LCMNE with FOCUSS can be used to estimate the brain interactions on locations found using DICS.

Chapter 7

General conclusions and future work

In this thesis are presented two different approaches based on the most used spatial filters for the estimation of the functional brain interactions using MEG signals. The first approach is based on the linearly constrained minimum variance beamformer, whose design was modified to considerer the brain interactions as presented in chapter 5. The modified version of the filter is characterized by a bilinear structure, which increases the complexity and issues for its implementation compared with the LCMV. The second proposed approach is based on the minimum norm estimate spatial filter, and on the dynamic imaging of coherent sources, using the MNE in the same way that the LCMV is used in DICS. It proposed the use of the MNE instead of the LCMV because it is not affected by the presence of correlated brain activity, however, the MNE limitations constrain its use for specific scenarios. The conclusions related to these two approaches are presented in Section 7.1.

The results obtained during the development of this thesis allows us to suggest additional implementations of techniques in order to reduce some of the introduced problems. Techniques such as the augmented Lagrange multipliers and numerical approaches based on the least-squares method to solve the bilinear problem presented in chapter 5, while techniques such as the unbiased minimum norm spatial filter and the full width half maximum metric are proposed to reduce the weighed and distorted solutions of the LCMNE with the FOCUSS method. These suggestions are presented in more detail in Section 7.2.

7.1 Conclusions

Functional brain dynamics studies using MEG data are often related to characteristic problems found with the techniques used to estimate the brain activity, see Chapters 3 and 4. The LCMV beamformer and the MNE spatial filter are two of the most used techniques, which show good performance under different scenarios, see Section 3.3, but because of the brain complexity, it is almost impossible to have complete certainty that those scenarios are present. As was presented in Chapter 3, the LCMV has its best performance in the presence of uncorrelated brain activity, as it was built under an uncorrelated brain sources assumption, while the MNE has its best performance estimating the brain activity located on the cortex, as its solution is weighted to locations near the MEG sensors.

Many analyses of functional brain dynamics are implemented using the spatial filters to estimate the brain activity time series, or spectrum in the frequency domain, which requires a lot of computational processing if the interactions between all locations used to look for the brain activity are estimated, see Chapter 4. An alternative solution was given with DICS, see Section 4.3.1, which uses the LCMV to estimate the functional brain dynamics from the cross-spectral density matrix of the MEG data, which is possible because of the beamformer design. This reduces the computational cost for the estimation of all-to-all brain interactions, as the connections are obtained by filtering the matrix for locations related to the interactions, instead of calculating the interactions from the estimated brain activity spectrum for the different locations.

7.1.1 BCMV conclusions

A modified version of the LCMV beamformer known as the Bilinear Constrained Minimum Variance (BCMV) spatial filter was introduced in Chapter 5. Its design was planned in order to decrease the effects that correlated brain activity has on the LCMV performance. This was achieved by changing the expression for the covariance matrix of the measured magnetic fields used, in order to consider the effects of correlated sources. Therefore, Equation 3.31 was changed to Equation 5.17 as presented in Chapter 5, which considers the off-diagonal elements of the covariance matrix to be different or equal to zero, or to remove the LCMV uncorrelated brain sources assumption.

The modified version of the LCMV beamformer, the BCMV spatial filter, was designed to be implemented for the estimation of the functional brain dynamics, to be used in the same way

that DICS uses the LCMV bemformer. The estimation is possible using two sets of weights obtained from different mathematical equations related with specific brain locations in which interactions are interested. On the other hand, DICS, or the LCMV, relies on two set of weights obtained using the same Equation. The mathematical expressions for the weights of the BCMV spatial filter are presented in Equation 5.25, which can be compared against the LCMV expression presented in Equation 3.33.

The mathematical expressions for the BCMV spatial filter weights were obtained following the same approach used for the LCMV beamformer, using the Lagrange multipliers on a set of constrained equations, Section 5.2.1. However, the BCMV problem requires the solution of a bilinear system of equations, which makes the problem more complex than the LCMV linear problem. The use of the Lagrange multipliers on a bilinear system of equations was possible using different constraints that in the LCMV case. Unfortunately, the obtained expressions for the set of weights did not fulfil all the constraints used for its design. The effect of this was high gains for specific locations, or brain interactions, resulting in high activity or interactions for locations where there were not any.

The constraints fulfilment problem was related with the expression of the constraints used, as it was not possible to find critical points with them. However, this problems may be present if different constraints are used due to the nature of the problem, see Section 5.2.2. One of the main reasons for this is that solutions for a system of bilinear equations are normally inconsistent. Nevertheless, even when it was proved that the BCMV spatial filter did not works as expected, it was proved that the filter can be implemented, helping people interested on the reconstruction of brain interactions using MEG data by providing them new ideas. The BCMV spatial filter defined in Chapter 5 give the basis for people interested to improve the idea, especially using the future work presented on this thesis, see Section 7.2.1.

7.1.2 LCMNE conclusions

Through the development of this project, we have been looking for an approach that allows the estimation of functional brain dynamics directly from the output of a spatial filter. However, the use of the bilinear constrained minimum variance beamformer idea did not fulfil this criteria. Thus, we looked for alternative ways to accomplish the aim for this thesis. The second proposed idea uses the MNE spatial filter as a basis, because its solution is less affected by the presence of correlated brain activity. Therefore, as was presented in Chapter 6, it was proposed to use the MNE spatial filter for the direct estimation of functional brain interactions by using it in the same way DICS uses the LCMV beamformer.

Unfortunately, the MNE could not be used in the same way because of the constraints required for the stop and pass bands used in the LCMV. Then, a different version of the filter was used, the Linearly Constrained Minimum Norm Estimates spatial filter. This filter is designed following the same approach used in the LCMV beamformer, but uses the least-squares method to estimate the expression for the filter weights instead of the Lagrange multipliers. Other important difference between these two approaches is that the LCMV beamformer relies on the use of the covariance matrix of the measured magnetic fields, that gives the filter its adaptability property. On the other hand, the LCMNE is defined as a non-adaptive spatial filter, the same as the MNE.

However, the LCMNE spatial filter shares the same limitations found with the least-squares method spatial filter, characterized to give distorted and weighted solutions to locations near the sensors used to measure the magnetic fields, see Chapter 6. These problems cause the finding of spurious brain interactions in brain dynamics studies. Spurious connections are found since the distorted output gives scattered estimations, where locations near positions where the brain activity is generated present similar behaviours. On the other hand, the weighted solution generates the estimation of brain interactions that mismatch the real brain connections locations, increasing the finding of false brain interactions, see Section 6.2.3.

The LCMNE weighted solution problem is reduced limiting its use for the estimation of cortical brain interactions. However, it is impossible to have complete certainty that all the brain activity responsible for the generation of the MEG data is located on the cortex, because of the brain complexity. Nevertheless, more certainty can be obtained relying on simulation analysis, as presented in Section 6.4, helping with the validation of the proposed approach. The distorted output of the filter was reduced using the focal undetermined system

solution algorithm, an algorithm that uses the estimated brain activity in order to reduce the distortion on each of the algorithm iterations, see Section 3.4.2. Therefore, it was possible to use the LCMNE spatial filter for brain dynamics studies, limiting its use for the estimation of cortical brain interactions, used in combination with the FOCUSS algorithm.

The LCMNE implementation requires the selection of two important parameters that can affect the accuracy of the estimations, depending on the SNR of the MEG system. The first parameter is the threshold value, or tolerance value, used for the inversion of the gram matrix, see Section 6.1. If this parameter is not correctly chosen, the brain interactions estimations can be due to the effects of the external noise, rather than from the brain activity. The second important parameter is the number of iterations for the FOCUSS algorithm, see Section 6.2.1, as a small number of iterations would give a high number of estimated spurious connections, while a high number of iterations can reduce, or eliminate, the real brain interactions. Unfortunately, it is difficult to give specific values for those parameters, as they depend on the SNR of the MEG acquisition system and on the brain mesh used to solve the inverse problem. In this thesis a trial and error approach was used for the selection of these parameters values.

Chapter 6 proved the feasibility of the LCMNE spatial filter in combination with the FOCUSS algorithm for the estimation of simulated functional brain interactions. The simulations were used in order to test the distorted and the weighted solution effects of the proposed method in different scenarios. The simulated brain activity was generated as AR processes, with different amounts of correlation coefficients between them. The LCMNE distortion effects was tested on the simulations analysis by comparing the estimated solutions when the simulated brain activity matched the brain mesh used to look for the brain activity, against the distortion obtained when the simulated activity did not match the brain mesh. The weighed solution effect was also tested, by locating the simulated brain activity on locations deeper than the brain surface.

The implemented simulations gave encouraging results, especially when compared against DICS for the estimation of all-to-all functional brain interactions, see Chapter 6. The use of FOCUSS highly reduced the finding of spurious brain interactions, but the selection of the number of iterations is difficult as there is not a defined procedure to follow. On the other hand, the LCMNE weighted solution needs to be sorted out in order to give certainty to the results obtained using the LCMNE with FOCUSS method on real data. The LCMNE estimated brain interactions from the simulated activity were compared with brain interac-

tions estimated using DICS, as it is a well established technique. The comparison helped to validate the proposed approach, see Section 6.4, even when both techniques gives different views of the data, both of them gave useful results.

The results obtained in this work showed that it is suitable to use the LCMNE spatial filter in combination with the FOCUSS algorithm for the estimation of the functional brain dynamics. When the LCMNE with FOCUSS method is used in the same way the LCMV beamformer is used in DICS, this focuses the use of the spatial filter for the estimation of the brain dynamics instead of the reconstruction of the brain activity time series, see Section 4.3. However, the proposed idea still has some important issues that need to be solved before being implemented on real functional brain dynamic studies, as was mentioned before. Some possible solutions are presented in the next section.

7.2 Future work

According to the results obtained in the estimation of brain activity from the hypothesis of this thesis, as stated in Chapter 1, and implemented in Chapters 5 and 6, the main future work would be the finding of a consistent solution for the bilinear constrained minimum variance beamformer, and the correction of the biased and distorted solution for the linearly constrained minimum norm spatial filter. Thus, this work could be developed further using techniques such as the augmented Lagrange multipliers and the implementation of iterative least-squares methods to get a consistent solution for the bilinear problem, and techniques such as the unbiased minimum norm, group of voxels analysis, and permutation tests to improve the LCMNE performance. The possible ideas for the future work are presented in more detail in the following subsections.

7.2.1 Bilinear constraint minimum variance beamformer

The inconsistent solution obtained in Chapter 5 for the modified version of the LCMV beamformer limits its use, as it is not possible to estimate the brain interactions with it. This problem can be found also in robotics and control fields, where it is required for solutions of models which are parametrized by two set of unknown variables. For example, in computer vision problems the Augmented Lagrange Multipliers (ALM) iterative algorithm (Del Bue et al., 2012) is used to find the solutions to a bilinear set of equations, where one of the variables is constrained. A different approach for the solution of a set of bilinear equations

problem is found with the least-squares method (Cohen and Tomasi, 1997). Some of the approaches based on the least-squares method are the normalized iterative method, the over parametrization method, and the numerical method (Bai and Liu, 2005). However, these are not the only techniques that have been implemented for the solution of similar problems, there are many techniques implemented in different fields from the ones already mentioned (Leedan and Meer, 2000; Abrahamsson et al., 2007; VanAntwerp and Braatz, 2000).

Then, the aim for the proposed future work for the bilinear constrained minimum variance beamformer is the implementation of the numerical methods introduced in the previous paragraph to find the set of weights that define the filter, while at the same time fulfilling the constraints used for its design. Most of these techniques have not been used on MEG data, but as in the least squares and the Lagrange multipliers methods cases, its implementation is possible since similar techniques are used to find solutions for set of equations as in the MNE and LCMV spatial filters problems. The implementation and validation of the proposed methods to solve the bilinear problem is likely to be a demanding work, as it requires a lot of computational process, especially for the finding of a pair of weights for each brain interaction.

In the case of all-to-all brain interaction estimations the computational cost can be very demanding, but once the expressions for the filter weights are obtained they can be used in the same way DICS uses the LCMV beamformer to estimate the brain interactions from the cross-spectral density matrix of the measured magnetic fields. Moreover, it is highly probable that the solutions obtained with those methods will give better results than the ones obtained using the the Lagrange multipliers weights. This is because the finding of critical points with the solutions are approximations depending on a cost function, not on an exact solution which may not be related with any critical points.

7.2.2 Linearly constrained minimum norm and FOCUSS

The problems presented in Chapter 6 for the LCMNE spatial filter can be reduced using techniques such as the unbiased minimum norm, voxel group-level analysis, and permutation tests. The unbiased minimum norm (Clarke and Braginski, 2006), presented in Section 3.4.1, can be used to reduce the weighted solution characteristic of the least-squares spatial filters. This technique is implemented in the same way FOCUSS is, but the weights are used to compensate the bias for locations near the sensors. Once the adjustment is implemented, deeper locations will have the same weight as cortical locations, allowing a better estimation

of the brain activity. However, the implementation of the unbiased minimum norm is difficult, and its complexity increases as the number of elements in the brain mesh used increases. There exist some predefined procedures to estimate the unbiased weights, but its uses are limited to a few brain mesh locations or when the locations are near the space of the sensors distribution (Gorodnitsky et al., 1995). Nevertheless, it is possible to be implemented, but it will require a lot of work to find the set of weights that compensate all brain mesh locations for different depths.

If the unbiased minimum norm can be implemented, then the distortion problem will be the most important issue to be solved. The use of FOCUSS should be one of the best options for that, but as was observed with the results obtained, there were still spurious interactions in the obtained estimations, and therefore, it is required more reduction for the distortion effect. We suggest the addition of two techniques for that, the voxel group-level analysis (Jerbi et al., 2007), and the permutation test (Nichols and Holmes, 2002). The voxel group-level analyses the brain connections, or activity, between a bundle of voxels instead of among all of them. This reduce the computational processing and the distortion. The distortion is reduced as locations close to the brain activity present similar behaviours, therefore, all those voxels will be considered as one. The size of the bundle, or cluster, of voxels can be determined using metrics such as the full width half maximum (FWHM) (Barnes and Hillebrand, 2003; Schoffelen and Gross, 2011), for repetitions of the same experiment. The permutation test, see Section 4.3.2, can be used after the voxels group-level analysis (Satoru and Nichols, 2004), in order to have a different perspective for the estimation of the brain interactions, replacing the results obtained from the contrast between conditions.

The proposed techniques for the improvement of the LCMNE spatial filter performance, in combination with the FOCUSS algorithm, relies on the implementation of the unbiased minimum norm. If the weighted solution problem is not fixed, then all the estimates for the brain interactions obtained using the addition of the mentioned improvements will not match the real locations for the brain interactions, in cases where the brain activity is not located on the brain surface. The implementation of the mentioned techniques in this subsection should improve the performance of the LCMNE spatial filter in combination with the FOCUSS algorithm, allowing its use with real data, and therefore, a more complete validation.

Appendices

Appendix A

Minimum Norm Estimates algorithm

The Minimum Norm Estimates spatial filter (MNE) algorithm is introduced by Hamalainen (Hämäläinen et al., 1993). It is used to estimate or reconstruct the brain activity from MEG signals, relying on the following parameters:

- $diag(\lambda_1, \lambda_2, \ldots, \lambda_N)$ Diagonal matrix composed by the N eigenvalues λ
- $\mathbf{H}$ Composite leadfield matrix
- $\boldsymbol{L}(\mathbf{r}_i)$ Leadfield matrix for the $\mathbf{r}_i$ brain source
- N Number of locations to look for the brain activity
- $\widehat{\mathbf{q}_i}$ Estimated equivalent current dipole activity located at $\mathbf{r}_i$
- $\mathbf{r}_i$ Location for the neuronal currents
- SVD Singular Value Decomposition
- Tol Tolerance value for the generalize inverse of the gram matrix
- $\mathbf{W}_{ls}(\mathbf{r}_i)$ Weights for the MNE spatial filter
- $\mathbf{x}$ Magnetic fields measurements due to the effects of the neuronal currents

The MNE algorithm can be listed as:

Algorithm 1 Minimum Norm Estimates

procedure MNE($\mathbf{H}$,$\mathbf{x}$, Tol)

$\mathbf{U}\mathbf{\Sigma}\mathbf{V}^T \leftarrow SVD(\mathbf{H}\mathbf{H}^T)$

$\mathbf{\Sigma} \rightarrow diag(\lambda_1, \lambda_1, \ldots, \lambda_N)$

$\widehat{\mathbf{\Sigma}}^{-1} \leftarrow diag(\lambda_1^{-1}, \ldots, \lambda_k^{-1} \geq Tol, 0_{k+1}, \ldots, 0_N)$

$[\mathbf{H}\mathbf{H}^T]^{-1} \leftarrow \mathbf{V}\widehat{\mathbf{\Sigma}}^{-1}\mathbf{U}^T$

for $i \leftarrow 1, N$ **do**

$\boldsymbol{L}(\mathbf{r}_i) \leftarrow \mathbf{H}(\boldsymbol{L}(\mathbf{r}_i))$

$\mathbf{W}_{ls}(\mathbf{r}_i) \leftarrow \boldsymbol{L}^T(\mathbf{r}_i)[\mathbf{H}\mathbf{H}^T]^{-1}$

$\widehat{\mathbf{q}}(\mathbf{r}_i) \leftarrow \mathbf{W}_{ls}^T(\mathbf{r}_i)\mathbf{x}$

end for

end procedure

The unbiased MNE algorithm can be listed as:

Algorithm 2 Unbiased Minimum Norm Estimates

procedure UMNE($\mathbf{H}$,$\mathbf{x}$, Tol)

$\mathbf{W}_u \leftarrow diag(||\mathbf{H}(\boldsymbol{l}_x(\mathbf{r}_1))||^{-1}, ||\mathbf{H}(\boldsymbol{l}_y(\mathbf{r}_1))||^{-1}, \ldots, ||\mathbf{H}(\boldsymbol{l}_z(\mathbf{r}_N))||^{-1})$

$\mathbf{U}\mathbf{\Sigma}\mathbf{V}^T \leftarrow SVD(\mathbf{H}\mathbf{W}_u\mathbf{W}_u^T\mathbf{H}^T)$

$\mathbf{\Sigma} \rightarrow diag(\lambda_1, \lambda_1, \ldots, \lambda_N)$

$\widehat{\mathbf{\Sigma}}^{-1} \leftarrow diag(\lambda_1^{-1}, \ldots, \lambda_k^{-1} \geq Tol, 0_{k+1}, \ldots, 0_N)$

$[\mathbf{H}\mathbf{W}_u\mathbf{W}_u^T\mathbf{H}^T]^{-1} \leftarrow \mathbf{V}\widehat{\mathbf{\Sigma}}^{-1}\mathbf{U}^T$

$\widehat{\mathbf{m}} \leftarrow \mathbf{W}_u\mathbf{W}_u^T\mathbf{H}^T[\mathbf{H}\mathbf{W}_u\mathbf{W}_u^T\mathbf{H}^T]^{-1}\mathbf{x}$

end procedure

Appendix B

Linearly Constrained Minimum Variance beamformer algorithm

The Linearly Constrained Minimum Variance beamformer (LCMV) algorithm is introduced by Van Veen (Van Veen et al., 1997). It is used to estimate or reconstruct the brain activity from MEG signals, relying on the following parameters:

- $\mathbf{Cq}_i$ Covariance matrix for the brain source located at $\mathbf{r}_i$
- $\mathbf{C}(\mathbf{x})$ Covariance matrix for the measured magnetic fields
- $\mathbf{H}$ Composite leadfield matrix
- $\boldsymbol{L}(\mathbf{r}_i)$ Leadfield matrix for the $\mathbf{r}_i$ brain source
- N Number of locations to look for the brain activity
- $\widehat{\mathbf{q}_i}$ Estimated equivalent current dipole activity located at $\mathbf{r}_i$
- $\mathbf{Q}_n^n$ Higher order covariance matrix for $\mathbf{n}$
- $\mathbf{r}_i$ Location for the neuronal currents
- $tr(\mathbf{A})$ Trace for the $\mathbf{A}$ matrix
- $Var(\mathbf{r}_i)$ Variance or brain activity power found at $\mathbf{r}_i$
- $\mathbf{W}_b(\mathbf{r}_i)$ Weights for the LCMV spatial filter
- $\mathbf{x}$ Magnetic fields measurements due to the effects of the neuronal currents

The LCMV algorithm can be listed as:

Algorithm 3 Linearly Constrained Minimum Variance beamformer

procedure LCMV($\mathbf{H}$,$\mathbf{x}$,$\mathbf{Q}_n$)

$\mathbf{C}(\mathbf{x}) \leftarrow \langle [\mathbf{x} - \langle \mathbf{x} \rangle][\mathbf{x} - \langle \mathbf{x} \rangle]^T \rangle$

for $i \leftarrow 1, N$ **do**

$\boldsymbol{L}(\mathbf{r}_i) \leftarrow \mathbf{H}(\boldsymbol{L}(\mathbf{r}_i))$

$\mathbf{W}_b(\mathbf{r}_i) \leftarrow [\boldsymbol{L}^T(\mathbf{r}_i)\mathbf{C}^{-1}(\mathbf{x})\boldsymbol{L}(\mathbf{r}_i)]^{-1}\boldsymbol{L}^T(\mathbf{r}_i)\mathbf{C}^{-1}(\mathbf{x})$

$\widehat{\mathbf{q}}(\mathbf{r}_i) \leftarrow \mathbf{W}_b^T(\mathbf{r}_i)\mathbf{x}$

$\widehat{Var}(\mathbf{r}_i) \leftarrow \frac{tr\{[\boldsymbol{L}^T(\mathbf{r}_i)\mathbf{C}^{-1}(\mathbf{x})\boldsymbol{L}(\mathbf{r}_i)]^{-1}\}}{tr\{[\boldsymbol{L}^T(\mathbf{r}_i)\mathbf{Q}_\mathbf{n}^{-1}\boldsymbol{L}(\mathbf{r}_i)]^{-1}\}}$

$NAI(\mathbf{r}_i) \leftarrow \widehat{Var}(\mathbf{r}_i)$

end for

end procedure

Appendix C

Mosher's equivalences of linear approaches for MEG inverse solutions

In this appendix is presented the equivalent expression described by Mosher for the MNE and LCMV spatial filters, used to express the spatial filters similarities. These similarities are shared with other techniques that are not presented as they are not used on this work, for more details check (Mosher et al., 2003).

- $\mathbf{C}(\mathbf{m})$ Covariance matrix for the brain sources or ECDs
- $\mathbf{C}(\mathbf{x})$ Covariance matrix for the measured magnetic fields
- $\mathbf{H}$ Composite leadfield matrix
- $\boldsymbol{I}_{N\times N}$ Identity matrix with $N \times N$ dimension
- $\boldsymbol{L}(\mathbf{r}_i)$ Leadfield matrix for the $\mathbf{r}_i$ brain source
- $\mathbf{m}$ Composite matrix for the brain sources
- N Number of locations to look for the brain activity
- $\widehat{\mathbf{q}}_i$ Estimated equivalent current dipole activity located at $\mathbf{r}_i$
- $\mathbf{r}_i$ Location for the neuronal currents
- $\mathbf{x}$ Magnetic fields measurements due to the effects of the neuronal currents

The LCMV algorithm can be listed as:

Algorithm 4 Mosher's equivalence solutions for the MEG inverse problem

procedure MOSHERINVERSESOLUTION($\mathbf{H}$,$\mathbf{x}$,$Method$)

if $Method$=MNE **then**

$\mathbf{C}(\mathbf{m}) \leftarrow \boldsymbol{I}_{N\times N}$

$\widehat{\mathbf{q}}(\mathbf{r}_i) \leftarrow \mathbf{C}(\mathbf{m})\mathbf{H}^T[\mathbf{H}\mathbf{C}(\mathbf{m})\mathbf{H}^T]^{-1}\mathbf{x}$

end if

if $Method$=LCMV **then**

$\mathbf{C}(\mathbf{x}) \leftarrow \langle[\mathbf{x}-\langle\mathbf{x}\rangle][\mathbf{x}-\langle\mathbf{x}\rangle]^T\rangle$

$\mathbf{C}(\mathbf{m}) \leftarrow diag(\langle[\mathbf{m}-\langle\mathbf{m}\rangle][\mathbf{m}-\langle\mathbf{m}\rangle]^T\rangle)$

for $i \leftarrow 1, N$ **do**

$\boldsymbol{L}(\mathbf{r}_i) \leftarrow \mathbf{H}(\boldsymbol{L}(\mathbf{r}_i))$

$\widehat{\mathbf{q}}(\mathbf{r}_i) \leftarrow \mathbf{C}^{-1}(\mathbf{x})\boldsymbol{L}^T[\boldsymbol{L}(\mathbf{r}_i)\mathbf{C}^{-1}(\mathbf{x})\boldsymbol{L}^T(\mathbf{r}_i)]^{-1}\mathbf{x}$

end for

end if

end procedure

Appendix D

FOCal Undetermined System Solution algorithm

The FOCal Undetermined System Solution (FOCUSS) algorithm is introduced by Gorodnitsky (Gorodnitsky et al., 1995). It is used to reduce the distortion on the inverse problem solutions obtained using the minimum norm estimates spatial filter, relying on the following parameters:

- $diag(\mathbf{A})$ Diagonal elements of the $\mathbf{A}$ matrix
- $\mathbf{H}$ Composite leadfield matrix
- $\widehat{\mathbf{q}}$ Estimated equivalent current dipole activity
- $\mathbf{r}_i$ Location for the neuronal currents
- $tr(\mathbf{A})$ Trace for the $\mathbf{A}$ matrix
- Tol Tolerance value for the FOCUSS algorithm to stop the recursion
- $\mathbf{W}_{ls}(\mathbf{r}_i)$ Weights for the MNE spatial filter
- $\mathbf{W}_u$ Unbiased MNE weights matrix
- $\mathbf{W}_{Fk}$ FOCUSS weights matrix
- $\mathbf{x}$ Magnetic fields measurements due to the effects of the neuronal currents

The recursive FOCUSS algorithm can be listed as:

Algorithm 5 FOcal Understimated System Solution

procedure FOCUSS($\widehat{\mathbf{m}}$, $\mathbf{W}_{ls}$, $\mathbf{H}$,$\mathbf{x}$,Tol)
  $\widehat{\mathbf{m}} \leftarrow \mathbf{W}_{ls}^T\mathbf{x}$
  $k \leftarrow 0$
  $Error \leftarrow tr(\widehat{\mathbf{m}})$
  while $Error \geq= Tol$ **do**
    $\mathbf{W}_{F_k} \leftarrow diag(\widehat{\mathbf{m}})$
    $\widehat{\mathbf{m}} \leftarrow \mathbf{W}_{F_k}\mathbf{W}_{F_k}^T\mathbf{H}^T[\mathbf{H}\mathbf{W}_{F_k}\mathbf{W}_{F_k}^T\mathbf{H}^T]^{-1}\mathbf{x}$
    $k \leftarrow k+1$
    $Error \leftarrow tr(\widehat{\mathbf{m}})$
  end while
end procedure

The recursive FOCUSS algorithm using the unbiased MNE to compensate for the weighted can be listed as:

Algorithm 6 Unbiased FOcal Understimated System Solution

procedure FOCUSSUNBIAS($\widehat{\mathbf{m}}$,, $\mathbf{W}_u$, $\mathbf{H}$, $\mathbf{x}$,Tol)
  $\widehat{\mathbf{m}} \leftarrow \mathbf{W}_u\mathbf{W}_u^T\mathbf{H}^T[\mathbf{H}\mathbf{W}_u\mathbf{W}_u^T\mathbf{H}^T]^{-1}\mathbf{x}$
  $k \leftarrow 0$
  $Error \leftarrow tr(\widehat{\mathbf{m}})$
  while $Error \geq= Tol$ **do**
    $\mathbf{W}_{F_k} \leftarrow diag(\widehat{\mathbf{m}})$
    $\widehat{\mathbf{m}} \leftarrow \mathbf{W}_{F_k}\mathbf{W}_{F_k}^T\mathbf{H}^T[\mathbf{H}\mathbf{W}_{F_k}\mathbf{W}_{F_k}^T\mathbf{H}^T]^{-1}\mathbf{x}$
    $k \leftarrow k+1$
    $Error \leftarrow tr(\widehat{\mathbf{m}})$
  end while
end procedure

Appendix E

Dynamic Imaging of Coherent Sources algorithm

The Dynamic Imaging of Coherent Sources spatial filter (DICS) algorithm is introduced by Gross (Gross et al., 2001). It is used to estimate the functional brain dynamics directly from the output of the spatial filter, relying on the following parameters:

- λ Singular value
- $\mathbf{\Gamma}(\mathbf{f})$ Cross spectral density matrix for $\mathbf{x}$
- $\mathbf{\Gamma}_{\mathbf{r}_i\mathbf{r}_j}(f)$ Cross spectral density matrix for brain sources located at $\mathbf{r}_i$ and $\mathbf{r}_j$
- FFT Fast Fourier transform
- $\mathbf{H}$ Composite leadfield matrix
- $\boldsymbol{L}(\mathbf{r}_i)$ Leadfield matrix for the $\mathbf{r}_i$ brain source
- N Number of locations to look for the brain activity
- $\mathbf{r}_i$ Location for the neuronal currents
- $R_{\mathbf{r}_i\mathbf{r}_j}(f)$ Spectral coherence for brain sources located at $\mathbf{r}_i$ and $\mathbf{r}_j$
- SVD Singular value decomposition
- $tr(\mathbf{A})$ Trace for the $\mathbf{A}$ matrix
- $\mathbf{x}$ Magnetic fields measurements due to the effects of the neuronal currents

The DICS algorithm can be listed as:

Algorithm 7 Dynamic Imaging of Coherent Sources

procedure DICS($\mathbf{H}$,$\mathbf{x}$,$\mathbf{Q}_n$)
  $\mathbf{g}(f) \leftarrow FFT(\mathbf{x})$
  $\mathbf{\Gamma}(\mathbf{f}) \leftarrow \langle \mathbf{g}(f)\mathbf{g}(f)^H \rangle$
  for $i \leftarrow 1, N$ **do**
    $\boldsymbol{L}(\mathbf{r}_i) \leftarrow \mathbf{H}(\boldsymbol{L}(\mathbf{r}_i))$
    $\mathbf{W}_b^T(\mathbf{r}_i, f)) \leftarrow [\boldsymbol{L}^T(\mathbf{r}_i)\mathbf{\Gamma}^{-1}(f)\boldsymbol{L}(\mathbf{r}_i)]^{-1}\boldsymbol{L}^T(\mathbf{r}_i)\mathbf{\Gamma}^{-1}(f)$
  end for
  for $i \leftarrow 1, N$ **do**
    for $j \leftarrow 1, N$ **do**
      $\boldsymbol{\gamma}_{\mathbf{r}_i\mathbf{r}_i}(f) \leftarrow MaxStrDir(\mathbf{W}_b(\mathbf{r}_i, f)\mathbf{\Gamma}(f)\mathbf{W}_b^H(\mathbf{r}_i, f))$
      $\boldsymbol{\gamma}_{\mathbf{r}_j\mathbf{r}_j}(f) \leftarrow MaxStrDir(\mathbf{W}_b(\mathbf{r}_j, f)\mathbf{\Gamma}(f)\mathbf{W}_b^H(\mathbf{r}_j, f))$
      $\boldsymbol{\gamma}_{\mathbf{r}_i\mathbf{r}_j}(f) \leftarrow MaxStrDir(\mathbf{W}_b(\mathbf{r}_i, f)\mathbf{\Gamma}(f)\mathbf{W}_b^H(\mathbf{r}_j, f))$
      $R_{\mathbf{r}_i\mathbf{r}_j}(f) \leftarrow \frac{|\gamma_{\mathbf{r}_i\mathbf{r}_j}(f)|^2}{|\gamma_{\mathbf{r}_i\mathbf{r}_i}(f)||\gamma_{\mathbf{r}_j\mathbf{r}_j}(f)|}$
    end for
  end for
end procedure

procedure MaxStrDir($\mathbf{\Gamma}_{\mathbf{r}_i\mathbf{r}_j}(f)$)
  $\mathbf{U}\mathbf{\Sigma}\mathbf{V}^T \leftarrow SVD(\mathbf{\Gamma}_{\mathbf{r}_i\mathbf{r}_j}(f))$
  $\mathbf{\Sigma} \rightarrow diag(\lambda_1, \lambda_2, \lambda_3)$
  if $\lambda_1 \geq \lambda_2 \geq \lambda_3$ **then**
    $\gamma_{\mathbf{r}_i\mathbf{r}_j}(f) \leftarrow \lambda_1$
  else
    $\gamma_{\mathbf{r}_i\mathbf{r}_j}(f) \leftarrow tr\{\mathbf{\Gamma}_{\mathbf{r}_i\mathbf{r}_j}(f)\}$
  end if
end procedure

Appendix F

Linearly Constrained Minimum Norm Estimates algorithm

The Linearly Constrained Minimum Norm Estimates (LCMNE) parameters required and pseudo code for its implementation are following presented:

- λ Singular value
- $\mathbf{\Gamma}(\mathbf{f})$ Cross spectral density matrix for $\mathbf{x}$
- $\mathbf{\Gamma}_{\mathbf{r}_i\mathbf{r}_j}(f)$ Cross spectral density matrix for brain sources located at $\mathbf{r}_i$ and $\mathbf{r}_j$
- FFT Fast Fourier transform
- $\mathbf{H}$ Composite leadfield matrix
- $\boldsymbol{I}$ 3×3 identity matrix
- $\boldsymbol{L}(\mathbf{r}_i)$ Leadfield matrix for the $\mathbf{r}_i$ brain source
- N Number of locations to look for the brain activity
- $\mathbf{r}_i$ Location for the neuronal currents
- $R_{\mathbf{r}_i\mathbf{r}_j}(f)$ Spectral coherence for brain sources located at $\mathbf{r}_i$ and $\mathbf{r}_j$
- SVD Singular value decomposition
- $tr(\mathbf{A})$ Trace for the $\mathbf{A}$ matrix
- $\mathbf{x}$ Magnetic fields measurements due to the effects of the neuronal currents

Algorithm 8 Linearly Constrained Minimum Norm Estimates

procedure LCMNE($\mathbf{H}$,$\mathbf{x}$,Tol)

$\mathbf{g}(f) \leftarrow FFT(\mathbf{x})$

$\mathbf{\Gamma}(f) \leftarrow \langle \mathbf{g}(f)\mathbf{g}(f)^H \rangle$

$\mathbf{U\Sigma V}^T \leftarrow SVD(\mathbf{HH}^T)$

$\widehat{\mathbf{\Sigma}}^{-1} \leftarrow diag(\lambda_1^{-1}, \ldots, \lambda_k^{-1} \geq Tol, 0_{k+1}, \ldots, 0_N)$

for $i \leftarrow 1, N$ **do**

$\mathbf{D}(\mathbf{r}_i) \leftarrow [\mathbf{I}_{\mathbf{r}_1=\mathbf{r}_i}, \mathbf{0}_{\mathbf{r}_2\neq\mathbf{r}_i}, \ldots, \mathbf{0}_{\mathbf{r}_N\neq\mathbf{r}_i}]$

$\mathbf{W}^T(\mathbf{r}_i) \leftarrow \mathbf{D}(\mathbf{r}_i)\mathbf{H}^T[\mathbf{U}\widehat{\mathbf{\Sigma}}^{-1}\mathbf{V}^T]$

end for

for $i \leftarrow 1, N$ **do**

for $j \leftarrow 1, N$ **do**

$\boldsymbol{\gamma}_{\mathbf{r}_i\mathbf{r}_i}(f) \leftarrow MaxStrDir(\mathbf{W}(\mathbf{r}_i, f)\mathbf{\Gamma}(f)\mathbf{W}^T(\mathbf{r}_i, f))$

$\boldsymbol{\gamma}_{\mathbf{r}_j\mathbf{r}_j}(f) \leftarrow MaxStrDir(\mathbf{W}(\mathbf{r}_j, f)\mathbf{\Gamma}(f)\mathbf{W}^T(\mathbf{r}_j, f))$

$\boldsymbol{\gamma}_{\mathbf{r}_i\mathbf{r}_j}(f) \leftarrow MaxStrDir(\mathbf{W}(\mathbf{r}_i, f)\mathbf{\Gamma}(f)\mathbf{W}^T(\mathbf{r}_j, f))$

$R_{\mathbf{r}_i\mathbf{r}_j}(f) \leftarrow \frac{|\gamma_{\mathbf{r}_i\mathbf{r}_j}(f)|^2}{|\gamma_{\mathbf{r}_i\mathbf{r}_i}(f)||\gamma_{\mathbf{r}_j\mathbf{r}_j}(f)|}$

end for

end for

end procedure

procedure MaxStrDir($\mathbf{\Gamma}_{\mathbf{r}_i\mathbf{r}_j}(f)$)

$\mathbf{U\Sigma V}^T \leftarrow SVD(\mathbf{\Gamma}_{\mathbf{r}_i\mathbf{r}_j}(f))$

$\mathbf{\Sigma} \rightarrow diag(\lambda_1, \lambda_2, \lambda_3)$

if $\lambda_1 \geq \lambda_2 \geq \lambda_3$ **then**

$\gamma_{\mathbf{r}_i\mathbf{r}_j}(f) \leftarrow \lambda_1$

else

$\gamma_{\mathbf{r}_i\mathbf{r}_j}(f) \leftarrow tr\{\mathbf{\Gamma}_{\mathbf{r}_i\mathbf{r}_j}(f)\}$

end if

end procedure

Appendix G

Brain meshes used to solve the inverse problem

In this appendix are presented the brain mesh elements, or voxels, distributions used to estimate the functional brain dynamics in chapter 6. The brain meshes are presented to be used as maps for the results presented. Most of the elements are shown in the figures, however, because of the high number of elements, some of them are not labelled. In the case of the 10 [mm] brain mesh, the brain mesh map is divided into 4 parts, as the mesh has 1848 elements. The 15 [mm] brain mesh is presented in figure G.1, while the 10 [mm] brain mesh is presented in figures G.2 to G.5.

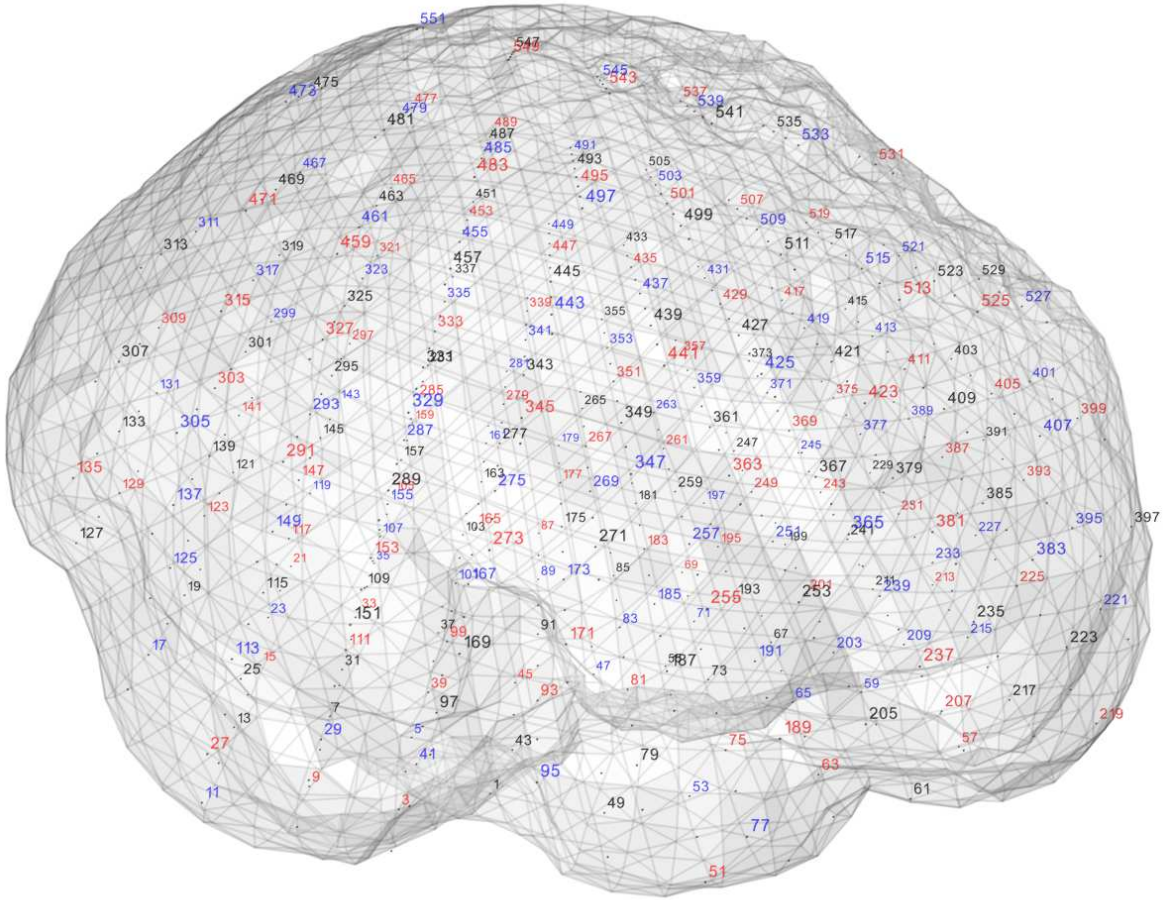

Figure G.1: Brain mesh with 15 mm of distance between elements.

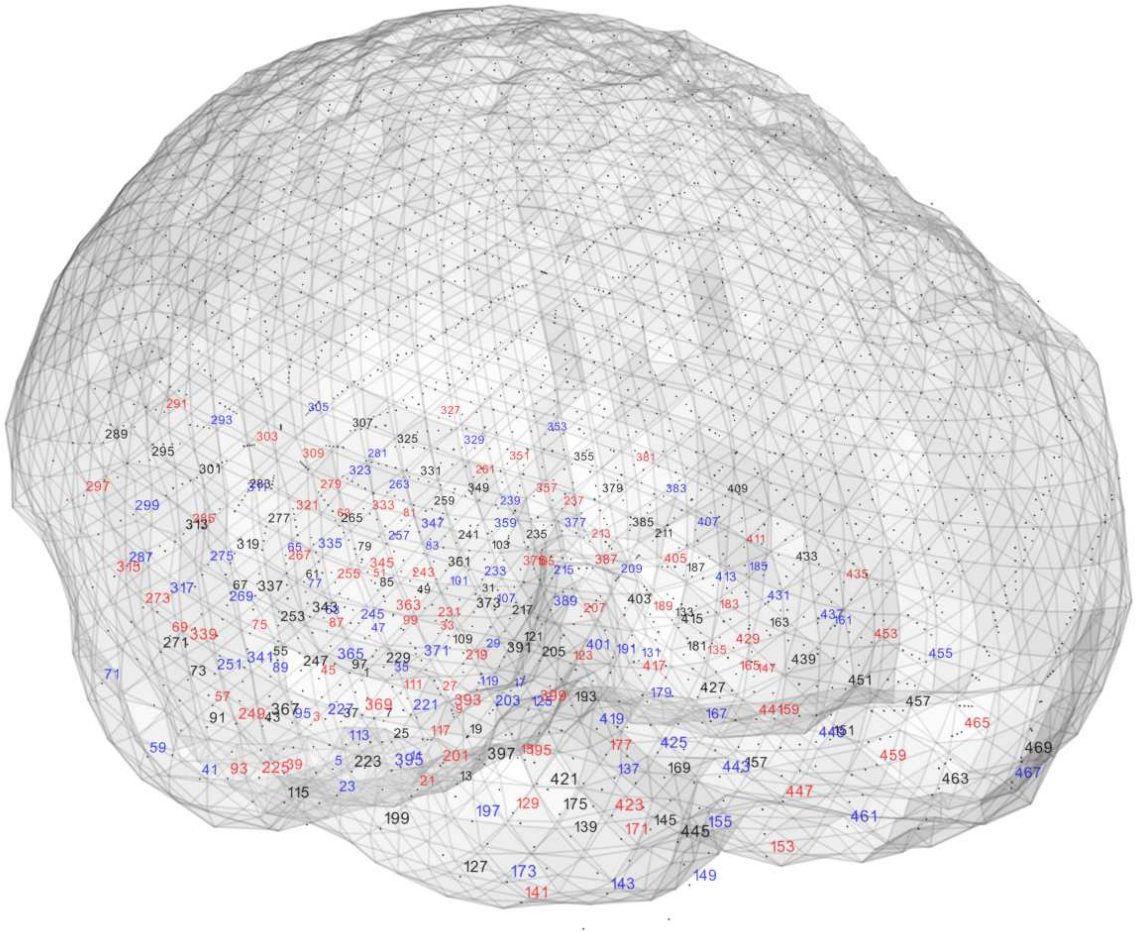

Figure G.2: Brain mesh with 10 mm of distance between elements, presenting elements 1 to 470 of the mesh.

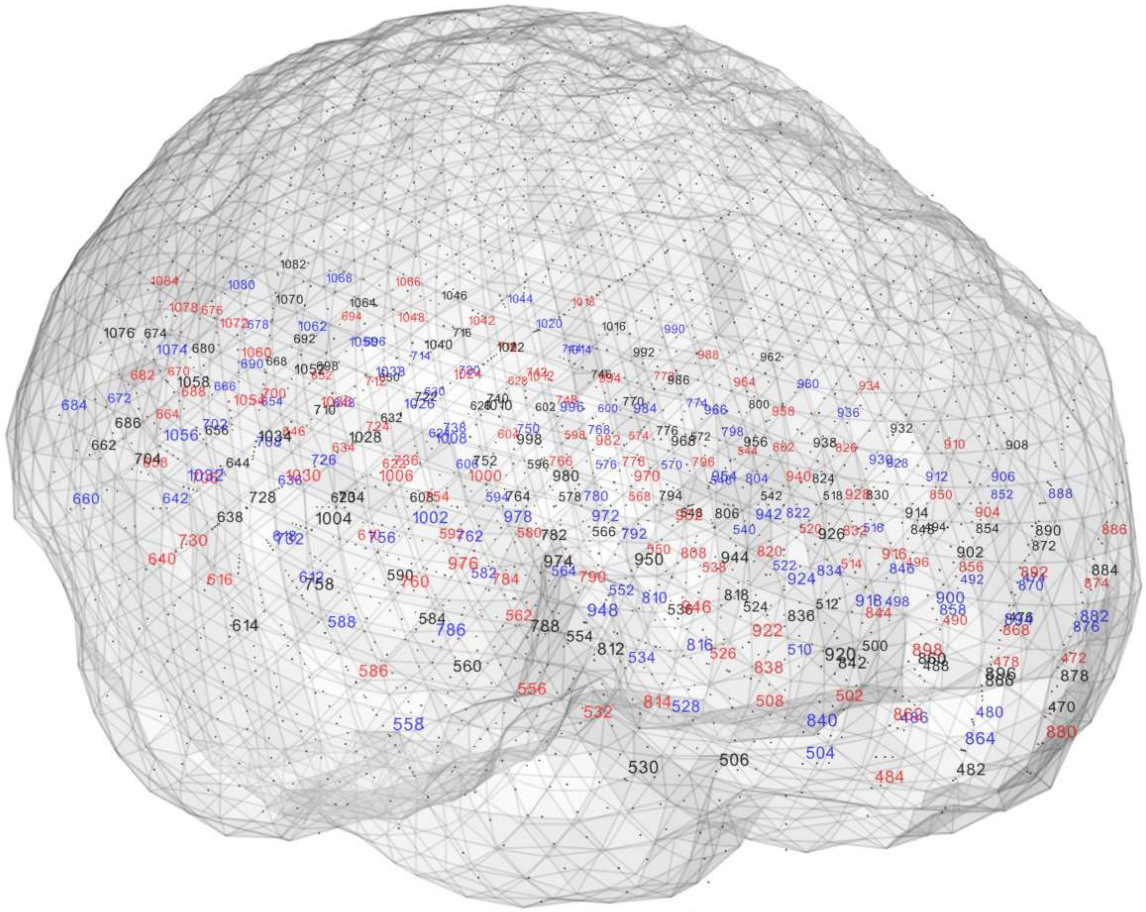

Figure G.3: Brain mesh with 10 mm of distance between elements, presenting elements 471 to 880 of the mesh.

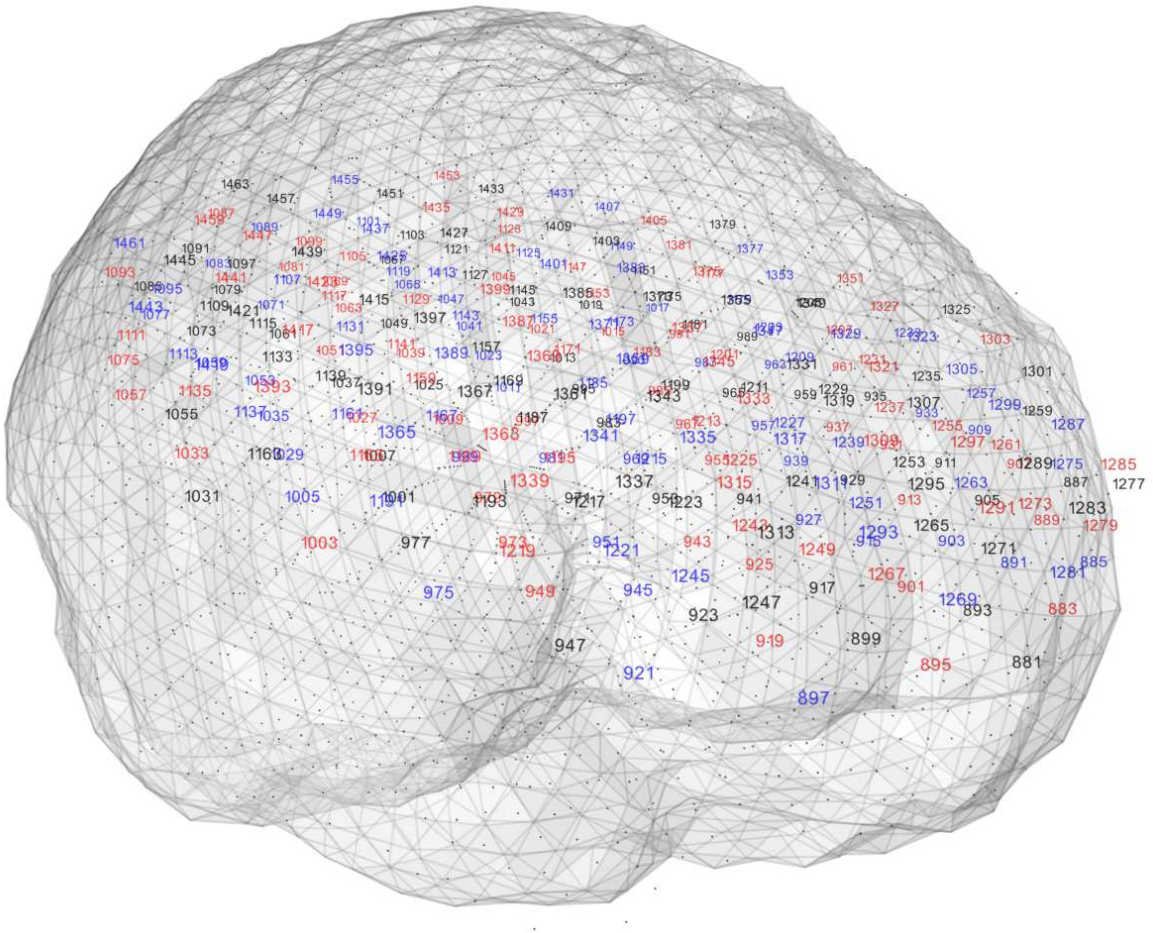

Figure G.4: Brain mesh with 10 mm of distance between elements, presenting elements 881 to 1464 of the mesh.

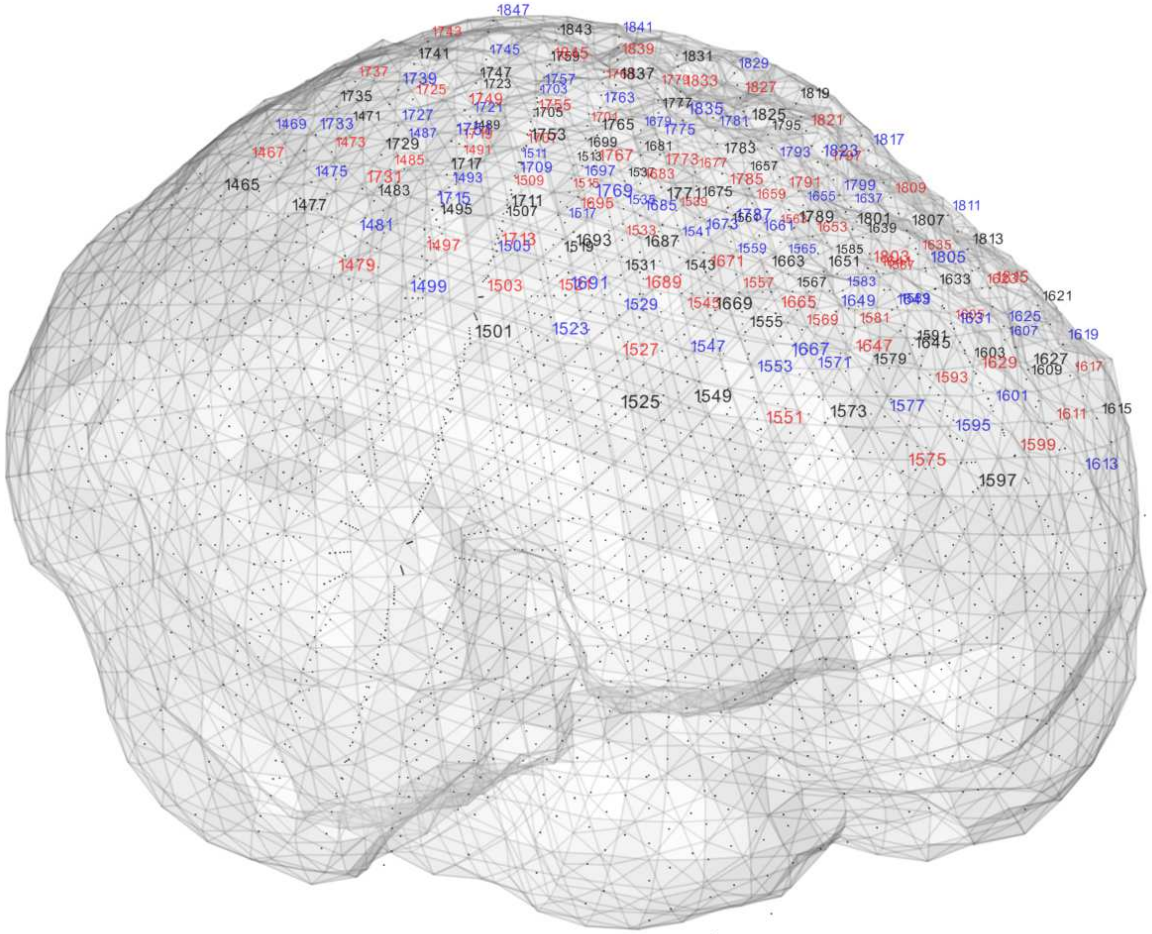

Figure G.5: Brain mesh with 10 mm of distance between elements, presenting elements 1465 to 1848 of the mesh.

Appendix H

Simulated and estimated coherence distributions

In this appendix are presented the statistical distributions for the simulated activity generated for 100 repetitions of three different experiments, as was presented in Section 6.3. The distributions are presented for the simulated activity used on the experiments and for the estimation of the coherence values obtained using the Linearly Constrained Minimum Norm Spatial filter in combination with the FOcal Undetermined System Solution algorithm, and using the Dynamic Imaging of Coherence Sources method. Moreover, the distributions are presented for two specific cases, when the brain interactions were simulated with a SNR of 22, and with a SNR of 11. The coherence distributions were obtained using the Fisher's transform for the spectral coherence obtained from the simulation and the estimations of the brain interactions. More details for the simulated activity and the implementation of the methods can be find in Chapter 6.

H.0.3 Simulated MEG activity with a SNR of 22

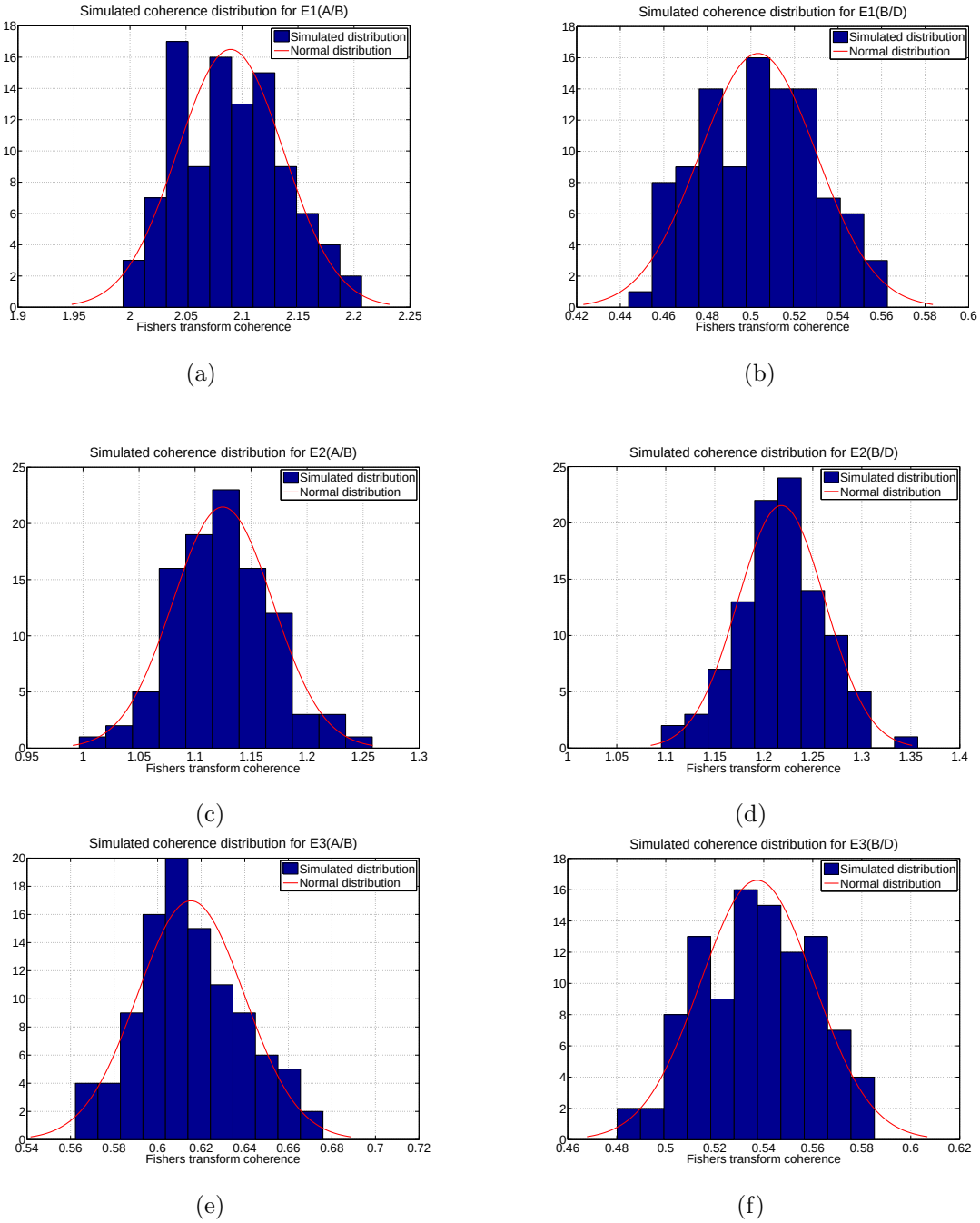

Figure H.1: Distribution for simulated interactions for three experiments, for a SNR of 22. The three experiments are labelled as *E1*, *E2* and *E3*, while the simulated interactions are represented as *A/B* and *B/D*. The correlation values used for the simulations can be observed in Table 6.10.

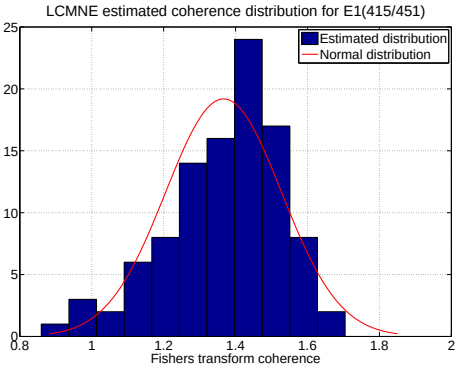

(a)

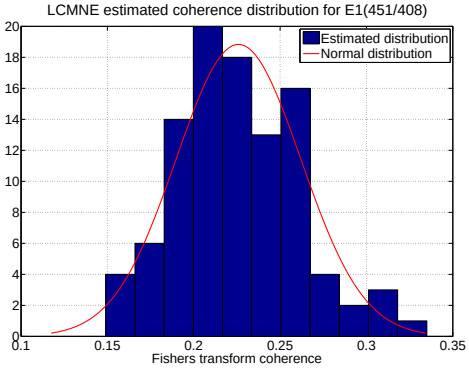

(b)

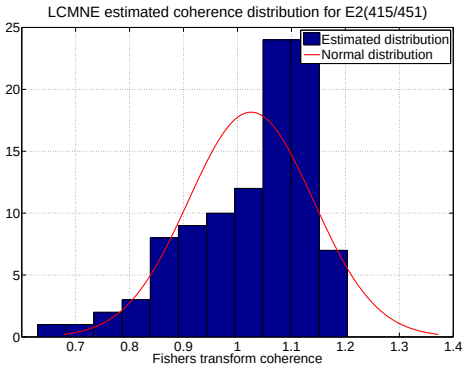

(c)

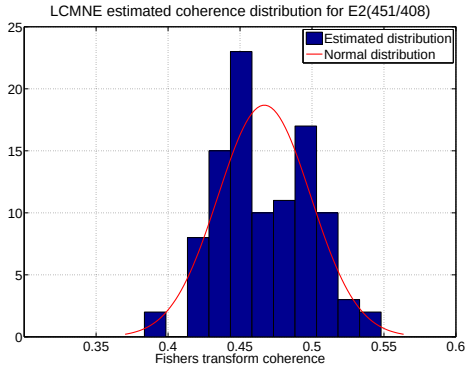

(d)

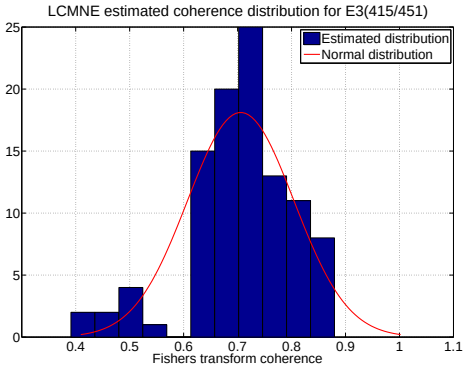

(e)

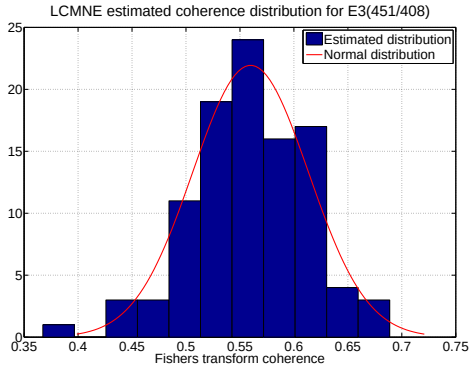

(f)

Figure H.2: Distribution for the active condition estimated brain interactions using the LCMNE with FOCUSS method for three different experiments, for a SNR of 22. The three experiments are labelled as *E1*, *E2* and *E3*, while the estimated interactions are represented as $415/451(\widehat{A}/\widehat{B})$ and $451/408(\widehat{B}/\widehat{D})$. The correlation values used for the simulations can be observed in Table 6.10.

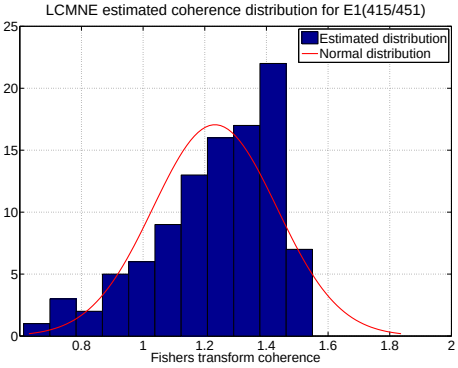

(a)

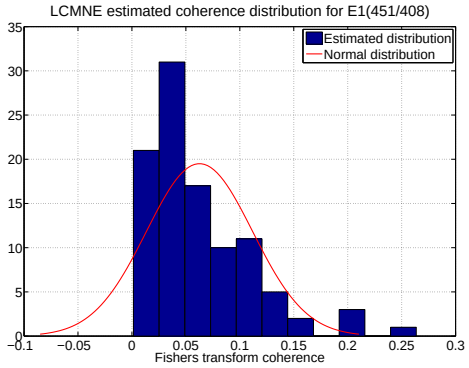

(b)

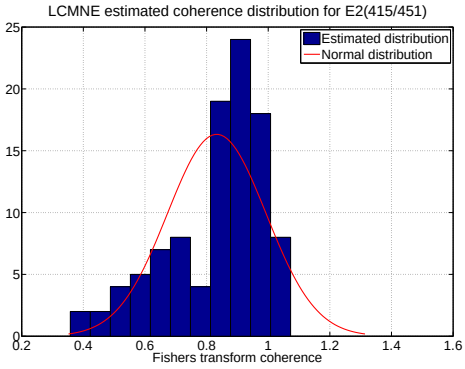

(c)

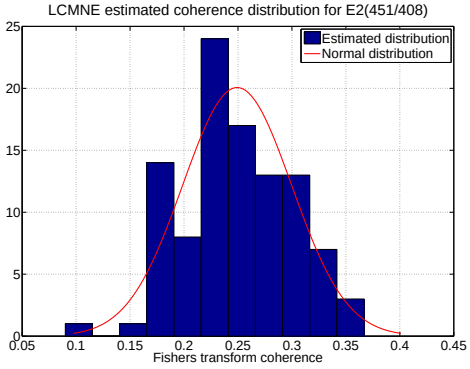

(d)

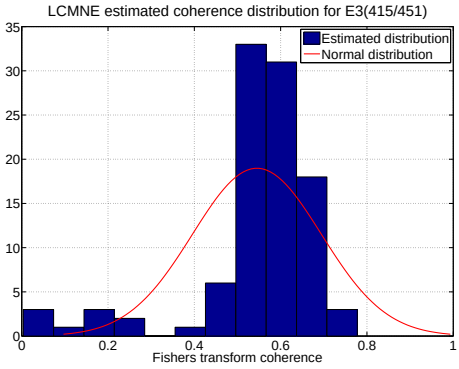

(e)

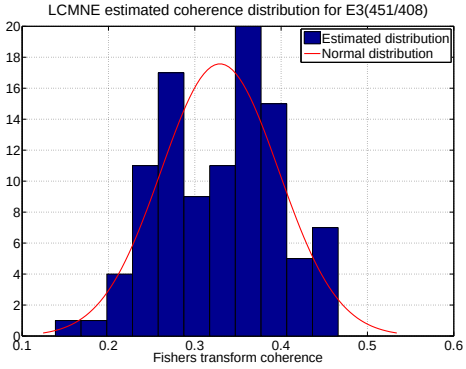

(f)

Figure H.3: Distribution for the difference between the active and control conditions estimated interactions using the LCMNE with FOCUSS method for three experiments, for a SNR of 22. The experiments are labelled as *E1*, *E2* and *E3*, while the estimated interactions are represented as $415/451(\widehat{A}/\widehat{B})$ and $451/408(\widehat{B}/\widehat{D})$. The correlation values used for the simulations can be observed in Table 6.10.

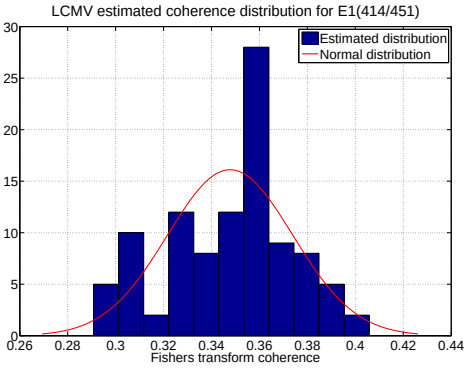

(a)

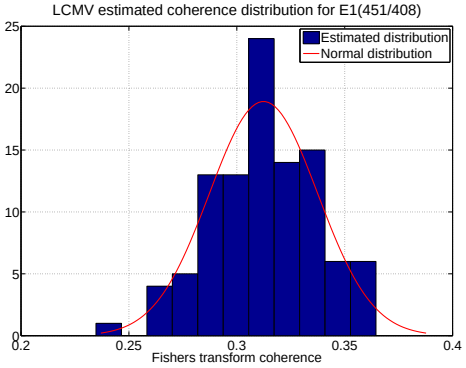

(b)

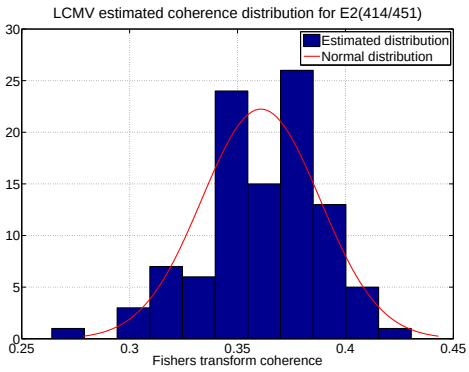

(c)

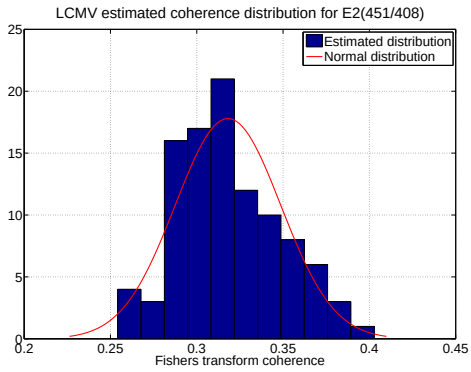

(d)

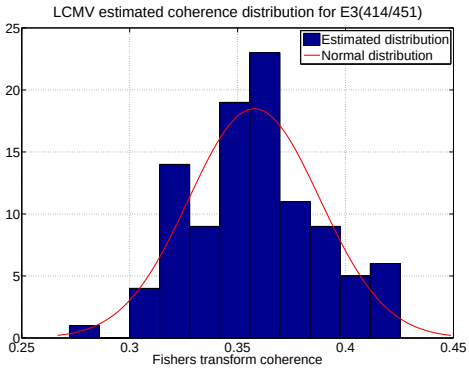

(e)

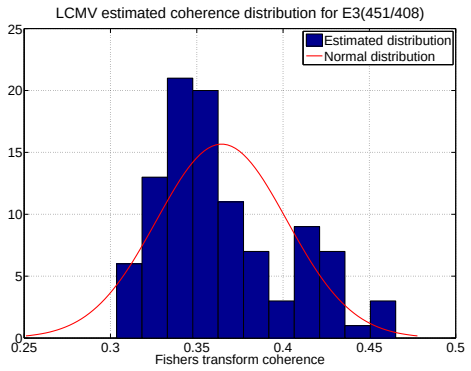

(f)

Figure H.4: Distribution for the active condition estimated brain interactions using DICS for three different experiments, for a SNR of 22. The three experiments are labelled as *E1*, *E2* and *E3*, while the estimated interactions are represented as $414/451(\widehat{A}/\widehat{B})$ and $451/408(\widehat{B}/\widehat{D})$. The correlation values used for the simulations can be observed in Table 6.10.

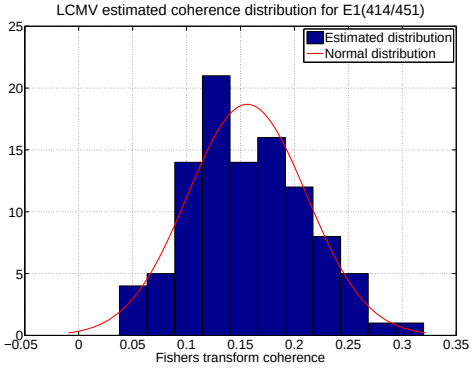

(a)

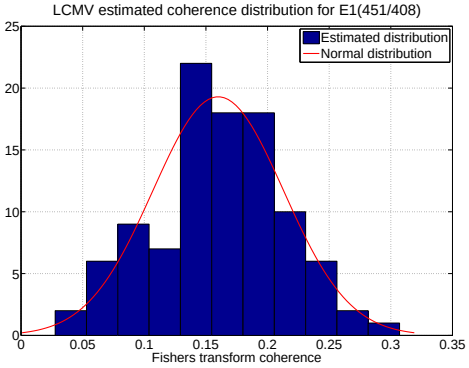

(b)

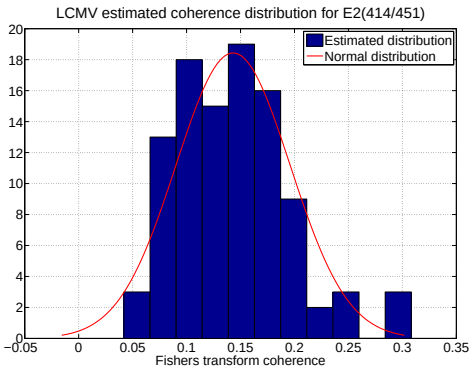

(c)

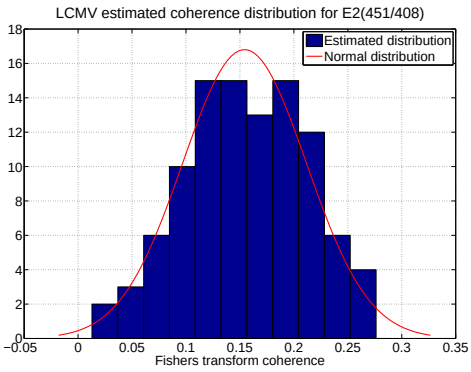

(d)

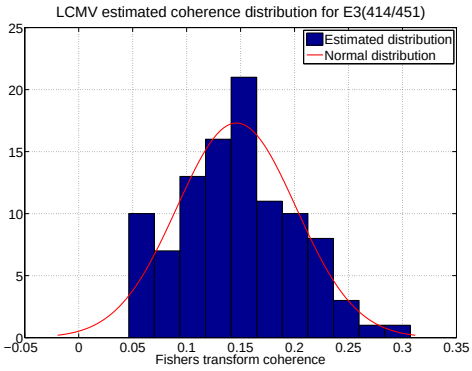

(e)

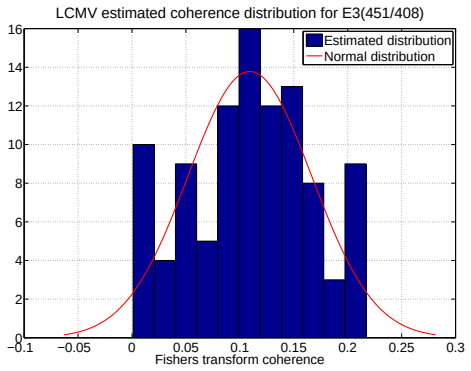

(f)

Figure H.5: Distribution for the difference between the active and control conditions estimated interactions using DICS for three experiments, for a SNR of 22. The experiments are labelled as *E1*, *E2* and *E3*, while the estimated interactions are represented as $414/451(\widehat{A}/\widehat{B})$ and $451/408(\widehat{B}/\widehat{D})$. The correlation values used for the simulations can be observed in Table 6.10.

H.0.4 Simulated MEG activity with a SNR of 11

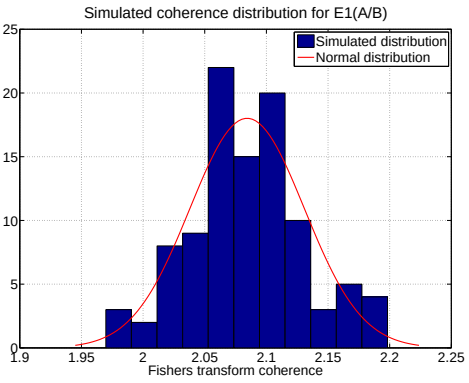

(a)

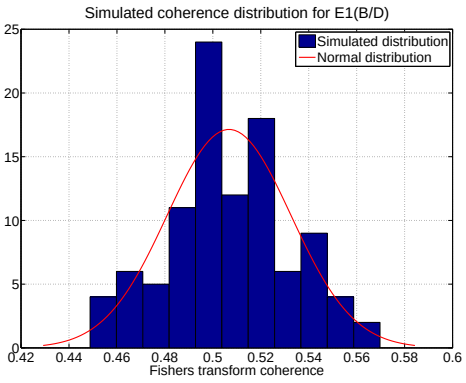

(b)

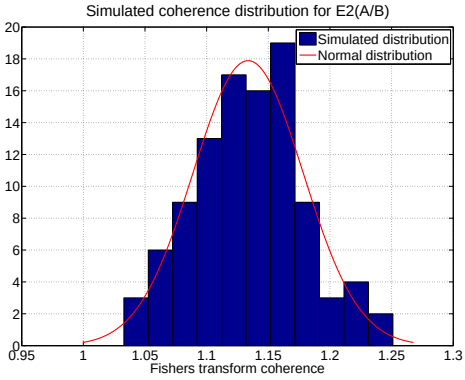

(c)

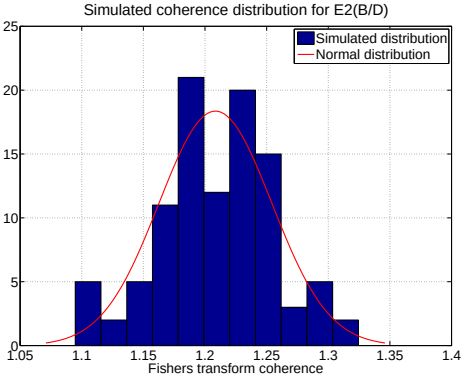

(d)

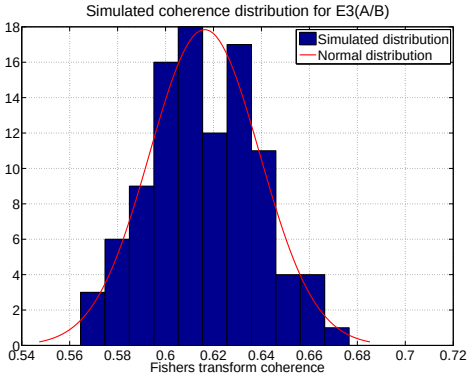

(e)

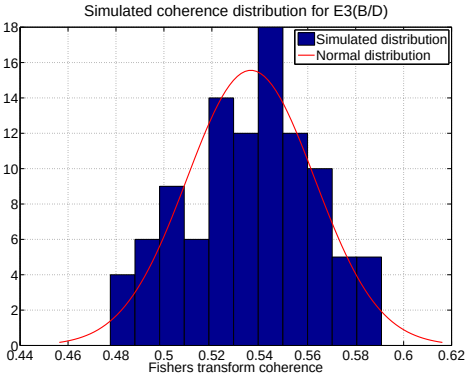

(f)

Figure H.6: Distribution for simulated interactions for three experiments, for a SNR of 11. The three experiments are labelled as *E1*, *E2* and *E3*, while the simulated interactions are represented as *A/B* and *B/D*. The correlation values used for the simulations can be observed in Table 6.10.

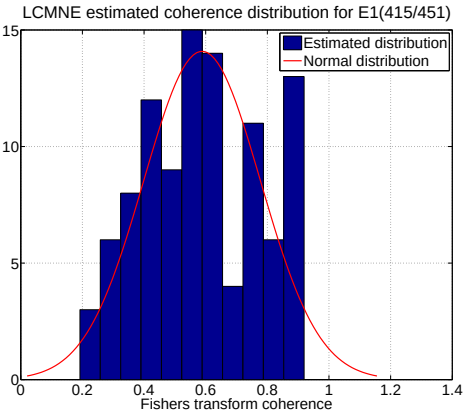

(a)

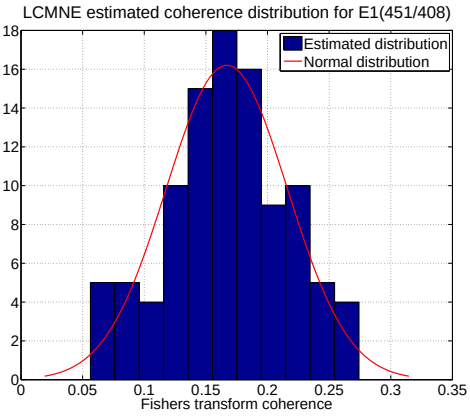

(b)

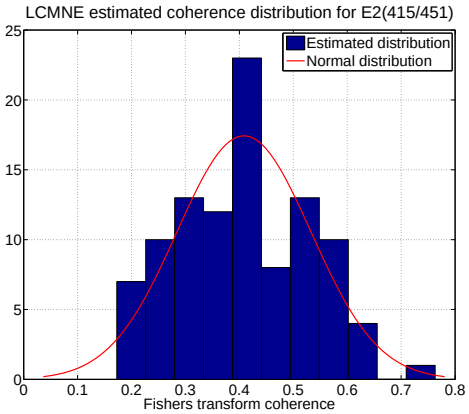

(c)

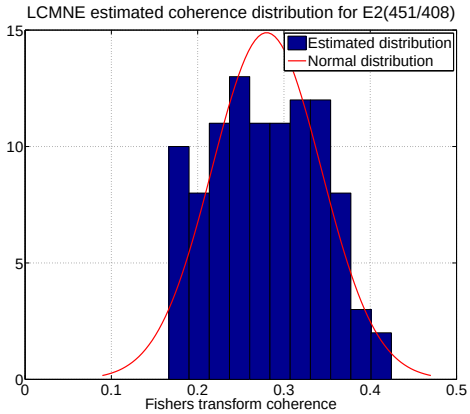

(d)

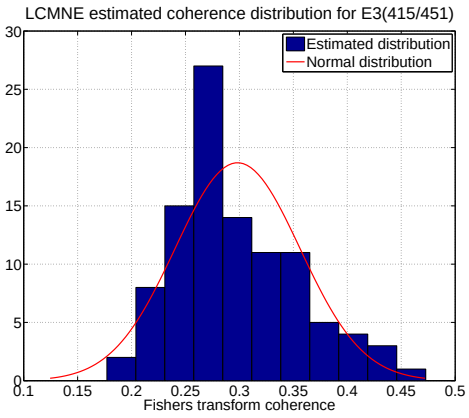

(e)

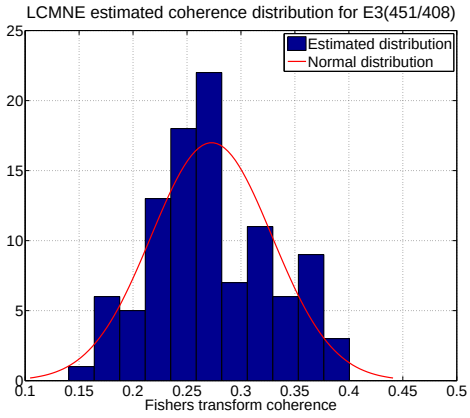

(f)

Figure H.7: Distribution for the active condition estimated brain interactions using the LCMNE with FOCUSS method for three different experiments, for a SNR of 11. The three experiments are labelled as *E1*, *E2* and *E3*, while the estimated interactions are represented as $415/451(\widehat{A}/\widehat{B})$ and $451/408(\widehat{B}/\widehat{D})$. The correlation values used for the simulations can be observed in Table 6.10.

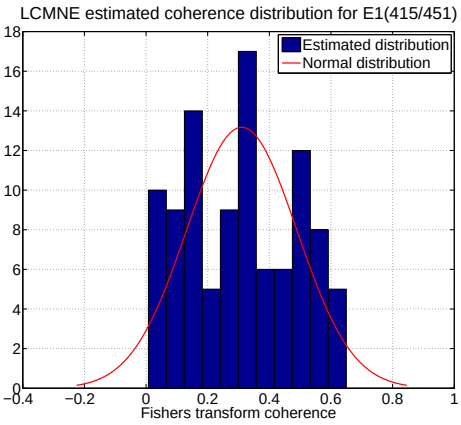

(a)

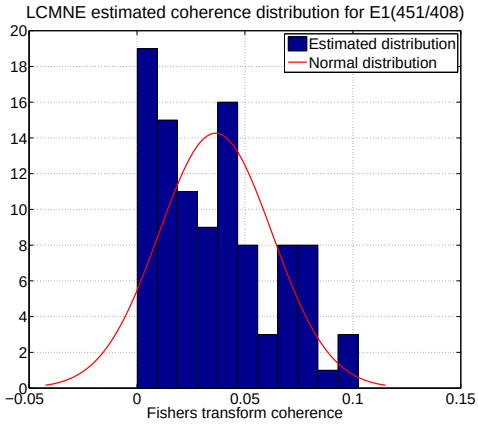

(b)

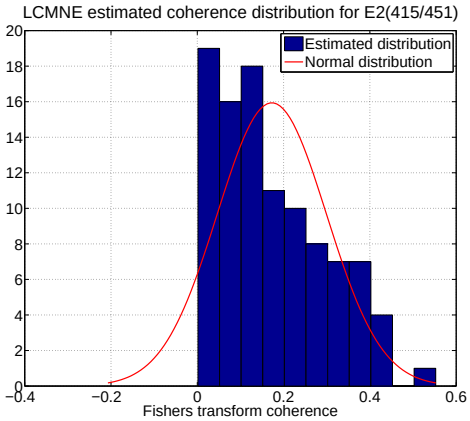

(c)

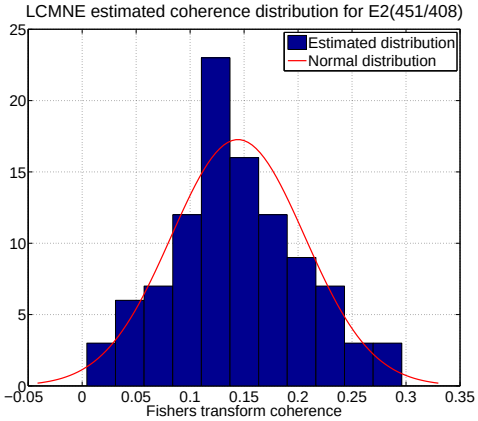

(d)

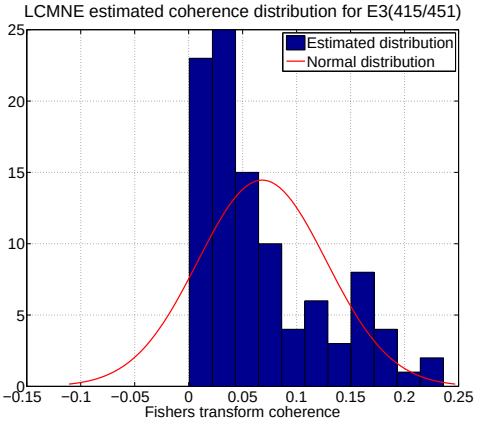

(e)

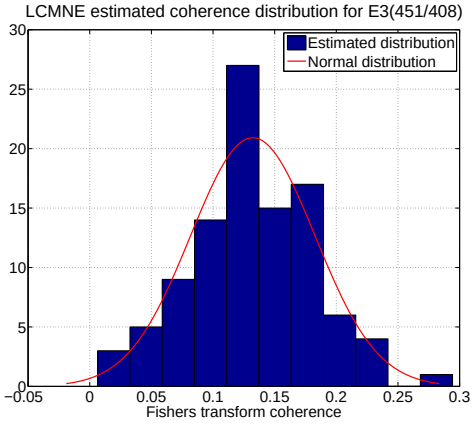

(f)

Figure H.8: Distribution for the difference between the active and control conditions estimated interactions using the LCMNE with FOCUSS method for three experiments, for a SNR of 11. The experiments are labelled as *E1*, *E2* and *E3*, while the estimated interactions are represented as $415/451(\widehat{A}/\widehat{B})$ and $451/408(\widehat{B}/\widehat{D})$. The correlation values used for the simulations can be observed in Table 6.10.

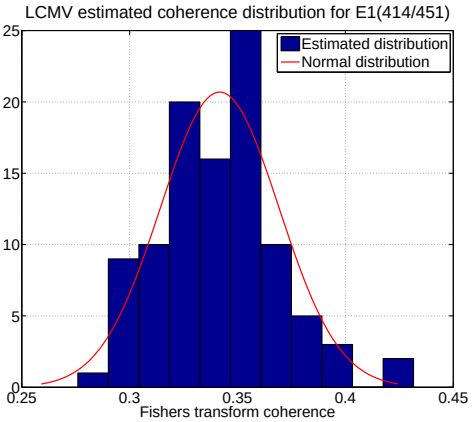

(a)

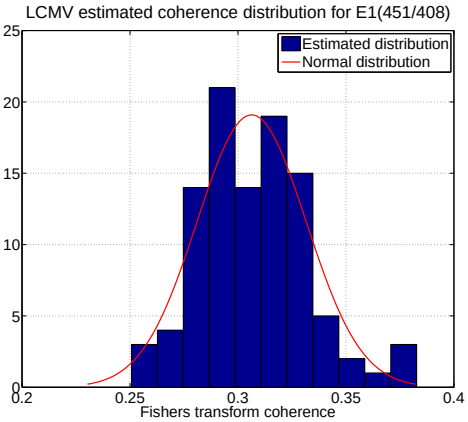

(b)

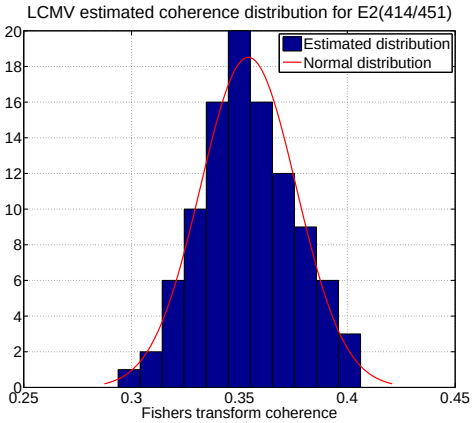

(c)

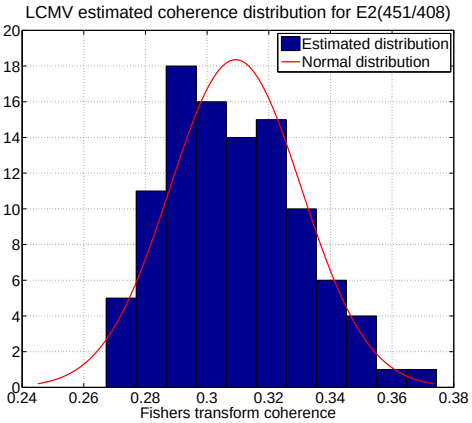

(d)

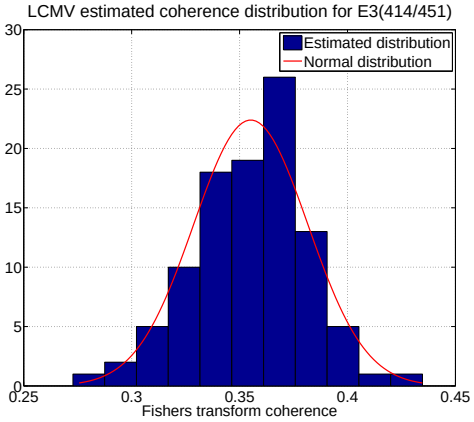

(e)

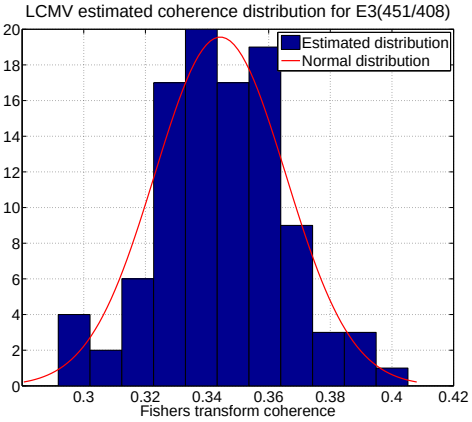

(f)

Figure H.9: Distribution for the active condition estimated brain interactions using DICS for three different experiments, for a SNR of 11. The three experiments are labelled as *E1*, *E2* and *E3*, while the estimated interactions are represented as $414/451(\widehat{A}/\widehat{B})$ and $451/408(\widehat{B}/\widehat{D})$. The correlation values used for the simulations can be observed in Table 6.10.

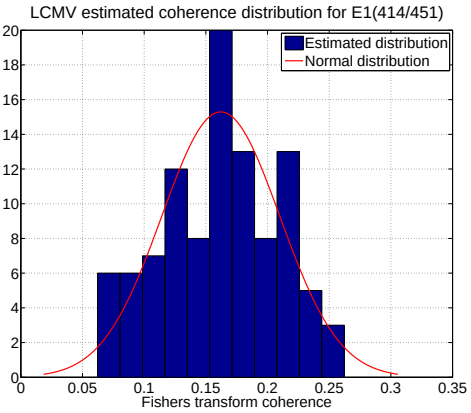

(a)

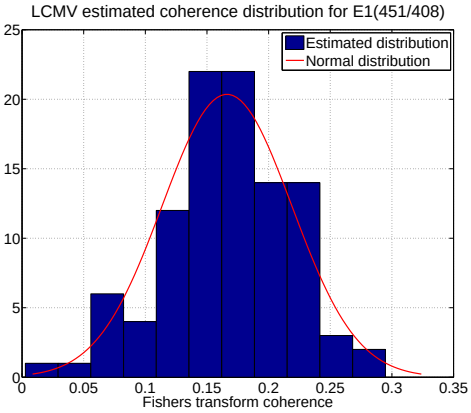

(b)

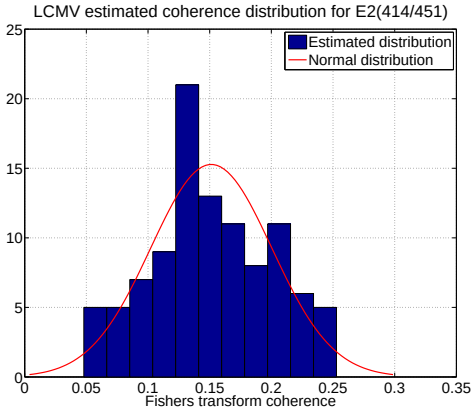

(c)

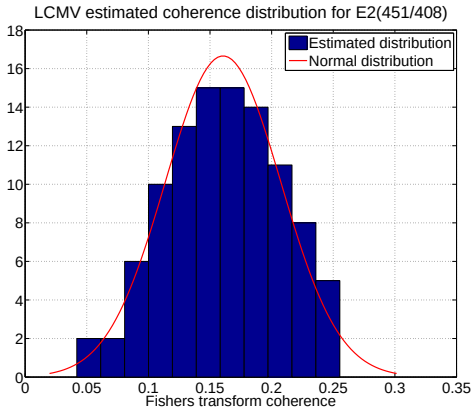

(d)

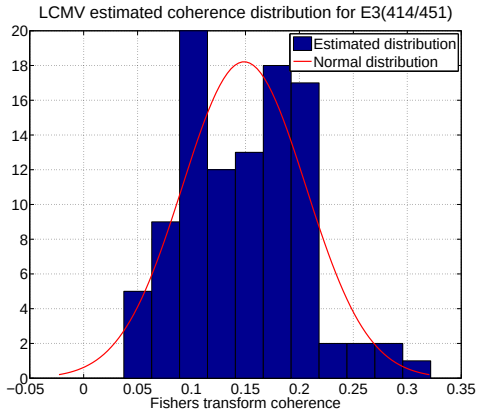

(e)

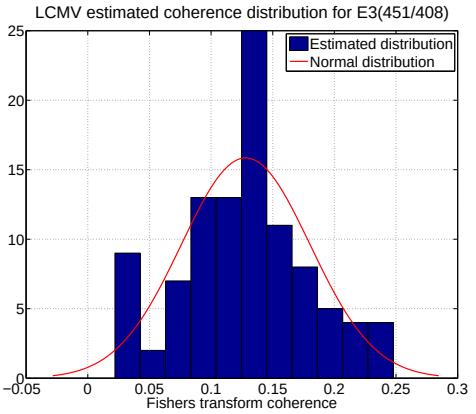

(f)

Figure H.10: Distribution for the difference between the active and control conditions estimated interactions using DICS for three experiments, for a SNR of 11. The experiments are labelled as *E1*, *E2* and *E3*, while the estimated interactions are represented as $414/451(\widehat{A}/\widehat{B})$ and $451/408(\widehat{B}/\widehat{D})$. The correlation values used for the simulations can be observed in Table 6.10.

Abbreviations

ALM Augmented Lagrange Multipliers

AR Autoregressive

BCI Brain Control Interface

BCMV Bilinear Constraints Minimum Variance

DICS Dynamic Imaging of Coherent Sources

ECD Equivalent Current Dipole

EEG Electroencephalography

FFT Fast Fourier Transform

fMRI functional Magnetic Resonance Imaging

FOCUSS FOCal Undertermined System Solution

FWER Family Wise Error Rate

FWHM Full Width Half Maximum

LCMNE Linearly Constrained Minimum Norm Estimates

LCMV Linearly Constrained Minimum Variance

MEG Magnetoencephalography

MNE Minimum Norm Estimates

MUSIC MUltiple SIgnal Classification

NAI Neural Activity Index

sLORETA Standardized low-resolution electromagnetic tomography

SNR Signal to Noise Ratio

SQUID Superconductor QUantum Interface Device

SVD Singular Value Decomposition

SVDT Singular Value Decomposition Truncation

YNIC York NueroImaging Centre

Nomenclature

σ Brain conductivity

μ_0 Permeability of the free space

λ_{LM} Lagrange multipliers

$\nabla\cdot$ Divergence operator

$\nabla\times$ Curl operator

$\delta/\delta t$ Partial derivative operator

σ_x Standar deviation for the $\mathbf{x}$ variable

$\gamma_{xy}(f)$ Cross-spectrum between variables $\mathbf{x}$ and $\mathbf{y}$

$\mathbf{\Gamma}_{\mathbf{r}_i\mathbf{r}_j}(f)$ Cross spectral density matrix between ECDs located at positions $\mathbf{r}_i$ and $\mathbf{r}_j$

$\widehat{\mathbf{\Gamma}}_{\mathbf{r}_i\mathbf{r}_j}(f)$ Estimated cross spectral density matrix for ECDs located at positions $\mathbf{r}_i$ and $\mathbf{r}_j$

$\mathbf{\Gamma}(f)$ Cross spectral density matrix for $\mathbf{x}$, for a specific frequency

$\mathbf{\Gamma}(F_w)$ Cross spectral density matrix for $\mathbf{x}$, for a band of frequencies

$\mathbf{a}_m$ Unity vector normal to the m SQUID sensor surface

$\mathbf{B}$ Magnetic fields generated by the neuronal currents

c_{xy} Correlation between variables $\mathbf{x}$ and $\mathbf{y}$

$\mathbf{C}^n$ Higher order covariance matrix for the measured magnetic fields

$\mathbf{C}(\mathbf{x})$ Covariance matrix for the measured magnetic fields

$\mathbf{Cq}_i$ Covariance matrix for the brain source located at position $\mathbf{r}_i$

$\mathbf{C}(\mathbf{q}_p, \mathbf{q}_i)$ Cross covariance matrix for ECDs located at positions $\mathbf{r}_i$ and $\mathbf{r}_j$

$\widehat{\mathbf{C}}(\mathbf{q}_p, \mathbf{q}_i)$ Estimated cross covariance matrix for ECDs located at positions $\mathbf{r}_i$ and $\mathbf{r}_j$

$\mathbf{C}(\mathbf{m})$ Covariance matrix for the brain sources or ECDs

$\mathbf{D}(\mathbf{r}_i)$ Matrix of constraints used on the LCMNE design

$\mathbf{E}$ Electric fields generated by the neuronal currents

f Specific frequency

Fw Band of frequencies

$g_m(f)$ FFT for the m sensor measured magnetic fields

$\mathbf{g}(f)$ Frequency domain representation of $\mathbf{x}$

$\mathbf{H}$ Composite leadfield matrix

$\mathbf{H}^+$ Generalize inverse of the composite leadfield matrix

$\boldsymbol{I}$ Identity matrix

$\mathbf{J}^p$ Transmembrane or primary currents

$\mathbf{J}^v$ Passive or volume currents

$\mathbf{J}$ Neuronal currents

$\boldsymbol{l}_m(\mathbf{r}_i)$ Leadfield vector for the $\mathbf{r}_i$ brain source and the m SQUID sensor

$\boldsymbol{L}(\mathbf{r}_i)$ Leadfield matrix for the $\mathbf{r}_i$ brain source

$\mathbf{L}_{DUAL}$ Dual leadfields for the dual-core beamformer

$\mathbf{m}$ Equivalent current dipoles composite matrix

$\widehat{\mathbf{m}}$ Estimated ECDs composite matrix

M Number of SQUID sensors used

N Number of equivalent current dipoles or brain sources used

$\mathbf{n}$ Magnetic fields measurements due to the effects of the external noise

$\mathbf{q}$ Equivalent current dipole

$\widehat{\mathbf{q}}$ Estimated equivalent current dipole activity

q Scalar magnitude for the equivalent current dipole

$\mathbf{Q_n}$ Covariance matrix for the external noise

$\mathbf{Q}_n^n$ Higher order covariance matrix for $\mathbf{n}$

$\mathbf{r}_1$ Location for the ECD positive charge

$\mathbf{r}_2$ Location for the ECD negative charge

$\mathbf{r}$ Location for the measurements of the magnetic fields

$\mathbf{r}_i$ Location for the neuronal currents

$R_{xy}(f)$ Spectral coherence for the $\mathbf{x}$ and $\mathbf{y}$ variables

t Time instant for the measurements of the brain magnetic fields or neuronal currents

V Scalar value for the neuron membrane potential

$\mathbf{x}$ Magnetic fields measurements due to the effects of the neuronal currents

$\overline{x}$ Mean for the $\mathbf{x}$ variable

$\mathbf{W}_{ls}(\mathbf{r}_i)$ Weights for the MNE spatial filter

$\mathbf{W}(\mathbf{r}_i)$ Weights for the LCMNE spatial filter

$\mathbf{W}_b(\mathbf{r}_i)$ Weights for the LCMV spatial filter

$\mathbf{W}_{1b}(\mathbf{r}_i)$ Weights for the BCMV spatial filter

$\mathbf{W}_{2b}(\mathbf{r}_i)$ Weights for the BCMV spatial filter

$\mathbf{W}_{b4}(\mathbf{r}_i)$ Weights for the LCMV-type 4 spatial filter

$\mathbf{W}_u$ Unbiased MNE weights matrix

$\mathbf{W}_{Fk}$ FOCUSS weights matrix

Bibliography

Richard Abrahamsson, Steven M. Kay, and Petre Stoica. Estimation of the parameters of a bilinear model with applications to submarine detection and system identification. *Digital signal processing*, 17(4):756–773, 2007.

A. Angelidou, M. G. Strintzis, S. Panas, and G. Anogianakis. On AR modelling for MEG spectral estimation, data compression and classification. *Computers in biology and medicine*, 22(4):379–387, 1992.

Luiz A. Baccalá and Koichi Sameshima. Partial directed coherence: a new concept in neural structure determination. *Biomedical Cybernetics*, 84(6):463–474, 2001.

Er-Wei Bai and Yun Liu. On the least squares solutions of a system of bilinear equations. *IEEE conference on decision and control*, 44(2):1197–1201, 2005.

Er-Wei Bai and Yun Liu. Least squares solutions of bilinear equations. *Systems & control letters*, 55(6):466–472, 2006.

Sylvain Baillet, John C. Mosher, and Richard M. Leahy. Electromagnetic Brain Mapping. *Signal Processing Magazine, IEEE*, 18(6):14–30, 2001.

Gareth R. Barnes and Arjan Hillebrand. Statistical flattening of MEG beamformer images. *Human brain mapping*, 18(1):1–12, 2003.

Mark F. Bear, Barry W. Connors, and Michael A. Paradiso. *Neuroscience: Exploring the Brain*. Lippincott Williams & Wilkins, 3th edition edition, 2007.

Maxwell R Bennett, Peter Michael Stephan Hacker, and MR Bennett. *Philosophical foundations of neuroscience*. Blackwell Oxford, 2003.

Matthew J. Brookes, Claire M. Stevenson, Gareth R. Barnes, Arjan Hillebrand, Michael I. G. Simpson, Susan T. Francis, and Peter G. Morris. Beamformer reconstruction of correlated sources using a modified source model. *Neuroimage*, 34(4):1454–1465, 2007.

Matthew J. Brookes, Mark Woolrich, Darren Price, Joanne R. Hale, Mary C. Stephenson, Gareth R. Barnes, Stephen M. Smith, and Peter G. Morris. Investigating the electrophysiological basis of resting state networks using magnetoencephalography. *National Acad Sciences*, 108(40):16783–16788, 2011.

Richard B. Buxton. *Introduction to functional magnetic resonance imaging: principles and techniques*. Cambridge university press, 2nd edition, 2009.

Joseph Carey and Lydia V Kibiuk. *Brain facts: A primer on the brain and nervous system*. Society for Neuroscience, 1990.

Chris Chatfield. *The analysis of time series: an introduction*. Chapman & Hall/CRC, fifth edition, 1995.

Wilkin Chau, Anthony R. McIntosh, Stephen E. Robinson, Matthias Schulz, and Christo Panteva. Improving permutation test power for group analysis of spatially filtered MEG data. *NeuroImage*, 23(3):983–996, 2004.

David Keun Cheng. *Field and wave electromagnetics*. Addison-Wesley New York, 1989.

Eric H. Chudler. *Inside Your Brain*. Infobase Publishing, 2009.

John Clarke and Alex I Braginski. *The SQUID handbook: fundamentals and technology of SQUIDs and SQUID Systems, Volume I*. Wiley-VCH Verlag GmbH&Co, KGaA, Weinheim, 2004.

John Clarke and Alex I Braginski. *The SQUID handbook. Vol. 2. Applications of SQUIDs and SQUID systems*. Wiley-VCH Verlag GmbH&Co, KGaA, Weinheim, 2006.

Scott Cohen and Carlo Tomasi. *System of bilinear equations*. Stanford University, Department of Computer Science, 1997.

Sarang S Dalal, Kensuke Sekihara, and Srikantan S Nagarajan. Modified beamformers for coherent source region suppression. *Biomedical Engineering, IEEE Transactions on*, 53(7): 1357–1363, 2006.

Sarang S. Dalal, Adrian G Guggisberg, Erik Edwards, Kensuke Sekiraha, Anne M. Findlay, Ryan T. Canolty, Mitchel S. Berger, Nicholas M Barbaro Knight, Heidi E. Kirsh, and Srikantan S. Nagarajan. Five-dimensional neuroimaging: localization of the time–frequency dynamics of cortical activity. *NeuroImage*, 40(4):1686–1700, 2008.

Olivier David, Diego Cosmelli, Jean-Philippe Lachaux, Sylvain Baillet, Line Garnero, and Jacques Martinerie. A theoretical and experimental introduction to the non-invasive study of large-scale neural phase synchronization in human beings. *International Journal of Computational Cognition*, 1(4):53–77, 2003.

Olivier David, Diego Cosmelli, and Karl J. Friston. Evaluation of different measures of functional connectivity using a neural mass model. *NeuroImage*, 21(2):659–673, 2004.

Olivier David, Stefan J Kiebel, Lee M Harrison, Jérémie Mattout, James M Kilner, and Karl J Friston. Dynamic causal modeling of evoked responses in EEG and MEG. *NeuroImage*, 30 (4):1255–1272, 2006.

Alessio Del Bue, Joao Xavier, Lourdes Agapito, and Marco Paladini. Bilinear modeling via augmented lagrange multipliers (balm). *Pattern Analysis and Machine Intelligence, IEEE Transactions on*, 34(8):1496–1508, 2012.

Mithun Diwakar, Ming-Xiong Huang, Ramesh Srinivasan, Deborah L. Harrington, Ashley Robb, Annemarie Angeles, Laura Muzzatti, Reza Pakman, Tao Song, Rebecca J. Theilmann, and Roland R. Lee. Dual-core beamformer for obtaining highly correlated neuronal networks in MEG. *Neuroimage*, 54(1):253–563, 2011.

Andrew A Fingelkurts, Alexander A Fingelkurts, and Seppo Kähkönen. Functional connectivity in the brainis it an elusive concept? *Neuroscience & Biobehavioral Reviews*, 28(8): 827–836, 2005.

Stanley Finger. *Origins of neuroscience: a history of explorations into brain function*. Oxford University Press, 2001.

Armin Fuchs. Beamforming and its applications to brain connectivity. In Viktor K. Jirsa and A. R. McIntosh, editors, *Handbook of Brain Connectivity*, pages 357–378. Springer, 2007.

William Gaetz and Douglas Cheyne. Localization of sensorimotor cortical rhythms induced by tactile stimulation using spatially filtered MEG. *NeuroImage*, 30(3):899–908, 2006.

Gene H Golub and Charles F Van Loan. *Matrix computations*, volume 3. JHU Press, 2012.

Irina F Gorodnitsky and Bhaskar D Rao. Sparse signal reconstruction from limited data using FOCUSS: A re-weighted minimum norm algorithm. *Signal Processing, IEEE Transactions on*, 45(3):600–616, 1997.

Irina F. Gorodnitsky, John S. George, and Bhaskar D. Rao. Neuromagnetic source imaging with FOCUSS: a recursive weighted minimum norm algorithm. *Electroencephalography and clinical Neurophysiology*, 95(4):231–251, 1995.

L John Greenfield, James D Geyer, and Paul R Carney. *Reading EEGs: a practical approach*. Lippincott Williams & Wilkins, 2012.

David Jeffrey Griffiths and Reed College. *Introduction to electrodynamics*, volume 3. Prentice hall Upper Saddle River, NJ, 1999.

Joachim Gross, Jan Kujala, Matti Hämäläinen, Lars Timmermann, Alfons Schnitzler, and Riitta Salmelin. Dynamic imaging of coherent sources: studying neural interactions in the human brain. *Proceedings of the National Academy of Sciences*, 98(2):694–699, 2001.

Joachim Gross, L Timmermann, J Kujala, R Salmelin, and A Schnitzler. Properties of MEG tomographic maps obtained with spatial filtering. *NeuroImage*, 19(4):1329–1336, 2003.

Matti Hämäläinen, Riitta Hari, Risto J Ilmoniemi, Jukka Knuutila, and Olli V Lounasmaa. Magnetoencephalographytheory, instrumentation, and applications to noninvasive studies of the working human brain. *Reviews of modern Physics*, 65(2):413, 1993.

Matti S Hämäläinen and RJ Ilmoniemi. Interpreting magnetic fields of the brain: minimum norm estimates. *Medical & Biological Engineering & Computing*, 32(1):35–42, 1994.

Todd C. Handy, editor. *Brain signal analysis: advances in neuroelectric and neuromagnetic methods*. MIT Press, 2009.

Per Christian Hansen. The truncatedsvd as a method for regularization. *BIT Numerical Mathematics*, 27(4):534–553, 1987.

Peter C. Hansen, Morten L. Kringelbach, and Riitta Salmelin. *MEG An Introduction to Methods*. Oxford University Press, 2nd edition edition, 2010.

M-X Huang, J. J. Shih, R. R. Lee, D. L. Harrington, R. J. Thoma, M. P. Weisend, F. Hanlon, K. M. Paulson, T. Li, K. Martin, and J. M. Canive. Commonalities and differences among vectorized beamformers in electromagnetic source imaging. *Brain Topography*, 16(3):139–158, 2004.

Toshiaki Imada. A method for MEG data that obtains linearly-constrained minimum-variance beamformer solution by minimum-norm least-squares method. In *17th Interna-*

tional Conference on Biomagnetism Advances in Biomagnetism–Biomag2010, pages 152–154. Springer, 2010.

Kazufumi Ito and Karl Kunisch. *Lagrange multiplier approach to variational problems and applications*, volume 15. SIAM, 2008.

O. Jensen and Simo Vanni. A new method to identify multiple sources of oscillatory activity from magnetoencephalographic data. *Neuroimage*, 15(3):568–574, 2002.

Karim Jerbi, Jean-Philippe Lachaux, Karim N'Diaye, Dimitrios Pantazis, Richard Leahy, Line Garnero, and Sylvain Baillet. Coherent neural representation of hand speed in humans revealed by MEG imaging. *Proceedings of the National Academy of Sciences*, 104(18):7676–7681, 2007.

Viktor K Jirsa and Anthony R McIntosh. *Handbook of brain connectivity*. Springer, 2007.

Jan Kujala, Kristen Pammer, Piers Cornelissen, Alard Roebroeck, Elia Formisano, and Riitta Salmelin. Phase coupling in a cerebro-cerebellar network at 8–13 Hz during reading. *Cerebral Cortex*, 17(6):1476–1485, 2007.

Jan Kujala, Joachim Gross, and Riitta Salmelin. Localization of correlated network activity at the cortical level with MEG. *Neuroimage*, 39(4):1706–1720, 2008.

Isamu Kumihashi and Kensuke Sekihara. Array-gain constraint minimum-norm spatial filter with recursively updated gram matrix for biomagnetic source imaging. *IEEE Transactions on Biomedical Engineering*, 57(6):1358–1365, 2010.

Yoram Leedan and Peter Meer. Heteroscedastic regression in computer vision: Problems with bilinear constraint. *Internation journal of computer vision*, 37(2):127–150, 2000.

Alberto Leon Garcia. *Probability and Random Processes for Electrical Engineering*. Addison-Wesley, second edition, 1994.

M Liljeström, J Kujala, O Jensen, and R Salmelin. Neuromagnetic localization of rhythmic activity in the human brain: a comparison of three methods. *NeuroImage*, 25(3):734–745, 2005.

Fa-Hsuan Lin, Thomas Witzel, Matti S Hämäläinen, Anders M Dale, John W Belliveau, and Steven M Stufflebeam. Spectral spatiotemporal imaging of cortical oscillations and interactions in the human brain. *NeuoImage*, 23(2):582–595, 2004.

Bin Liu and Mauricio D. Sacchi. Minimum weighted norm interpolation of seismic records. *Society of Exploration Geophysicists*, 69(6):1034–1043, 2004.

Zhong-Lin Lu and Lloyd Kaufman. *Magnetic source imaging of the human brain.* Taylor & Francis, 2003.

Bernd Lütkenhöner. Magnetoencephalography and its Achilles' heel. *Journal of Physiology-Paris*, 97(4):641–658, 2003.

Jaakko Malmivuo. Biomagnetism. In Joseph H. Bronzino, editor, *The Biomedical Engineering Handbook*. CRC press, 2000.

Jaakko Malmivuo, Veikko Suihko, and Hannu Eskola. Sensitivity distributions of EEG and MEG measurements. *Biomedical Engineering, IEEE Transactions on*, 44(3):196–208, 1997.

Eric Maris and Robert Oostenveld. Nonparametric statistical testing of EEG-and MEG-data. *Journal of neuroscience methods*, 164(1):177–190, 2007.

Peter C. Mignerey. Constrained estimates of multipath covariance. *Antennas and Propagation, IEEE Transactions on*, 37(1):107–113, 1989.

John C. Mosher and Richard M. Leahy. Recursive MUSIC: A Framework for EEG and MEG Source Localization. *Biomedical Engineering, IEEE Transactions on*, 45(11), November 1998.

John C. Mosher, Richard M. Leahy, and Paul S. Lewis. EEG and MEG: forward solutions for inverse methods. *Biomedical Engineering, IEEE Transactions on*, 46(3):245–259, 1999.

John C Mosher, Sylvain Baillet, and Richard M Leahy. Equivalence of linear approaches in bioelectromagnetic inverse solutions. In *Statistical Signal Processing, 2003 IEEE Workshop on*, pages 294–297. IEEE, 2003.

Thomas E. Nichols and Andrew P. Holmes. Nonparametric permutation tests for functional neuroimaging: a primer with examples. *Human brain mapping*, 15(1):1–25, 2002.

Ernst Niedermeyer and Fernando Lopes Da Silva. *Electroencephalography: basic principles, clinical applications, and related fields.* Lippincott Williams & Wilkins, 2005.

Paul L. Nunez and Ramesh Srinivasan. *Electric fields of the brain: the neurophysics of EEG.* Oxford university press, 2nd edition edition, 2006.

Dimitrios Pantazis, Thomas E. Nichols, Sylvain Baillet, and Richard M. Leahy. Spatiotemporal localization of significant activation in MEG using permutation tests. In *Information Processing in Medical Imaging*, pages 512–523. Springer, 2003.

Andrew C. Papanicolaou. *Clinical magnetoencephalography and magnetic source imaging.* Cambridge University Press, 2009.

R. D. Pascual-Marqui. Standardized low-resolution brain electromagnetic tomography (sLORETA): technical details. *Methods Find Exp Clin Pharmacol*, 24(Suppl D):5–12, 2002.

Wilder Penfield and Herbert Jasper. *Epilepsy and the functional anatomy of the human brain.* Little, Brown & Co., 1st edition edition, 1954.

Dimitrios Pentazis, Thomas E. Nichols, Sylvain Baillet, and Ruchard M. Leahy. A comparison of random field theory and permutation methods for the statistical analysis of MEG data. *NeuroImage*, 25(2):383–394, 2005.

Luis R. Peraza R. *Fourier Bayesian networks; A novel approach for network structure inference with application to brain connectivity studies from magnetoencephalographic recordings.* PhD thesis, University of York, 2012.

Donald B. Percival and Andrew T. Walden. *Spectral analysis for physical applications.* Cambridge University Press, 1998.

Vittorio Pizzela, Stefania Della Penna, Cosimo Del Gratta, and Gian Luca Romani. SQUID systems for biomagnetic imaging. *Superconductor Science and Technology*, 14(7):R79–R114, 2001.

H. Preissl. *Magnetoencephalography.* Gulf Professional Publishing, 2005.

J. A. Sanchez and D. M. Halliday. Reducing the effect of correlated brain sources in meg using a linearly constrained spatial filter based on minimum norm. In *Signals, Systems and Computers, 2013 Asilomar Conference on*, pages 1828–1832. IEEE, 2013.

Jukka Sarvas. Basic mathematical and electromagnetic concepts of the biomagnetic inverse problem. *Physics in medicine and biology*, 32(1):11, 1987.

Hayasaka Satoru and Thomas E. Nichols. Combining voxel intensity and cluster extent with permutation test framework. *Neuroimage*, 23(1):54–63, 2004.

G. Schalk, D. J. McFarland, T. Hinterberger, N. Birbaumer, and J. R. Wolpaw. BCI2000: a general-purpose brain-computer interface (BCI) system. *Biomedical Engineering, IEEE Transactions on*, 51(6):1034–1043, 2004.

Jan-Mathijs Schoffelen and Joachim Gross. Source connectivity analysis with MEG and EEG. *Human Brain Mapping*, 30(6):1857–1865, 2009.

Jan-Mathijs Schoffelen and Joachim Gross. Improving the interpretability of all-to-all pairwise source connectivity analysis in MEG with nonhomogeneous smoothing. *Human Brain Mapping*, 32(3):426–437, 2011.

Kensuke Sekihara and Srikantan S. Nagarajan. *Adaptive spatial filters for electromagnetic brain imaging*. Springer, 2008.

Kensuke Sekihara and Srikantan S Nagarajan. Residual coherence and residual envelope correlation in meg/eeg source-space connectivity analysis. In *Engineering in Medicine and Biology Society (EMBC), 2013 35th Annual International Conference of the IEEE*, pages 4414–4417. IEEE, 2013.

Kensuke Sekihara, Srikantan S. Nagarajan, David Poeppel, Alec Marantz, and Yasushi Miyashita. Reconstructing spatio-temporal activities of neural sources using an MEG vector beamformer technique. *IEEE Transactions on Biomedical Engineering*, 48(7):760–771, 2001.

Kensuke Sekihara, Srikantan S. Nagarajan, David Poeppel, and Alec Marantz. Performance of an MEG adaptive-beamformer technique in the presence of correlated neural activities: effects on signal intensity and time-course estimates. *Biomedical Engineering, IEEE Transactions on*, 49(12):1534–1546, 2002.

Kensuke Sekihara, Maneesh Sahani, and Srikantan S. Nagarajan. Localization bias and spatial resolution of adaptive and non-adaptive spatial filters for MEG source reconstruction. *Neuroimage*, 25(4):1056–1067, 2005.

Carl Ed Senior, Tamara Ed Russell, and Michael S Gazzaniga. *Methods in mind*. The MIT press, 2006.

Krish D. Singh and Arjan Barnes, Gareth R. Hillebrand. Group imaging of task-related changes in cortical synchronisation using nonparametric permutation testing. *Neuroimage*, 19(4):1589–1601, 2003.

Warren E. Smith. Estimation of the spatio-temporal correlations of biological electrical sources from their magnetic fields. *Biomedical Engineering, IEEE Transactions on*, 39 (10):997–1004, 1992.

Olaf Sporns. *Networks of the Brain*. The MIT Press, 3rth edition edition, 2011.

Olaf Sporns and Giulio Tononi. Structural Determinants of Functional Brain Dynamics. In Viktor K. Jirsa and A. R. McIntosh, editors, *Handbook of Brain Activity*, pages 117–148. Springer, 2007.

Ramesh Srinivasan, William R. Winter, Jian Ding, and Paul L. Nunez. EEG and MEG coherence: measures of functional connectivity at distinct spatial scales of neocortical dynamics. *Journal of neuroscience methods*, 166(1):41–52, 2007.

C. J. Stam. Use of magnetoencephalography (MEG) to study functional brain networks in neurodegenerative disorders. *Journal od the Neurological Sciences*, 289(1):128–134, 2010.

C. J. Stam, B. F. Jones, I. Manshaden, A. M. Van Cappellen van Walsum, Montez T., J. P A. Verbunt, J. C. de Munck, B. W. van Dijk, H. W. Berendse, and P. Scheltens. Magnetoencephalographic evaluation of resting-state functional connectivity in Alzheimer's disease. *NeuroImage*, 32(3):1335–1344, 2006.

Thomas P. Trappenberg. *Fundamentals of Computational Neuroscience*. Oxford University Press, 2002.

Kimmo Uutela, M. Hmlinen, and Erkki Somersalo. Visualization of magnetoencephalographic data using minimum current estimates. *NeuroImage*, 10(2):173–180, 1999.

W. van Drongelen, M. Yuchtman, Barry D. Van Veen, and A. C. van Huffelen. A spatial filtering technique to detect and localize multiple sources in the brain. *Brain Topography*, 9(1):39–49, 1996.

Barry D. Van Van Veen and Kevin M. Buckley. Beamforming: A versatile approach to spatial filtering. *IEEE assp magazine*, 5(2):4–24, 1988.

Barry D. Van Van Veen, Win van Drogelen, Moshe Yuchtman, and Akifumi Suzuki. Localization of brain electrical activity via linearly constrained minimum variance spatial filtering. *Biomedical Engineering, IEEE Transactions on*, 44(9):867–880, 1997.

Jeremy G. VanAntwerp and Richard D. Braatz. A tutorial on linear and bilinear matrix inequalities. *Journal of Process Control*, 10(4):363–385, 2000.

J. Vrba. Magnetoencephalography: the art of finding a needle in a haystack. *Physica C: Superconductivity*, 368(1):1–9, 2002.

J. Vrba and Stephen E. Robinson. Signal processing in magnetoencephalography. *Methods*, 25(2):249–271, 2001.

Peter D. Welch. The use of fast Fourier transform for the estimation of power spectra: a method based on time averaging over short, modified periodograms. *IEEE Transactions on audio and electroacoustics*, 15(2):70–73, 1967.

Samuel J. Williamson and Leon Kaufman. Biomagnetism. *Journal of Magnetism and Magnetic Materials*, 22(2):129–201, 1981.

Liu Zhongming, Masaki Fukunaga, Jacco A. de Zwart, and Jeff H. Duyn. Large-scale spontaneous fluctuations and correlations in brain electrical activity observed with magnetoencephalography. *NeuroImage*, 51(1):102–111, 2010.

M. J. Zigmond, F. E. Bloom, S. C. Landis, J. L. Roberts, and L. R. Squire. *Fundamental neuroscience*. Academic Press, 1999.